

Alma Mater Studiorum - Università' di Bologna

DOTTORATO DI RICERCA

Fisica

Ciclo XXI

Settore scientifico disciplinare di afferenza: FIS/04

Improved cross-section on $n+^{197}\text{Au}$ from high resolution time-of-flight measurements at n_TOF and GELINA: the road to a new standard

Presentata da: Dott. Cristian Massimi

Coordinatore Dottorato
Prof. Fabio Ortolani

Relatore
Prof. Gianni Vannini

Esame finale anno 2009

**Improved cross-section on $n+^{197}\text{Au}$ from high resolution time-of-flight
measurements at n_TOF and GELINA: the road to a new standard**

by Cristian Massimi

Thesis submitted for the degree of Doctor of Science

Promotor: Prof. Gianni Vannini

This thesis is based on researches performed in collaboration with Dr. N. Colonna, Dr. P. Schillebeeckx and Dr. A. Borella.

A special thanks goes to S. Kopecky, A. Mengoni and M.C. Moxon for their valuable comments.

The measurements of this thesis have been carried out at CERN in Geneva, Switzerland and at the Institute of Reference Materials and measurements (IRMM) in Geel, Belgium.

Contents

Introduction	1
1 Nuclear data for science and technology	5
1.1 Stellar nucleosynthesis	5
1.1.1 Stellar evolution	6
1.1.2 The s-process	7
1.1.3 The Maxwellian-averaged neutron capture cross-section	10
1.1.4 Cosmos-chronometer	12
1.2 Nuclear data for nuclear energy	13
1.2.1 Nuclear waste transmutation	14
1.2.2 The Thorium cycle	16
1.3 Importance of the $^{197}\text{Au}(n, \gamma)^{198}\text{Au}$	18
1.4 Neutron data libraries	18
1.5 Status of ^{197}Au data libraries	20
1.6 Neutron time-of-flight facilities	23
2 Neutron induced reactions	27
2.1 Theory of resonance neutron reactions	27
2.1.1 Parametrisation of resonance neutron cross-sections	32
2.1.2 The R-Matrix expressions	33
2.1.3 Single Level Breit Wigner formula	36
2.2 Doppler broadening	38
2.3 Angular distribution of the gamma radiation	39
2.4 Resonance analysis of the experimental data	40
2.4.1 Area analysis	41
2.4.2 Resonance Shape Analysis (RSA)	44
3 n_TOF and GELINA neutron time-of-flight facilities	47
3.1 The time-of-flight method	47
3.2 Resolution function of TOF-spectrometers	52

3.3	n_TOF facility at CERN	55
3.3.1	Beam characteristics	57
3.3.2	Capture and fission instrumentation	59
3.4	GELINA Facility at EC-JRC-IRMM	60
3.4.1	Neutron production	60
3.4.2	Measurement stations	63
3.5	About the present $^{197}\text{Au}(n, \gamma)$ measurements	64
4	Measurement techniques and detectors	71
4.1	Transmission experiment	71
4.1.1	Principle	71
4.1.2	Transmission detector	72
4.2	Capture experiment	74
4.2.1	Principle	74
4.2.2	Neutron flux measurements	78
4.2.3	Capture detection systems	79
4.2.4	Total energy detection with C_6D_6 detectors	81
4.2.5	Total γ -ray absorption detector	84
4.3	Self-indication experiment	87
4.4	RSA codes REFIT and SAMMY	88
5	Measurements at CERN-n_TOF	93
5.1	Introduction	93
5.2	Total Absorption Calorimeter (TAC)	95
5.3	Analysis procedures	99
5.3.1	Capture yield determination	100
5.3.2	Capture yield normalization	102
5.3.3	Background measurements	103
5.3.4	Corrections to the capture yield	105
5.4	Results	112
5.4.1	Discussion of uncertainties	113
5.4.2	Capture kernels	113
5.4.3	Comparison between n_TOF data	123
5.4.4	Comparison with libraries	126
6	Measurements at IRMM-GELINA	129
6.1	Introduction	129
6.2	Transmission measurements	130
6.2.1	Experimental conditions	130
6.2.2	Data reduction	131
6.2.3	Results	133

6.3	Capture measurements	136
6.3.1	Experimental conditions	136
6.3.2	Data reduction	139
6.3.3	Normalization	141
6.3.4	Results	143
6.4	Self-indication measurement	146
6.4.1	Experimental conditions	146
6.4.2	Data reduction	146
6.4.3	Results	146
6.5	Resonance shape analysis of the experimental data	148
6.5.1	The new resonance parameters up to 200 eV	149
6.5.2	The adjusted parameters of the first 4.9 eV resonance	149
6.6	Comparison with n_TOF TAC data	154
	Conclusions	155
	Appendix	158
	A Boundary conditions to the R-matrix	159
	B Practical approximations to the R-matrix	161
	B.1 Reich-Moore approximation	161
	B.2 Multi Level Breit Wigner approximation	162
	C Statistical properties of the resonance parameters	163
	D Principles of neutron flux measurement	171
	D.0.1 The $^{10}\text{B}(n, \alpha)$ reaction	171
	D.0.2 The $^6\text{Li}(n, \alpha)$ reaction	172
	Bibliography	174

Introduction

One of the most striking features of neutron-nucleus interactions is the resonance structure observed in the reaction cross-sections at low incident neutron energies. Since the electrically neutral neutron has no Coulomb barrier to overcome, and has a negligible interaction with the electrons in matter, it can directly penetrate and interact with the atomic nucleus, even at very low kinetic energies, of the order of millielectron-volts. The cross-sections can show variations of several orders of magnitude on an energy scale of only a few eV. The origin of the resonances is well understood: they are related to the excitation of nuclear states in the compound nuclear system formed by the neutron and the target nucleus, at excitation energies lying above the neutron binding energy of typically several MeV.

The compound nucleus model was introduced by Niels Bohr to explain the observed resonances in neutron-nucleus reactions. The wavelength of low energy neutrons is comparable to the size of the nucleus. Typical widths Γ of measured resonances are of the order of millielectron-volts. According to Heisenberg's uncertainty principle, the corresponding life time of the compound nucleus is of the order of $\tau = \hbar/\Gamma \approx 10^{-15}$ s, several orders of magnitude larger than the typical time needed by a neutron to cross a nucleus without interaction. In this picture, the neutron binding energy which becomes available to the compound nucleus, is rearranged among all nucleons, and gives rise to a complex configuration corresponding to a well defined nuclear state with given energy, spin and parity. The compound nucleus may then decay through the energetically allowed channels. The mode of decay and the decay probability of the compound nucleus is considered to be independent from the way the compound nucleus was formed. The decay probability is equal to the branching ratio Γ_x/Γ where Γ_x is the width related to the decay by emission of a particle x , which at low energy is mainly a γ -ray (radiative capture) or a neutron (elastic scattering) or a fission fragment (fission). All these reactions show resonances at the energies corresponding to the excitation of the nuclear levels in the compound nucleus. The shapes of the resonances are different and related to the involved widths. Isolated resonances have the familiar Breit-Wigner shape.

In the energy interval from thermal neutron energies to a few MeV the neutron cross-sections have a resonance-type energy dependence and large differences exist among the neighbouring isotopes. In the resonance region, two energy domains need

to be established:

- the resolved resonance region where the resonances are well separated (the distance between them is larger than the natural width and the instrumental resolution);
- the unresolved resonance region where the resonances structure still exists, but it can not be resolved due to the limited instrumental limitation.

The resonance structure, which largely differs from isotope to isotope, can not be predicted or reproduced by models. Therefore, experiments with high energy resolution over the whole spectrum are necessary and the required resolution and accuracy can be only obtained at neutron Time-Of-Flight (TOF) facilities.

In the resolved resonance region, which includes the thermal region, the reaction cross-sections can be rigorously described in terms of resonance parameters, which reflect the properties of the excited states like energy, decay widths, spin and parity. This is done by means of the R-matrix theory, which is outlined in more detail in Chapter 2. Especially developed R-matrix codes allow to calculate accurate resonance parameters by using the technique of resonance shape analysis.

The parameterization of resonant cross-sections by the R-matrix formalism needs relatively few data and permits to establish reliable data base of reactions, which are essential for many areas of research and applications. The R-matrix description can be extended to the unresolved resonance region, where average resonance parameters can be used to obtain the cross-sections. Therefore, in this energy region the experimental data are compiled and once evaluated, made available through nuclear data libraries. At higher energies optical model calculations are used: the interaction with the nucleus is modelled by a complex potential well. The cross-sections can be calculated solving the Schrödinger equation. The difficulty lies in the parameterization of the potential, which can only be optimised by comparison with experimental data.

Neutron induced reaction cross-sections are of great importance for reactor physics. In particular they are vital when evaluating the safety and risks related to the operation of nuclear power plants and to nuclear waste management. Furthermore the development of innovative systems like accelerator-driven transmutations system or new concepts of nuclear power production must rely on complete, accurate and consistent neutron data libraries. Finally, reducing uncertainties in the neutron cross-section data can result in an enhanced safety and efficiency of present and future nuclear power systems. Accurate neutron cross-sections also play a role in several other fields, including astrophysics and fundamental symmetries. More in detail, to understand the present chemical abundance of elements in stars, neutron cross-sections are the basic ingredient, since the formation of elements heavier than Iron is due to

successive radiative capture followed by β -decay. In this picture, the neutron cross-sections of particular isotopes can be used to derive the age of the Universe. Some items will be discussed in Chapter 1. In addition, important information on level densities, a key ingredient in many nuclear reaction codes, can be obtained directly from neutron resonance spectroscopy.

Motivation of the present work

Neutron cross-section standards are important for measuring and evaluating all other reaction cross-sections. Only few cross-section can be defined as absolute, while most of known cross-sections are measured relative to the so-called standards [1, 2]. The need to improve and extend the cross-section standard in wide energy ranges is based on the need of new and accurate precise experimental data, related to Nuclear Astrophysics and to application to advanced nuclear system (like the sub-critical Accelerator Driven System and the Generator IV fast reactors). The new development in the measurements and analysis techniques as well as in the neutron facilities, can in principle result in more accurate data on a variety of isotopes. The accuracy of cross-section measurements is however limited by the uncertainty in the standard cross-sections used as reference, needed for determining absolute values. Improvements in all cross-sections can therefore be obtained only if the standards are improved.

The cross-section standards in the ENDF/B-VI library are the $H(n,n)$, ${}^3\text{He}(n,p)$, ${}^6\text{Li}(n,t)$, ${}^{10}\text{B}(n, \alpha)$, ${}^{10}\text{B}(n, \alpha_1\gamma)$, ${}^{12}\text{C}(n,n)$, ${}^{197}\text{Au}(n, \gamma)$ and ${}^{235}\text{U}(n,f)$ reactions. The Nuclear Energy Agency Nuclear Data Committee/International Nuclear Data Committee (NEANDC/INDC) Nuclear Standards Files includes the ${}^{238}\text{U}$ cross-section as a standard, while it does not consider the ${}^3\text{He}(n,p)$ cross-section to be a standard (see Table 1). These particular reactions have gained the status of standards over the years and are widely used to normalise the data from neutron cross-section ratio experiments. Each reaction used as standard is associated with a specific energy range over which it is well known.

For the neutron capture reactions, ${}^{197}\text{Au}(n, \gamma)$ is considered a standard of measurement in the energy range between 0.2 MeV to 2.5 MeV, where in fact it is the only standard. At thermal energy, beside ${}^{197}\text{Au}$, ${}^{59}\text{Co}$ and ${}^{55}\text{Mn}$ are also considered well known.

The aim of this work is to propose an extension of the energy region of the $\text{Au}(n, \gamma)$ standard also in the Resolved Resonance Region (RRR). The new data reported here are based on extensive and very accurate measurements of partial and total reaction cross-section performed at different facilities and with different detectors and detection techniques.

Chapter 3 presents an overview of both neutron time-of-flight facilities n_TOF (at CERN) and GELINA (at the EC-JRC-IRMM multidisciplinary laboratory of the Eu-

Table 1: Cross-sections considered as a standards in the ENDF/B-VII evaluation [3] and/or in the NEANDC/INDC [4]. A series of complementary cross-sections have been involved in the standard evaluation, but they cannot be considered as a standard (for example: ${}^6\text{Li}(n,n)$, ${}^{10}\text{B}(n, \alpha_0)$, ${}^{10}\text{B}(n,n)$ and ${}^{238}\text{U}(n, \gamma)$).

Nuclear reaction	ENDF/B-VI standard	IAEA standard	Energy range of standard
H(n,n)	Yes	Yes	1 keV to 20 MeV
${}^3\text{He}(n,p)$	Yes	No	Thermal to 50 keV
${}^6\text{Li}(n,t)$	Yes	Yes	Thermal to 1 MeV
${}^{10}\text{B}(n, \alpha)$	Yes	Yes	Thermal to 250 keV
${}^{10}\text{B}(n, \alpha_1\gamma)$	Yes	Yes	Thermal to 250 keV
${}^{12}\text{C}(n,n)$	Yes	Yes	Below 1.8 MeV
${}^{197}\text{Au}(n, \gamma)$	Yes	Yes	Thermal and 0.2 to 2.5 MeV
${}^{235}\text{U}(n,f)$	Yes	Yes	Thermal and 0.15 to 20 MeV
${}^{238}\text{U}(n,f)$	No	Yes	Thermal to 20 MeV

ropean Commission). In these TOF facilities, neutrons are produced by the impact of a narrow pulse of high-energy particles on a neutron-producing target. The impinging particles at n_TOF are protons, which generate neutrons via the spallation reaction, while at GELINA neutrons are produced via electron bremsstrahlung and consecutive photonuclear reactions.

The description of the detectors and experimental techniques used in the measurements are reported in Chapter 4. Capture detectors are based on the detection of the γ -ray cascade following the neutron capture reaction. At GELINA an array of two or four liquid scintillator C_6D_6 detectors has been used for the capture cross-section measurement, while at n_TOF the reaction was studied with the new and more complex 4π "Total Absorption Calorimeter" (TAC). Such a device was used in the n_TOF measurement for the first time, so that an accurate study of its response and performances had to be performed. A part of the thesis work was devoted specifically on this point, discussed in detail in Chapter 5.

The procedure adopted at GELINA for data reduction from raw data to capture yield or transmission factor has been already described and explained in several publications, and it has become a standard procedure. Therefore in Chapter 6, we only report the main results: the resonance parameters resulting from the R-Matrix calculations from thermal energy up to 200 eV, thus including the first 4,9 eV resonance.

Chapter 1

Nuclear data for science and technology

Data on neutron induced reactions are of great importance for reactor physics and play also an important role in several other fields, including Astrophysics, fundamental physics and symmetries. Some of these motivations are discussed in the following sections. Many of the existing experimental data have been compiled and, once evaluated, made available through nuclear data libraries. Nevertheless new developments in the field of emerging nuclear technologies require more accurate data and new measurements for a large number of isotopes. Precise data are also required to refine models in Nuclear Astrophysics, as well as to improve the knowledge in fundamental Nuclear Physics and related theories.

1.1 Stellar nucleosynthesis

The origin of the chemical elements in the stars has always been a very interesting topic, especially since its comprehension helps to gain insight on the evolution of the Universe. Hydrogen and Helium, and small amounts of Lithium, were formed in the time period between about 100 seconds and 30 minutes after the Big Bang [5]. This period of primordial nucleosynthesis was followed by galactic condensation and the formation of stars. All elements heavier than Lithium have been formed in stars. Up to Iron, the dominant process is fusion and charged particle reactions. Elements heavier than Fe are instead mostly produced by neutron capture processes. The isotopic abundances in the solar system reflect the average composition of the galaxy as it was 4.5×10^9 years ago, the period of its formation. Spectral information of stellar environments and isotopic analysis of presolar dust grains are some of the most important observations that can be used to study isotopic abundances and models of stellar evolution.

1.1.1 Stellar evolution

The classification of stars is made by means of the Hertzsprung-Russel (HR) diagram, where the luminosity or brightness of a star is plotted against its surface temperature. The surface of a star emits nearly black body radiation with a spectral distribution showing a dominant component on the blue spectral side for hotter stars and on the red side for cooler stars. The HR diagram reveals interesting patterns, as can be seen in Figure 1.1. The positions of the stars are not randomly distributed and more than 90% of the stars are on the so-called main sequence, a large band going from the hot and bright heaviest stars to cooler and less luminous lighter ones. Note that the temperature on the x-axis is decreasing, since it was historically represented by increasing wavelength. In the main sequence the luminosity of a star is related to the mass of the star. Above the main sequence the red giants and supergiants can be identified. These stars are very luminous, but have a relatively low surface temperature. On the lower side of the main sequence are the white dwarfs, relatively small stars with a high surface temperature. The diagram does not represent a static situation. During its evolution a star follows a path through the Hertzsprung-Russel diagram, starting somewhere on the main sequence, where it spends about 90% of its life. In a simple picture, a star in its early stage consists of a mixture of Hydrogen and Helium. The temperature increases due to the gravitational contraction and the Coulomb barrier for protons can be overcome to start fusion reactions, which build up ${}^4\text{He}$. The radiation pressure counter-balances the gravitational force and the star is in equilibrium. Our Sun is at this stage together with the majority of the stars in the main sequence. When all Hydrogen has been burned the gravitational collapse starts again, increasing the temperature until it reaches a value higher than the Coulomb barrier between ${}^4\text{He}$ nuclei. The outer envelope of the star increases while the surface temperature decreases. In this phase the star has become a red giant. At this stage Carbon is formed through the $3\ {}^4\text{He} \rightarrow {}^{12}\text{C}$ reaction, possible because of the presence of a ${}^{12}\text{C}$ resonance at an excited state of 7.65 MeV. Subsequent (α , γ) reactions produce heavier nuclei, with a decreasing abundance for heavier isotopes because of the increasing Coulomb barrier. The less massive stars with masses up to a few Solar masses, will end up as a hot carbon core which eventually cools down to become a white dwarf. For more massive stars, when the ${}^4\text{He}$ fuel has been mostly consumed, the carbon core collapses due to the gravitational force. The temperature of the star increases again, so allowing fusion reactions of heavier nuclei. This chain of nucleosynthesis by charged particle reactions, in combinations with photodissociation reactions, ends up at the $A=56$ nuclei with a large abundance of ${}^{56}\text{Fe}$. For heavier nuclei, charged particle fusion reactions are energetically not allowed anymore. The Iron core may in turn collapse until it reaches a nuclear density so high that other infalling matter bounces off the core producing a supernova explosion.

The HR diagram is a picture of the situation at a given fixed instant. During their

evolution, stars spend most of their life in the main sequence burning Hydrogen. At the end of their lives, when the Hydrogen has been exhausted, they leave the main sequence for the final phase of their evolution. The lifetime of a star strongly depends on its mass. A small cool red star with a temperature of about 3000 K can have a lifetime as long as 10^{14} years, while a heavy supermassive star of 2×10^4 K may live for only 10^6 years. Our Sun with a surface temperature of 6000 K has a lifetime of about 8×10^9 .

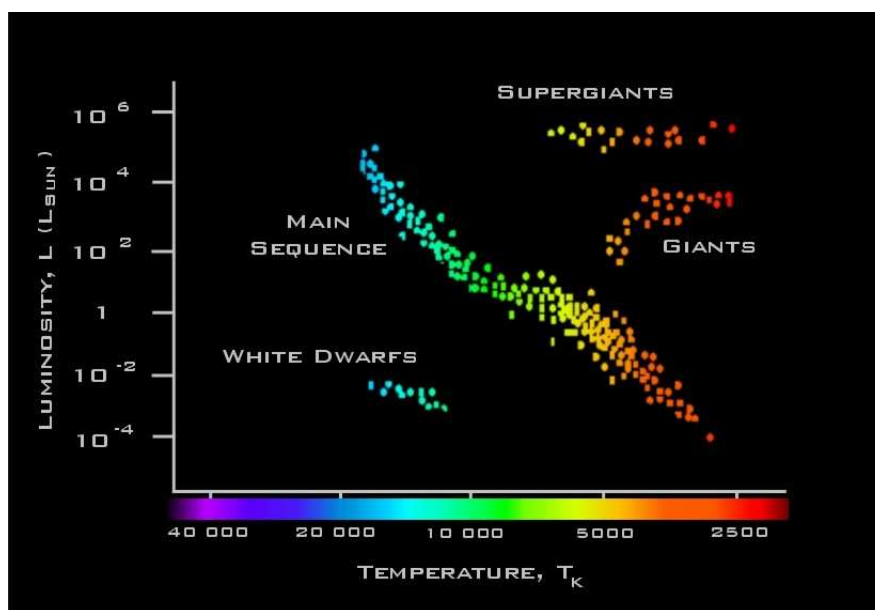


Figure 1.1: Schematic view of the Hertzsprung-Russel diagram. Picture from [6].

1.1.2 The s-process

Stellar Nucleosynthesis has first been extensively reviewed in the reference work [7] and more recently in Ref. [9, 10]. The isotopes up to ^{56}Fe can be synthesized by fusion reactions during the different stages of evolution of a star. It is nowadays well established that neutron capture processes in red giant stars and supernovae are responsible for the formation of nearly all isotopes with mass higher than Fe ($A > 60$) [7, 11]. This was first recognized by the discovery of Technetium in giant stars [12]. The element Tc has no stable isotopes and the lifetimes are short compared to the stellar evolution times, proving that the element had been formed in the star. The neutron capture mechanisms are divided into the s-process and r-process, where "s" stands for slow and "r" for rapid, referring to the time scale on which the neutron capture takes place. The neutrons needed for the capture process are produced mainly from the $^{22}\text{Ne}(\alpha, n)^{25}\text{Mg}$ and $^{13}\text{C}(\alpha, n)^{16}\text{O}$ reactions. The s- and r-process are important in

the production of stable and neutron rich isotopes. A competing mechanism is the p-process, which includes photodisintegration reactions like (γ, n) , (γ, p) and (γ, α) . These reaction influence the abundance from the proton rich side of the chart of the nuclei. If the nucleus formed after neutron capture is unstable against beta decay, it may decay before it captures a second neutron. This is typically what happens in the s-process, the principal process in the red giant stars, where thousands of years may pass between two successive neutron captures. In this way, many of the isotopes from ^{56}Fe to ^{209}Bi are formed. Nuclei heavier than Bismuth are unstable and can not be formed by neutron capture of the s-type. The s-process path follows closely the valley of stability in the chart of the nuclei and ends at ^{209}Bi . A thorough knowledge of the s-process, for which extensive experimental data are available, helps in putting constrains on the r-process.

In the r-process the neutron capture process is much faster and occurs on a much shorter time scale. The time between consecutive neutron captures is of the order of the second. The extremely high neutron fluxes, needed in the r-process are available only in astrophysical site of explosive nature, like in a supernovae. The competition between neutron capture and beta decay follows much longer sequences of successive neutron captures, until the beta decay half life is too short and the path proceeds through beta decays towards stability. Since the path of the r-process can go very far towards the neutron drip line before beta decay occurs, nuclei heavier than ^{209}Bi can be formed in this way. The actinides, which can not be formed by the s-process, have been formed mainly by the r-process.

At a given point in the neutron capture chain the probability of beta decay and neutron capture may be comparable. This constitutes a branching point in the nucleosynthesis path. Neutron capture cross-sections are a key ingredient in the development of stellar models that can be used for understanding nuclear abundances in stellar environments. At the branching points, uncertainties in the cross-sections can propagate into large differences in the production of higher mass nuclei within a given model.

For the classical s-process one has to assume that there exists a steady neutron flux, low enough so that β -decay is faster than neutron capture. A pre-existing seed distribution has to be exposed to this neutron irradiation. The change in time of the abundance N_A of an element with atomic mass A and charge number Z can be written as:

$$\begin{aligned} \frac{dN_{A,Z}}{dt} &= \sum \text{creation terms} - \sum \text{destruction terms} = \\ &= \lambda_{A-1,Z}^n N_{A-1,Z} + \lambda_{A,Z-1}^\beta N_{A,Z-1} + \\ &\quad - \lambda_{A,Z}^n N_{A,Z} - \lambda_{A,Z}^\beta N_{A,Z} \end{aligned} \quad (1.1)$$

where λ^n and λ^β are the neutron capture and β -decay rate, respectively. λ^n is defined

as:

$$\lambda_A^n = \frac{1}{\tau_n} = n \langle \sigma v \rangle_A, \quad (1.2)$$

being n the neutron density, σ the capture cross-section and v the relative velocity. The β -decay rate $\lambda^\beta = \frac{1}{\tau_\beta}$ must be considered only if the isotope is unstable. When an unstable isotope ${}^A_N X_Z$ is formed by neutron capture of the previously formed stable isotope ${}^{A-1}_{N-1} W_Z$, it will decay (via β decay) to the next isotope ${}^A_{N-1} Y_{Z+1}$. Thus, the abundance of ${}^A Y$ is completely determined by the neutron capture rate of ${}^{A-1} W$. Therefore, Eq. 1.1 can be rewritten as:

$$\begin{aligned} \frac{dN_A}{dt} &= \lambda_{A-1}^n N_{A-1} - \lambda_A^n N_A - \lambda_A^\beta N_A = \\ &= \lambda_{A-1}^n N_{A-1} - N_A (\lambda_A^n + \lambda_A^\beta) \end{aligned} \quad (1.3)$$

Eq. 1.3 leads to a set of coupled differential equations which can not be solved for the most general cases. Therefore, some simplifications are generally adopted. Assuming constant temperature and neutron density, it follows that [7]:

$$\langle \sigma v \rangle_A = \sigma_A v_T \quad (1.4)$$

with σ_A the Maxwellian-averaged neutron capture cross-section (MACS, discussed in the next section) for an isotope with atomic mass A and v_T the mean thermal neutron velocity. When either $\lambda^n \ll \lambda^\beta$ or $\lambda^n \gg \lambda^\beta$, Eq. 1.1 can be simplified. Denoting with τ the neutron exposure¹, the following equation can be written:

$$\frac{dN_A}{d\tau} = \sigma_{A-1} N_{A-1} - \sigma_A N_A \quad (1.5)$$

The processes described by this set of coupled differential equations have the tendency to be self-regulating. This means that after sufficiently long irradiation an equilibrium between the destructing and formation terms establishes, leading to $\frac{dN_A}{d\tau} = 0$. Therefore for a s-only² nucleus the product of the average capture cross-section $\langle \sigma_\gamma \rangle_{kT,A}$ and the abundance of isotope $N_{s,A}$ is constant:

$$\langle \sigma_\gamma \rangle_{kT,A} N_{s,A} = \text{constant}. \quad (1.6)$$

Indeed observations confirm that this is roughly the case, except for nuclei with neu-

¹It represents the time integrated neutron flux:

$$\tau = \int_0^t \phi(t') dt' = v_T \int_0^t n(t') dt'$$

where $\phi(t)$ is the neutron flux, defined as $v_T n(t)$.

²A nucleus that can be formed only by the s-process.

tron magic numbers ($N=28,50,82,126$) around $A=88,140$ and 208 , which have very low capture cross-sections. These nuclei are bottlenecks in the s-process paths, and show up as peaks in the abundance distribution.

The s-only nuclei are shielded from the r-process by stable isobars of nuclei with lower Z and for which contributions from the proton rich side of the valley of stability are commonly neglected. In the same way r-only³ nuclei have no contribution from the s-process. In Figure 1.2 the neutron capture path of the s-process and r-process are

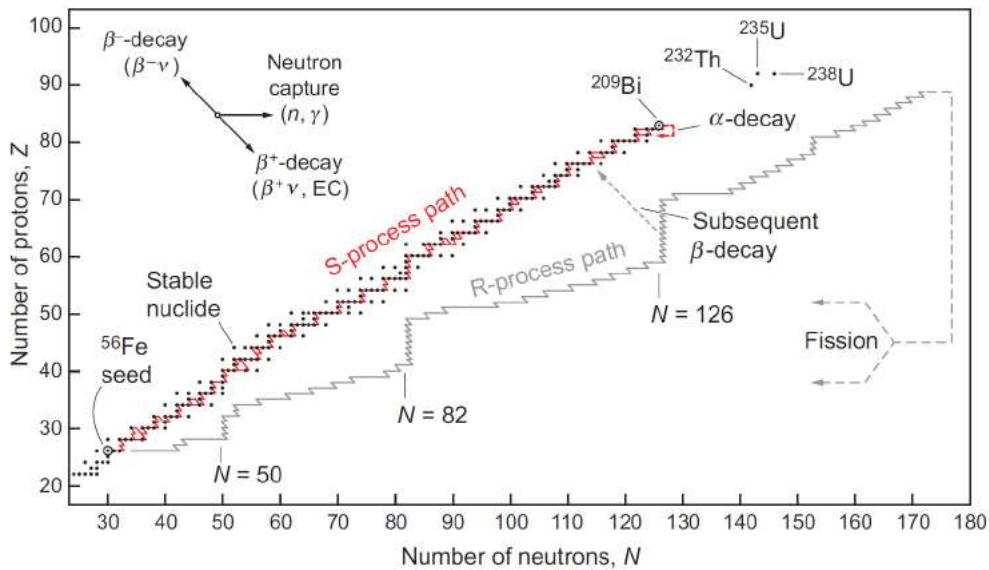


Figure 1.2: Neutron capture path of the s-process and r-process shown on the chart of the nuclides. Hatched zone indicates the r-process nucleosynthetic pathway for a plausible neutron flux. Neutron ‘magic numbers’ are indicated by vertical lines, and mass numbers of nuclide abundance peaks are marked. Picture from [8].

shown. Some stable nuclides are not reached by the s-process path and are endpoints of r-process and beta-decay cascades.

1.1.3 The Maxwellian-averaged neutron capture cross-section

In the refinement of stellar models, the neutron data input is needed in the form of cross-sections averaged over the kinetic energy distribution of the stellar neutrons. Average neutron capture cross-sections can be calculated from the energy dependent ones. In stellar environments, the relative velocities v between the neutrons and the target isotopes follow a Maxwell-Boltzmann distribution at a temperature T . The reaction rate, λ_A^n describing the formation of a nuclide is $n\langle\sigma_\gamma v\rangle$ (Eq. 1.2), which in

³A nucleus that can be formed only by the r-process.

certain assumption can be written as $n\langle\sigma_\gamma\rangle_{kT}v_T$. The reaction rates are therefore proportional to the Maxwellian-averaged neutron capture cross-section, given by:

$$\sigma_A = \langle\sigma_\gamma\rangle_{kT} = \frac{\langle\sigma_\gamma v\rangle}{\langle v\rangle} = \frac{2}{\sqrt{\pi}(kT)^2} \int_0^\infty \sigma_\gamma(E) E e^{-\frac{E}{kT}} dE. \quad (1.7)$$

Here σ_γ is the neutron capture cross-section at the total kinetic energy in the centre of mass system. Relevant temperatures for current models range from $kT=5$ keV to 100

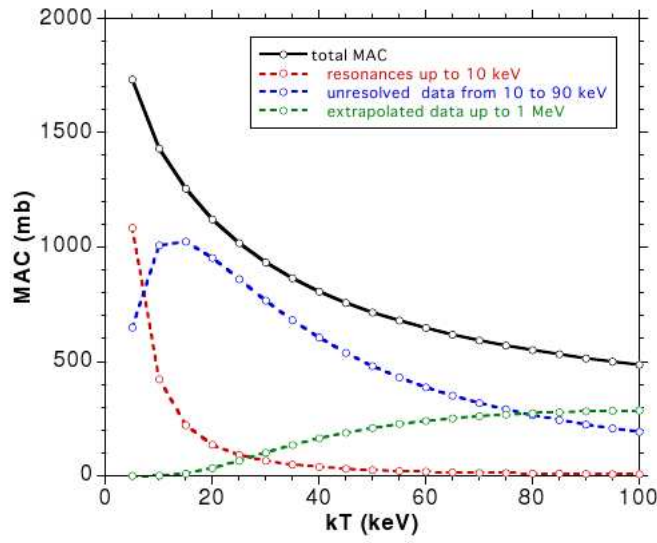


Figure 1.3: The Maxwellian averaged capture cross-section for ^{99}Tc as a function of the stellar temperature. The contributions from both the resolved and the unresolved resonance region are also given. Picture from [13].

keV. In fig 1.3 the MACS is shown for the radioactive nuclide ^{99}Tc as a function of the temperature. The contribution of the resolved resonances in the cross-section below 5 keV is also given. Its importance is far from being negligible at low stellar temperatures. A more sophisticated modelization requires, as a consequence, an accurate knowledge of the neutron cross-sections to test stellar evolution models against observational data.

Neutron cross-section are known for many isotopes but the quality of existing data is not always sufficient, in particular for isotopes with small cross-sections or for radioactive isotopes. Innovative neutron facilities characterized by high instantaneous neutron flux and very low background are the only installation where accurate measurement of neutron capture cross-section for these isotopes can be performed. The n_TOF facility is one of such installations.

1.1.4 Cosmos-chronometer

The age of the universe can be obtained by summing over the duration of the following four stages:

1. Big bang nucleosynthesis with the production of the lightest elements such as ^1H , ^2H , ^3He , ^4He , and ^7Li (time interval $\cong 10^6$ y).
2. Galaxy formation (time interval $\cong 1 \sim 2$ Gyr).
3. Stellar nucleosynthesis with fusion reactions involving charged particles ($^4\text{He} \sim A \lesssim 60$), neutron capture nucleosynthesis by the s- and r- process complemented by the p processes ($A \geq 60$). Time interval (Δ) to be determined by means of Nuclear cosmo-chronology).
4. Formation of the Solar System (time interval = 4.55 Gyr).

One way of determining the duration of nucleosynthesis prior to the Solar system is to study the decay of long-lived nuclei (they are shown in Table 1.1).

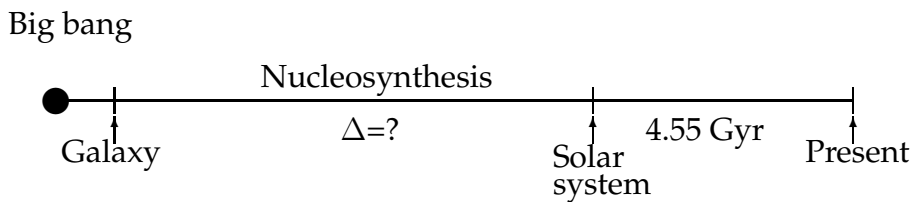


Figure 1.4: Time line of nuclear cosmo-chronology

The $^{232}\text{Th}/^{238}\text{U}$, $^{235}\text{U}/^{238}\text{U}$ and $^{244}\text{Pu}/^{238}\text{U}$ ratios refer to the abundances at the beginning of the Solar system and can be extrapolated back in time by means of their known half lives. The determination of the age of the Universe is therefore reduced to the problem of estimating their production in time through a chemical evolution model.

Table 1.1: Long-lived nuclear chronometers

Nucleus	Daughter	Decay mode	Half-life (yr)	Nucleosynthesis
^{232}Th	^{208}Pb	Decay chain	1.4×10^{10}	r - process
^{238}U	^{206}Pb	Decay chain	4.5×10^9	r - process
^{235}U	^{207}Pb	Decay chain	7.0×10^8	r - process
^{187}Re	^{187}Os	β^-	4.5×10^{10}	r - process

The nucleosynthesis of Os and Re represents an important alternative with respect to the actinides chronometers. While ^{186}Os and ^{187}Os are synthesized only by the

s process, an important fraction of the observed abundance of ^{187}Os is due to the extremely slow β -decay of ^{187}Re ($t_{1/2} = 41.2$ Gyr). Clayton [14, 15] proposed to use this decay to determine the time-duration of the Galactic nucleosynthesis, and hence, the age of the Universe. That is the so-called Re/Os clock.

For the analysis of the Re/Os clock, the essential nuclear data are the neutron capture cross-sections of $^{186,187}\text{Os}$. With the aim of improving the nuclear data requirements for the Re/Os clock, accurate measurements of those cross-section were recently performed at n_TOF[16, 17].

Preliminary results based on the n_TOF measurements set the age of the universe at 15.3 ± 3 Gyr, while other nuclear chronometer such as the Th/U clock provide 13.4 ± 3 Gyr. From astronomical and cosmological observations the age of the universe correspond to 13.7 ± 0.2 Gyr and 14 ± 1 Gyr respectively.

1.2 Nuclear data for nuclear energy

Another field that heavily relies on neutron cross-section data is the field of nuclear technology, in particular for energy production. Within the next 50 years, the world's energy need is expected to double. In order to face this demand, a long term energy supply strategy is indispensable. At present about 80% of the energy production comes from fossil resources, i. e. coal, oil and gas [18, 19]. The known and exploitable reserves are thought to be exhausted in about 100 years for oil and gas, and in about 250 years for coal. The apparent abundance of fossil fuel has for long time inhibited a strong effort for the search of alternative energy sources. Only recently, global warming associated to the emission of green-house gasses like CO_2 , produced by the combustion of fossil fuel, is becoming a widely spread concern. Other energy sources, like solar or wind, are in full technological development but can only satisfy a small fraction of the total energy needs. Nuclear fusion is still in a research phase and its commercial exploitation is far beyond the near future.

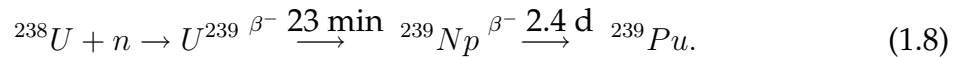
On the contrary, energy from nuclear fission is a well mastered technique today. For example, in France, about 75% of the electricity production comes from nuclear energy. The nuclear electricity production is about 30% in the European Union and 7% worldwide. In addition to non-proliferation concerns, a satisfactory solution of the nuclear waste problem is a necessary condition for the public acceptance of nuclear energy in the years to come. Several research lines address this issue. Safe solutions for geological disposal are studied. Also considered, possibly as a complementary solution, is the option of transmutation of nuclear waste. This consists in transforming the radioactive isotopes into stable or less radiotoxic ones via neutron capture and neutron fission reactions. Other options are the reduction of the long-term radiotoxic inventory of nuclear waste by using different fuel cycles in existing or conceptually new reactors [20, 21, 22, 23, 24]. A fuel cycle based on thorium, pro-

ducing much less radiotoxic actinides is a promising alternative.

In parallel, research is concentrated on the development of a future generation of nuclear power reactors, also known as Generation IV [25], to be operational by 2030. A number of concepts have been retained for investigation, research and development, namely the Very High Temperature Reactor (VHTR), the Gas Cooled Fast Reactor (GFR), the Lead-Cooled Fast Reactor (LFR), the Sodium Cooled Fast Reactor (SFR), the Supercritical Water Cooled Reactor (SCWR), and the Molten Salt Cooled Reactor (MSR). In all cases, an efficient use of the fuel is being pursued, which has the consequence of a smaller production of nuclear waste. Furthermore, the use of the fast reactors would ensure that a large fraction of the transuranic elements are burned, thus minimizing the high level nuclear waste to be disposed in geological repositories.

1.2.1 Nuclear waste transmutation

Conventional nuclear power reactor are based on the fission process of ^{235}U and ^{239}Pu . While ^{235}U is fissile, the fertile uranium isotope ^{238}U produces the fissile ^{239}Pu isotope as a consequence of the neutron capture reaction followed by beta-decay during the operation of the reactor:



The abundance of ^{235}U in natural Uranium is about 0.7%. In order to be used in a thermal reactor an enrichment of the fuel to about 3% is typically used, leaving a remaining 97% of ^{238}U . A large range of radiotoxic isotopes, with a wide variety of half lives and yields, is generated as a consequence of fission or successive neutron captures. A plot of the half life versus the individual fission yield, reported in Figure 1.5, shows clearly the long living fission products. On a relatively short time scale, most radiotoxicity is due to those fission products, with relatively few long lived fission products remaining after a few hundreds years.

Transmutation can change the nuclear properties drastically. This is illustrated by the fission product ^{99}Tc which has a half life of 2×10^5 years. After capture of a neutron, the formed nucleus ^{100}Tc decays with a half life of 15.8 s to the stable isotope ^{100}Ru . Considering its ability to migrate in storage glasses, ^{99}Tc is a particularly suited candidate for transmutation. For these reasons the neutron induced cross-sections of long lived fission products such as ^{99}Tc and ^{93}Zr have been recently investigate [27, 28, 29, 30].

The large amount of ^{238}U in the fuel is the basis of the production of the highly radiotoxic actinides by successive neutron captures and beta decays, leading to the formation of isotopes of Pu, Am and Cm. In Table 1.2 the composition of the long-lived nuclear waste produced per year in France is given.

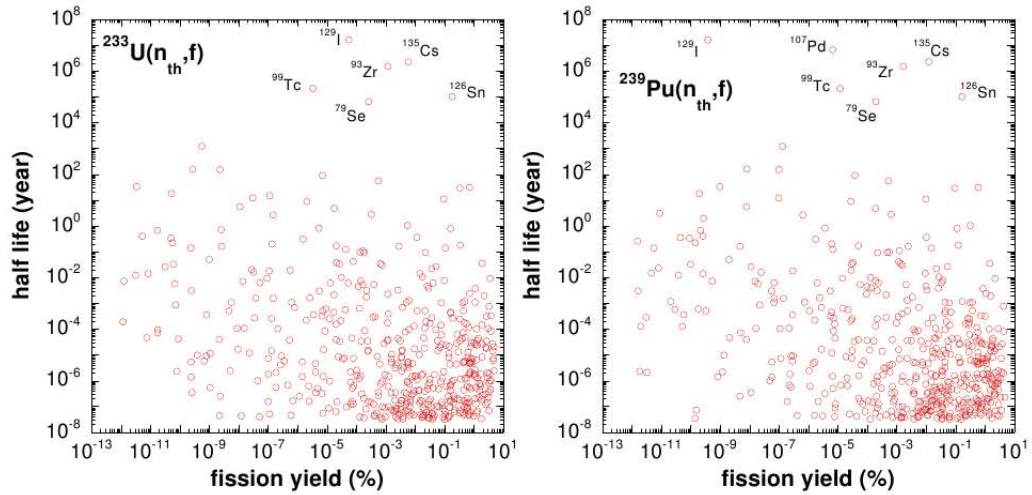


Figure 1.5: The half-life and yield of fission products produced with thermal neutrons on ^{235}U and ^{239}Pu . Data from [26]

Table 1.2: Inventory of the yearly production in France (about 1/2 of all European production) of the most important long living fission products and minor actinides, considered as a nuclear waste. Data from [31]

isotope	production (kg/year)	half life (year)
^{79}Se	5	1.1×10^6
^{93}Zr	800	1.5×10^6
^{99}Tc	900	2.1×10^5
^{107}Pd	200	6.5×10^6
^{126}Sn	20	1.0×10^5
^{129}I	200	1.6×10^7
^{135}Cs	400	2.3×10^6
^{237}Np	500	2.1×10^6
^{241}Am	250	432
^{243}Am	100	7370
^{244}Cm	25	18.1
^{245}Cm	1.5	8500

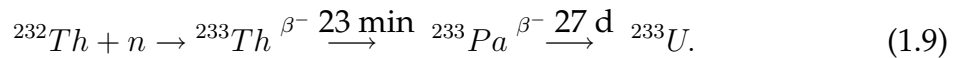
The transmutation process can take place in a high neutron flux environment. For fission fragments the transmutation proceeds through capture reactions, so that the neutron flux present in thermal reactors can be used. For actinides (in particular Np, Am, Cm) the most effective process is fission, whose cross-section however may present a threshold around 1 MeV. For this reason fast reactor are needed.

Alternatively, Accelerator Driven Systems (ADS) can be used. An ADS consist of a high energy proton accelerator, a spallation target and a subcritical core [32, 33] and has an increased passive safety as compared to conventional critical reactors. Different types of subcritical system have been proposed. In many design studies a liquid core of lead and bismuth is considered, acting as a spallation neutron source. The use of ADS systems has been proposed in configurations useful for waste transmutation but also for energy production, for example in combination with thorium-based fuel.

A large worldwide research programme on nuclear data in the second half of the 20th century has permitted the construction of vast databases of continuously growing quality. However, they are not adequate for a precise assessment of the transmutation rates⁴ in given neutron fluxes with given energy spectra as well as for criticality and safety calculations, accurate values of the relevant cross-sections are still needed. Since today's nuclear power reactors are all based on the uranium cycle, important lacks exist in nuclear data for these new applications.

1.2.2 The Thorium cycle

Another approach to reduce the amount of nuclear waste, notably the higher actinides, is to use an alternative fuel cycle based on ²³²Th. Detailed concepts can be found in References [32, 33]. The isotope ²³²Th is not fissile but after neutron capture followed by beta decay, the fissile isotope ²³³U is produced. In the Th/U cycle the fissile isotope ²³³U results from the following chain:



An interesting advantage from the point of view of production of radioactive waste in using the ²³²Th/²³³U-based fuel cycle as compared to the Uranium cycle is related to the low production of higher mass actinides. The lower atomic number of Thorium (Z = 90 instead of Z = 92 for Uranium) reduces significantly the build-up of heavy transuranium isotopes, in particular Plutonium Americium and Curium. This is also clearly demonstrated by detailed simulations on the isotopic composition of a Thorium-based ADS system [34]. In Figure 1.6 a schematic view of the isotope production in the thorium cycle is shown. The natural abundance of thorium is three to five times larger than that of uranium, thus extending potentially the existing fuel re-

⁴Considering the loading of the reactor cores with quantities of isotopes to be transmuted.

sources. Furthermore, the number of neutrons produced for each absorbed thermal neutron in a reactor environment is larger for ^{233}U than for ^{235}U or ^{239}Pu , opening the possibility, although technically still quite complicated, for a “thermal breeder”. Several experimental projects using Thorium have already been worked out in the

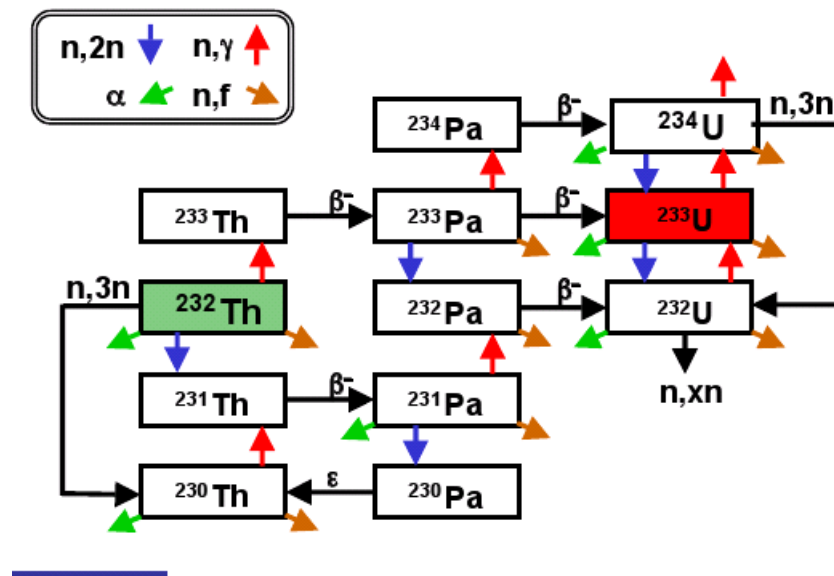


Figure 1.6: The actinides production chain for the Thorium fuel cycle.

past on critical assemblies (Molten Salt Reactor, CANDU-Th, High-Temperature Gas Reactor). Due to technical problems encountered on the Th/U fuel cycle, and following the rapid industrialised production of Uranium-based reactors, research and development has naturally focused on the Uranium based cycle, nowadays the standard for all operating power plants. For this reason, an important R&D⁵ is at present still missing for Thorium. This is however changing recently, since the use of Thorium in the nuclear fuel cycle for either critical or subcritical systems has become a topic of interest.

Many developments and studies are being devoted to subcritical reactors driven by an accelerator. Such an ADS has clear advantages on the criticality and safety aspects of nuclear energy production as compared to critical assemblies and opens new perspectives for nuclear waste management [32, 33]. This type of reactors can be used to incinerate radioactive waste (primarily long-lived minor actinides), to burn the massive stocks of Plutonium, or to produce energy in an efficient and safe way. An innovative concept using an ADS with $^{232}\text{Th}/^{233}\text{U}$ is the Energy Amplifier [35]. The present state of the knowledge of the cross-sections related to the thorium-cycle is below the level of data for the Uranium cycle. The conceptual design and realization

⁵Research and Development.

of nuclear reactors based on the use of Thorium, either in a critical or subcritical system, require therefore an improvement in the knowledge of the reaction cross-sections for a variety of isotopes involved in the thorium cycle. As indicated in “The NEA high priority nuclear data request list” [36], the capture cross-section of ^{232}Th with uncertainties smaller than 5% is needed in the region between 1 eV and 500 keV. An even greater precision with uncertainties of 1-2% is requested for ^{232}Th , and of 5-10% for ^{231}Pa , ^{234}U and ^{236}U , in a dedicated study on nuclear data needs for the Thorium fuel cycle [37, 38].

The new applications have triggered a renewed interest in neutron-nucleus reactions in particular for isotopes essential for the development and optimised design of the above mentioned concepts. Indeed many of the relevant isotopes have received little attention in the past and at present the existing experimental data are still insufficient, incomplete or sometimes even lacking. For this reason, in the past few years, a large effort has been devoted by several groups to measure, as an example, the neutron induced cross-sections on the important isotope ^{232}Th [39, 40, 41, 42, 43, 44, 45, 46] or the fission cross-section of ^{233}U [47, 48].

1.3 Importance of the $^{197}\text{Au}(n, \gamma)^{198}\text{Au}$

Once the importance of neutron-induced reaction measurements is assessed, the experimental physicists have to measure in accurate way the cross-sections of several reactions. The radiative capture cross-section on Au is typically used at the neutron facilities to normalise capture measurements. Therefore this reaction constitutes a reference for the measurement of (n, γ) reaction, since it is needed to extract absolute values. Moreover the Gold capture cross-section is of great importance for applications, in particular for the determination of neutron flux in the field of reactor physics. As a consequence new and more accurate data on its capture cross-section can improve the accuracy of other measurements and enhance the reliability of other techniques, such as the Neutron Activation Analysis (NAA) and the Integral Analysis (IA) [49, 50].

1.4 Neutron data libraries

Historically, the interaction of neutrons with nuclei has been of primary interest for conventional nuclear reactor physics. The industrial needs concerning safety and criticality as well as modelization and development of new reactors, have lead, in the past, to the development of standardized formats of nuclear data for storage and retrieval of compiled [51, 52] and evaluated nuclear data. Typically, experimental data do not singularly cover the whole energy range needed for application, and in many

cases different data taken in the same energy range show discrepancies (often outside the systematic errors). Evaluated data are therefore necessary to extract a unique set, compatible with the measurements, and covering the whole energy region (usually from thermal to 20 MeV). To this end, evaluators combine experimentally measured cross-section data with predictions of nuclear model calculations also in order to extrapolate where no data are present. The evaluated data set is adopted in the library after extensive benchmarking and reviewing. The evaluated libraries, like JEFF (Europe) [53], JENDL (Japan) [54], ENDF/B (United States) [55], BROND (Russia) [56] or CENDL (China) [57], contain several sublibraries, each one corresponding to a particular type of data, such as incident charged particle data, photo-nuclear data and several other reaction types. In all libraries data are contained for a variety of mate-

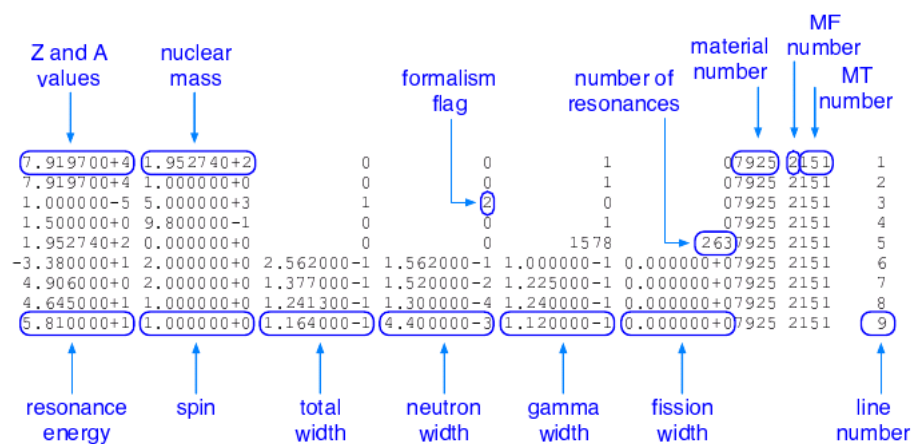


Figure 1.7: Part of the neutron data on ^{197}Au from JEFF-3.0. Picture from [13].

rials, each identified by a material number. The most natural materials are nuclides, for which the nuclear reaction parameters correspond to physical properties. Natural elements or even compounds are also allowed. With time and more accurate nuclear data the tendency in modern evaluated libraries is to remove as much as possible compounds and natural elements and include only isotopes and metastable states. Each material in an incident-neutron sublibrary has several “files”, flagged by a file number known as MF, containing for example general information (MF=1 or file 1), resonance parameter data (file 2), point-wise cross-section in the form of interpolation tables (file 3), angular and energy distributions, multiplicities, radioactivity and fission-product yield data, covariance information and other data, resulting in about 40 files. Not all files are necessarily present in an evaluated data file. The files contain indicators, the so-called MT numbers, giving further specification. For example for point-wise cross-sections (MF=3), MT=1 represents the total cross-section, MT=2 the elastic scattering cross-section, MT=18 the total fission cross-section and MT=102 the

radiative capture cross-section. The data are represented according to strict formatting rules, the ENDF format, documented in [58]. This format, originally only used in the ENDF library, has been adopted for all other libraries as well. As an example, Figure 1.7 shows a small fraction of the data corresponding to resonance parameters (file 2) for the ^{197}Au isotope. Evaluated data libraries contain basic data. Codes like NJOY [59] or PREPRO [60] can be used to retrieve such data and further process them, for example by calculating the Doppler broadened or group averaged cross-section and expressing them in a format useable by transport codes. New data needs or newly available experimental data may lead to new evaluations. An updated library can be released only when the full library has passed extensive testing, giving coherent results in benchmarks on a variety of applications like reactor criticality calculations.

1.5 Status of ^{197}Au data libraries

Accurate measurements of the (n, γ) cross-section of ^{197}Au have been performed up to date in and above the Unresolved Resonance Region⁶ (URR) and at the thermal point by using activations and prompt γ -ray detection techniques. The $\text{Au}(n, \gamma)$ reaction is considered as a standard above 0.2 MeV, although it could be extended to lower energy as asserted in Ref. [61, 62]. In spite of its importance, only few measurements in the Resolved Resonance Region (RRR) are present in the literature (see [51] for a list). In Figure 1.9 and 1.10 these measurements are listed. It is shown, for example, that no transmission data are present above 2.5 keV, and resonance parameters rely only on capture measurements [63]. In particular, above 2634 eV scattering widths were obtained from the capture kernels by assuming an average radiative width of 124 meV and resonance spins of either 2 or 1.

Concerning the spin assignment at energies below 2634 eV few data are reported in literature: Alves et al. [64] determined the spin of resonances below 2.1 keV, Alix et al. [65] below 1 keV, Asghar et al. [66] below 500 eV, while Desjardins et al. [67] revisited the spin of few resonances up to 1 keV (see Table 1.3).

Moreover it has to be noted that there is no measurement that covers the full resolved resonance region. Another important aspect is that the measurements are old (before 1980) and each of them covers only a small energy region. The only exception is a work of Block et al. [68] in which the parameters of few resonances up to 78 eV have been extracted from an old transmission measurement. Evaluations are available only in the ENDF/B-VI (2001) and ENDF/B-VII (2007) libraries, showing 5% discrepancies in the area of the resonances. In addition, a number of resonances are considered to be "doubtful" and, therefore, only partly included in the ENDF/B-VI and ENDF/B-VII evaluations. These cases are summarized in Table 1.4 and an

⁶In this case, incoming neutron energy greater than about 5 keV.

Table 1.3: Spin assignment from literature, up to 500 eV. Resonance energy from ENDF/B-VII (the same as in Alix et al. [65]). Flags: blank = no assignment; X = resonance not included; * = Spin assignment uncertain.

Resonance energy (eV) ENDF/B-VII	Spin from:				ENDF/B-VII [55]
	Alix [65]	Alves [64]	Asghar [66]	Desjardins [67]	
4.89	2				2
46.45					1
57.92		1			1
60.10	2	2	2	2*	2
78.27	2	1	1		1
107.0	2	2	2		2
122.1					2
144.4		1			1
151.4	2	2	2	2	2
162.9	1	1	1		1
164.9	2	2			2
190.3	2	X		1*	1
240.6	2	2	2	2	2
255.7	X		X		1 ^a
262.4	2	1	1	1	1
273.8					2
293.4	2	2	2		2
329.3	2	2	X		2
330.8	1	1	X		1
355.3	2	2	2		2
370.7	2	2	2		2
375.1					1
381.5	2	2	2		2
400.0		2			2
401.3		1	X	X ^b	1
4.398	1	1	1	1	1
450.5	2	2		1*	2
476.9	2	2		2*	2
489.2	1	1	X		1
493.3	2	2	X		2

^aIt is present only in ENDF/B-VI.

^bProbably doublet.

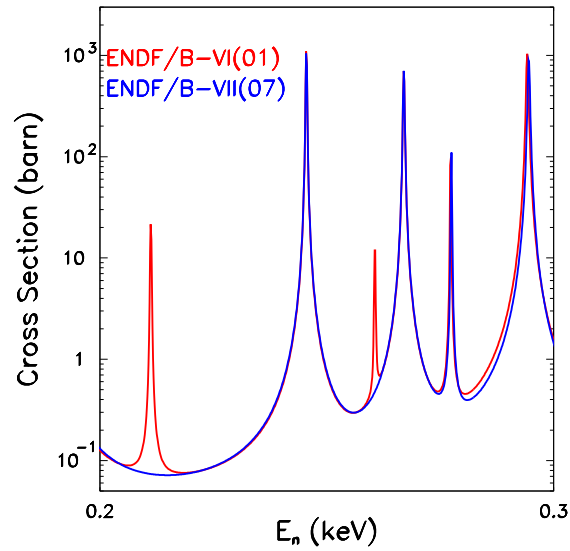


Figure 1.8: Existing evaluations, in ENDF/B-VI and in ENDF/B-VII, for the $^{197}\text{Au}(n, \gamma)$ cross-section. Discrepancies are present and some resonance are not considered.

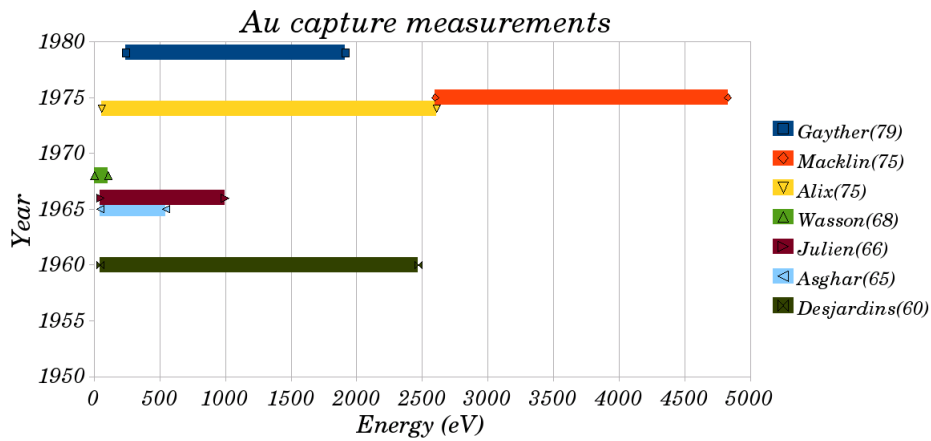


Figure 1.9: Experimental (n, γ) data considered in Ref. [51] for ^{197}Au resonance parameter compilation.

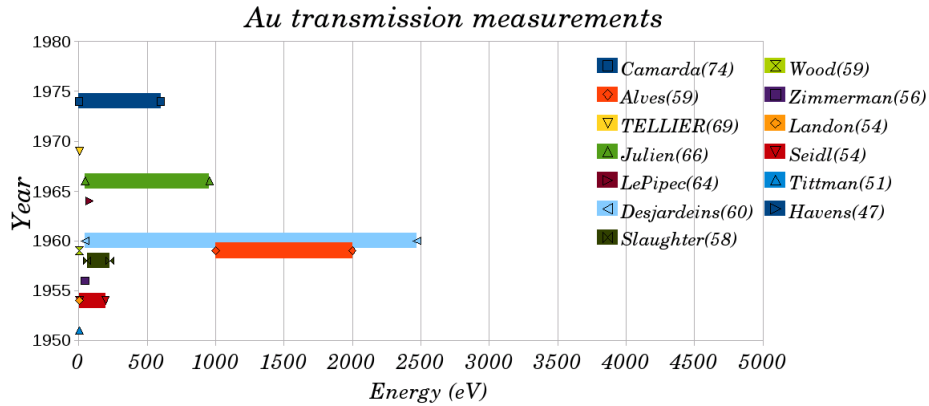


Figure 1.10: Experimental total reaction cross-section measurements considered in Ref. [51] for ^{197}Au resonance parameter compilation.

example of discrepancies is given, in Figure 1.8. The European neutron library JEFF adopts the ENDF/B-VI parameters, while data on this element are missing in JENDL and BROND.

Table 1.4: "Doubtful" resonances which were only partly considered in evaluated data files.

E_R (eV)	209.3	255.7	401.3	561.4	955.2	1022.	1233
ENDF/B-VI	<i>yes</i>	<i>yes</i>				<i>yes</i>	
ENDF/B-VII			<i>yes</i>	<i>yes</i>	<i>yes</i>		<i>yes</i>

1.6 Neutron time-of-flight facilities

For measurements of neutron induced cross-sections several neutron sources can be used. Neutron from reactors are widely used in experiments to determine Maxwellian averaged cross-sections in the thermal region. Thanks to the high flux available, low mass samples of a few micrograms are sufficient. At higher energies, typically in the MeV range, nearly monochromatic neutron beams can be obtained by means of an accelerator via light particle reactions like $^7\text{Li}(p,n)^7\text{Be}$ or $^9\text{Be}(\alpha,n)^{12}\text{C}$. On the contrary, the use of thick targets, often coupled with moderators, allows to produce neutrons in a wide energy range. Cross-section at specific neutron energies averaged over a tailored neutron spectrum can be measured in this way. For high-resolution neutron spectroscopy, a high intensity neutron source covering a large energy range is most convenient (see for example Figure 1.11). Accelerator-based pulsed white neutron sources are suitable for this purpose. A moderator made of

a material rich in hydrogen can be applied in order to increase the fraction of low-energy neutrons. These sources can provide neutron beams with energy spectrum ranging from several meV up to several hundreds of MeV. It is necessary that the source be pulsed because the selection of the neutron energy is determined by the time-of-flight method. Such pulsed neutron sources are mostly based on electron or proton accelerators. The electron-based sources produce neutrons via photoproduction using Bremsstrahlung γ -rays. The cross-section for this process is approximately proportional to Z^2 , thus favouring photoproduction for heavy mass nuclei. Neutrons are generated through photonuclear reactions (γ,n) as well as, if the target is fissionable, photofission reactions (γ,f). For γ -ray energy in the range between 10 and 20 MeV, the cross-sections for photodisintegration reactions increase considerably due to the giant dipole resonance and are approximately proportional to NZ/A , thus again favouring targets of heavy mass nuclei. Examples of white pulsed neutron sources are GELINA [70, 71, 72, 73] of the EC-JRC-IRMM at Geel in Belgium, which use a 140 MeV electron beam incident on a uranium target [70, 74, 75], ORELA [76] at Oak Ridge National Laboratory, using 180 MeV electrons on a tantalum target, the RPI facility [77] at Troy (USA) and KURRI [78] at Kyoto.

In proton-based machines, neutrons are produced in (p,n) reactions in the MeV region up to about 100 MeV. At even higher incident proton energies neutrons are produced by the spallation process with a very high yield of neutrons per proton, if a high Z target is used. Examples are the LANSCE [79] facility at Los Alamos National Laboratory, based on 800 MeV protons, and the spallation source at KEK in Tokyo. A more recent facility is n_TOF at CERN, based on a 20 GeV proton beam incident on a lead target [80, 81, 82, 83, 84, 85, 86, 87, 88]. Chapter 3 describes these facilities more in detail.

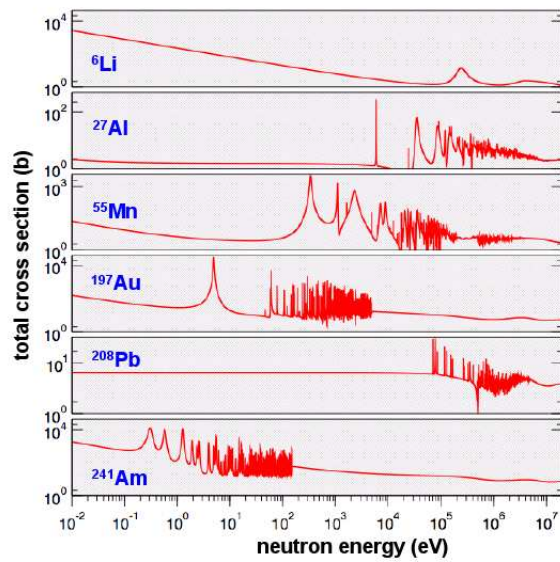


Figure 1.11: The neutron capture cross-section of several elements: low A elements such as Lithium or Aluminum and neutron shell closed isotopes (${}^{208}\text{Pb}$) as well present resonances at higher energies with respect to high A elements such as Gold or Americium. Picture from [69].

Chapter 2

Neutron induced reactions

Cross-sections in neutron-nucleus reactions show large fluctuations of several orders of magnitude even for small changes in the neutron kinetic energy. The large peaks correspond to excitations of eigenstates in the compound nucleus. In this chapter a brief introduction on the R-matrix formalism, the most accurate way to describe cross-sections in the resonance region, is presented. This method describes a reaction cross-section using only the properties of nuclear reaction excitation levels. The potential of the interaction is extremely complicated and it cannot be approximated, therefore the cross-sections cannot be exactly calculated and needs to be measured. In addition, important information on level densities, a key ingredient in many nuclear reaction codes, can be obtained directly from neutron resonance spectroscopy.

2.1 Theory of resonance neutron reactions

For all the studies presented in the previous chapter, cross-sections for particular reactions must be known or estimated, often very accurately. Because nuclear theory has not been developed to the stage where cross-sections can be calculated from basic principle, the cross-sections must be obtained from measured data. To establish a reliable database of reaction cross-sections, measured cross-section data are parameterised by theoretical reaction models. In particular, in order of increasing energy the following theories and models are employed:

- R-matrix theory in the thermal and resolved resonance region (parameters: level energies, level spin, partial widths). See next section;
- level-statistical (Hauser-Feshbach) theory in the unresolved resonance region (parameters: level density, strength functions and average partial widths, or the equivalent channel transmission coefficient). Some details are given in Appendix C;

- the optical model at higher energies, where levels overlap strongly but compound reaction still dominate (parameters: radius depth, diffuseness and deformation of the real and imaginary potential well).

The parametrisation of the cross-section by means of a nuclear reaction theory [89, 90]:

1. ensures consistency between partial and total cross-sections;
2. ensures consistency between cross-section data in different energy regions;
3. allows inter- and extrapolation into energy regions for which no or insufficient experimental data exist;
4. allows to estimate the cross-sections for nuclides not directly accessible to experiments;
5. permits the calculation of Doppler broadened reactions and self-shielding¹ factor;
6. accounts for the instrumental resolution.

At relatively low energies² many neutron induced reaction cross-section are characterised by resonance structures. The resonances are well separated and the mean distance between them (the level distance D) is large compared to their natural width Γ and the instrumental resolution Δ_R . With increasing energy the level distance decreases and the total natural width increases. Although at intermediate energies the resonance structure still exists ($D > \Gamma$), the resonance structure can no longer be resolved due to the limited instrumental resolution. Therefore, in the region where $D > \Gamma$, one distinguishes between the resolved resonance region (RRR), for which $D > \Delta_R$, and the unresolved resonance region (URR), for which $D < \Delta_R$. At higher energies the level distances is smaller than the resonance width ($D < \Gamma$) and the resonance structure disappears. This energy region is called the continuum region.

As an example, in Figure 2.1 the neutron capture cross-section of ¹⁹⁷Au is shown on an energy scale spanning more than ten decades.

Different processes have to be invoked to describe the probability that a neutron interacts with a nucleus. The statistical model describes resonances with relatively small widths and correspondingly long lifetimes, whereas non-resonant interactions are accounted for by a short-lived direct process. The lifetime for semi-direct capture

¹The self-shielding describes the flux perturbation due to the existence of neutron absorption within the sample. It is expressed as: $1 - e^{-n\sigma_{tot}}$.

²Depending on the nuclear mass of the isotope and shell effects the resolved resonance region can be found in the eV region for heavy elements, or in the keV region for medium heavy elements, or in the MeV region for light nuclei or neutron shell close isotopes, see Figure 1.11.

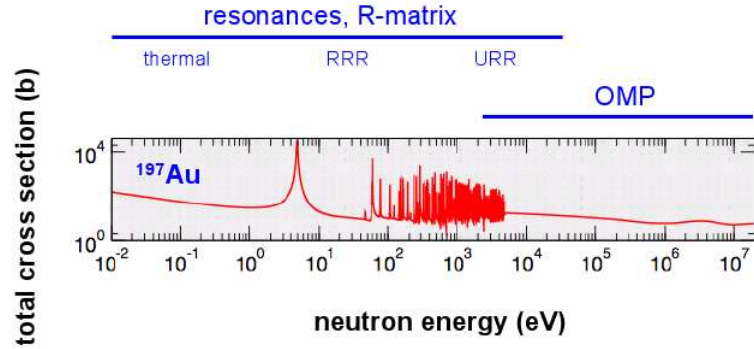


Figure 2.1: The neutron capture cross-section of ^{197}Au from the thermal point at 25.3 meV up to the MeV region. The Resolved Resonance Region (RRR) ranges up to 5 keV. The Unresolved Resonance Region (URR) and the Optical Model Potential (OMP) domain are also reported. Picture from [69].

lies somewhere between these two limits. In the statistical model, the incoming neutron interacts with a nucleus, forming a compound system in which the excitation energy is distributed among all nucleons. The compound nucleus successively decays, usually via neutron emission or gamma decay, or fission in some heavy nuclei. In direct reactions, the neutron interacts with the nucleus as a whole or with some of the nucleons. The two types of reactions differ in the time of interaction, which is of the order of 10^{-22} s for direct reactions, corresponding to the transit time of the neutron through the nucleus, while in the case of compound nucleus reactions the reaction time is orders of magnitude bigger. The semi-direct mechanism was introduced in the MeV energy range to account for the absorption in the giant dipole resonances (GDR). Direct and semi-direct reactions play a dominant role at energies higher than about 1 MeV. The GDR dominates the gamma-ray strength at MeV neutron energies and contributes significantly at excitation energies as low as 5-7 MeV.

The compound nucleus reactions can be described in the frame of Bohr's theory, which is known as the extreme statistical model. It is assumed that the incident neutron, with a kinetic energy E_n , interacts with the nucleus to form an excited state in which the incident particle plays no special role. In the first stage of the reaction, the system of incident neutron and the target nucleus X with mass number A may form the so-called compound nucleus with mass $A+1$. Many of the target nucleons participate collectively and the total excitation energy is shared between a large number of nucleons. Due to the binding energy of the neutron, B_n , this compound nucleus is in an excited state with energy E^* :

$$E^* = B_n + E_{n,cm}, \quad (2.1)$$

where $E_{n,cm}$ represents the neutron channel kinetic energy in the centre of mass system. In Figure 2.2 a schematic picture of such a reaction is shown.

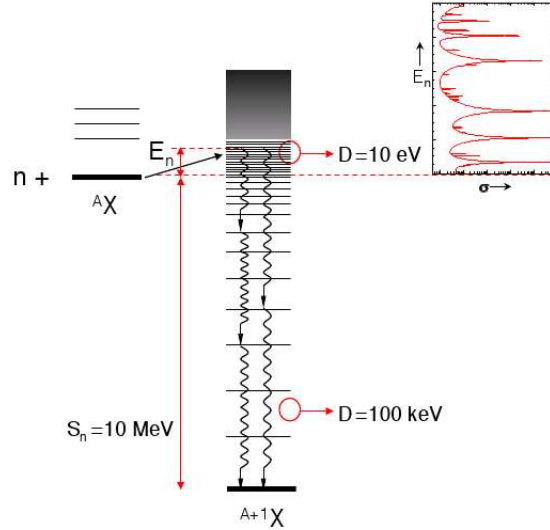
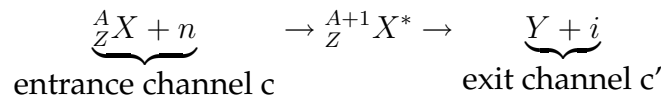


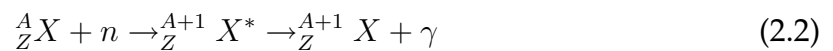
Figure 2.2: Schematic view of the formation and de-excitation of a compound nucleus with typical values of level spacing and neutron separation energy. The resonances observed in the reaction cross-section correspond to the excitation of nuclear levels. After the formation of the highly excited state by an incident neutron, the compound nucleus can decay by emission of γ radiation, giving rise to the so-called radiative neutron capture, or by emission of a neutron, in elastic scattering. Picture from [13].

The compound nucleus has several modes of decay, or channels, at its disposal:



One of the channel is the elastic scattering reaction in which the neutron is re-emitted and the nucleus returns to its ground state. If the energy in the centre-of-mass system exceeds the energy of the first excited state in the target, inelastic scattering becomes possible. In the case of inelastic scattering the neutron is emitted with a lower energy, leaving the target nucleus in an excited state.

The compound system can decay, through the emission of often a large number of γ -rays, to its ground state:



The gamma rays following immediately the capturing state are called primary gamma-rays, while the gamma-rays of the further decay are called secondary. In Bohr's as-

sumption the decay mode of the compound nucleus is independent of the way it has been formed.

Cross-sections for neutron induced reactions below about 1 MeV are characterised by resonances. These resonances correspond to excited levels of the compound nucleus, which are quasi-bound states with a relatively long lifetime. The lifetime τ_r is correlated to the total width of the resonance Γ_r by the Heisenberg's uncertainty principle:

$$\Gamma_r \tau_r \approx \hbar \quad (2.3)$$

The equivalence in the time and energy domain is illustrated in Figure 2.3.

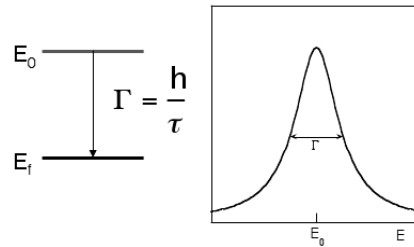


Figure 2.3: The Breit-Wigner shape of the energy profile (right) of a quantum state with a finite life time τ (left). Picture from [13].

The total width of the level Γ_r is the sum of partial widths Γ_{rc} corresponding to the decay of the compound nucleus. According to the Bohr's compound nucleus theory, the probability of decay through the c channel is given by:

$$P_c^{Bohr} = P_{CN} \frac{\Gamma_{cr}}{\Gamma_r}, \quad (2.4)$$

where the P_{CN} is the probability to form the compound nucleus.

In the resonance region both the statistical mechanism of neutron capture and other components of non-statistical nature are present. In general, the neutron capture process can be divided in a resonant and a non-resonant interaction. The resonance capture reaction can be described as a series of two-body interactions [91], beginning with the entrance channel one-particle-zero-hole state (1p-0h with respect to the target nucleus), exciting the so-called doorway states (2p-1h or collective modes) and through a succession of more complex p-h interactions, leading ultimately to a statistical equilibrium involving many nucleons and forming the compound nucleus.

In the non-resonant interaction, the valence capture process corresponds to the direct capture of the neutron into a specific shell configuration and the valence neutron undergoes a radiative transition without perturbing the core. This process is also

indicated as a 1p-0h interaction. Radiative decay can also occur from the doorway components of a resonance, either by particle-hole annihilation or by a particle transition in the presence of an excited core. Potential scattering can be considered as a non-resonant direct reaction.

2.1.1 Parametrisation of resonance neutron cross-sections

In the resolved and unresolved resonance region the experimental data can be parameterised in terms of resonance parameters. An individual resonance is characterised by the resonance energy (E_0), the total natural width (Γ), the partial reaction widths (e.g. the neutron width Γ_n , the capture width Γ_γ), the total angular momentum of the level and the orbital momentum of the incoming neutron. These parameters can be extracted from experimental data using Resonance Shape Analysis (RSA) codes, such as REFIT [92] and SAMMY [93], based on the multi-level R-matrix reaction theory [94, 95]. In the unresolved resonance region the parameterisation is based on statistical model [89], implemented in e.g. FITACS [96] and HARFOR [97]. Both theories rely on input average parameters (i.e. level densities and strength functions) resulting from a statistical analysis of the resolved resonance region. In the following section we give the basic concepts of the R-matrix theory, its different approximations in the resolved resonance region are presented in Appendix B.1 and B.2.

The hypothesis of the statistical model have direct consequences on the observables of the reaction. The channel widths are proportional to the square of the matrix elements, and depending on the reaction, observed widths follow different distribution:

- (n, n) reaction: the elastic widths tends to a chi-squared distribution with one degree of freedom, also called the Porter-Thomas distribution;
- (n, γ) reaction: the gamma width of a resonance is the sum of many, for medium and heavy nuclei several tens of thousand, individual gamma widths and tend therefore to a Gaussian distribution;
- (n, f) reaction: the fission widths correspond to a relatively small number of fission channels, at maximum three or four. The resulting distribution can be approximated by an effective chi-squared distribution with a small number of degrees of freedom.

With increasing excitation energy the widths of the states start to overlap and the resulting cross-sections become smooth. The properties of the eigenstates, like the decay widths, fluctuating from one state to another, are values averaged over many resonances. These average values can be predicted by nuclear models, parametrised

with average properties. Hints are present in Appendix C with more emphasis for ^{197}Au . Measured average cross-sections can therefore be used to fine-tune the parameters used in these models. At even higher excitation energies, many more decay channels open up and the interpretation of the cross-section measurements becomes very difficult or impossible.

2.1.2 The R-Matrix expressions

For all binary reactions, the cross-section can be described by the R-matrix theory [94, 98]. This theory is especially applicable to cross-section data in the resonance region [89]. Hereafter our notation will be that of Lane and Thomas [94]. We recall that in nuclear reaction theory one talks about reaction channels. A channel is specified by the set of quantum numbers that defines it uniquely:

- α , the partition of the compound system into reaction partners, (e.g. $^{197}\text{Au} + n$ or $^{198}\text{Au} + \gamma$, both involving the same compound nucleus);
- \mathbf{J} , the total angular momentum in units of \hbar ;
- ℓ , the orbital angular momentum in units of \hbar ;
- \mathbf{s} , the channel spin in units of \hbar , defined as $\vec{s} = \vec{I} + \vec{i}$.

Total energy, total angular momentum and parity (for all practical purpose) are conserved in nuclear reactions. Considering neutron induced reactions, the total angular momentum of the resonance \vec{J} is given by the vector sum of the target spin \vec{I} , the neutron spin \vec{i} , and the neutron orbital angular momentum $\vec{\ell}$:

$$\vec{J} = \vec{I} + \vec{\ell} + \vec{i} \quad (2.5)$$

The resonance parity π is given by the product of the parity of the target nucleus π_1 and the factor $(-1)^\ell$:

$$\pi = (-1)^\ell \pi_1 \quad (2.6)$$

The so-called statistical spin factor g is related to the probability of obtaining the total angular momentum J from the intrinsic spins of the target nucleus I and of the incident neutron:

$$g = \frac{2J + 1}{(2i + 1)(2I + 1)} \quad (2.7)$$

g is the ratio of the number $2J+1$ of substates for the compound system and the numbers of substates of the initial system consisting of a free neutron, with two substates, and the target nucleus, with $2I+1$ substates. For the reaction $^{197}\text{Au}+n$ we list in Table 2.1 the J^π value with the corresponding statistical factor for s- and p-wave incoming neutrons. The principle of the R-matrix formalism consists in assuming

Table 2.1: The value of J^π and of the statistical factor g for $^{197}\text{Au}+n$.

	ℓ	s	J^π	g	wave
$^{197}_{118}\text{Au}_{79}$	0	1	1^+	0.375	s
		2	2^+	0.625	s
$(I^\pi = 3/2^+)$	1	1	$0^-, 1^-, 2^-$	0.125, 0.375, 0.625	p
		2	$1^-, 2^-, 3^-$	0.375, 0.625, 0.875	p

both incident particles as well as emerging reaction products as ingoing and outgoing wave functions. Since the nuclear forces are short-ranged, the configuration space is divided into an external and an internal region separated by an imaginary closed surface of radius a_c . A reasonable choice [51] for a_c is the so called channel radius defined as:

$$a_c \cong 1.35A^{\frac{1}{3}} \quad (\text{fm}) \quad (2.8)$$

where A is the mass number of the target nucleus. In the external region the nuclear force are negligible, so that the wave function governing the dynamics of the free particles may be known analytically. On the contrary, in the internal region the nuclear forces predominate. The neutron and the nucleus are merged together to form a system of $A+1$ nucleons in which the interaction increases the complexity of the wave function of the nuclear system. Although the internal wave function is unknown, the internal domain may be treated in terms of the collision matrix $U_{cc'}$. For a given ingoing wave in the channel c , leading to an outgoing wave in the channel c' the partial neutron cross-section $\sigma_{cc'}$, for total spin J may be expressed as:

$$\sigma_{cc'} = \pi\lambda^2 g |\delta_{cc'} - U_{cc'}|^2 \quad (2.9)$$

with

$$U_{cc'} = U_{\alpha ls, \alpha' l' s'}^J \quad \text{and} \quad \delta_{cc'} = \delta_{\alpha\alpha'} \delta_{\ell\ell'} \delta_{ss'} \quad (2.10)$$

where $|U_{cc'}|^2$ is the probability of a transition from channel c to channel c' . The elastic cross-section is then expressed as follows:

$$\sigma_{\alpha\alpha} = \pi\lambda^2 \sum_J g \sum_{\ell, s} (|1 - U_{cc}|^2 + \sum_{\ell', s' \neq \ell, s} |U_{cc'}|^2) \quad (2.11)$$

The expression of the reaction cross-section ($\alpha \neq \alpha'$) quadratically depends on the $U_{cc'}$:

$$\sigma_{\alpha\alpha'} = 2\pi\lambda \sum_J g \sum_{\ell, s} \sum_{\ell', s'} |U_{cc'}|^2 \quad (2.12)$$

By contrast, the total cross-section is a linear function of U_{cc} :

$$\sigma_{\alpha} = 2\pi\lambda^2 \sum_J g \sum_{\ell,s} (1 - \text{Re}(U_{cc})). \quad (2.13)$$

These equations are quite general for the cross-section of binary reactions. The R-matrix theory allows us to express the collision matrix U in terms of the matrix R as follows [89]:

$$U_{cc'} = e^{-i(\varphi_c + \varphi'_c)} \{ \delta_{cc'} + 2iP_c^{\frac{1}{2}} [(1 - RL^o)^{-1} R]_{cc'} P_c^{\frac{1}{2}} \} \quad (2.14)$$

$$R_{cc'} = \sum_r \frac{\gamma_{rc} \gamma_{rc'}}{E_r - E} \quad (2.15)$$

$$L_{cc'}^o = (S_c + iP_c - B_c) \delta_{cc'} \quad (2.16)$$

where:

- $R_{cc'}$ is the R-matrix element;
- φ_c is the hard-sphere (potential) scattering phase shift;
- S_c is called shift factor and is the real part of the logarithmic derivative of the outgoing wave function at the channel radius a_c ;
- P_c is the penetration factor and is the imaginary part of the logarithmic derivative of the outgoing wave function at the channel radius a_c . For neutron induced reactions this penetration factor is defined by the centrifugal-barrier penetrability;
- B_c are boundary conditions at the channel radius a_c .

Alternatively the collision matrix can be expressed in terms of the level matrix A,

$$U_{cc'} = e^{-i(\varphi_c + \varphi'_c)} (\delta_{cc'} + i \sum_{\mu,\lambda} \Gamma_{\lambda c}^{\frac{1}{2}} A_{\lambda\mu} \Gamma_{\mu c'}^{\frac{1}{2}}), \quad (2.17)$$

$$\Gamma_{\lambda c}^{\frac{1}{2}} = \gamma_{\lambda c} \sqrt{2P_c}, \quad (2.18)$$

$$(A^{-1})_{\lambda\mu} = (E_{\lambda} - E) \delta_{\lambda\mu} - \sum_c \gamma_{\lambda c} L_c^o \gamma_{\mu c}, \quad (2.19)$$

where Roman subscripts refer to reaction channel and Greek subscripts to compound levels.

To calculate collision matrix U several matrix inversion have to be performed (Eq. 2.14). From a computational point of view this is not trivial. Therefore, some approximations have been introduced.

The eigenvalues of the problem can be identified with the energy E_r . The reduced width amplitudes γ_{rc} and $\gamma_{rc'}$ of the resonance r are a measure of the probability

of the formation of the compound state via the entrance channel c and of its decay via the exit channel c' . The eigenvalues of the nuclear system are determined by the boundary condition taken at the surface of the hard sphere of radius a_c . More details are given in Appendix A. According to the R-matrix theory, γ_{rc} and $\gamma_{rc'}$ are real, independent, and have normal distribution with zero mean [99]. E_r , γ_{rc} , $\gamma_{rc'}$ can only be obtained from experimental cross-section data. Therefore, the cross-section formulae are usually written in terms of experimental observables, such as the partial width Γ_{rc} , rather than the decay amplitudes. The partial width is related to the square of the amplitude via the penetration factor P_c :

$$\Gamma_{rc} = 2\gamma_{rc}^2 P_c \quad (2.20)$$

The basic resonance parameters E_r and the partial widths Γ_{rc} depend on the nuclear interaction. In typical applications of R-Matrix theory, they just serve as fit parameters adjustable to experimental data. The practically important variants of the R-matrix formalism are the Reich-Moore approximation [100], the Single Level Breit-Wigner formalism (SLBW) and the Multi Breit-Wigner formalism (MLBW) [101], which are discussed in Appendix B.1 and B.2.

2.1.3 Single Level Breit Wigner formula

Before the R-matrix Theory was introduced, the Single-Level-Breit-Wigner (SLBW) formulas were used to parameterize cross-section data in the resonance region. The SLBW may be seen as an approximation of the R-matrix formalism, by considering only one level. For isolate resonances, which are not affected by multi-level interference, accurate results can be obtained. According to the R-matrix formalism, the single level collision matrix for s-wave neutrons may be defined as follows [89]:

$$U_{cc'} = e^{-ikR'} \left(\delta_{cc'} + \frac{i\sqrt{\Gamma_{rc}\Gamma_{rc'}}}{E_r - E - i\Gamma_r/2} \right) e^{-i\varphi_{c'}} \quad (2.21)$$

Where $\Gamma_r = \sum_c \Gamma_{rc}$ represents the total width. And R' is the potential scattering radius. The resulting total and partial cross-section in the case of $R'/\lambda \ll 1$ are expressed for a given J and $T=0$ K as follows:

$$\sigma_c = 4\pi g R'^2 + 4\pi\lambda^2 \frac{g\Gamma_{rc}\Gamma_r}{\Gamma_r^2 + 4(E_r - E)^2} - 16\pi\lambda R' \frac{g\Gamma_{rc}(E_r - E)}{\Gamma_r^2 + 4(E_r - E)^2} \quad (2.22)$$

$$\sigma_{cc'} = 4\pi\lambda^2 \frac{g\Gamma_{rc}\Gamma_{rc'}}{\Gamma_r^2 + 4(E_r - E)^2} \quad (2.23)$$

The total cross-section is a sum of three terms:

1. the constant potential scattering cross-section;

2. a symmetric resonance term;

3. an asymmetric term arising from interference between the potential and resonance scattering

If we suppose that only the elastic scattering ($c=n$) and capture ($c'=\gamma$) may occur, Eq. 2.22 and 2.23 become,

$$\sigma_c = 4\pi gR'^2 + 4\pi\lambda^2 \frac{g\Gamma_{rn}\Gamma_r}{\Gamma_r^2 + 4(E_r - E)^2} - 16\pi\lambda R' \frac{g\Gamma_{rn}(E_r - E)}{\Gamma_r^2 + 4(E_r - E)^2} \quad (2.24)$$

$$\sigma_\gamma = 4\pi\lambda^2 \frac{g\Gamma_{rn}\Gamma_{r\gamma}}{\Gamma_r^2 + 4(E_r - E)^2} \quad (2.25)$$

The reduced neutron wavelength λ and the scattering width γ_{rn} are functions of the energy E . The reduce neutron wavelength λ can be expressed through its value at the resonance energy as:

$$\lambda^2 = \lambda_r^2 \frac{E_r}{E} \quad (2.26)$$

while the energy dependence of Γ_{rn} can be expressed through its reduced value according to:

$$\Gamma_{rn}(E) = \Gamma_{rn}^\ell(E_i) \frac{P_\ell}{ka_c} \sqrt{E} \quad (2.27)$$

expressing E in eV. Γ_{rn}^ℓ is then called reduced neutron width. For s-wave ($\ell = 0$) resonance,

$$\Gamma_{rn} = \Gamma_{rn}^0 \sqrt{E} \quad (2.28)$$

This energy dependence, together with Eq. 2.25, explains the $1/v$ behaviour on the low energy side of s-wave resonance (Figure 2.4). The contribution from s-wave resonances to the capture cross-section at thermal neutron energy, expressed in barn, is approximately given by the following equation:

$$\sigma_\gamma(0.0253\text{eV}) = 4.099 \times 10^6 \frac{g\Gamma_{rn}^0 \gamma_{r\gamma}}{E_r^2} \quad (2.29)$$

By setting $E=E_r$ in Eq. 2.24 and 2.25 the total partial peak cross-section for a given spin J can be determined as:

$$\sigma_{tot}(E = E_r) = 4\pi gR'^2 + 4\pi\lambda_r^2 \frac{g\Gamma_{rn}}{\Gamma_r} \quad (2.30)$$

$$\sigma_\gamma(E = E_r) = 4\pi\lambda_r^2 \frac{g\Gamma_{rn}\Gamma_{r\gamma}}{\Gamma_r^2} \quad (2.31)$$

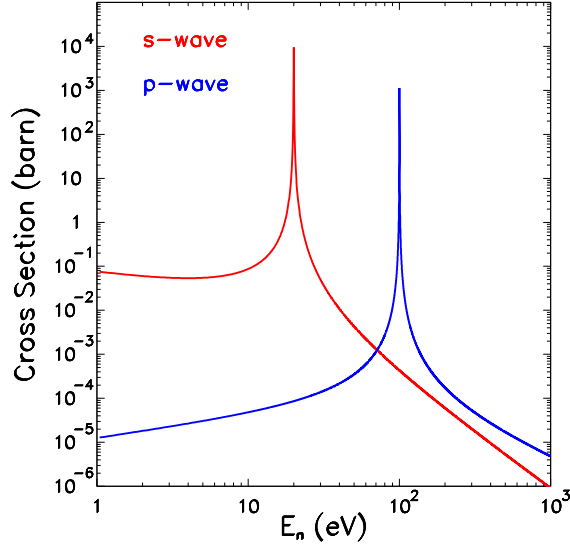


Figure 2.4: Example of the capture cross-section shape due to a s- and a p-wave resonance.

Or, expressing the cross-section in barns and E_r in eV,

$$\sigma_{tot}(E = E_r) = 4\pi g R^2 + \frac{2.608 \times 10^6 g \Gamma_{rn}}{E_r \Gamma_r} \quad (2.32)$$

$$\sigma_\gamma(E = E_r) = \frac{2.608 \times 10^6 g \Gamma_{rn} \Gamma_{r\gamma}}{E_r \Gamma_r^2} \quad (2.33)$$

All the energies are expressed in the laboratory system.

2.2 Doppler broadening

The natural shape of a resonance does not correspond to the cross-section observed in an experiment. The target nuclei are not at rest and have a distribution of velocities that depends on the sample material and its temperature. As a consequence, the thermal motion of the atoms in the target gives rise to a Doppler broadening of the Breit-Wigner shape of the resonance. The Doppler standard deviation³ of the Gaussian distribution of the laboratory energies, at a resonance energy E_0 is given by

³It follows that the full width at half maximum of the gaussian distribution is:

$$FWHM = 2\Delta_\theta \sqrt{\ln 2} \approx 1.665 \Delta_\theta$$

$\Delta_\theta/\sqrt{2}$, being:

$$\Delta_\theta = \sqrt{\frac{4k_B T_{eff} E_0}{A}} \quad (2.34)$$

where T_{eff} is the effective temperature of the target, k_B is the Boltzmann constant and A is the mass number of the target nucleus. The effective temperature is given by:

$$T_{eff} = \frac{3}{8}\theta \coth\left(\frac{3}{8}\frac{\theta}{T}\right) \quad (2.35)$$

where θ is the Debye temperature (two values have been found in literature for Au: $\theta \approx 165$ K, and $\theta \approx 240$ K, see Figure 2.5) , characterizing an approximate lattice phonon spectrum, and T is the sample temperature. To arrive at this expression the nuclear motion in the target is represented by the Maxwell distribution of motion in a gas. The Doppler broadening is often more important than the natural width of a resonance (see, for example, the calculation in Figure 3.15). For high precision cross-section measurements it can therefore be advantageous to cool the target sample, so that T_{eff} approaches $\frac{3}{8}\theta$. In any case, to compare with experimental data, the theoretical shape of the resonance must be modified by the Doppler broadening.

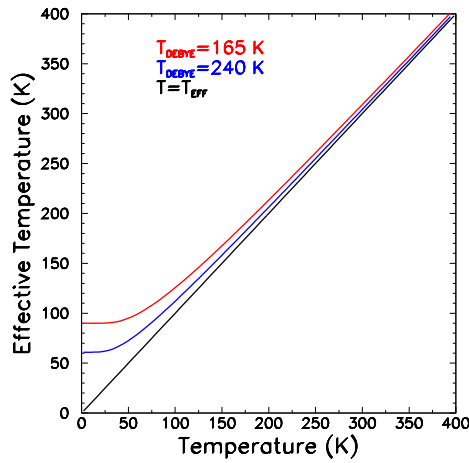


Figure 2.5: The effective temperature of Au for two different Debye temperatures. The effective temperature tends to the ambient temperature, for temperature greater than about 200 K.

2.3 Angular distribution of the gamma radiation

For s-wave resonance ($\ell=0$) the angular distribution of the gamma rays following neutron capture is isotropic. For resonances with $\ell \geq 1$ the gamma radiation has an

anisotropic angular distribution due to the orbital angular momentum $\ell > 0$, producing a preferred direction of the spins of the compound nucleus. In the case of $\ell \geq 1$ resonances the angular distribution $W(\theta)$ of the primary gamma-ray transition can be written as [110]

$$W(\theta) = \sum_{k=0}^{\ell} A_{2k} P_{2k}(\cos\theta) \quad (2.36)$$

where θ is the angle of emission with respect to the neutron beam and where P_{2k} denotes the Legendre Polynomial of order $2k$ and n is the . The maximum order of the angular distribution coefficients A_{2k} is restricted by the maximum value of the compound state spin J , the angular momentum of the neutron ℓ and the multipolarity of the gamma transition L . It is customary to measure using a geometry with the detectors positioned at an angle of 125° with respect to the neutron direction. The 125° geometry minimize anisotropic effects of gamma rays emitted from resonances formed by p-waves.

2.4 Resonance analysis of the experimental data

For a non fissile nucleus the total, capture and elastic scattering cross-sections can be parameterized by the following resonance parameters: the potential scattering radius, the resonance energy, the neutron and radiation width, and the spin and parity of the resonance. The spin determines the statistical factor of the resonance. A full set of resonance parameters can be determined by a combination of different type of measurements [111], such as:

- transmission measurements, in which one measures that fraction of a beam of neutrons of a given energy which traverses, without interacting a sample. This simple type of measurement allows us to determine the total cross-section. When the cross-section has resonance structure, both "thin" and "thick" sample are employed in order to obtain good accuracy of the extracted cross-section (at the resonance peaks as well as in the valley between resonances);
- capture measurements, in which the fraction of neutrons that produce a capture event is determined by detecting the γ -rays emitted after a neutron has been captured in the sample. A sample may be "thin" or "thick" depending on the resonance one considers, i.e. on the peak cross-section;
- self-indication measurements, which combine transmission and capture experiment: the neutrons pass trough a filter and then reach the capture detection setup containing the same material as a sample.

To extract the resonance parameters from the experimental data it is very important to understand the relation between the experimental observables and the reso-

nance parameters and, in the log run, to identify a combination of complementary measurements that should be performed.

2.4.1 Area analysis

The area method depends on the fact that the area below a resonance in a curve of one of the experimental observables (e. g. neutron transmission) plotted against energy is independent of the experimental resolution (provided that the energy limits enclosing the area are sufficiently far from the resonance energy). Therefore in the case of isolated resonances, the simplest method to extract resonance parameters from measured data is the area analysis [112, 113]. The type of data of interest in the present discussion are: transmission areas (A_{tot}), capture areas (A_γ), elastic scattering areas (A_n) and self-indication ratio (R_γ), these experimental areas are calculated as the number of counts times the energy bin-width (thus the area is expressed in eV). Every measurement of one of these observables yields an equation of the form: $F_{OBS} = F(\Gamma_\gamma, \Gamma_n)$, where F_{OBS} stands for the measured value, while $F(\Gamma_\gamma, \Gamma_n)$ is the mathematical expression which links the observable to the unknown parameters. For a well isolated resonance these expressions are, respectively [111]:

$$A_{tot} = \int (1 - e^{-n\sigma_{tot}})dE \quad (2.37)$$

$$A_\gamma = \int (1 - e^{-n\sigma_{tot}}) \frac{\sigma_\gamma}{\sigma_{tot}} dE \quad (2.38)$$

$$A_n = \int (1 - e^{-n\sigma_{tot}}) \frac{\sigma_n}{\sigma_{tot}} dE \quad (2.39)$$

$$R_\gamma = \frac{\int e^{-n_t\sigma_{tot}}(1 - e^{-n_c\sigma_{tot}}) \frac{\sigma_\gamma}{\sigma_{tot}} dE}{\int (1 - e^{-n_c\sigma_{tot}}) \frac{\sigma_\gamma}{\sigma_{tot}} dE} \quad (2.40)$$

where σ_{tot} , σ_γ and σ_n are the total, capture and neutron elastic cross-section, respectively. The sample thickness in atoms per unit area for the transmission, capture and elastic scattering measured is denoted by n . In the case of self-indication experiments n_t represents the number of atoms per unit area of the filter and n_c that one of the capture sample. The integrations are performed over the energy range of the resonance.

To solve the integrals we neglect the Doppler broadening effect and consider only the resonant part of the Single Level Breit-Wigner (SLBW) formalism for the parameterization of the total and capture cross-sections. In principle a measurement of two of the observables should be sufficient to determine Γ_γ and Γ_n . However one has to find the combination that yields the highest accuracy.

In the following, for sake of clarity, the index "r" on the partial and total width and the index "J" on the statistical spin factor are not reported in the text and equations. The peak cross-section and the energy of the resonance are represented by σ_0 and E_0 ,

respectively. Under these conditions, the following asymptotic relations in the limit of a very thin ($n\sigma_{tot} \ll 1$) or very thick ($n\sigma_{tot} \gg 1$) sample apply [111]:

$$A_{tot}(\text{thin}) = \frac{1}{2}\pi n\sigma_0\Gamma = 2n\pi^2\lambda^2 g\Gamma_n \quad (2.41)$$

$$A_{tot}(\text{thick}) = \sqrt{\pi n\sigma_0}\Gamma = 2\pi\lambda\sqrt{ng\Gamma_n\Gamma} \quad (2.42)$$

$$A_\gamma(\text{thin}) = \frac{1}{2}\pi n\sigma_0\Gamma_\gamma = 2n\pi^2\lambda^2 g\frac{\Gamma_n\Gamma_\gamma}{\Gamma} \quad (2.43)$$

$$A_n(\text{thin}) = \frac{1}{2}\pi n\sigma_0\Gamma_n = 2n\pi^2\lambda^2 g\frac{\Gamma_n\Gamma_n}{\Gamma} \quad (2.44)$$

$$R_\gamma = \frac{1}{\sqrt{\pi n_t\sigma_0}} = \frac{1}{2\pi\lambda}\sqrt{\frac{\Gamma}{n_t g\Gamma_n}} \quad (2.45)$$

where $\sigma_0 = 4\pi\lambda^2 g\Gamma_n/\Gamma$, λ is the reduced neutron wavelength at the resonance energy and σ_0 is the peak total cross-section of the resonance as defined in Eq. 2.32 without the potential scattering term. The quantity A_γ is related to the capture kernel, defined as:

$$k = g\frac{\Gamma_\gamma\Gamma_n}{\Gamma_\gamma + \Gamma_n} \approx \begin{cases} g\Gamma_n & \text{when } \Gamma_\gamma \gg \Gamma_n \\ g\Gamma_\gamma & \text{when } \Gamma_n \gg \Gamma_\gamma \end{cases} \quad (2.46)$$

by the following: $A_\gamma = 2n\pi^2 k\lambda^2$ and it is typically used instead of A_γ in capture experiment.

It is clear from Eq. 2.41 and Eq. 2.42 that thin and thick sample transmission measurements yield values of Γ and $g\Gamma_n$ and always provide complementary data. When $\Gamma_n \gg \Gamma_\gamma$ the neutron width will dominate the total width, such that $\Gamma_n \approx \Gamma$, and g and Γ_n can be determined from a combination of thin and thick transmission measurements. In this case, however no information can be obtained on the Γ_γ from transmission measurement. On the contrary, in the limit $\Gamma_\gamma \gg \Gamma_n$ the radiation will dominate the total width, such that $\Gamma_\gamma \approx \Gamma$, and the radiation Γ_γ width together with the product $g\Gamma_n$ is determined. In principle, either Eq. 2.43 and 2.44 together with Eq. 2.41 and 2.42 will yield g , Γ_n , Γ_γ and Γ . In practice, if $\Gamma_\gamma \gg \Gamma_n$, Eq. 2.43 reduce to Eq. 2.41 and an elastic scattering measurement is necessary to achieve a solution. If, on the other hand, $\Gamma_n \gg \Gamma_\gamma$, A_γ is proportional to Γ_γ , making the capture measurement the important factor. We can conclude that the reaction cross-section data, resulting from elastic scattering, capture measurement and transmission measurement are complementary and at least two measurements are needed to determine the partial widths. The result are summarized in Table 2.2. In Figure 2.6, taken from Rae et al. [114], we illustrate the method of area analysis to determine the parameters for the 5.2 eV resonance in ^{109}Ag . Using the relationships of Eq. 2.41, 2.42, 2.43 and 2.44, two sets of curves are constructed from the experimental data. The two sets correspond to the two possible values for the statistical factor g . For the correct choice of the statistical factor the curves should intersect in a common point. In this example $g=3/4$

Table 2.2: The resonance area as a function of the resonance parameters for different neutron cross-section measurement.

	Area	Resonant Part	
	$E_0, \Gamma_n, \Gamma_\gamma, g$	$\Gamma_n \gg \Gamma_\gamma$	$\Gamma_\gamma \gg \Gamma_n$
$A_{tot}(\text{thin})$	$2\pi^2\lambda^2ng\Gamma_n$	$\approx ng\Gamma_n$	$\approx ng\Gamma_n$
$A_{tot}(\text{thick})$	$2\pi\lambda\sqrt{ng\Gamma_n\Gamma}$	$\approx \sqrt{ng}\Gamma_n$	$\approx \sqrt{ng\Gamma_n\Gamma}$
$A_\gamma(\text{thin})$	$2\pi^2\lambda^2ng\frac{\Gamma_n\Gamma_\gamma}{\Gamma}$	$\approx ng\Gamma_\gamma$	$\approx ng\Gamma_n$
$A_n(\text{thin})$	$2\pi^2\lambda^2ng\frac{\Gamma_n\Gamma_\gamma}{\Gamma}$	$\approx ng\Gamma_n$	$\approx ng\frac{\Gamma_n\Gamma_n}{\Gamma}$
R_γ	$\frac{1}{2\pi\lambda}\sqrt{\frac{\Gamma}{n_tg\Gamma_n}}$	$\approx \frac{1}{n_tg}$	$\approx \sqrt{\frac{\Gamma}{n_tg\Gamma_n}}$

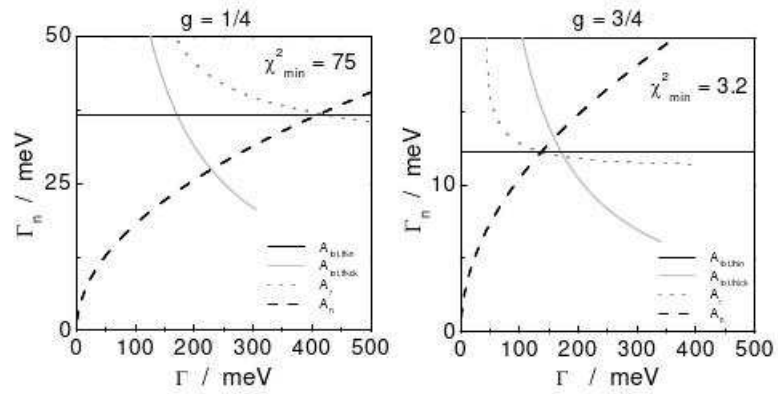


Figure 2.6: The method of area analysis for the 5.2 eV resonance in ^{109}Ag for two values of the statistical factor $g=1/4$ (left) and $g=3/4$ (right) [114].

is clearly the more likely value. A least-squares analysis provides the preferred value of g , and values on Γ_γ and Γ_n . Fröhner et al. [111] have compared the relative sensitivity of transmission, capture and scattering measurements. The theoretical curves for the three types of measurements are shown in Figure 2.7. The calculations are performed for different Γ_n/Γ_γ ratios. The results for both the correct ($g=3/4$) and incorrect spin assignment ($g=1/4$) are compared. These curves serve as a guide to the experimentalist for determining which particular set of resonance measurements will be required to determine in the most efficient way all the resonance parameters. From the curves in Figure 2.7 with the relations in Table 2.2 we can conclude that complementary data sets should be combined to determine a complete set of resonance parameters. Together with these conclusions we should add that very weak

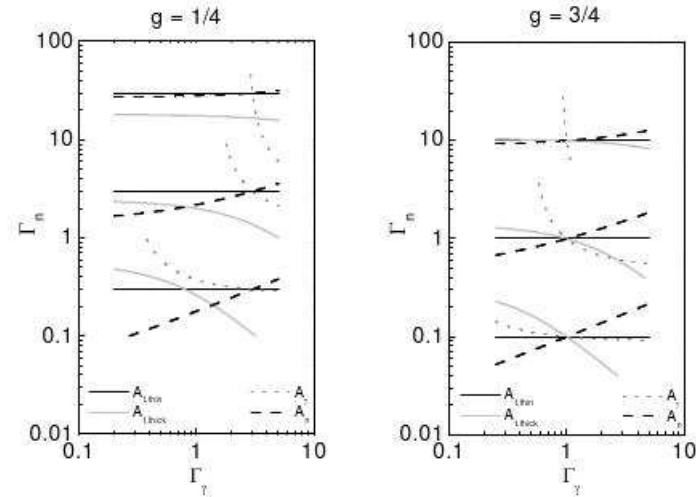


Figure 2.7: The method of the area analysis for $\Gamma_n/\Gamma_\gamma = 10$ (top), 1 (middle) and 0.1 (bottom) and $g=1/4$ (left) and $g=3/4$ (right).

resonance can only be determined by capture measurements and angular differential scattering data can be used to determine the spin of the resonance. In conclusion we summarize in the following table which measurements are complementary:

2.4.2 Resonance Shape Analysis (RSA)

In practice, several difficulties arise in applying the area analysis method. To obtain the experimental observable related to the areas defined in Eq. 2.41, 2.42, 2.43 and 2.44 one must still correct for the Doppler broadening, which affects the self shielding term, for the energy resolution of the spectrometer in case of overlapping resonances and for the multiple scattering in the case of the capture cross-section measurement. Procedures to correct for these effects have been applied in the past [112, 115]. How-

Table 2.3: List of complementary measurement that can be employed in area analysis.

Resonance type		Complementary measurements
Strong	$\Gamma_n > \Gamma_\gamma$	(A_γ, A_t) or (R_γ, A_t)
Intermediate	$\Gamma_n \approx \Gamma_\gamma$	(R_γ, A_t) or (R_γ, A_γ)
Weak	$\Gamma_n < \Gamma_\gamma$	(R_γ, A_γ) or (R_γ, A_t)
Very Weak	$\Gamma_n \ll \Gamma_\gamma$	(R_γ, A_γ)

ever nowadays one prefers to include these effects by performing a full Resonance Shape Analysis (RSA) of the data. When the resolution function of the spectrometer is well known, resonance shape analysis is superior to area analysis. Applying resonance shape analysis we can also determine the scattering radius from the resonances (Eq. 2.24) and account for multiple resonance interference.

In general, resonance shape analysis is more complete and utilizes all the information contained in the data. In ideal conditions, without any additional broadening due to the experimental resolution or Doppler effect, one could determine from one set of experimental data the resonance energy, the total width and the peak cross-section. Knowing the spin of the resonance (or the spin factor) one could deduce from one data set all resonance parameters. For instance, from an ideal total cross-section measurement we would be able to deduce the total natural width and the peak cross-section. These two parameters together with the spin factor define unambiguously the neutron width and capture width. However, in most cases additional broadening effects in the experimental data do not allow an accurate determination of the total width. For the determination of the complete set of resonance parameters additional complementary data are required according to the basic principles of the area analysis summarized in Table 2.2 and Figure 2.7.

In practice using the R-function expressed in Eq. B.4 the experimental data can not be completely described. The R-matrix theory shows that the cross-sections in a limited energy range depend not only on the internal levels in that range, but also on the external levels outside. Typically, problems arise in resonance analysis whenever compound levels below the neutron threshold (bound states at $E_n < 0$, see Figure 2.2) happen to be omitted. Although these external levels (or bound levels) are unobservable and therefore unknown, they must be introduced in the R-matrix formalism. A convenient approximation consists of accounting for the effect of such distant levels by tails of broad resonances having negative energies [89, 116]. The parameters of the negative resonances are adjusted in order to reproduce both the energy dependent total and capture cross-section data and the cross-section data at thermal energy (see Figure 2.4). To include the contribution of the external levels, the R-function may

be split into a sum over the external (ext) and internal (int) levels:

$$R_{nn} = \sum_{i=1}^{i_{int}} \frac{\gamma_{in}^2}{E_i - E - i\Gamma_{i\gamma}/2} + \sum_{j=1}^{j_{ext}} \frac{\gamma_{jn}^2}{E_j - E - i\Gamma_{j\gamma}/2}. \quad (2.47)$$

The second term in Eq. 2.47 is the so-called distant level parameter R_n^∞ . In practice, one defines the effective potential scattering length R' for s-wave channel [117]:

$$R' = a_n(1 - R_n^\infty). \quad (2.48)$$

The reason is that at low energies the potential scattering cross-section appears modified by a smooth contribution from the distant levels with the result:

$$\sigma_p = 4\pi R'^2 \quad (2.49)$$

even though this effective radius R' is connected to the potential scattering cross-section and the scattering cross-section at low energies, in the R-matrix shape analysis programs, R' is determined from the interference between the resonance part and the potential scattering for s-wave resonances.

Chapter 3

n_TOF and GELINA neutron time-of-flight facilities

In this chapter the main features of the neutron time-of flight facilities n_TOF, at CERN and GELINA, at IRMM are reported. Although the two facilities are conceptually very different, they have characteristics that make them very suitable for high accuracy measurement of neutron cross-sections on a variety of isotopes. The advantage of the n_TOF installation is the high instantaneous neutron flux that makes this facility particularly suited for measurements of radioactive isotopes. Typically the two facility are considered complementary. However, this common effort on measurement of the capture cross-section on the stable isotope ^{197}Au , offers the opportunity of a comparison.

3.1 The time-of-flight method

In order to perform neutron time-of-flight measurements, the neutron source must be pulsed. In a relatively short time, the neutrons with a broad energy spectrum are created at the reference start time t_0 (see later for a detailed definition of t_0). At a distance L (from the neutron source), ranging from a few to several hundred meters for high resolution experiments, a sample is placed in the neutron beam.

For measurements of reaction cross-sections, the reaction products, like fission fragments, alpha particles, capture γ -rays or scattered neutrons are detected. The time of detection t_n of the reaction product is used as a stop signal to determine the time of flight:

$$t = t_n - t_0 \quad (3.1)$$

of the neutron that induced the reaction. The kinetic energy E_n of neutrons with a speed $v = L/t$ can be expressed relativistically as:

$$E_n = E_{tot} - mc^2 = \sqrt{(c^2p^2 + m^2c^4)} - mc^2 = mc^2(\gamma - 1) \quad (3.2)$$

with $\gamma = (1 - v^2/c^2)^{-1/2}$, and c the speed of light. The first term of the series expansion gives the classical expression for the neutron kinetic energy:

$$E_n = \frac{1}{2}mv^2 = \alpha \frac{L^2}{t^2} \quad (3.3)$$

Taking the value of the speed of light $c = 2.99792458 \times 10^8$ m/s and $m = 939.6$ MeV/ c^2 for the neutron mass, it results $\alpha \approx 72.298$ when L is expressed in meters and t in microseconds and E_n in eV.

Electron- and proton-based neutron beams are generated by a primary beam of charged particles impinging on a thick neutron-producing target, for example U, W, Pb. This mechanism yields a large number of high energy gamma-rays travelling along the beam pipe, which cause the so-called gamma-flash in the detectors, often saturating them. Since gamma-rays travel at the speed of light, they reach the detector before the neutron bunch. Therefore the gamma-flash is used as a time reference (to determine the start time t_0):

$$t_0 = t_\gamma - L/c, \quad (3.4)$$

where t_γ is the time signal of the gamma-flash.

From Eq. 3.3 the expression of the relative energy resolution may be given by the formula¹:

$$\frac{\Delta E_n}{E_n} = 2 \times \sqrt{\left(\frac{\Delta t}{t}\right)^2 + \left(\frac{\Delta L}{L}\right)^2} \quad (3.5)$$

which may be written:

$$\frac{\Delta E_n}{E_n} = \frac{2}{L} \sqrt{1.91 E_n \Delta t^2 + \Delta L^2}. \quad (3.6)$$

Conventionally the quantity Δt is the quadratic sum of the contributions due to the time uncertainty of the primary beam burst and time resolution of electronics and detectors. Equally the total correction due to the neutron-producing target and the moderator assembly, to the angle of the flight path (FP) and to the detector thickness is included in ΔL [118]. As can be deduced from Eq. 3.5, the flight path length plays an important role in the achievable energy resolution (described in Section 3.2): the longer the flight path the better the energy resolution. However, this is obtained at the expenses of the neutron flux, which is proportional to $1/L^2$. Therefore one should always try to find a good compromise between resolution, neutron flux and energy range, depending on the application.

A further common feature of time-of-flight facilities is the use of filters. Two kind of filters can be distinguish in TOF measurements²:

1. permanent anti-overlap filters (described in section 3.1), which eliminate the

¹For sake of simplicity, the expression makes use of classical relation between time and energy.

²Both filter setups are placed close to the target hall, far from the detectors.

slowest neutrons of each burst;

- black resonance filters, which are used for determining the time dependent background (background filters).

Overlap filters

In TOF measurements one has to make sure that fast neutrons of one pulse do not overlap with the slow neutrons of a previous pulse. If the repetition period of the pulses is not low enough to cover the energy range down to subthermal energies, so to prevent the presence of slow neutrons from a cycle in a subsequent one, absorbing filters are needed. Such an overlap filter, inserted in the neutron beam, has to be thick enough to stop all neutrons with a flight time longer than the period of the primary beam, but thin enough to let neutrons at higher energy to go through with small attenuation. Depending on the flight path and on the beam frequency, different solution may be applied:

- Cd is a good choice, for stopping neutrons below 0.6 eV;
- ^{10}B is used to stop higher energy neutrons.

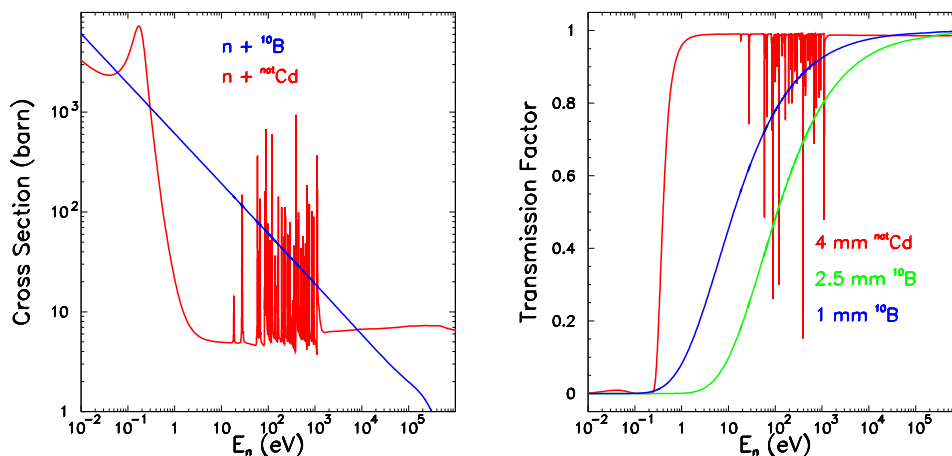


Figure 3.1: The total neutron cross-section on ^{nat}Cd and on ^{10}B , taken from ENDF/B-VI [55], together with the calculated transmission of the anti-overlap filters.

In Figure 3.1 the total cross-sections for the two isotopes are shown. It is evident, from the right panel in the figure, that a Cd overlap filter is more efficient since its cross-section drops down rapidly after about 0.6 eV, while the $^{10}\text{B}+n$ cross-section follow the typical $1/v$ shape.

At the n_TOF facility the overlapping between neutron bunches is not present, since the repetition rate of the primary beam is very low (0.25 Hz) thus allowing, in principle, for measurement down to the thermal region. It is interesting to note that at long flight paths, the gravity affects the shape of the neutron flux, for slow neutrons. Indeed, the effect of the gravity on thermal neutrons is sizeable. For example for a 185 m flight path thermal neutrons drop down 3.5 cm, the effect is already negligible at 1 eV: they drop down 0.08 cm.

Background filters

Adequate thickness³ slabs of Rh, Ag, W, Mo, Ge, Co, Na, S, Bi are placed in the neutron beam line in order to absorb nearly all neutrons in a given energy region (see Table 3.1), i.e. around a big resonance in the cross-section of mentioned isotopes. In that way, all counts measured at the energy of that resonance (called black resonance) can be attributed to the background, as shown in Figure 3.2. Since black filters affect

Table 3.1: Energy and thickness of some black resonance filters commonly used in TOF experiments.

Element	Energy [51]	Thickness
Rh	1.3 eV	2.0×10^{-3} atoms/barns
Ag	5.2 eV	1.2×10^{-3} atoms/barns
W	18.8 eV	6.2×10^{-4} atoms/barns
Mo	44.9 eV	5.6×10^{-3} atoms/barns
Ge	102.0 eV	1.9×10^{-2} atoms/barns
Co	132.0 eV	2.6×10^{-3} atoms/barns
Bi	800.0 eV	2.9×10^{-2} atoms/barns
Na	2850 eV	3.2×10^{-2} atoms/barns
S	102.7 keV	2.5×10^{-1} atoms/barns

the counting rate as well as the behaviour of the neutron flux energy distribution, with a flux reduction observed when black filters are in the beam, combinations of different filters have to be adopted depending on the energy region one is interested in. In Figure 3.3 an example of the neutron flux reduction is shown for a measurement with W, Mo and S background filters. This last element, Sulfur, is responsible for a loss of about 30% of incoming neutrons. Therefore it should be placed in the beam only for particular measurements.

Pb slabs in combination with Al is often used as a background filter to reduce the γ -flash. It is placed in the same position as common background filters, with the aim of absorbing photons and electrons travelling along the beam pipe.

³The resonance has to be saturated.

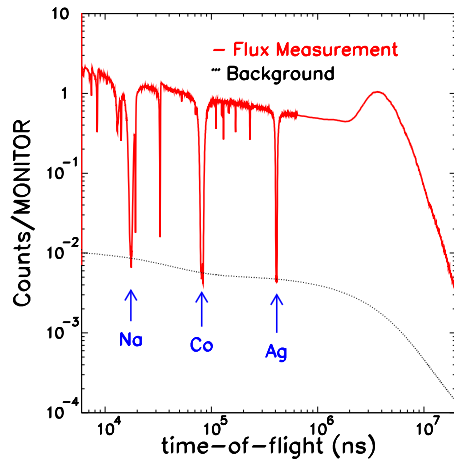


Figure 3.2: Typical neutron flux measurement with Ag, Co and Na background filters at GELINA. Three strong suppression of counts can be seen at TOF corresponding to the energy of the big resonances in Ag, Co and Na.

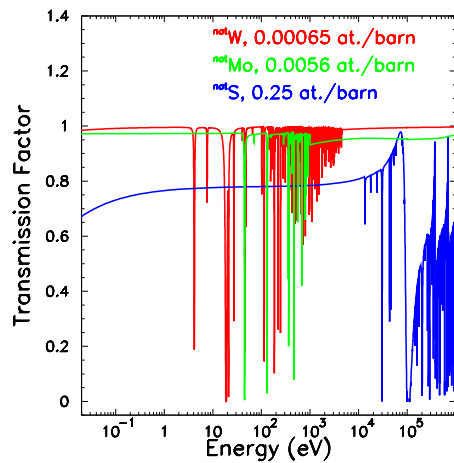


Figure 3.3: Neutron flux attenuation due to the presence of background filters in the beam: ^{nat}W , ^{nat}Mo , ^{nat}S .

Dead time

A typical problem of neutron time-of-flight measurements is the dead time, since a large number of neutrons is compressed in bunches of a few microseconds. The relatively long dead time (about $3 \mu\text{s}$) in conventional data acquisition systems (that provide simultaneously the pulse height and the time information for the detected events) hinders cross-section measurements with high counting rates. In particular this is the case for capture cross-section measurements using highly radioactive samples or thick samples of materials having strong resonances. Either the high average counting rate (e.g. due to the radioactivity of the sample) or the high instantaneous counting rate for strong resonances results in a large dead time correction, which may introduce systematic bias effects. One solution to reduce the impact of the dead time is the use of a data acquisition system based on fast digitizers [88, 119, 120]. Indeed the entire waveform of the detector signal is recorded and the required information is deduced by off-line processing. However such systems require large data storage capabilities, and on-line verification of the results is almost impossible. In case of on-line analysis the total dead time is defined by the dead time of the Digital Signal Processing (DSP) algorithms, which depends on the characteristics of the pulse, and on the re-arming time of the trigger (in this case the dead time is about 500 ns). It has to be noticed that in case of low repetition rate operation, the time between two consecutive neutron bunch is long enough to process off-line all the signals recorded during the neutron bunches, thus in principle allowing to measure without dead time.

The dead time can be measured by registering the time difference between two consecutive events. In the resulting time interval spectra (see Figure 3.4) the dead time corresponds to the time-duration of the region without counts.

A correction for a non-extendable dead time system has to be applied [121]. For pulsed beam a more accurate correction can be introduced [122] but requires a stable beam. In this case the dead time corrected number of counts in time-of-flight channel I , $N_c(I)$, is related to the number of observed counts $N_0(I)$ by the expression:

$$N_c(I) = \frac{N_0(I)}{1 - \sum_{J=I_d}^{I-1} \frac{N_0(J)}{N_b} - \frac{N_0(I)}{2N_b}} \quad (3.7)$$

where N_b is the total number of bursts and where the dead time is given in channels by the difference $I - I_d$.

3.2 Resolution function of TOF-spectrometers

The energy resolution of TOF-spectrometer plays an important role in the analysis of cross-section data in the resolved resonance region. In TOF experiments the neutron

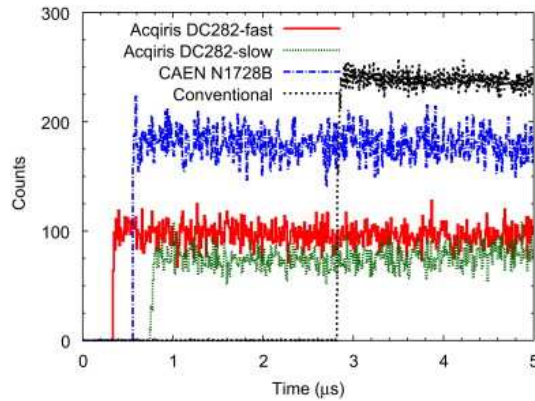


Figure 3.4: Time interval spectrum recorded with a C_6D_6 detector and a random gamma-ray source at GELINA facility with conventional ADC system and with fast digitizers. The acquisition systems have the following values for the dead time: 350, 750, 560 and 2800 ns. From [119].

energy is determined from the time when it is created (t_0) to the time of its detection (t_n) at a given distance from the source. However t_0 and t_n have a time distribution, and therefore the time-of-flight is characterised by a distribution in time or its equivalent in distance, which is called the resolution function⁴. The effect of this spread in time (or equivalently in distance) is to broaden, together with the Doppler effect, the observed widths of the resonances, as can be seen in Figure 3.5. Therefore the resolution function is required for the resonance shape analysis [92, 93, 123] of cross-section data, to extract the nuclear parameters from the observed data.

Several process contribute to the resolution: the neutron producing pulse, the finite size of the neutron-producing target, the water moderator, the detector, etc. Therefore the resolution function is different for each facility and depends strongly on the type (spallation or photoreaction) and geometry of the neutron source (see Figure 3.8 and 3.12). The components of the resolution function are considered to be independent distributions, therefore they are convoluted with each other to obtain the total shape of the resolution function of the TOF-spectrometer (the total resolution function $I(t)$ is the convolution, denoted by $*$, of up to 6 separate components $I_i(t)$: $I(t) = C \times (I_1(t) * I_2(t) * \dots * I_6(t))$).

Typically the total resolution function is estimated by means of extended Monte Carlo calculations. In R-matrix codes (such as REFIT or SAMMY) an analytical detailed description of the single distributions $I_i(t)$, is present. The parameters used to characterize $I_i(t)$ are function of physically measurable quantities.

Two equivalent ways can be followed to express each distribution as a function of the measured quantities such as the “start time” (t_0), the “stop time” (t_n) and the

⁴Also called resolution.

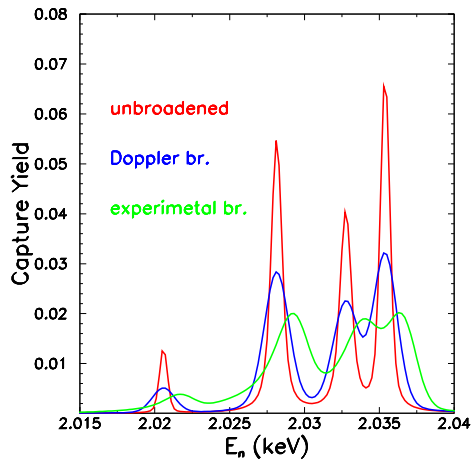


Figure 3.5: Au capture yield calculated from ENDF/B-VII parameters at 0 K (red curve), Doppler broadened at 300 K (blue curve), and broadened by experimental resolution as well (green curve). The n_TOF resolution function has been used for calculation (an energy shift is applied).

geometrical flight path (L_0):

- one possibility is to introduce an average time t_m that the neutrons spend rattling around in the source and detector system, so that the velocity of a neutron is defined as $V = L_0 / \{t_n - [t_0 + t_m(V)]\}$;
- another possibility is to introduce an equivalent additional distance to the geometrical flight path, so that: $V = [L_0 + L_m(V)] / (t_n - t_0)$.

This second approach is adopted at GELINA and n_TOF. It has to be noted that in both case the time-energy relation cannot be considered independently from the resolution function since the value of the mean equivalent distance of the resolution function is changing with energy.

A brief description of the main components of the resolution function is here presented.

Initial pulse. The neutron pulse is closely related to the timing of the primary charged-beam impinging on the producing target. The uncertainty of the neutron generation time, i.e. the electron/proton burst duration, is of the order of 1-2 ns (FWHM) for electron pulse, while it is larger for spallation sources, ranging between 7 ns (at n_TOF facility) and 250 ns (at the LANSCE facility). For low neutron energy, up to the keV region, the contribution of this quantity to the energy resolution is negligible.

Water moderator. This is the main component of the resolution function. The distribution of the time t_m of neutrons leaving a moderator (with a large fraction of Hydrogen) with a velocity V after slowing down is supposed to be related to a chi-square

distribution [124]:

$$I_m(t) \propto \frac{1}{2} \left(\frac{V t_m}{\lambda} \right)^2 e^{-\frac{V t_m}{\lambda}} \quad (3.8)$$

where λ is the effective mean free path of the neutron in the moderator which is a slowly varying function of the energy. In this case the use of the distribution of the equivalent distance $L_m = V \cdot t_m$ of neutrons escaping from the moderator with a velocity V has the advantage of being almost constant for different neutron energies [125].

Moderator angle. When the flight path is at an angle θ with respect to the normal of the moderator, a difference in flight distance of $d \sin(\theta)$ from one side of the projection of the collimator on the moderator to the other side, has to be taken into account.

Detector. In-beam neutron detectors, as used for transmission experiments, can be several centimetres thick so their contribution to the resolution function is not negligible. For capture experiments the gamma-ray detector is not in the neutron beam and capture sample are usually thin, thus it is assumed that this two components of the resolution function are negligible. The time resolution of the detector may however contribute significantly.

Timing channel. Also the binning of time-of-flight events into channels of fixed width introduces a supplementary resolution broadening.

Moreover, additional gaussian resolution components which may be due to the electronics, could be added.

3.3 n_TOF facility at CERN

The construction and commissioning of a new neutron time-of-flight facility at CERN, n_TOF, based on an idea of Rubbia et al. [127], was finished in 2001. The facility has become fully operational with the start of the scientific measurement programme in May 2002. It has been designed to measure capture and fission cross-section on high radioactive isotopes taking advantage of the high instantaneous neutron flux in combination with the low duty cycle, which is low enough to cover the energy range down to subthermal energies, preventing overlapping of slow neutrons in subsequent cycles. A good energy resolution is achieved by using a long flight path.

The spallation mechanism is a remarkably powerful source of neutrons. At the proton energy of 20 GeV of the CERN PS accelerator, about 300 neutrons per proton are produced in the n_TOF spallation target. The high current pulses of up to 7×10^{12} protons delivered to the n_TOF facility at a nominal repetition rate of 0.4 Hz and with a very short pulse width of 7 ns root mean square (r.m.s.), result in a high instantaneous neutron flux with a considerable potential for high resolution cross-section measurements on radioactive isotopes, in a wide range in neutron energy, from thermal to several GeV. The neutrons produced by spallation in a lead block

surrounded by a water moderator [128, 129, 130, 131] are canalized through an evacuated tube along the flight path to an experimental area at about 185 m downstream of the target, making use of the existing TT2-A tunnel (see Figure 3.6). The main

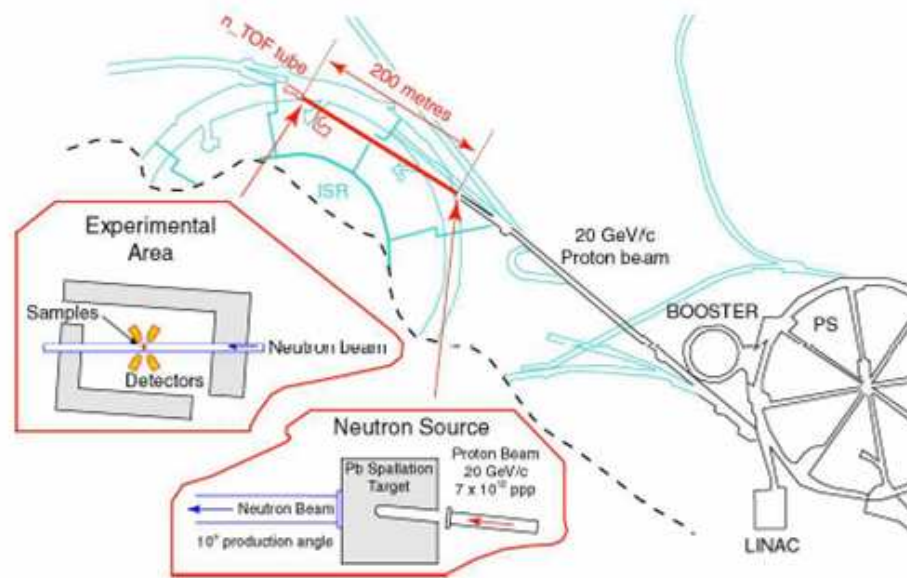


Figure 3.6: General layout of the n_TOF facility. The proton beam is extracted via the TT2 transfer line and hits the lead target. At the end of the TOF tunnel (TT2-A) the experimental station is placed at about 185 m from the primary target. Picture from [132].

characteristics of the proton beam are:

- a momentum of 20 GeV/c, corresponding to the maximum attainable energy within a magnetic cycle of 1.2 s of the proton synchrotron (PS);
- proton bunches of 7×10^{12} particles with a width of 7 ns (r.m.s.);
- up to six bunches per supercycle of typically 16.8 s. Of these, up to five bunches per supercycle can be used due to limitations on the maximum power dissipation allowed on the spallation target and on the radiation level in the target area.

The beam is extracted from the PS and sent onto the spallation target by using a fast extraction system. In terms of peak intensity, the proton beam for n_TOF can be considered among the highest for the PS, thanks to a special compression procedure, which allows us to reduce the original pulse width of 14 ns to 7 ns. A more detailed technical description of the facility can be found in [133]. The facility can be operated

in two ways: in dedicated and, with a reduced intensity, in parasitic mode. In dedicated mode one or more bunches per supercycle are delivered to the n_TOF target with the full nominal intensity of 7×10^{12} protons/bunch. In parasitic mode, a bunch of half intensity is delivered at 24 GeV/c momentum. The intensity, in this case, is limited to about 4×10^{12} protons/bunch.

The angle of impact of the proton beam axis on the spallation target is 10° in order to minimize the number of undesired secondary particles in the experimental area. At the end of the primary section a sweeping magnet is used to remove the remaining charged particles from the beam line.

3.3.1 Beam characteristics

In Figure 3.7 the energy distribution of the neutron flux at the sample position at 185 m for a standard bunch of 7×10^{12} protons is shown. This particular isoenergic⁵ shape is obtained moderating the initially fast neutron spectrum with 5.8 cm water layer surrounding the lead target. The data are based on a measurement performed with a ^{235}U loaded parallel plate fission ionization chamber and below 1 keV from a ^6Li -based in-beam neutron flux monitor (see next section). More details can be found in Ref. [46].

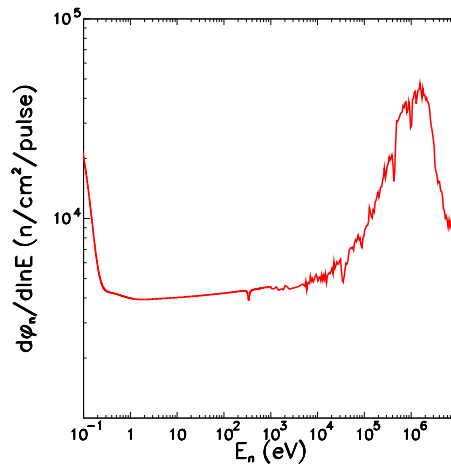


Figure 3.7: The n_TOF neutron flux per bunch at the sample position in the experimental area at 185 m for a standard pulse of 7×10^{12} protons.

The diameter of the beam tube is progressively reduced from 800 mm at the exit of the spallation target to 400 mm before the first collimator, which is located at 137 m from the target. In the primary section massive concrete and iron shielding are

⁵Flat shape of the neutron flux as a function of the logarithm of the incoming neutron energy.

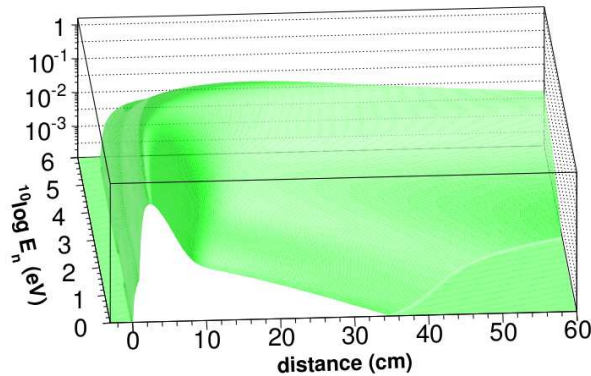


Figure 3.8: The resolution function at the sample position (185 m) of the n_TOF facility, given as a distribution of the equivalent distance as a function of the neutron energy, in the range from 1 eV and 1 MeV. Picture from [126].

placed at about 72 m and 140 m. At 175 m the diameter of the tube is reduced to 200 mm before the second collimator. Starting from this point the tube is made from an Aluminum alloy. Before entering the experimental area the tube crosses a 3.2 m thick concrete shielding.

A 20 GeV/c proton beam interacting with a lead target is a source of many charged and neutral particles [134]. While charged particles are strongly suppressed by the sweeping magnet at 145 m from the spallation target, neutral particles and gamma-rays can reach the measuring station. Photons are produced in spallation reactions and during neutron moderation. These photons can be separated into two groups: a “fast” component resulting from the spallation process itself with a time-of-flight to the measuring station of less than 1 microsecond, and a “slow” component, mainly due to thermal neutron capture in the moderator and the lead target, with arrival times between 1 and a few hundreds μs . The “fast” component, also called gamma-flash, is used to measure the t_o of each pulse (see expression 3.4).

The γ -rays of the “slow” component arrive at the measuring station along with neutrons of a few keV energies. Though this gamma-flux is more than an order of magnitude lower than the neutron flux[133], it represents a severe source of background in capture cross-section measurements. From the energy spectrum of these photons one finds that 40% are due to the neutron capture on hydrogen, which produces 2.2 MeV gamma-rays. Another 5% contribution comes from photons with energies around 7 MeV resulting from the capture on lead, on the Aluminum alloy container and on the iron target support.

The n_TOF MicroMegas detector. MicroMegas [135] is a new gaseous detector based on a simple geometry with planar electrodes developed by Nobel Laureate

G. Charpak. It consists of a conversion gap where radiation produces ionization electrons, and of a thin amplification gap, where the free electrons create an avalanche. The two regions are separated by a thin $5\ \mu\text{m}$ mesh grid. The avalanches produced in the amplification gap can then be collected on printed electrodes of any shape to achieve high spatial resolution. These detectors are also very fast and well suited for high counting rates [136]. It has been employed during the commissioning to measure the beam profile. A series of test measurements [137] demonstrated background rejection properties and detection efficiency for the charged particles produced by neutron reactions. The detector was shown to have a neutron detection efficiency of up to 0.1 and a spatial resolution of less than $250\ \mu\text{m}$, matching the requirements of the n_TOF experiment.

Silicon Monitors (SiMON). For routine neutron beam monitoring a robust and simple system based on Silicon detectors has been developed [83]. Four Silicon detectors are viewing a target consisting of a pure ${}^6\text{Li}$ layer $200\ \mu\text{g}/\text{cm}^2$ in thickness and 6 cm in diameter, which is deposited on a substrate of a $3\ \mu\text{m}$ thick Mylar foil. The geometry is designed such that only the ${}^6\text{Li}$ sample is exposed to the neutron flux, whereas the Si detectors are placed inside a carbon-fibre vacuum chamber, but outside the neutron beam (see Figure 3.9). The ${}^6\text{Li}$ deposit is protected against oxi-

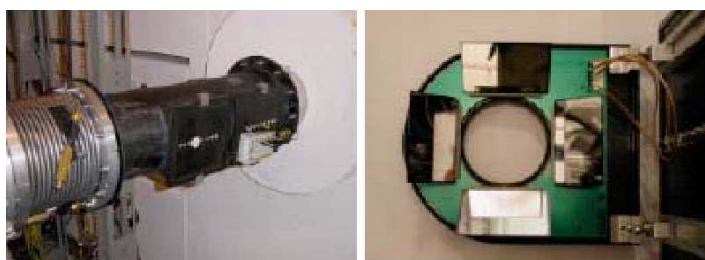


Figure 3.9: Carbon-fibre chamber (left) and internal geometry of the SiMON detectors (right).

dation by an evaporated carbon layer, less than $10\ \mu\text{g}/\text{cm}^2$ in thickness. In this way, the ${}^6\text{Li}$ deposit could be maintained in proper state even after four months of operation and several air/vacuum cycles (venting operations). The spectrum of the energy deposited in the Si [138] detectors shows a double peak with the tritons and alpha particles from the ${}^6\text{Li}(n,\alpha){}^3\text{H}$ reaction clearly separated. To avoid threshold problems, the neutron flux analysis is performed by selecting only the triton peak.

3.3.2 Capture and fission instrumentation

For capture and fission experiments different detectors are available. In the n_TOF measurements campaigns 2001-2003 deuterated benzene C_6D_6 γ -ray detectors were built, with a container made of low mass carbon fibre [139]. These detector were

used for neutron capture measurements on several isotopes. The samples are placed in position by a carbon fibre sample changer. The low neutron capture cross-sections for carbon and deuterium assure a low contribution of the background from sample scattered neutrons.

A second capture detector has become available in 2004. It is a 4π 100% efficiency Total Absorption Calorimeter (TAC) made of 42 BaF₂ crystals inserted in ¹⁰B loaded carbon fibre capsules, and coupled to XP4512B photomultipliers. Samples are placed in the centre of the calorimeter and are surrounded by a neutron absorber. This device will be fully described later, in Section 4.2.5.

Fission experiments have been performed with two different detector systems. A fission ionization chamber (FIC) has been developed for use at the n_TOF facility using deposits of fissile isotopes on 100 μm thick Aluminum foils (see Ref. [47, 48, 140] for a detailed description). Parallel plate avalanche counters (PPACs) have been also developed with target deposits on 1.5 μm thin Mylar or 2 μm Aluminum foils, allowing to detect the two fission fragments in coincidence. The use of standard cross-sections to measure the neutron flux (in particular ²³⁵U(n, f) and ²³⁸U(n, f)) allows also to determine accurate neutron induced fission cross-sections with the ratio method.

The data acquisition system [141] is based on Flash Analogue to Digital Converters (FADC) used for sampling and recording the waveform of the detector signals. After zero suppression, the data are sent to CERN's data storage facility CASTOR, while an on-line analysis with dedicated pulse shape analysis routines [88, 120] for each detector is performed for monitoring the quality of the data.

3.4 GELINA Facility at EC-JRC-IRMM

The Geel Electron Linear Accelerator (GELINA) of the Institute for Reference Materials and Measurements (IRMM) is a neutron TOF-facility built in 1965 and subsequently upgraded in 1976, 1984, 1994 and 2004.

It has been especially designed and built for high-resolution cross-section measurements. It is a multi-user facility, serving up to 10 different experiments simultaneously, and providing a pulsed white neutron source, with a neutron energy range between 10 meV and 20 MeV.

The GELINA facility consists of four main parts: a linear electron accelerator, a compression system, a neutron production target with a moderator and finally a series of neutron beam lines.

3.4.1 Neutron production

Electrons with an energy of 100 keV are injected by a triode gun that produces bursts with a pulse length of about 10 ns. These electrons are accelerated in three sections:

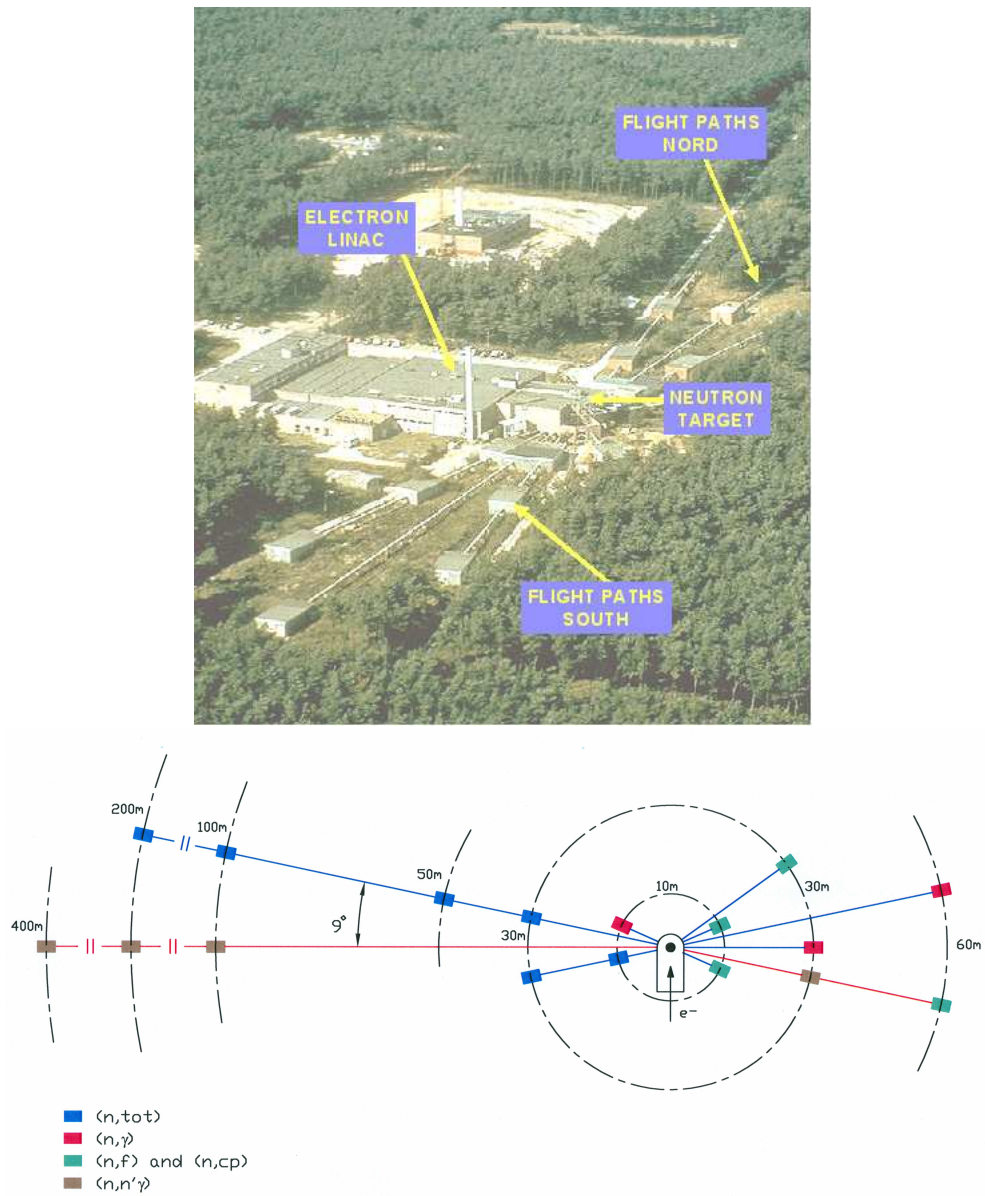


Figure 3.10: A photo and a scheme of the GELINA facility. 11 flight paths and measurement stations (for capture, elastic, fission, inelastic, self-indication and total cross-section) are present. Picture from [142].

a 2 m standing wave accelerator section and two 6 m travelling wave sections. In the first section the electrons reach a velocity close to the speed of light and in the following 2 sections they mainly gain energy in the form of mass. This results in a maximum energy of 140 MeV.

The 10 ns time spread of the relativistic electrons leaving the accelerator sections is reduced using a unique post-acceleration compression magnet. The pulse width of the electrons is reduced to less than 1 ns (FWHM) with an associated peak intensity of about 100 A [75].

The high energy electron beam hits a mercury cooled rotating uranium target, generating Bremsstrahlung radiation. The neutrons are mainly produced via photonuclear (γ, n) and ($\gamma, 2n$) reaction and via photofission (γ, f) reactions [74]. To increase the flux in the low-energy region, two water-filled beryllium moderators are placed above and below the uranium target. Water and beryllium are good neutron moderators because neutrons are slowed down efficiently by collisions with low mass nuclei; moreover hydrogen has a very large neutron scattering cross-section. The resulting neutron energy distribution is characterised by a Maxwellian distribution at thermal energy and a high energy tail with approximately a $1/E$ -shape.

Moderated neutrons are emitted in all directions and enter the 11 different flight paths which lead to the measurement stations. The flight paths have lengths ranging from 8 m to 400 m (as shown in Figure 3.10). Depending on the repetition frequency of the Linac (1 Hz to 800 Hz) and the flight path length, the neutron beams available for the experiments cover an energy range from 10 meV up to several MeV (see Table 3.2). Since the neutrons are emitted isotropically, the neutron flux at a distance L from the neutron target is proportional to $1/L^2$.

In Figure 3.11 the flux at the measurement station at 28 m is shown. Its resolution function is presented in Figure 3.12. At 800 Hz operating frequency, the neutron intensity is about 3.4×10^{13} neutrons/s.

Using suitable collimators, either the direct neutron spectrum (from 100 keV to 20 MeV) or the moderated spectrum (from 10 meV to 1 MeV) can be utilized. As already

Table 3.2: Minimum energy available at the GELINA flight paths, depending on the repetition rate of the Linac. The energy refers to the overlap of neutron bunches. At longer flight paths only the unmoderated neutrons are available.

Flight Path (nominal) length	LINAC frequency		
	50 Hz	400 Hz	800 Hz
12.8 m	0.001 eV	0.137 eV	0.548 eV
12.8 m	0.002 eV	0.137 eV	0.548 eV
28. m	0.011 eV	0.733 eV	2.931 eV
50. m	0.032 eV	2.058 eV	8.230 eV
60. m	0.044 eV	2.814 eV	11.254 eV

pointed out in Section 3.1 Cd filters may be used only at 50 Hz repetition rate, since the overlapping energy is below the 0.6 eV resonance, in the Cd cross-section (see Figure 3.1). At higher Linac frequency, a ^{10}B filter is used. This introduces a limit on the minimum energy available (around 100-200 eV), due to the large attenuation of the neutron flux and the consequent small signal to background ratio.

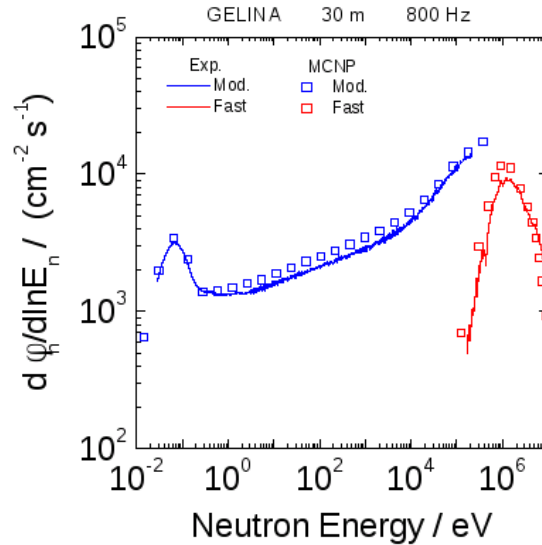


Figure 3.11: The GELINA neutron flux obtained by means of simulations and measurements. Picture from [143].

The total emission of neutrons is continuously monitored also by several BF_3 proportional counters (using the reaction $^{10}\text{B}+n$) placed at different positions around the producing target. These monitors measure the energy-integrated neutron flux. The counting rate of these detectors is used to monitor the stability of the accelerator and to normalise the measurements to the same total neutron flux. In the following, these monitor will be called CM (Central Monitor).

3.4.2 Measurement stations

The measurement stations are equipped with different instrumentation needed to perform transmission and partial reaction cross-section measurements. Transmission reactions can be measured at the 25 m, 50 m, 100 m, 200m, 400 m flight paths using Li-glass detectors [145, 146] or plastic scintillators [147]. To study the Doppler broadening one of the measurement stations is equipped with a cryostat, which is able to cool the sample down to 10 K [148]. For capture measurements, standard C_6D_6 scintillator are used at 12.8 m, 28 m and 60 m flight paths. Fission cross-section

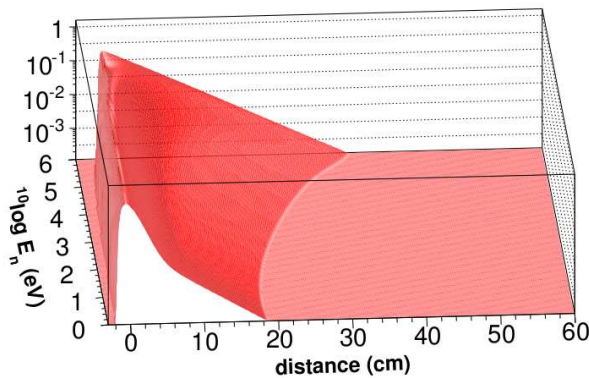


Figure 3.12: The resolution function of the spectrometer GELINA at the measurement station at 28 m, given as a distribution of the equivalent distance as a function of the neutron energy, in the range from 1 eV and 1 MeV. Picture from [144].

measurements are performed at 12.8 m and at 28 m station using Frisch gridded ionization chambers and surface barrier detectors [149]. These stations are also used to study neutron induced charged particle reactions [150]. Studies of $(n, xn\gamma)$ reactions are performed at 28 m and at 200 m using HPGe detectors [151].

3.5 About the present $^{197}\text{Au}(n, \gamma)$ measurements

The calculated shape of the resolution function for the n_TOF as well as for the GELINA target-moderator assembly is not symmetric, as shown in Figures 3.8 and 3.12. The two resolution functions are different so that it is not straightforward to compare the resolution of the GELINA and n_TOF installations. As explained in Ref. [123] a quantitative comparison can be done by assuming the FWTM⁶ as the uncertainty related to the distribution of the resolution function. Figure 3.13 shows this comparison. Thanks to its long flight path, the energy resolution at n_TOF is better than that of GELINA at low energies (below 2 keV), while at higher energies a better resolution can be obtained at the 60 m FP at GELINA.

Figure 3.14 shows the results of calculations in which the experimental broadened capture yield for a thin gold sample is folded with the expected n_TOF and GELINA resolution functions. The common effect of the reduction of the peak cross-section due to the energy resolution and the broadening of the resonances can be seen. Moreover, Figure 3.14 confirms the results of Coceva et al. [123].

The contribution of the experimental resolution to the energy resolution plays

⁶Full Width at one-Tenth of the Maximum.

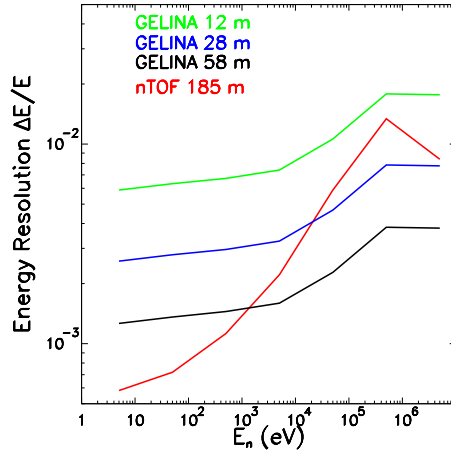


Figure 3.13: Comparison of the expected energy resolution for the measuring station of n_TOF at 185 m and for GELINA at a 12.8 m, 28 m and 60 m Flight path.

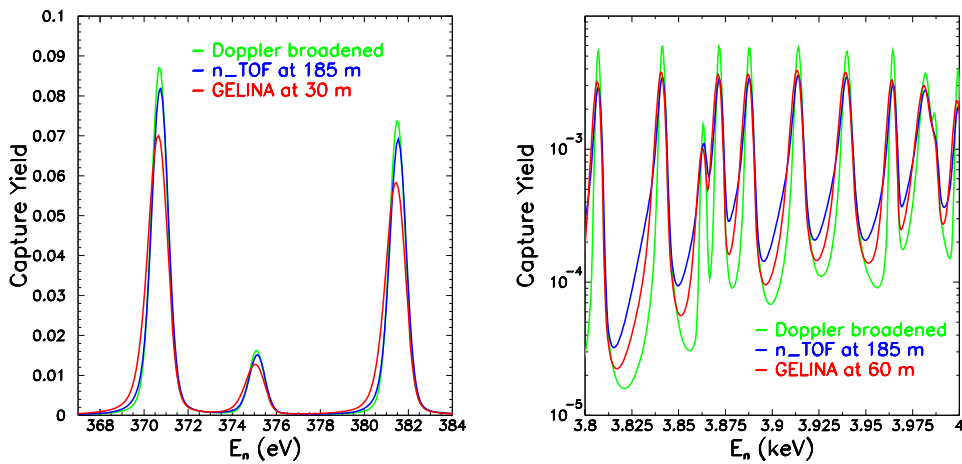


Figure 3.14: The calculated capture yield for a 50 μm thickness ^{197}Au sample. The yield is convoluted with n_TOF resolution function (Flight path 185 m) and GELINA resolution function (left: flight path 28 m; right: flight path 60 m).

an important role when it is higher than the Doppler effect (a feature, this last, of the isotope to be measured). Therefore the best experimental condition depend on to the nucleus to be measured. The observed widths (at half maximum) Γ_{obs} may be estimated from the quadratic sum of the contribution of the Doppler ΔE_{θ} and the experimental broadening ΔE_R , assuming that they are approximately Gaussian in shape and independent:

$$\Gamma_{obs}^2 \approx \Gamma^2 + \Delta E_R^2 + \Delta E_{\theta}^2. \quad (3.9)$$

In Figure 3.15 the total natural line width, taken from the ENDF/B-VII library, is compared with the broadening due to the Doppler effect and the experimental resolution for measurements at the capture measurement station of the n_TOF facility and at a 60 m flight path station of the GELINA facility. This figure reveals that below 1500 eV the observed line width is completely dominated by the Doppler broadening. Even for a 60 m flight path at GELINA only for the first strong s-wave resonance at 4.9 eV the resonance energy, total width and capture kernel can be deduced from a capture measurement. For all other resonances below 1700 eV the information obtained from a transmission and only the capture Kernel can be determined. Such measurements should be performed at a long flight path and require extremely long measurement times. Moreover from the figure it results that, depending on the flight path length, the Doppler effect dominates the experimental broadening of our data up to different energies, they are reported in Table 3.3. As can be seen in the series of figures 3.16 and 3.17, the point in which the Doppler curve meet the experimental curve, constitutes an important information to choose the flight path (where the measurement can be carry out). In particular when the Doppler broadening dominate the experimental one, measurements can be carry out with the same (good resolution and) results.

Table 3.3: The energy value at which the Doppler contribution to the energy resolution becomes lower than the experimental broadening (with respect to Figure 3.15).

Flight path length	Energy value
GELINA 12.8 m	55. eV
GELINA 28. m	560. eV
GELINA 60. m	1700. eV
n_TOF 185. m	1450. eV

In Figure 3.16 we present some capture yields obtained at different flight path at GELINA with a gold sample of 6.4×10^{-4} atoms/b. Since at n_TOF a 7.3×10^{-4} atoms/b gold sample has been measured (with a different detector), therefore with a similar thickness, it is possible to compare the measured capture yield. In Figure 3.17 we first compare in a narrow energy region the capture yield obtained at each flight

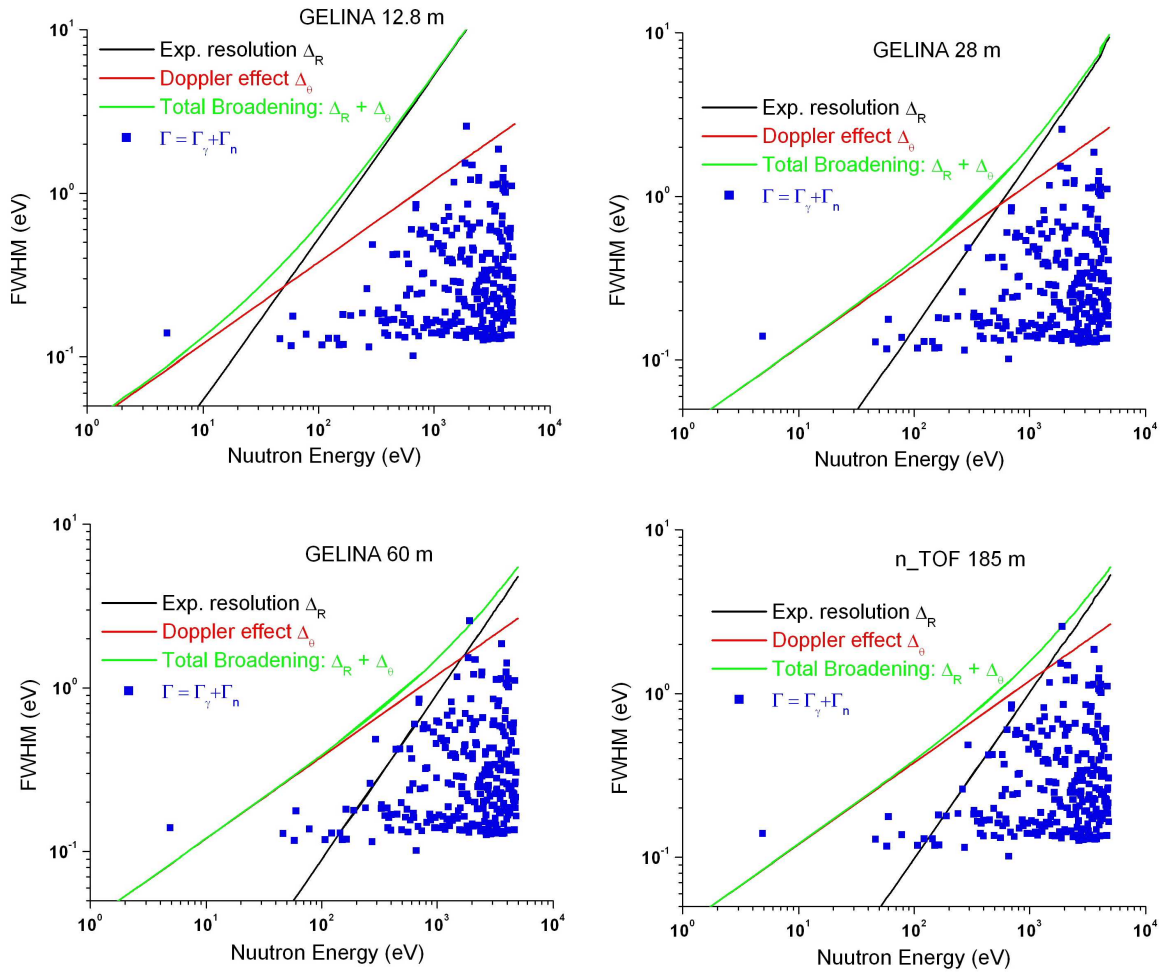


Figure 3.15: A comparison of the natural line width ($\Gamma = \Gamma_\gamma + \Gamma_n$) from [51] against the broadening due to the experimental resolution (Δ_R) and the Doppler effect (Δ_θ) for the n_TOF flight path lengths of 185 m and for the GELINA flight paths at 12.8 m, 28 m and 60 m.

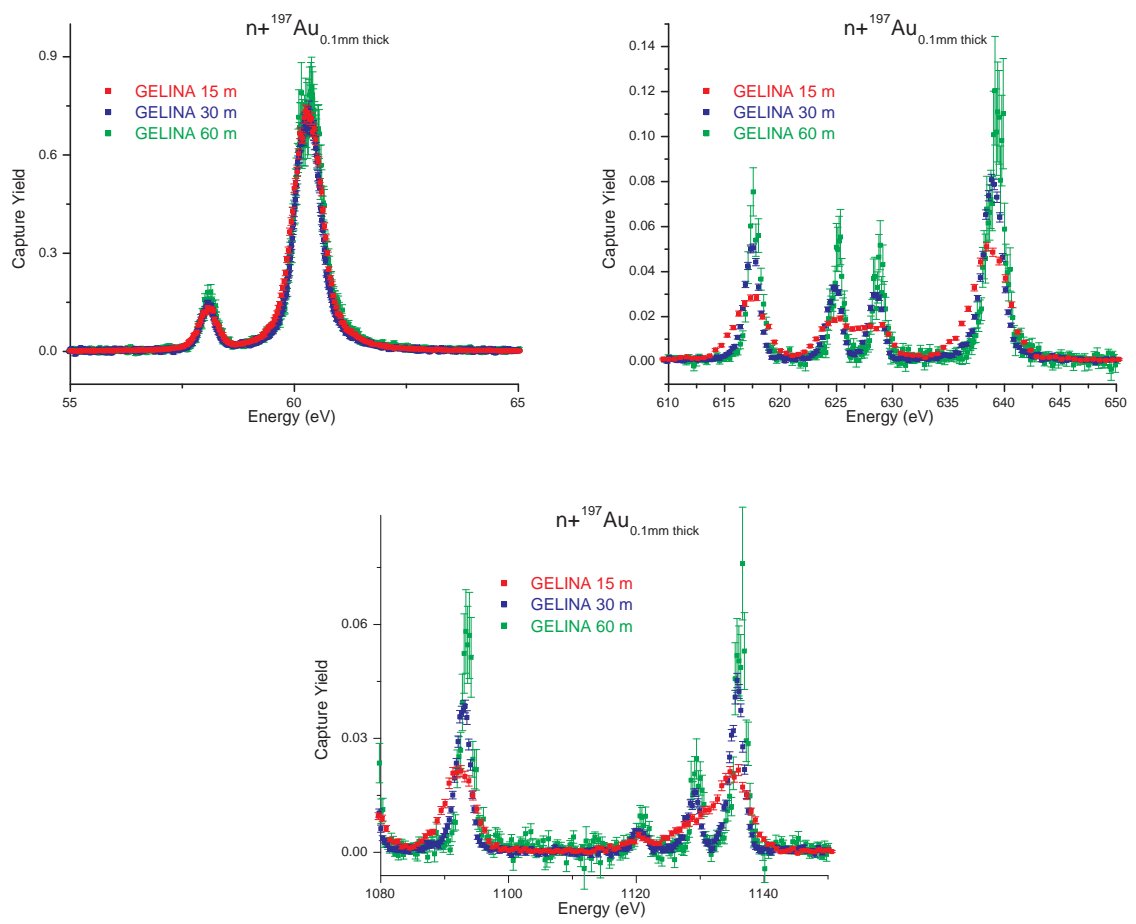


Figure 3.16: A real case with $^{197}\text{Au}+n$ experimental data and calculated Doppler-broadened capture yield. The same sample measured at different flight path.

path, making clear that the response function of n_TOF is similar to that of a 60 m GELINA flight path. In the second panel we just compare the capture yield in a higher energy region measured at a 185 m flight path and at a 60 m flight path.

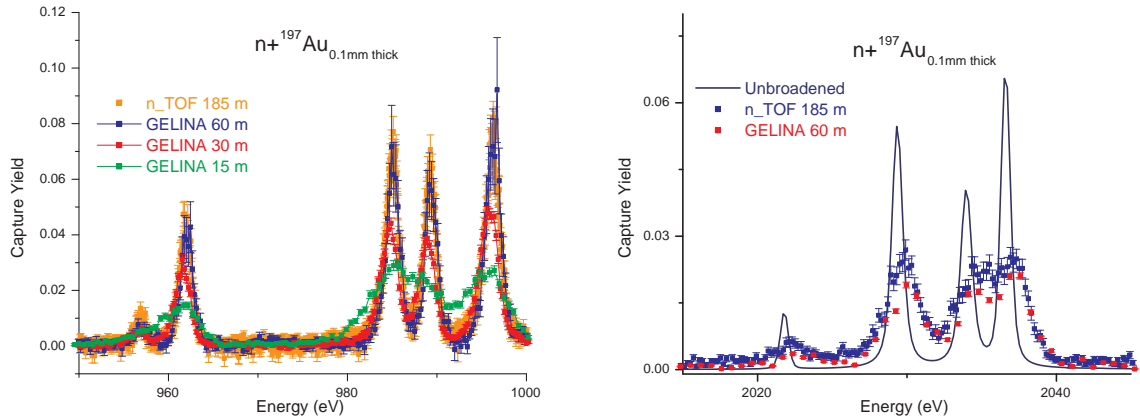


Figure 3.17: A real case with ¹⁹⁷Au+n experimental data and calculated Doppler-broadened capture yield. The thickness of the samples are slightly different.

Chapter 4

Measurement techniques and detectors

The main objective of this work is to improve the parameterization in terms of resonance parameters of the cross-section data for neutron induced reactions on ^{197}Au in the resolved resonance region. As mentioned in Section 2.4 the determination of a complete set of resonance parameters (i.e. resonance energy, neutron width, radiation width, spin, parity and scattering radius) requires a combination of complementary experimental data. For the design of the experiments and a resonance shape analysis of the data, it is of primary importance to understand the relation between the experimental observables and the cross-section or resonance parameters. In this chapter the basic principles of transmission, capture and self-indication measurements are explained. In the last paragraph the information which can be obtained from a resonance shape analysis of such data is discussed taking into account the specific characteristics of the resonance structure for the $^{197}\text{Au}+n$ system.

4.1 Transmission experiment

4.1.1 Principle

Transmission measurements are the simplest and most accurate type of cross-section measurements [111]. The observed quantity is the fraction of the neutron beam that traverses the sample without any interaction. This fraction, which is called the transmission factor T , is related to the total cross-section and the total number of nuclei per unit area by:

$$T = e^{-n\sigma_{tot}}. \quad (4.1)$$

The experimental observed transmission, T_{exp} , is obtained from the ratio of the counting rates of a sample-in measurement C_{in} and a sample-out measurement C_{out} ,

which are both corrected for their dead-time and background contributions:

$$T_{exp} = \frac{C_{in}}{C_{out}} \quad (4.2)$$

The experimental transmission T_{exp} can be directly related to the theoretical expectation value Eq. 4.1 when:

1. the target is perpendicular placed to a parallel incoming neutron beam;
2. all neutrons that are detected have crossed the sample;
3. neutrons scattered by the sample are not detected.

These conditions require experiments that are performed in a good transmission geometry and put constraints on the target characteristics. The good transmission geometry can be realized by properly collimating the neutron beam at the sample position and by a small solid angle between the sample and detector. In addition, the interpretation of T_{exp} in terms of the total cross-section requires a homogeneous target which does not contain pin holes. The optimum areal density (or thickness) depends on the total cross-section to be determined. As a general rule a transmission between 0.2 and 0.7, depending on the background conditions is recommended.

Since in Eq. 4.2 the incoming neutron fluence rate as well as the detector efficiency cancel out, there is no normalization uncertainty. In addition, corrections for multiple scattering, as required for capture cross-section measurements (see section 4.2), are unnecessary. Although fundamentally straightforward, there are several difficulties associated with transmission measurements. Correction for background effects requires a series of measurements based on black resonances covering the energy region of interest. In the energy region below 1 eV the background level can only be based on an extrapolation based on the background level observed for black resonances at higher energies. In addition, the background level at the detector position is affected by both the black resonance filter and the sample characteristics in case of the sample-in measurement. Therefore, specific background measurements for both the sample-in and sample-out conditions are required, as explained in Ref. [145]. To monitor accurately the background level, measurements with fixed background filters have to be performed.

4.1.2 Transmission detector

In the low energy region Li glass detectors, based on the ${}^6\text{Li}(n, \alpha)t$ reaction, are used. In the high energy region one mostly prefers plastic scintillators for which the elastic scattering on hydrogen is the most important reaction. Figure 4.1 shows a Li-glass scintillator that is used for transmission measurements in the resolved resonance region. The Li-glass scintillator (NE 912) has a 127-mm effective diameter and 6.35-mm

thickness. The Li-glass is placed in an Al canning and viewed by a EMI 9823 KQB PhotoMultipliers (PMT). The lithium is enriched to 95% in ^6Li . Small amounts of cerium (Ce^+) are added to be used as a scintillator medium. The resolution function of a transmission measurement depends on the response of the neutron detector. The additional time uncertainty component is mainly due to the finite size of the detector creating a spread in effective distance travelled by the neutron before being detected. This spread can be described either with analytical expressions or by Monte Carlo simulations. In both approaches, the properties of the detector, i.e. the size, the density, the energy dependent cross-sections are taken into account to provide the effective path length travelled by the neutron, inside the detector, before generating a time signal. Figure 4.2 compares the resolution function for a 10 eV neutron obtained from Monte Carlo simulations with the one deduced from analytical expressions for the detector of Figure 4.1. The response can be considered as a sum of two components: a component due to a single interaction event and a component resulting from multiple scattering events. The time dependent component resulting from the time jitter of the detector signal and electronics, which is about 1 ns (FWHM), can be represented by a Gaussian.

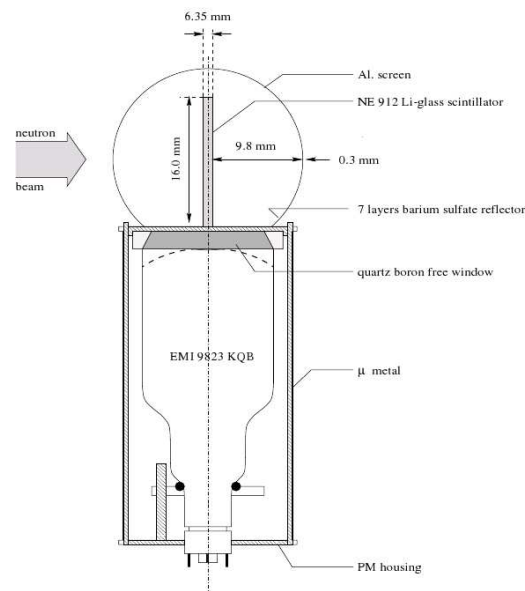


Figure 4.1: Drawing of the Lithium glass detector used in transmission measurement at the GELINA facility at 49.34 m flight path. Picture from [142].

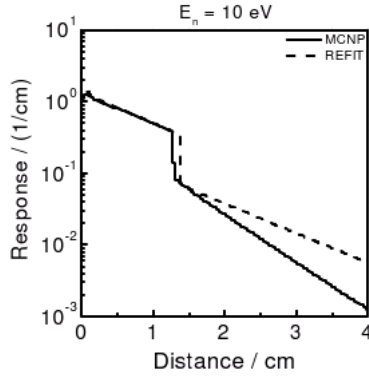


Figure 4.2: The resolution function of the transmission detector from MCNP simulation and analytical expression as a function of the distance travelled by the neutrons inside the detector. Both responses were normalized to the same total area. Picture from [142].

4.2 Capture experiment

4.2.1 Principle

The quantity determined in a capture experiment is the fraction of the incident neutrons undergoing a reaction in the sample and generating a signal in the detection system. For non fissionable nuclei and for energies below the inelastic scattering threshold, the capture and scattering yield, represented by Y_c and Y_n , respectively, can be expressed as a function of the total (σ_{tot}), capture (σ_γ) and scattering (σ_n) cross-section:

$$Y_c(E_n) = (1 - e^{-n\sigma_{tot}}) \frac{\sigma_\gamma}{\sigma_{tot}} + Y_M \quad (4.3)$$

and the scattering yield as:

$$Y_n(E_n) = (1 - e^{-n\sigma_{tot}}) \frac{\sigma_n}{\sigma_{tot}} - Y_M \quad (4.4)$$

where n is the number of nuclei per unit area and Y_M accounts for the contribution of capture events following at least one neutron scattering in the sample. The term in brackets is due to the neutron self-shielding. Full analytical expressions for both the capture and scattering yield, which are also valid for fissionable nuclei, can be found in Ref. [92]. The theoretical expectation value for the total observed yield Y is the sum of the contribution due to Y_c and Y_n :

$$Y = \varepsilon_c Y_c + \varepsilon_n Y_n \quad (4.5)$$

Where ε_c is the probability that a capture event is detected and ε_n is the probability that a neutron which is scattered in the sample undergoes a capture in the detector material and creates a signal in the detector.

The capture yield Y_c does not only depend on the capture cross-section but also on the total and elastic scattering cross-section. Only for thin samples, such that $n\sigma_{tot} \ll 1$, the capture yield is directly related to the capture cross-section:

$$Y_c(E_n) \approx n\sigma_\gamma \quad (4.6)$$

For thick samples it is convenient to express the total capture yield as a sum of three terms:

$$Y_c = Y_0 + Y_1 + Y_{\geq 2}. \quad (4.7)$$

where Y_0 represents the primary yield:

$$Y_0 = (1 - e^{-n\sigma_{tot}}) \frac{\sigma_\gamma}{\sigma_{tot}} \quad (4.8)$$

Y_1 is the contribution due to capture events after one elastic scattering in the target, and $Y_{\geq 2}$ refers to neutron capture events after more than one neutron scattering (for sake of clarity $Y_M = Y_1 + Y_{\geq 2}$). The contribution of the three components for the resonance in ^{197}Au are illustrated in Figure 4.3. In a relatively thin sample the single scattering yield Y_1 is mainly due to neutron scattering at 90° .

The yield Y_n represents the contribution due to neutrons which are scattered in the sample and subsequently captured in the detector environment. This contribution creates a time dependent background which cannot be distinguished from the real capture event and therefore contributes to the experimentally observed yield. The sensitivity to scattered neutrons plays an important role for all resonances with a neutron width that is much larger than the radiation width (i. e. the scattering probability much greater than capture probability). This is the case for light nuclei and for heavier nuclei around shell closure. To study such nuclei one chooses detectors with the lowest neutron sensitivity and one tries to reduce the amount of all the materials surrounding the sample-detector assembly. The consequences of this background component on the resonance parameters of large s-wave resonances have been illustrated by Koehler et al. [153], Corvi [154] and Beer et al. [155].

From the counting rate C_c (of the γ -rays), which is corrected for dead time and background, the experimental yield can be obtained as follows:

$$Y_{exp}(E_n) = \frac{C_c}{\Omega A \varphi_n} \quad (4.9)$$

where φ_n is the incident neutron flux, A the effective area of the target seen by the neutron beam and Ω the solid angle subtended by the detection system. This yield

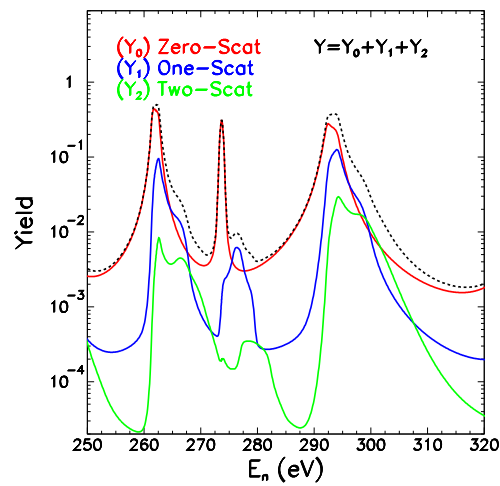
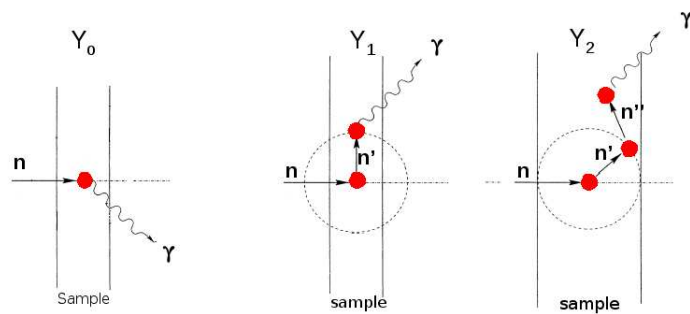


Figure 4.3: Top: Schematic view of the contributions from multiple-scattering events to the capture yield in ^{197}Au . Bottom: capture yield calculation of Y , Y_0 , Y_1 , Y_2 for a 1 mm thick Au sample.

can be compared with the theoretical expectation value given by Eq. 4.5. It has to be noted that the detection efficiency is already included in Eq. 4.5.

Equations 4.3 - 4.9 reveal that the determination of the capture yield (and of the cross-section) requires an additional measurement of the neutron flux. The detection efficiency for the partial reaction event and the neutron sensitivity of the detection system are required as well.

In most cases the geometry of the detection systems is not well defined and it is hard to determine the solid angle, the effective area and the the absolute neutron flux. As discussed in the next section (see 4.2.2) the energy dependence of the neutron flux can be accurately determined. Therefore, the normalization factor N is introduced and the experimental yield is expressed as:

$$Y_{exp}(E_n) = N \frac{C_c}{\varphi_n}. \quad (4.10)$$

This energy independent normalization factor can be deduced from capture measurements at energies where the theoretical yield Y is well known. It has been shown that for such measurements the impact of systematic effects can be largely reduced by a proper choice of the normalization procedure. One can distinguish between normalization measurements based on a standard cross-section or on samples with a resonance for which the neutron width is much smaller than the radiation width ($\Gamma_n \ll \Gamma_\gamma$). The reference cross-section can be a thermal capture cross-section, or a standard cross-section in the higher energy region, such as the $^{197}\text{Au}(n, \gamma)$ cross-section above 200 keV [156]. Normalization at a known resonance can be performed completely independent of any other capture cross-section for resonances with a neutron width that is much smaller than the radiation width. In the case when the macroscopic peak total cross-section is much less than unity ($n\sigma_{tot} \ll 1$) the capture area is almost proportional to the neutron width and can be determined very accurately from independent transmission measurements. Examples of resonances strong enough to be observed in transmission measurements and their use in normalizations of capture measurements are the 1.15 keV resonance of ^{56}Fe [157] and the 2.25 keV resonance of ^{60}Ni [158].

A special case occurs when the macroscopic total cross-section is much larger than unity ($n\sigma_{tot} \gg 1$). For a saturated resonance, i. e. a resonance for which all incoming neutrons are absorbed in the sample, all incident neutrons with energies in the vicinity of the resonance energy interact with the sample [159]. If, in addition, the neutron width is much smaller than the radiation width, the capture yield is close to unity:

$$Y(E_n) \approx \frac{\sigma_\gamma}{\sigma_{tot}} + Y_m \simeq 1. \quad (4.11)$$

An example of a saturated resonance is shown in Figure 4.4 for the first resonance

in the $\text{Au}(n, \gamma)$ reaction. Given this property, the “saturated resonance technique” can be effectively used for normalization purposes in capture measurements, i.e. to determine the efficiency of the (n, γ) detector and/or the neutron flux or, more often, their product, since the normalization is the value of the ratio Y_{exp}/Y_{th} in the energy region of the plateau.

Eq. 4.11 is valid only when the ratio Γ_γ/Γ_n is large, since in this case no matter how important is the contribution of the multiple scattering, all scattered neutrons are afterwards captured in the sample [159, 160, 161]. This is, for example, the case of the first 4.9 s-wave resonance in Au, for which $\Gamma_\gamma = 122.5$ meV and $\Gamma_n = 15.2$ meV. Another resonance suitable for applying this so-called saturated resonance method

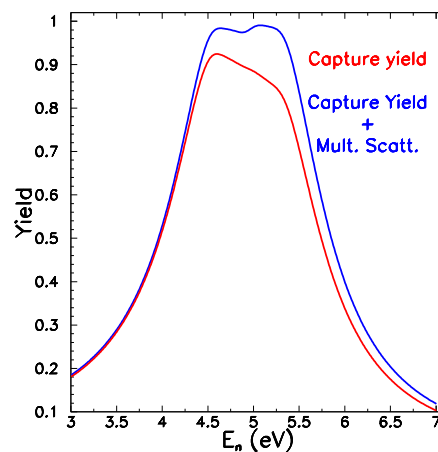


Figure 4.4: The theoretical yield for the first $\text{Au}(n, \gamma)$ resonance calculated with R-Matrix code Sammy using recommended resonance parameters listed in ENDF-VII with and without correction due to multiple scattering. The sample thickness is 0.1 mm.

is the 5.2 eV resonance of ^{109}Ag . The principle is illustrated in Figure 4.4, where the capture yield for the 4.9 eV resonance of ^{197}Au obtained with a 0.1 mm thick sample is shown.

4.2.2 Neutron flux measurements

The neutron flux can be determined from the measurement of a standard reaction, i. e. a reaction for which the cross-section is well known. Most of the neutron flux measurements at GELINA are performed by ionization chambers based on the $^{10}\text{B}(n, \alpha)^7\text{Li}$, $^{235}\text{U}(n, f)$ and $^{238}\text{U}(n, f)$ standard reactions. The $^{10}\text{B}(n, \alpha)$ reaction is used for measurements below 150 keV, while the $^{235}\text{U}(n, f)$ reaction for energies above 150 keV. At ORELA [76] and KURRI [78] the neutron flux is determined from measurements of the $^{10}\text{B}(n, \alpha\gamma)$ reaction using ^{10}B as a sample in the capture detector set-up. The

energy dependence of the neutron flux at n_TOF has been determined from measurements with a ^{235}U -loaded parallel plate chamber [84] and is continuously monitored with a ^6Li deposit viewed by four silicon detectors [83].

The neutron flux φ_n measurement produce a tof-spectrum. From this counting rate $C_\varphi(E_n)$, which is corrected for dead time and background, the yield can be expressed as:

$$Y_\varphi(E_n) = \frac{C_\varphi(E_n)}{\Omega A \varphi_n}, \quad (4.12)$$

here φ_n is the incident neutron flux, A the effective area of the target seen by the neutron beam and Ω the solid angle subtended by the detection system. Since the detectors are made of very thin samples of Li or B and since they are typically characterised by structureless cross-sections (see Appendix D) the theoretical yield for the reaction under investigation is:

$$Y_\varphi(E_n) = (1 - e^{-n\sigma_{tot}}) \frac{\sigma_{st}}{\sigma_{tot}} \approx n\sigma_{st} \quad (4.13)$$

where n is the thickness of the sample and σ_{st} is the standard $^{10}\text{B}(n, \alpha)^7\text{Li}$ or $^7\text{Li}(n, \alpha)^4\text{He}$ cross-section. Combining Eq. 4.12 and Eq.4.13 it results that the energy dependence of the neutron flux is expressed as:

$$\varphi_n = \frac{KC_\varphi}{\sigma_{st}}. \quad (4.14)$$

It has to be noted that both ^6Li and ^{10}B cross-sections are proportional to $1/v$ up to the keV region, therefore in this energy range, the normalization is obtained from the shape of the cross-section, (and not on the absolute value).

4.2.3 Capture detection systems

Neutron capture events are characterised by prompt γ -ray de-excitation cascades leading from the excited state to the ground state of the compound nucleus formed in the reaction. The total energy emitted, E^* , is the sum of neutron separation and kinetic energy (see Eq. 2.1). The separation energy ranges from few MeV up to 10 MeV, depending on the isotopes (in the case of the $^{197}\text{Au}+n$ system the binding energy is 6.512 MeV). When a low energy neutron is captured, the energy of the gamma cascade is essentially the Q-value itself. A capture reaction, therefore, can be measured by detecting one or more of the prompt γ -rays emitted in the de-excitation cascade.

A detection system to study the resonance structure of neutron induced capture cross-sections should satisfy the following requirements [154, 162]:

- the detection efficiency for a capture event should be independent of the subsequent γ -ray cascade, i.e. independent of the multiplicity of the γ -ray spectrum

and the γ -ray energy distribution;

- the sensitivity to scattered neutrons should be as low as possible;
- the detector should have a very good timing response.

Total absorption detectors rely on the detection of all γ -rays emitted in a capture event. The ideal detector has a 4π geometry and a 100% detection efficiency for all γ -rays in the cascade. Most of these detectors also have the ability to measure the multiplicity distribution of the γ -ray cascades. This feature was successfully exploited at the Kurchatov institute by Muradyan et al.[163] using a multi-sectional detector based on 48 NaI(Tl) crystals. A similar system, containing 16 NaI(Tl) crystals, is used for capture cross-section measurements in the thermal and epi-thermal energy region at the TOF-facility of the Rensselaer Polytechnic Institute [77]. A detection assembly of 12 BGO-crystals is installed at the linear accelerator of the Kyoto University, Research Reactor Institute (KURRI) [78]. A BaF₂ detection system made of 42 individual crystals with a truncated pyramidal shape [164] is used at the FZK Karlsruhe to determine capture cross-sections in the unresolved resonance and high energy region [165]. Capture measurements with a similar system have been performed at the n_TOF facility at CERN. The Detector for Advanced Neutron Capture Experiments (DANCE), which is an 4π array consisting of 162 BaF₂ elements, has been installed at the Los Alamos Neutron Science Center (LANSCE) to carry out neutron capture cross-section measurements [166]. The initial design work of this detector and of the one used at n_TOF is described in Ref. [167]. The n_TOF BaF₂ calorimeter is carefully described in Section 4.2.5.

The second method for the measurement of capture reactions is the total energy technique. This method is based on the use of low efficiency detectors with a γ -ray detection efficiency that is proportional to the γ -ray energy. This technique is based on an original suggestion by Maier-Leibnitz and was first applied by Macklin and Gibbons [169] using C₆F₆ detectors. Nowadays one prefers to use detectors with minimized neutron sensitive, such as C₆D₆ scintillators [139, 153, 154]. Such systems are also extensively used at GELINA, ORELA [76], n_TOF at CERN and at KURRI [170].

The difference between these two techniques, just described, is related to the possibility to minimize either the contribution of the background, or the neutron sensitivity. In particular, the total absorption technique, in which the whole de-excitation cascade is reconstructed, is more adequate for distinguishing capture γ -rays from the background related to γ -ray activity of the sample, and from competing reactions such as the neutron induced fission. On the other hand, the total energy method is more appropriate to minimize the sensitivity of the capture set-up to elastic neutron scattering, which severely limits the accuracy of the results whenever the scattering-to-capture ratio is large.

4.2.4 Total energy detection with C_6D_6 detectors

The total energy detection principle is based on the use of a low efficiency detection system with a γ -ray detection efficiency ε_γ that is assumed to be proportional to the gamma ray energy E_γ :

$$\varepsilon_\gamma = k \cdot E_\gamma. \quad (4.15)$$

When the γ -ray detection efficiency of such a detector is very small ($\varepsilon_\gamma \ll 1$), such that essentially only one γ -ray out of the capture cascade is registered at a time, the efficiency to detect a capture event can be approximated by:

$$\varepsilon_c = 1 - \prod_i (1 - \varepsilon_{\gamma,i}) \approx \sum_i \varepsilon_{\gamma,i}. \quad (4.16)$$

Under these conditions the detection efficiency for a capture event ε_c is directly proportional to the total energy released in the capture event E^* (the sum of the neutron binding B_n and neutron kinetic energy E_n in the centre of mass system):

$$\varepsilon_c \approx k \sum_i E_{\gamma,i} \approx kE^* = k(B_n + E_{n,cm}). \quad (4.17)$$

and independent of the actual cascade path.

The Moxon-Rae detector achieves approximately the proportionality between the γ -ray energy and detection efficiency by a proper design of the detector [171]. However, the use of this type of detectors has been abandoned due to the non-proportionality of the efficiency below 0.5 MeV and its low detection efficiency [154]. An alternative approach is the pulse height weighting technique by means of the so-called weighting function. This technique is based on an original suggestion by Maier-Leibnitz and was first applied by Macklin and Gibbons [169] using C_6F_6 detectors. In the present work we discuss the total energy detection principle using C_6D_6 detection systems for the determination of the neutron induced capture cross-sections in the resonance region based on experimental data obtained at GELINA.

The Pulse Height Weighting Technique (PHWT)

The γ -ray detection efficiency for a typical C_6D_6 detector is small, but not directly proportional to the γ -ray energy. However this proportionality can be achieved through the pulse height weighting technique, in which the response function of the detection system is mathematically modified [87, 160], so to achieve the proportionality between the detection efficiency and the γ -ray energy. A weighting function $W(E_d)$ is defined such that it follows the relationship:

$$\int_0^\infty R_d(E_d, E_\gamma) W(E_d) dE_d = kE_\gamma \quad (4.18)$$

with $R_d(E_d, E_\gamma)$ the detector response, i.e. the probability that a gamma ray with an energy E_γ results in a deposited energy E_d . The proportionality factor k is usually taken equal to 1 MeV^{-1} when deriving $W(E_d)$. The overall efficiency $\varepsilon(E_\gamma)$ for detecting a γ -ray of energy E_γ corresponds to the integral of the function $R_d(E_d, E_\gamma)$:

$$\int_0^\infty R_d(E_d, E_\gamma) dE_d = \varepsilon(E_\gamma) \quad (4.19)$$

In a capture experiment at TOF-facilities the time-of-flight of the neutron creating the capture event is recorded together with the energy deposited in the detector by the γ -ray. Using the weighting function defined in Eq. 4.18 a weighted TOF-spectrum $C_w(T_n)$ is obtained from:

$$C_w(T_n) = \int C(T_n, E_d) W(E_d) dE_d \quad (4.20)$$

where $C(T_n, E_d)$ is the distribution of the energy E_d deposited by the detected γ -ray, observed at the time-of-flight T_n , related to the kinetic energy E_n of the incident neutron.

In the past, $W(E_d)$ was derived experimentally [172] from a system of Eq. 4.18 for known response functions $R_d(E_d, E_\gamma)$ relative to various E_γ values, covering the whole energy range of interest in neutron capture (from a few hundreds of keV up to 10 MeV). The weighting function was determined once for each capture set-up, and was assumed independent on the sample to be measured.

Recently, it has become customary to use simulation to calculate $R_d(E_d, E_\gamma)$, thanks to the high reliability of current Monte Carlo codes. To obtain reliable weighting functions, accurate response of the detection system have to be calculated for a set of γ -ray energies. By implementing a detailed software replica of the complete experimental setup, the calculated $R_d(E_d, E_\gamma)$ takes also into account effects of the sample. Typically GEANT [173] and MCNP [174] codes are used with an accurate geometry description (see, for example, Figure 4.5 from Ref. [160]) that reflects the experimental conditions at GELINA: 2 (or 4) C_6D_6 -liquid scintillator contained in an Aluminum cylindrical cell 10 cm diameter and 7.5 cm height, placed at 90° and 125° with respect to the beam axis, each cell coupled to a photomultiplier through a boron free quartz window. The response is obtained by a convolution of the simulated response $R_e(E_e, E_\gamma)$ with a Gaussian function, that represents the energy resolution of the detector, studied by means of γ -ray sources.

The weighting function is obtained by expressing $W(E_d)$ as a smooth function (polynomial form) of the observed deposited energy E_d . The parameters of the func-

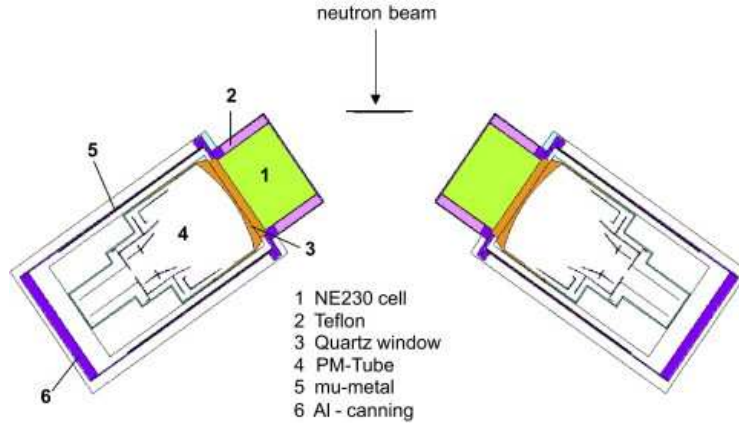


Figure 4.5: Details of the geometrical description (horizontal cross-section) as implemented in MCNP input file. Picture from [152].

tion are obtained by minimising for a number of γ -ray responses, the χ^2 defined as:

$$\chi^2 = \sum_j \left(kE_{\gamma,j} - \int_{E_L}^{\infty} R_e(E_d, E_{\gamma,j})W(E_d)dE_d \right)^2. \quad (4.21)$$

The recorded energy spectra do not go all the way to zero, because of the use of a finite discriminator threshold E_D , needed to reject electronic noise. To account for the missing part of the observed spectrum, two approaches are followed:

THRESHOLD = 0 The weighting function is calculated with $E_L=0$ in Eq. 4.21 and a correction is applied for the missing contribution of both γ -rays whose energy is below the experimental discriminator level E_D and γ -rays that contribute only partly to the observed spectrum (to this purpose, tabulated transitions probabilities, i.e. γ -rays emission spectrum, are needed for additional Monte Carlo simulations) [87].

THRESHOLD = experimental threshold The weighting function is calculated with $E_L=E_D$ in Eq. 4.21.

With the first method accurate weighting function include only positive powers in the polynomial form, for the second approach also negative powers are needed, in particular when the γ -ray transport in the sample material cannot be neglected. The expression for the weighting function in this case becomes:

$$W(E_d) = \sum_{i=-3}^4 a_i E_d^i \quad (4.22)$$

In Figure 4.6 three different weighting function, for different sample thickness and calculated with the method “threshold $\neq 0$ ” are shown.

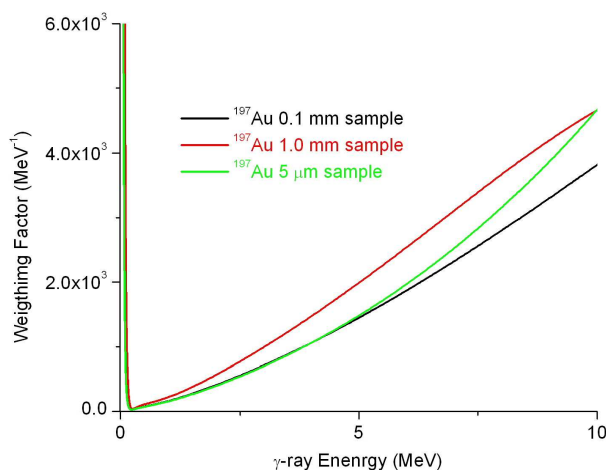


Figure 4.6: The weighting function, or weighting factor for different thickness of Au sample disc of 8 cm diameter, calculated with $E_L=E_D = 200$ keV threshold.

Other improvements

Required improvements in nuclear data always need higher accuracy data, which can be achieved with developments in measurement techniques and analysis. At the GELINA facility a further improvement on PHWT was implemented [145, 160]. The idea is the following: for a given sample, the weighting function depends not only on the sample characteristic but also on the neutron flux distribution in the sample (and thus on the resonance strength). Indeed for a weak resonance the assumption of a homogeneous distribution of γ -rays in the sample is valid, while for a strong resonance one needs to account for the neutron flux attenuation so that γ -rays are not generated homogeneously in the sample.

4.2.5 Total γ -ray absorption detector

The principle of using a 4π detector with high γ -ray efficiency and reasonably good energy resolution is the complete detection of the prompt γ -ray cascade. This concept offers the advantage of obtaining a clear signature for capture events via the sum energy of γ -ray cascades, which reflect the binding energy of the captured neutron. Provided that the detector is segmented into a sufficiently large number of independent modules, valuable additional information on event multiplicities can be

obtained. Based on combined information on the multiplicity and deposited energy it is possible to distinguish real capture events from single γ -ray background and competing reactions such as fission.

Some constraints have to be considered in the choice of the scintillator. Since the detector volume has to be large to absorb the whole γ -ray cascade, the chemical composition of the scintillator must exclude elements with high (n, γ) cross-section (for example NaI and CsI, because of the large capture cross-section of Iodine). Among the remaining suitable scintillators the final choice is a compromise between: a) energy resolution; b) time resolution; c) sensitivity to scattered neutrons. A detailed comparison of suitable scintillators can be found in [167]. The choice of BaF₂ for the n_TOF 4 π array was based on the fact that it exhibits similar sensitivity to scattered neutrons than CeF₃ and bismuth germanate (BGO) but has the advantage of better time and energy resolution¹. The light output of BaF₂ scintillator has two main components, the shorter decay time is 0.6 ns, which is better suited for fast timing applications, whereas the longer decay time is 630 ns.

There are various possibilities to cover the full solid angle with an arrangement of closely packed crystals. In order to facilitate the interpretation of event multiplicities, the crystal should be shaped such that they cover equal solid angles. Such geometries are known to correspond to fullerene-type structures consisting of a few configurations with certain, fixed number of element [175].

The n_TOF TAC [176, 177, 178] consists of 40 BaF₂ crystals, 12 pentagonal and 28 hexagonal, covering 95% of the 4 π solid angle. Both types of crystals are shaped from BaF₂ cylinders, 14 cm in diameter and 15 in thickness with raw and final weight of 12 and 7.5 kg respectively. The reflector of each crystal is made of 0.1 mm Teflon foil followed by 0.1 mm polished Aluminum sheet. Each crystal is viewed by a 12.7 cm Photonis XP4508 photomultiplier with an Aluminum housing that is mounted on an honey-comb structure also made of Aluminum, holding the complete detector. The detector assembly is divided into two hemispheres, one of which can be moved to access the interior of the detector, and in particular the centre of the TAC where the sample is placed. Figure 4.7 shows a picture of one of the hemispheres with the neutron absorber. placed in the centre of the assembly.

One of the main sources of the background in (n, γ) measurements is related to the detection of the gamma cascades originating from neutrons scattered from the sample and absorbed in the detectors itself. This kind of background follows the same resonant behaviour as the capture events, resulting in a systematic increase of the area of the resonances. The amount of background depends on the neutron sensitivity of the detector [154, 139], defined as the ratio between the efficiency for detecting scattered neutrons ε_n , and that for capture events ε_γ . In the design of the TAC, its neutron sen-

¹For sake of completeness: a better choice would be C₆F₆ even though it requires larger volume. With BaF₂, comparable values could only be reached using isotopically pure ¹³⁸Ba, due to its very small (n, γ) cross-section.

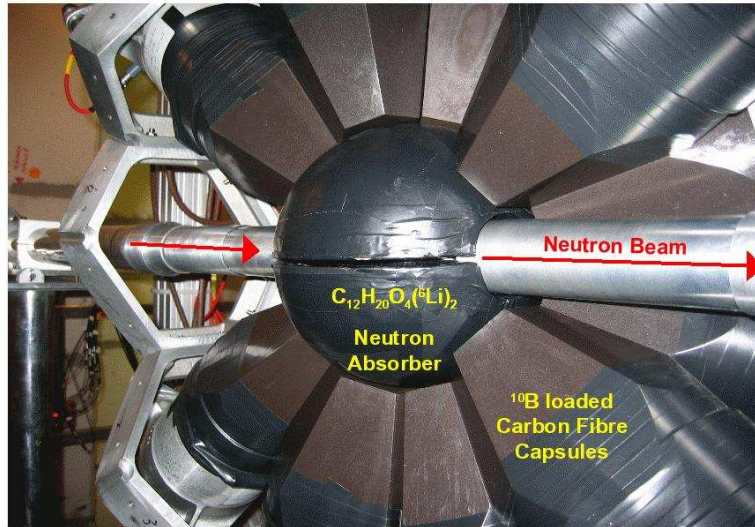


Figure 4.7: Two views of the BaF₂ array. One (and both) of the hemispheres of the TAC with the neutron absorber placed in the centre and the neutron beam line passing through the detector assembly.

sitivity has been minimized by mounting a spherical neutron absorber/moderator around the sample and ^{10}B -loaded carbon fibre capsules surrounding each crystal. The high ^{10}B content (16% in mass) of the 1 mm thick carbon fibre capsules is aimed at stopping neutrons (thermalized but not absorbed in the inner sphere the absorber) before they reach the crystal.

The composition of the material of the neutron absorber has been chosen from Monte Carlo simulations [179, 180]. They indicated that the best neutron moderator/absorber combination is ^6LiH , which in addition has the advantage of a very low perturbation of the γ -ray spectrum thanks to its low effective atomic number Z . However, safety rules at CERN exclude the use of ^6LiH [181] due to its high flammability and toxicity. Instead, the Lithium salt $\text{C}_{12}\text{H}_{20}\text{O}_4(^6\text{Li})_2$ [180] was used, an inert and inflammable compound satisfying the safety requirements. For mechanical stability the compound was encapsulated in a spherical 0.5 mm thick Aluminum shell with inner and outer radii of 5 and 10 cm, respectively. The absorber is placed in the geometrical centre of the TAC.

4.3 Self-indication experiment

Self-indication experiments involve a combination of both capture and transmission measurements. Two samples are used: the one closer to the source is used for transmission and the other is used for capture. Both samples contain the nuclide of interest (they have the same resonance structure, thus the term “self-indication”). Such an

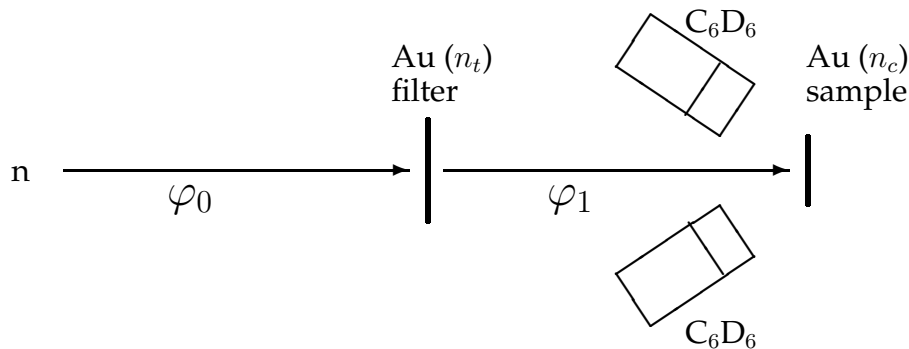


Figure 4.8: Scheme of the self-indication experiment.

experiment preferentially removes neutrons near the peak of the resonances for this isotope, thus focusing on the shoulders or wings of a resonance. Furthermore, for a saturated resonance, this measurement provides an unambiguous identification of the background at the resonance position.

For the determination of the complete set of resonance parameters additional complementary data are required. To find an ideal combination of complementary data the basic principles of resonance area analysis are very instructive, as demon-

strated in the section 2.4.1. Using the Single Level Breit-Wigner formalism, the simplest variant of the R-matrix theory, one obtains simple relationships between the experimental observables and the resonance parameters. From these relations it can be drawn that self-indication measurements are always complementary to both transmission and capture measurements.

In practice self-indication measurements are similar to a capture measurement (since γ -ray are detected) with the only difference that a filter of the same material of the sample is employed.

Analysis of a self-indication experiment requires both calculation of transmission through the first sample (with thickness n_t) and calculation of capture yield with self-shielding and multiple-scattering corrections for the second sample (with thickness n_c). Transmission is calculated as described in Section 4.1, using parameters appropriate for that sample (thickness, temperature, etc ...). The capture yield Y is calculated as described in Section 4.2, using parameters appropriate for the capture sample; note that the normalizations described in that section may be applied to the "capture yield" calculation here. The self-indication result is the product of the transmission and the capture yield:

$$SI(E) = T(E) \cdot Y(E). \quad (4.23)$$

More in detail, the counting rate C_{SI} for self-indication measurements (neglecting the neutron sensitivity) is given by:

$$C_{SI} = \varepsilon_c Y_c(E_n) e^{-n_t \sigma_{tot}} \varphi_0(E_n).$$

Note that the flux is the one recorded without the filter in the beam.

The importance of self-indication measurements in particular for the analysis in the URR is shown by Fröhner [96, 182] in the evaluation of the average resonance parameters.

4.4 RSA codes REFIT and SAMMY

Resonance Shape Analysis (RSA) codes, such as REFIT [92] or SAMMY [93], can be used to deduce resonance parameters from experimental data. Both codes are based on the Reich-Moore approximation of the multi-level R-matrix formalism. These codes account for the Doppler broadening and the self shielding and multiple scattering effects in partial cross-section measurements. The theoretical reaction yield and transmission factors are folded with the experimental resolution. The resonance parameters together with some other parameters linked to the experimental set up (e. g. normalization, background level, effective temperature, target thickness and homogeneity) can be determined by a least-square fit to the experimental data.

The REFIT code allows a simultaneous analysis of different data sets (the familiar least-square method), while SAMMY carries out a sequential fit on the different data sets, applying the Bayes' Theorem (generalized least-square).

In SAMMY code the experimental data have to be expressed as a function of energy, while REFIT code performs the fit in the time-of-flight domain. In the REFIT code the total effective flight path length, also accounts for transport of the neutron within the neutron source and the with detector or sample in case of transmission and partial reaction measurements respectively. The resulting effective flight path length depends on the neutron energy and is related to the resolution of the spectrometer. We recall that the time-energy relation cannot be seen independently from the resolution function, since the mean equivalent distance of the resolution function is changing with energy. It follows that in REFIT the definition of the energy of the resonance is more clear as compared to the SAMMY code, which requires the conversion of the time-of-flight into energy prior to the resonance shape analysis (in which the resolution function is applied).

Hereafter we will use the notation used in REFIT, noting that the difference with SAMMY is basically the definition of the normalization:

$$N_{REFIT} = 1/N_{SAMMY}.$$

Moreover, concerning the present work, the experimental data are background-free, thus in the following $B=0$. The fitting procedure consists in the minimization of the χ^2 defined as:

$$\chi^2(\vec{a}, \vec{b}) = (\vec{Z}_{exp} - \vec{Z}_{calc}(\vec{a}, \vec{b}))^T V_{Z_{exp}}^{-1} (\vec{Z}_{exp} - \vec{Z}_{calc}(\vec{a}, \vec{b})) \quad (4.24)$$

where Z_{exp} is the experimental observable, i.e. the transmission factor or the capture yield or the self-indication yield. The corresponding quantity, Z_{calc} as a function of the time-of-flight t_n , is calculated starting from the theoretical quantity $Z(E_n)$ broadened for the experimental effects as in the following:

$$Z_{calc}(t_n) = \frac{\int R_t(t_n, E_n) \varepsilon_c(E_n) Z(E_n) dE_n}{N} + B$$

in particular for the transmission factor:

$$T_{calc}(t_n) = \int R_t(t_n, E_n) e^{-n\sigma_{tot}(E_n)} dE_n \quad (4.25)$$

for the capture yield:

$$Y_{calc}(t_n) = \int R_t(t_n, E_n) \varepsilon_c(E_n) Y_c(E_n) dE_n \quad (4.26)$$

and for the self-indication:

$$SI_{calc}(t_n) = \int R_t(t_n, E_n) e^{-n_t \sigma_{tot}} \varepsilon_c(E_n) Y_c(E_n) dE_n. \quad (4.27)$$

where $R_t(t_n, E_n)$ is the neutron time-of-flight resolution function, $\varepsilon_c(E_n)$ is the detection efficiency for capture events, N is the normalization and B is the background. The matrix V_{Zexp}^{-1} is the covariance matrix and \vec{a} is the vector of resonance parameters, while \vec{b} is the vector of experimental parameters. In particular:

$$\vec{a} \equiv (J, a_J, R_J^\infty, E_{r,i}, \Gamma_{\gamma,i}, \Gamma_{n,i}) \quad i = 1, \text{ number of resonances}$$

and the vector \vec{b} takes into account the sample characteristic, the flight path length, sample temperature (Doppler), resolutions, ...

The SAMMY code has the advantage of treating the full covariance matrix V_{Zexp}^{-1} , while in REFIT only the diagonal terms of the matrix can be considered. Moreover three important differences between the two codes are present typically for capture reactions, are related to:

- 1) the correction for the neutron sensitivity of the detector;
- 2) the correction for the gamma attenuation in the sample;
- 3) the correction for multiple scattering.

In the REFIT code corrections 1) and 2) are applied during the fitting procedure because: the correction 1) depends on the parameter to be fitted (Γ_n/Γ_γ ratio); the correction 2) can not be applied to the experimental yield [160] (see Section 6.3.3). In SAMMY it is possible to correct for them in an iteratively way. For example in SAMMY, for the neutron sensitivity, one has to subtract the "point wise" neutron background produced by the sample-scattered neutrons (the correction in this approach depends on the sample under investigation). Nevertheless when $\Gamma_n \ll \Gamma_\gamma$ one expects that these listed differences are negligible.

The relation 4.28 expresses the correction due to the neutron sensitivity (with respect to point 1), as implemented in REFIT:

$$Y_{calc}(t_n) = \frac{\int R_t(t_n, E_n) [\varepsilon_c(E_n) Y_c(E_n) + \varepsilon_n(E_n) Y_n(E_n)] dE_n}{N} + B \quad (4.28)$$

where Y_n is the scattering yield and $\varepsilon_n(E_n)$ is the efficiency for detecting a scattered neutron. The relation 4.29 expresses the correction due to gamma attenuation in the sample (with respect to point 2) as implemented in REFIT:

$$Y_{calc}(t_n) = \frac{\int R_t(t_n, E_n) k_c(\sigma_{tot}) \varepsilon_c(E_n) Y_c(E_n) dE_n}{N} + B \quad (4.29)$$

where $k_c(\sigma_{tot})$ is correction depending on the total cross-section. This correction is important for "thick" samples since it has been demonstrated [160] that for a given resonance the weighting function depends on the sample characteristics and the neutron flux distribution in the sample. Consequently, for a given sample the weighting function depends on the resonance strength ($g\Gamma_n$) and may differ from resonance to resonance. For weak resonances a homogeneous distribution of the γ -rays is valid, while for strong resonances one needs to account for the neutron flux attenuation. Hence, each resonance requires in principle its own weighting function. This is from a practical point of view not realistic. Therefore, for the analysis of capture data the expression 4.29 is used in REFIT, for more details see [160]. In REFIT the equation for Z is the combination of Eq. 4.28 and 4.29:

$$Y_{calc}(t_n) = \frac{\int R_t(t_n, E_n)[k_c(\sigma_{tot})\varepsilon_c(E_n)Y_c(E_n) + \varepsilon_n(E_n)Y_n(E_n)]dE_n}{N} + B. \quad (4.30)$$

Concerning the third correction, only in REFIT the "full multiple scattering correction" is implemented and it takes into account the energy spread of the scattered neutrons. The differences between the two codes have been tested in the analysis of the capture yields obtained at n_TOF and at GELINA. The comparison demonstrated that such differences are negligible.

Chapter 5

Measurements at CERN-n_TOF

High accuracy measurements of the capture cross-section of ^{197}Au have been performed at the n_TOF facility, in the energy range between 1 eV and 5 keV. In the n_TOF measurements, a total energy detection system with two C_6D_6 liquid scintillator detectors as well as the total γ -ray absorption calorimeter (TAC) have been used. The full procedure from raw data to the extraction of the capture yield is here described, with particular emphases on the data reduction of the TAC measurement. We present the results in the RRR, in particular a preliminary R-matrix analysis performed with the R-Matrix code SAMMY.

5.1 Introduction

The measurement of the capture reaction $^{197}\text{Au}(n, \gamma)$ has been carried out with two different detector systems, the new¹ n_TOF detector, i. e. the BaF_2 4π calorimeter (TAC), and the C_6D_6 liquid scintillator array. The aims of the measurements are twofold: first to study in details the performance of the TAC detector (in view of future neutron reaction measurements with radioactive and rare samples) and, second, to improve the knowledge of the ^{197}Au cross section.

Regarding the analysis of the n_TOF C_6D_6 data, in several published papers the experimental set-up and the techniques are reported. A detailed description can be found, for example, in [183]. We just want to recall that at n_TOF, C_6D_6 detectors have been developed by using a carbon fibre container and minimising the mass of the detector. In this way, a very low neutron sensitivity has been achieved, one order of magnitude lower than for commercial detectors [139].

Concerning the performances of the TAC, two aspects have been studied carefully: the neutron sensitivity and the pile up. Since for the resonances of ^{197}Au the ratio Γ_n/Γ_γ ranges from very low values to a maximum of about 20, the comparison of the results obtained with the two detection systems allowed to minimize the systematic uncertainties related to the neutron sensitivity, thanks to the use of the C_6D_6

¹It has become available in 2004.

detectors. The pile up effect in the detectors may be a limit for the measurement with the TAC. For this reason the capture yield obtained with dedicated and with parasitic neutron beam have been separately analyzed and then compared. Since for parasitic bunches the counting rate is half of that expected for dedicated pulses, the comparison between the results obtained for the two modes allowed us to verify the correctness of dead-time corrections. Again a further check was the comparison with C_6D_6 data. The results reported in this chapter have been obtained with dedicated beam. However for few resonances characterised by high counting rate, data from parasitic beam measurement have been used.

To sum up, the combination of C_6D_6 and TAC data is important to keep under control effects related to the measurement techniques², and to derive the ^{197}Au capture cross-section with high accuracy.

Figure 3.15 shows that the Doppler effect dominates the experimental resolution of the n_TOF data. Moreover, the broadening due to the experimental resolution is in general much larger than the natural widths of the $^{197}\text{Au}+n$ resonances. In this situation the shape-analysis of the capture yield is not fruitful, while the area-analysis can be carry out³. According to the Table 2.2, the area analysis provides $g\Gamma_n$, when the radiation width dominates over the total width, and $g\Gamma_\gamma$, when the elastic width is larger than the capture one. In some cases, to improve the quality of the fit, the preliminary R-matrix analysis has been performed fitting the data having as free parameters both partial widths. Even though in these cases the values of extracted parameters, Γ_n and Γ_γ , are not accurate this procedure has been adopted to calculate reliable capture kernels and compare the results between data sets taken with different setups.

Since RSA codes need starting values for the resonance parameters (in particular: the spin, the scattering radius and values for partial widths), initial parameters have been taken from neutron data libraries.

The capture samples

The gold sample used in this TAC measurement was a disc of about 0.1 mm thickness and 1 cm diameter. In addition to the 0.1845 g Au sample, a 70 mg ^{nat}C and 171 mg ^{208}Pb samples (same diameter of the Au sample) have been measured, in order to evaluate the background caused by sample-scattered neutrons and the one related to in-beam γ -rays. The characteristics of the Au samples are listed in Table 5.1.

²Neutron sensitivity and pile up for the TAC; intrinsically low efficiency and the use of the pulse height weighting technique for C_6D_6 .

³In determining the partial widths of a resonance using only capture data, resonance shape analysis is similar to an area analysis: the smaller of the two partial widths is determined from the area of the resonance (see Eq. 2.46), while the other width is calculated from the difference between the total width obtained from the shape fit and the smaller of the two partial widths.

Table 5.1: Sample features for the capture measurements at n_TOF.

	TAC	C_6D_6
Diameter (cm)	1.0	2.205
Weight (g)	0.1854	1.871
Thickness (cm)	1.22×10^{-2}	2.5×10^{-2}
Areal density (atoms/barn)	7.3×10^{-4}	1.498×10^{-3}

5.2 Total Absorption Calorimeter (TAC)

In the first step of this analysis we concentrate on the single BaF₂ crystal performance, after which the overall TAC performance is analyzed. At n_TOF, each BaF₂ crystal is acquired independently of other crystals. The informations from all the 40 BaF₂ crystals are then combined by software, via a calorimetric routine.

Single crystal performance

One of the most important and innovative feature of the n_TOF TAC is the acquisition system (DAQ) [141]. Since the n_TOF facility has been built to deal with very high counting rates (as high as several counts per μ s), an acquisition system based on flash ADCs [184] with high sampling rate (up to 1 GS/s) had to be used. In this measurement the FADCs were operating at 500 MHz, allowing to record the full sequence of signals in the detector, for neutron energies down to 1 eV. The same DAQ has been used at n_TOF both for the C₆D₆ and TAC apparatus. The system allows for off-line pulse shape discrimination, reconstruction of the deposited energy, time-of-flight determination and finally for the treatment of the pile-up [88, 120, 185, 186, 187, 188]. After zero suppression and data formatting, data are stored in the CERN central data recording system. At this stage, especially designed pulse shape analysis routines [189] (see for example, Figure 5.1) are used to extract from the digitized detector signals the necessary information for the data analysis (i.e. integrated slow and fast component of the signal, the time-of-flight (Tof), etc ...). The advantage of the use of FADC, and off-line reconstruction routine, is the possibility to correctly identify and analyze a signal overlapped on the tail of a preceding one. In this case, the baseline of the last detected signal is not considered constant, but an exponentially decaying function, with 630 ns decay constant (the longest decay constant of the BaF₂ light output).

In principle, the effect of the pile up of two consecutive γ -rays in the same detector is negligible since the pulse shape of the two signals is reconstructed (see Figure 5.1). However the reconstruction routine may fail to find and separate two signals when they are too close, depending on their relative amplitude. It follows that the dead

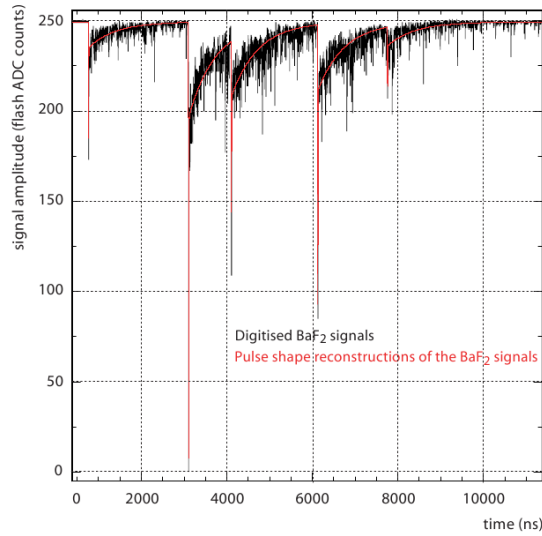


Figure 5.1: Digitized BaF₂ signals and the corresponding reconstruction after the pulse shape analysis. Picture from [189].

time for the single crystal is not a fixed value, as can be seen in Figure 5.2. For randomly incoming events, the time difference between two successive events follows a Poisson distribution, in particular for the γ -ray background. Figure 5.2 shows the distribution of time difference (ΔT_{of}) measured for the Au(n, γ) reaction. For time difference above 800 ns, the distribution follows a Poissonian shape. From 600 to 800 ns, the ΔT_{of} distribution is above the Poissonian law. This excess is most probably due to the shape of the BaF₂ signal, which shows a bump around 600 ns after the start of the signal, generating sometimes false triggering. Applying a relatively high fixed threshold (150 or 300 or 500 keV) on the single crystal it is possible to minimize the bump at 600-800 ns. Moreover in the next section we will show that the 600 ns bump is not present in the coincidence spectrum. This indicates that this problem does not affect significantly the TAC performance.

A further check was obtained comparing the ΔT_{of} spectra produced by parasitic and dedicated bunches. Since the neutron flux in dedicated pulses is double than in parasitic ones, some changes in the time interval spectra are expected. Figure 5.3 shows that differences in the spectra obtained in the two modes are negligible when a threshold of 150 keV is present. For this reason, in the analysis a single crystal threshold of 150 keV has been adopted.

Pulse shape discrimination

The BaF₂ scintillator material is not pure but it contains Po and Ra contaminations, which cause a characteristic α radioactivity in the scintillator. The ratio between the

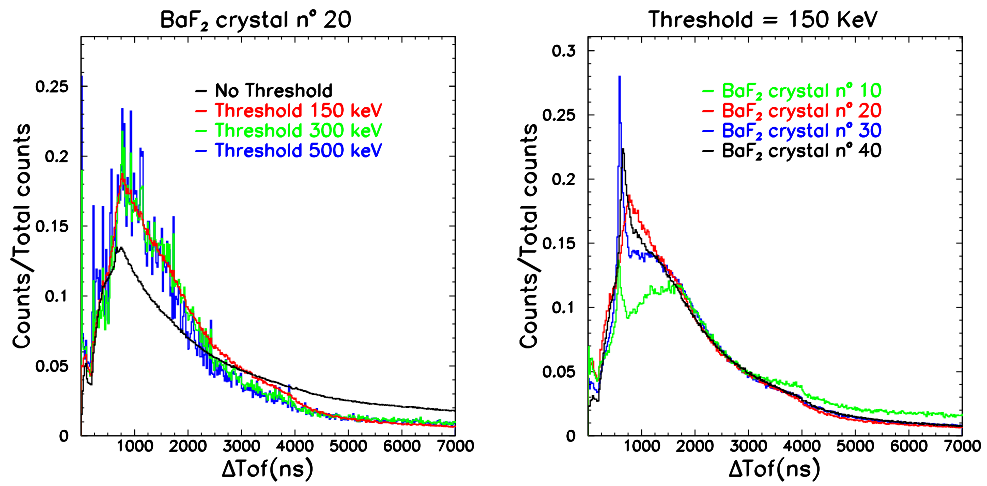


Figure 5.2: Time interval spectra comparison. Left: signals from the BaF₂ crystal number 20, in dedicate mode with and without thresholds. Right: signals from few BaF₂ crystals with a threshold of 150 keV.

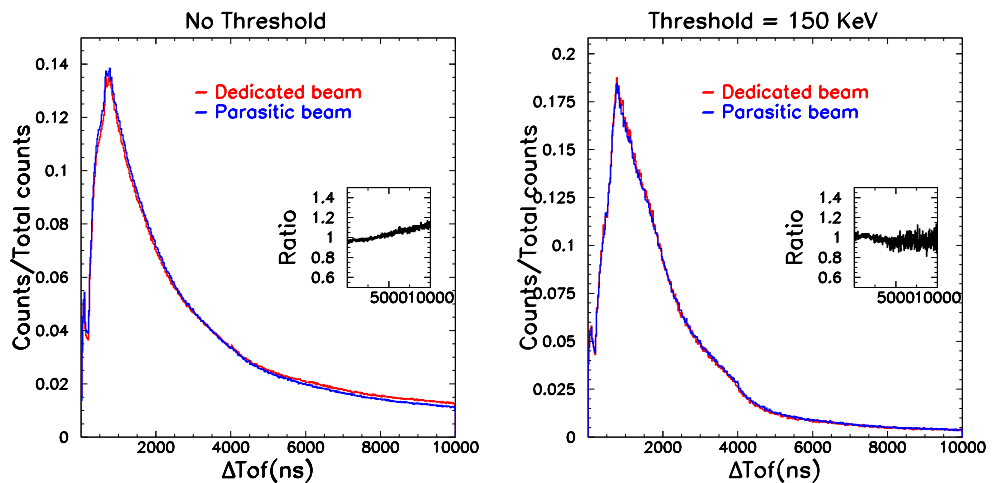


Figure 5.3: Time interval spectra comparison. Signals from the same BaF₂ crystals in dedicate and parasitic mode respectively, with and without a threshold.

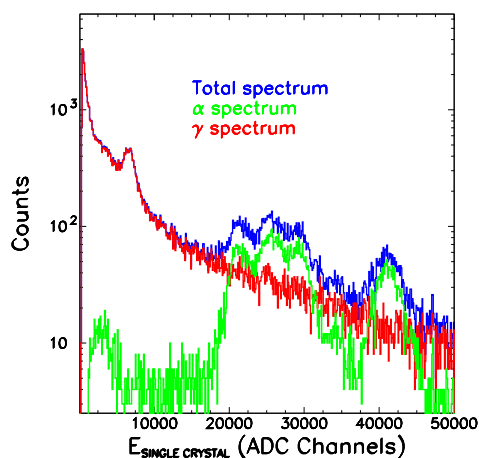


Figure 5.4: Total energy spectrum obtained from a single BaF₂ (in blue). The α spectrum (green) and the γ spectrum (red) have been obtained with the pulse shape analysis during a Au(n, γ) measurement.

amplitude of the fast component and the signal integral can be used to discriminate γ -rays from α particles. Indeed for α particles the fast component signal is strongly reduced, so that the ratio is expected to be smaller than for γ -rays. Figure 5.4 shows the deposited energy distribution (in one crystal) for the Au measurement. In the figure the results of the pulse shape discrimination on a single BaF₂ crystal can be seen. Since they can be identified, α -particles can be used to monitor the light output of the crystals and the gain of the photomultipliers. The stability in the gain of each module has been checked by using the α spectrum relative to the ²¹⁴Po and ²²⁶Ra decay.

Energy calibration and resolution

The energy calibration of each crystal was obtained by means of standard γ -ray sources: ¹³⁷Cs (662 keV), ⁸⁸Y (898 and 1836 keV) and Pu/C (6131 keV from ¹⁶O). An example of the deposited energy distribution measured with ¹³⁷Cs and ⁸⁸Y is presented in Figure 5.5, together with a curve obtained by fitting the observed distribution. This curve was obtained convoluting 3 Gaussian functions, one for each γ -ray energy of the sources. An exponential function was also added to fit the background. The energy of the most energetic peak (1836 keV γ -ray from ⁸⁸Y) is not always recorded completely, as can be noted from the deviation from the Gaussian law. Energy calibration has been performed by fitting the mean of the Gaussian distribution to the nominal γ -ray energy, while the linearity has been estimated by looking at the regression coefficient. The sources allowed also to determine the energy reso-

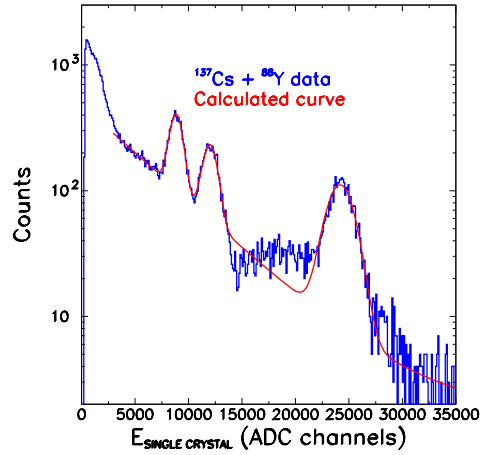


Figure 5.5: Deposited energy distribution of the standard γ -ray calibration source containing ^{137}Cs and ^{88}Y .

lution of each BaF_2 module and of the whole apparatus. The TAC is characterised by an energy resolution of 15% at 662 keV and of 6% at 6.1 MeV.

5.3 Analysis procedures

The processed informations from each of the 40 BaF_2 crystal are combined off-line in a calorimetric routine with the aim of identifying capture events. The condition that defines an event⁴ is the detection of two or more γ -rays within a coincidence window of 25 ns ($-13 < \Delta T_{of} < 12$ ns). Although the time resolution of each crystal is 1 ns, thanks to the very fast decay time of one components of the BaF_2 light output (0.6 ns), the overall time resolution of the TAC is larger (about 20 ns FWHM) due to the uncertainty in the calibration of different Flash ADC. The time resolution of the overall TAC has been reduced to about 10 ns (FWHM, see Figure 5.6) with a synchronization procedure. To optimize the width of the coincidence window, it is necessary to study the time difference distribution ΔT_{of} between γ signals in all detectors. Figure 5.6 shows the ΔT_{of} distribution obtained during the measurement of the 0.1 mm thick gold sample. Two regions can be clearly seen in Figure 5.6. From -13 to 12 ns (red region) the distribution shows a typical structure of coincidence events. In the remaining regions (the blue zones), the distribution becomes almost flat, as expected for uncorrelated events. From this figure, the width of the coincidence window has been chosen of 25 ns. As reported in the figure the Gaussian fit of the peak in the ΔT_{of} spectrum indicates a FWHM of 10 ns, so that the chosen window includes al-

⁴Hereafter we will refer to “event” as “capture event”.

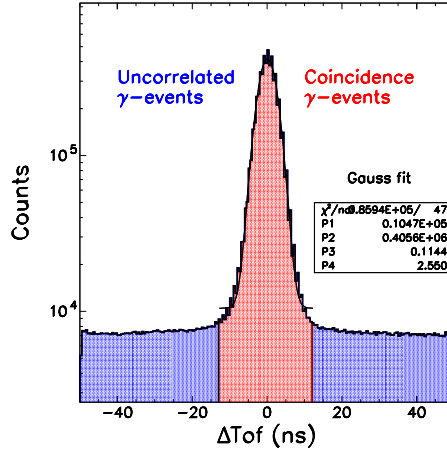


Figure 5.6: Minimum time distribution between γ -rays signals coming from two (or more) detectors. The coincidence events are in red ($-13 \leq \Delta Tof \leq 12$ ns) while uncorrelated events are in blue.

most 100% of the true γ -ray coincidences, while minimising the background related to the random coincidences.

5.3.1 Capture yield determination

For each capture event, the calorimetric routine provides the following information: the total energy deposited in the TAC (E_{TAC}), the time-of-flight (Tof) and the multiplicity (M_γ), i. e. the number of BaF₂ crystals in which a γ -ray is detected above threshold. The experimental capture yield can be determined from the number of γ -ray cascades $C_{Au}(E_n)$ as a function of the neutron energy (E_n) determined from the measured time-of-flight, according to the calibration procedure described in Ref. [82]. The background-free distribution is obtained by subtracting the spectrum measured with an empty-sample (also called “sample holder”), C_{empty} , i.e. a measurement in which the Au sample is removed from the beam, leaving only the sample holder in. The capture yield is then given by:

$$Y_{exp}(E_n) = \frac{C_{Au} - C_{empty}}{\epsilon} \cdot \frac{1}{f \cdot \Phi(E_n)}, \quad (5.1)$$

here $\Phi(E_n)$ is the neutron flux integrated over the neutron beam profile, as a function of the energy E_n , ϵ is the efficiency of the TAC for detecting the capture event, and f is the fraction of the neutron beam intercepted by the sample. This fraction is typically ≈ 0.2 , since the dimension of the sample (1 cm diameter) is smaller than the neutron beam profile. Both factors, ϵ and f , in a first approximation, do not depend on the

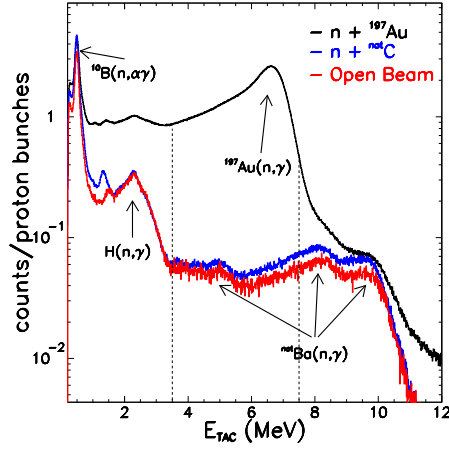


Figure 5.7: The spectrum of the energy deposited in the TAC, with conditions on incoming energy neutrons: $1 < E_n < 5000$ eV. Measurements on Au, on C and empty measurement (also called open beam) are shown. Dashed vertical lines indicate the analysis conditions.

incoming neutron energy, in the range here considered, being f related only to the geometry of the sample, and ϵ to the analysis conditions, such as multiplicity and cuts on energy deposition, i. e. $\epsilon = \epsilon(E_{TAC}, M_\gamma)$.

The subtraction in Eq. 5.1 of the Au and empty spectra has been done after the normalization to the number of proton delivered during the Au and empty measurements.

The measured yield has been self-normalized by using the saturated resonance technique, applied to the 4.9 eV resonance [159] (more details are given in Section 5.3.2). The normalization constant, in this case, is the inverse of the product of the detection efficiency multiplied by the fraction of neutrons impinging on the sample: $N = 1/\epsilon \cdot f$. Therefore the experimental capture yield as a function of the incoming neutron energy can now be written as:

$$Y_{exp}(E_n) = N \frac{C_{Au} - C_{empty}}{\Phi(E_n)}.$$

Figure 5.7 shows the total energy deposited in the TAC for the Au(n, γ) measurement. The capture peak at 6.5 MeV can be clearly identified, together with the various components of the background. A delicate part of the data analysis consists in the choice of the optimal conditions that maximize the capture-to-background ratio.

Figure 5.7 and 5.8 show the selection criteria adopted in the present analysis. For the total energy deposited E_{TAC} , the condition chosen is $3.5 < E_{TAC} < 7.5$ MeV, with a minimum bias on the multiplicity ($M_\gamma \geq 2$). As shown later, the choice on E_{TAC}

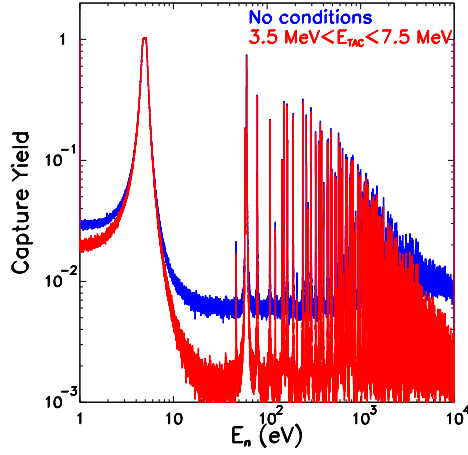


Figure 5.8: Different experimental capture yield for Au(n,γ) reaction extracted with and without conditions on energy deposition. No conditions are applied on multiplicity: $M_\gamma \geq 2$.

minimizes the background due to the neutron sensitivity, since it allows to reject completely the 2.2 MeV γ -rays produced by Hydrogen capture in the inner sphere of the calorimeter. Furthermore, this condition removes also a fraction of background caused by neutrons captured in the crystals by some Ba isotopes ($^{135,137}\text{Ba}$), whose separation energy is above 7 MeV. Another advantage of this condition is that it minimizes pile-up of two consecutive capture cascades, which simulates events with large total energy deposition. Although the applied condition reduces the overall efficiency down to 60%, the resulting signal-to-background ratio is drastically improved, as shown in Figure 5.8.

5.3.2 Capture yield normalization

We have studied the impact of resonance parameters on the normalization when applying the saturates resonance techniques. Figure 5.9 shows that when a saturated resonance is dominated by the capture channel, the value of the normalization is nearly independent of the resonance parameters, as demonstrated by Borella et al. [160]. The theoretical yield in this case is expected to be ≈ 1 (see Eq. 4.11), on the contrary when the neutron width is of the same order of magnitude of the capture width (or higher) not all scattered neutrons are absorbed in the sample. In this case it follows that: $Y_c(E_n) = \frac{\sigma_\gamma}{\sigma_{tot}} + Y_m < 1$.

The Independence on the resonance parameters is demonstrated in Table 5.2 which lists the normalization factor N that was deduced from a resonance shape analysis of the experimental yield at the 4.9 eV resonance, measured with a 0.1 mm thick sample.

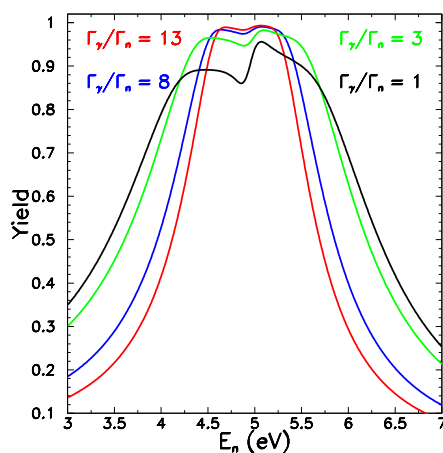


Figure 5.9: The theoretical calculation for the first Au(n, γ) resonance calculated with R-Matrix code SAMMY varying partial widths. The sample thickness is 0.1 mm.

An example of the goodness of the fit is shown in Figure 5.10. It has to be noted that the larger variation on the normalization factor N , deduced from the yield of the Au 4.9 eV saturated resonance, is reached when a 20% higher value for Γ_n is kept fixed while performing the fit. In the other cases the variation of the normalization factor is within 0.1%.

5.3.3 Background measurements

Figure 5.11 shows the spectra obtained for different samples, when the following analysis conditions are applied:

- single crystal threshold = 150 keV;
- $-13 \text{ ns} < \Delta\text{Tof} < 12 \text{ ns}$;
- $3.5 < E_{TAC} < 7.5 \text{ MeV}$;
- $M_\gamma \leq 2$.

The left panel in the figure shows the results for the Au (black histogram) and empty-sample (in red). The background-free Au capture yield, as pointed out in Eq. 5.1, is obtained subtracting bin by bin the histogram for the empty-sample from the one for Au.

Other sources of background that have to be taken into account are the sample-scattered neutrons and the γ -ray contamination in the neutron beam. These background components were evaluated by performing two other measurements: C+n

Table 5.2: The results of a resonance shape analysis (with SAMMY) of the 4.9 eV resonance of ^{197}Au . The chi-square is given together with the energy region considered in the fit. The superscript indicates the parameter that was kept fixed. Last row gives the values of Γ_γ and Γ_n in ENDF/B-VII.

N	Γ_γ (meV)	Γ_n (meV)	χ^2	Region
0.1249	124.*	15.2*	1.17	3 - 7 eV
0.1248	123.	15.2*	1.14	3 - 7 eV
0.1248	124.*	15.3	1.13	3-7 eV
0.1244	117.	15.8	1.11	3 - 7 eV
0.1238	144.	13.*	1.15	3 - 7 eV
0.1240	151.	13.*	1.16	4.6 - 5.2 eV
0.1263	99.	18.*	1.13	3 - 7 eV
0.1267	100.	18.*	1.12	4.6 - 5.2 eV
ENDF/B-VII	124.	15.2		

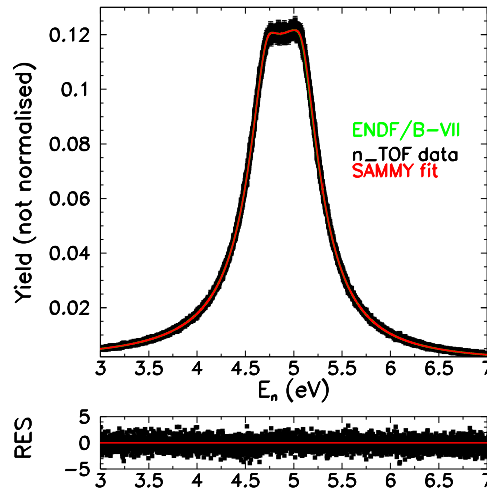


Figure 5.10: SAMMY fit of the *s-wave* ^{197}Au resonance at 4.9 eV with both resonance partial widths free to vary. The higher value on the plateau gives the corresponding normalization, in this case $N=0.125$. In the lower panel the residual are plotted.

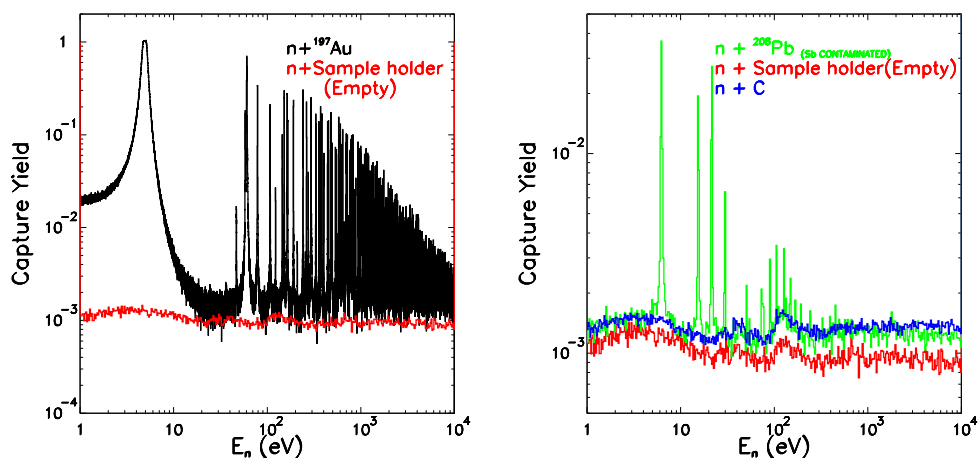


Figure 5.11: Left: Au and empty-sample experimental capture yield, extracted with the same conditions on energy deposition and multiplicity. Right: empty-sample, C+n and ${}^{208}\text{Pb}+n$ experimental capture yield, extracted with the same conditions on energy deposition and multiplicity ($M_\gamma \geq 2$). Resonances in Pb yield are due to a small contamination of Antimony (Sb).

and ${}^{208}\text{Pb}+n$. Both of these isotopes are characterised by a very low capture cross-section, moreover:

- because of its very low atomic number, the C+n measurement can be used to estimate the background due to the sample-scattered neutrons;
- ${}^{208}\text{Pb}+n$ can be used to check for the background induced by the γ -rays contamination in the neutron beam, thanks to its large atomic number.

The experimental yield of these measurements are reported in Figure 5.11. The reported spectra are normalise to the number of protons. As can be seen (beside the resonances due to a Sb contamination in the Pb sample) the C+n and the ${}^{208}\text{Pb}+n$ background, with the condition used in the analysis, are close to the one measured with the empty-sample, thus demonstrating the low level of the respective surviving background. Indeed it has to be noted that the yield of the background events is of the order of 10^{-3} .

5.3.4 Corrections to the capture yield

The capture yield measured with the TAC must be corrected for some systematic effects (before performing a resonance analysis with a R-Matrix code). The most important corrections are related to the dead-time of the apparatus and to its neutron sensitivity. A detailed description of these effects and applied corrections is given in the following.

Signal pile-up and detector dead-time

The large counting rate associated with the very high instantaneous neutron flux at n_TOF results in two different effects that have to be considered in the analysis of the TAC data:

- i) the pile-up between consecutive signals in each BaF₂ crystal,
- ii) the occurrence of two consecutive capture events within the coincidence window used in the calorimetric routine (25 ns).

For analogy with standard electronics, we will refer to this second effect as “detector dead-time”.

As pointed out in Section 5.2, contrary to standard electronic and acquisition systems, the n_TOF DAQ should not be affected by pile-up. However the pulse shape algorithm may fail to identify a small signal in the tail of a preceding large signal. For this reason, a fraction of low-energy γ -rays may be lost, thus distorting primarily the multiplicity and, to a less extent, the total energy deposited in the TAC. Since the pile-up probability depends on the counting rate, large resonances may be affected, both in shape and area. A correction for this effect requires a detailed knowledge of the signal shape in each crystal, and of the ability of the reconstruction routine to identify and recognize pile-up events. A possibility is to rely on detailed simulations of the detector response. A different approach, however, has been adopted in the present thesis, taking advantage of the feature of the n_TOF proton beam, that can be delivered in two different modes: a dedicated mode, with intensity of 7×10^{12} protons/pulse, and a parasitic one, with approximately half the intensity (as shown later, this feature is useful also for verifying the accuracy of dead-time corrections). A comparison between data collected in two modes reveals that pile-up problems affect only the low-energy part of the energy deposited in each crystal. A minimization of the problem is therefore obtained by applying a threshold of 150 keV on the individual crystal and keeping a minimum bias on the multiplicity ($M_\gamma \geq 2$). In this way, this problem does not affect significantly the TAC performance. Indeed Figure 5.12 shows that the dead time is about the expected one, i. e. the time window of 25 ns. The problem in the time distribution of a each crystal, that was reported in Figure 5.2, disappears when considering coincidences. It should be noted that the applied threshold of 150 keV to single crystal also minimizes effects related to the attenuation of γ -rays in the sample, limiting fluctuations in the reconstructed total energy and multiplicity of the cascade.

The second, important effect produced by the high counting rate at n_TOF is related to the occurrence of two capture events within the coincidence time window used in the calorimetric routine to identify and sum-up all γ -rays belonging to a capture event. For the largest counting rates, the probability of detecting two different

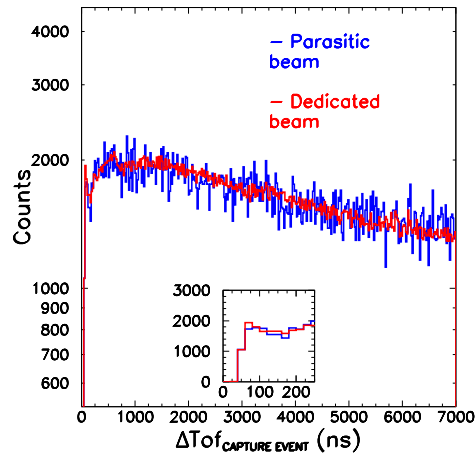


Figure 5.12: Time difference distribution between 2 capture events in parasitic and in dedicated mode, both distribution present a dead time of about 25 ns.

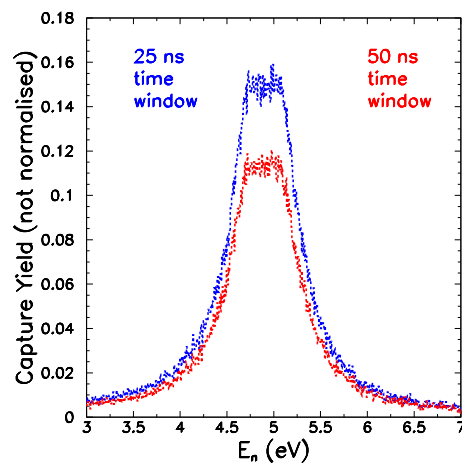


Figure 5.13: The first Au resonance. Two capture yield extracted from the same data set with two different time window (“detector dead-time”), 50 and 25 ns.

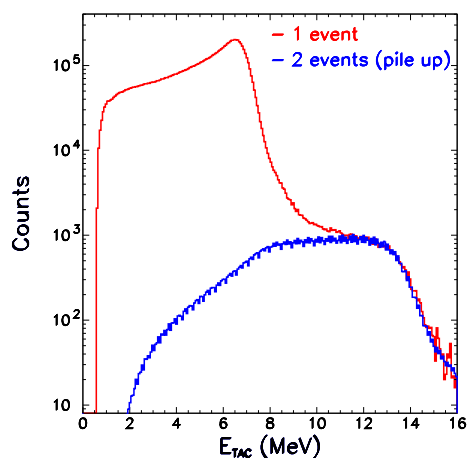


Figure 5.14: The experimental energy deposited in the TAC for $4 < E_n < 6$ eV (red curve) and the MC simulated energy spectrum (blue curve) for the "detector dead time" correction. The condition on neutron energy avoids contamination due to neutron sensitivity on energy spectrum, indeed all neutrons are absorbed in the sample when a resonance is saturated.

capture events in the coincidence time window cannot be neglected. As a result, a loss of events is produced, as evident in Figure 5.13, that shows how an increase in the time window from 25 to 50 ns produces a strong reduction of the capture yield. Due to the constraints on the total deposited energy, the combination of two (or more) capture reactions leads to the loss of one or both events, depending on whether the resulting E_{TAC} falls within the applied conditions. The effect is analogous to the loss of counts due to the dead-time in standard processing and acquisition systems. This kind of "detector dead-time" can be corrected in the first order by applying a correction for a standard non cumulative (non paralyzable) model (see Eq. 3.7) where the dead-time is the time width of the coincidence window, i. e. 25 ns.

The first order correction is valid in the standard assumption that, out of the two events in coincidence, only one is detected. In the calorimetric method, however, other cases should be considered. Given the conditions applied on E_{TAC} and M_γ , it is possible that both event are lost (the combination of the two falling outside the conditions). On the other hand, one should also consider that some events lost for dead-time, would have been lost anyway, because they did not originally match the analysis conditions. The number of events effectively lost by dead-time was estimated by means of Monte Carlo simulations. Two events, randomly chosen from the measured E_{TAC} spectrum were added together, and the resulting spectrum, shown in Figure 5.14, was analyzed in order to determine the second-order effect. It was found that, on average, the dead-time correction factor of Eq. 3.7 has to be increased by 30%.

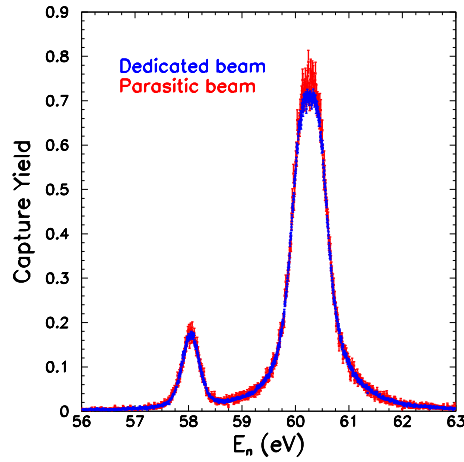


Figure 5.15: Au Capture yield obtained with dedicated and parasitic beam. For this resonance, at 60.3 eV the counting rate reaches the maximum values. A small difference at the top of the resonance can be seen.

To avoid effects due to neutron background in E_{TAC} spectrum, the condition: $4 < E_n < 6$ eV was set on incoming energy neutrons.

The overall correction is less than 6%, reached at the top of the strongest resonances (for dedicated beam). Although small, the dead-time affects the results of the resonances analysis, by distorting their shape. For this reason a correction was always applied. On the flat top of the 4.9 eV resonance, used for normalization purposes, such effect is about 2%.

After applying the dead-time correction, a systematic check was carried out by comparing parasitic and dedicated pulses. Except for the 60.3 eV resonance (see Figure 5.15), which shows the largest counting rate ($> 1 \mu s^{-1}$), the difference between yields extracted for the two proton beam modes was found to be less than 1%, thus providing confidence on the validity of the applied dead-time correction.

Neutron background

Neutrons elastically scattered by the sample can be captured inside the TAC, mainly by some Ba isotopes, and contaminate capture yield from the Au sample. This kind of background depends on the neutron sensitivity of the detector [139, 154], defined as the ratio between the efficiency for detecting scattered neutrons ϵ_n , and that for capture events $\epsilon(E_{TAC}, M_\gamma)$. The effect, particularly important for resonances with a neutron width larger than the radiation width, consists in an artificial increase of the resonance area. Several methods can be used to determine this background component (see Ref. [152, 167, 168] for details). In the present analysis the neutron sensitivity

was determined from a measurement with a thick graphite sample, and by the ratio of elastic cross-sections of Au and C, according to the following expression:

$$\frac{\epsilon_n}{\epsilon} = \frac{(C_C - C_{empty})}{(C_{Au} - C_{empty})} \cdot \frac{Y_c^{Au}}{Y_{(n,n)}^C}, \quad (5.2)$$

where C_C and C_{Au} are the measured number of counts as a function of the neutron energy (normalise to the neutron flux). The capture yield for ^{197}Au and that of elastic scattering in ^{12}C are calculated from the ENDF/B-VI evaluated cross-sections. As

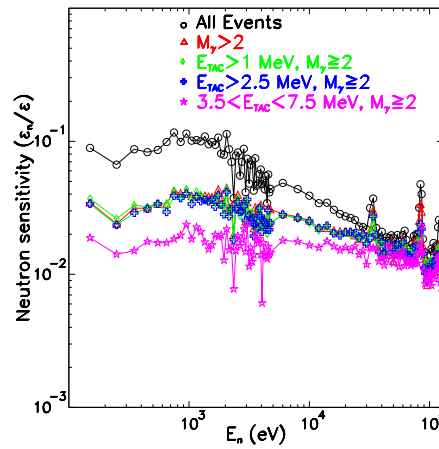


Figure 5.16: Experimental neutron sensitivity for the n_TOF TAC capture detection system as a function of neutron energy. The ratio ϵ_n/ϵ of the probability that a neutron entering the system creates a detected signal is calculated relative to different conditions on E_{TAC} and event multiplicity.

shown in Figure 5.16 for the 4π detection system, based on BaF_2 scintillator, the neutron sensitivity is very high, about 0.1, three orders of magnitude higher than that of the C_6D_6 setup. However, the background due to scattered neutrons can be reduced in an effective way, by applying a suitable condition on the total deposited energy E_{TAC} .

The optimal condition can be understood by looking at the distribution of the total energy deposited in the TAC, shown in Figure 5.7 for Au, as well as for C and empty-sample. Together with the peak at 6.5 MeV related to the $^{197}\text{Au}(n,\gamma)$ reaction, several other structures can be observed in the figure. Table 5.3 lists the origin of these structures. The peaks at low energy are associated with capture of scattered neutrons in the ^{10}B capsules (emitting a single 480 keV γ -ray), or with capture by the Hydrogen content in the inner shell of absorbing material (with the consequent emission of a 2.2 MeV γ -ray). The structure above 7.5 MeV is instead caused by capture of scattered neutrons by two Ba isotopes in the BaF_2 crystal. Below the capture

peak of Au, other reactions take place, such as capture by other Ba isotopes (in particular $^{130,132,134,136}\text{Ba}$, with neutron separation energy $S_n = 7.5, 7.2, 7$ and 6.9 MeV, respectively) as well as by ^{19}F , with capture energy of 6.6 MeV. However, due to the

Table 5.3: List of the main capturing isotopes present in the whole detector and their relative neutron binding energy. See Figure 5.7 for comparison.

Isotope	Reaction	Energy MeV	where
^{10}B	$(n, \alpha\gamma)$	0.48	capsules
H	(n, γ)	2.2	n-absorber
^{138}Ba	(n, γ)	4.8	scintillator
^{137}Ba	(n, γ)	8.6	scintillator
^{135}Ba	(n, γ)	9.1	scintillator

low capture cross-section and/or low natural abundances, their contribution is not evident in the spectrum of total energy E_{TAC} , shown in Figure 5.7. The neutron sensitivity calculated for different conditions on E_{TAC} and event multiplicity is shown in Figure 5.16. The strongest reduction, of about one order of magnitude, is obtained with the condition used in the present analysis, i.e. $3.5 < E_{TAC} < 7.5$ MeV, which allows to completely reject events related to neutron capture in the ^{10}B -loaded capsules as well as in the neutron absorber. Although strongly reduced by the analysis procedure, a residual background due to scattered neutrons still remains, as evident in Figure 5.7 from the difference between the C and empty-samples. For most resonances, this unavoidable background results in an increase of the neutron yield of a few percent, although it may reach up to 20% for resonances with very large Γ_n (i. e. with a large elastic-to-capture cross-section ratio). Therefore, a second step is needed in the analysis to subtract this residual background. Two techniques were investigated to this purpose, with the background calculated either on the basis of resonances parameters listed in literature or from the same experimental data collected at n_TOF. In the first case, the expression of the neutron background B_n was derived by scaling the carbon measurement to the Au sample, according to the following expression:

$$B_n = (Y_C - Y_{empty}) \cdot \frac{Y_{(n,n)}^{Au}}{Y_{(n,n)}^C}. \quad (5.3)$$

The elastic yields for Au and C ($Y_{(n,n)}^{Au}$ and $Y_{(n,n)}^C$, respectively) were derived from ENDF/B-VI cross-sections. The second method, described in more details in Ref. [168] and shown in Figure 5.17, relies exclusively on the measured E_{TAC} . In this case, the residual background is determined from the yield measured with C sample (subtracted for the empty-sample contribution), scaled so to match the tail above 7.5 MeV, in the E_{TAC} spectrum for Au. This method relies on the assumption that such a tail is

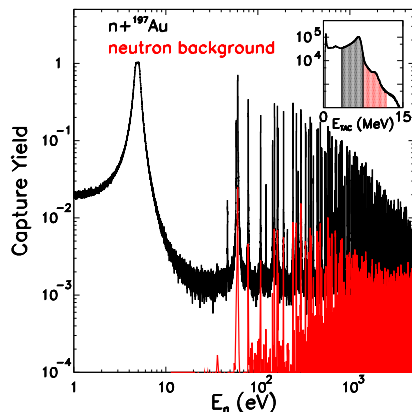


Figure 5.17: Au capture yield and the neutron background, obtained with the experimental method. The blue curve corresponds to events that fill the condition: $3.5 < E_{TAC} < 7.5$ MeV, while the red curve corresponds to events that satisfy $7.5 < E_{TAC} < 12$ MeV.

due only to neutron capture on Ba isotopes.

Both techniques for neutron background subtraction present problems. The first method suffers from the lack of reliable neutron widths in literature. Furthermore, it does not take into account a distortion in the reconstructed neutron energy, due to the moderation time of scattered neutrons. Therefore this first correction is an upper limit of the neutron background. In the second method the background may be overestimated, for the largest resonances, since the E_{TAC} region above 7.5 MeV may be affected also by pile-up events (see Figure 5.14).

In the present analysis, we choose to extract the neutron background with the second method but using in some cases additional information on $g\Gamma_n$ provided by the comparison with the C_6D_6 and with the results obtained with the first method.

5.4 Results

In the resolved resonance region the yield measured at n_TOF was analyzed with the resonance shape analysis code SAMMY. The code is based on the Reich-Moore approximation of the R-Matrix theory and accounts for self-shielding, multiple scattering and Doppler effects. The resolution function of the n_TOF neutron beam has been included in the code. The measured background, related to the neutron sensitivity of the detector described above (shown in Figure 5.17), was also included in the code, as “point wise” data, and kept fixed in the resonance fit.

As already explained in Section 5.1 the fitting procedure allowed to extract the capture kernels from the measured capture yields. Moreover other fitting strategies

were tried, in order to check the reliability of the extracted kernels:

1. both partial widths, Γ_γ and Γ_n free;
2. only the smaller of the two reaction widths free, with the other one fixed at the tabulated value;
3. only Γ_n free with Γ_γ fixed at an average value (124 meV) from ENDF/B-VII;
4. the choice of the parameters to vary identified from the minimization of the resulting χ^2 .

An overall agreement within few percent resulted from the different strategies.

In the energy range between 1 eV and 4.830 keV the kernels of 265 resonances have been determined separately by the analysis of the data from the TAC (see Figure 5.18) and the C_6D_6 detectors, the values of the kernels are reported in Section 5.4.2.

Figure 5.18 shows the capture yield obtained with the TAC and the quality of the fit in different energy regions. In the missing regions no resonances are present.

5.4.1 Discussion of uncertainties

The total uncertainty in the cross-section consists of several contributions that can be identified in the analysis procedure. An important source comes from the determination of the normalization factor (that is the inverse of the product of neutron beam interception factor and the efficiency of the TAC). This normalization has been determined from the analysis of the first $Au(n,\gamma)$ resonance, and its uncertainty is less than 0.1% (see Table 5.2). The additional uncertainties are related to the background subtraction, the dead-time and the pile-up corrections. Since the magnitude of each correction is among 0.1 and 2%, the overall uncertainty on the normalization can be assumed to be around 2%. An uncertainty of 2-3% is related to the determination of the shape of the neutron flux. Adding up these components the overall uncertainty is around 3%. To this uncertainty the statistical one has to be added.

5.4.2 Capture kernels

The Table 5.4 reports the resonance kernel obtained from the TAC data and from C_6D_6 data together with their uncertainties due to the fitting procedure. Moreover the radiative kernels calculated from resonance parameters listed in ENDF/B-VI and ENDF/B-VII libraries are also reported.

Although the resonance parameters are obtained from the resonance shape analysis, only the capture kernels in the present analysis are characterised by a high accuracy. Improving the accuracy on the individual parameters requires a combination

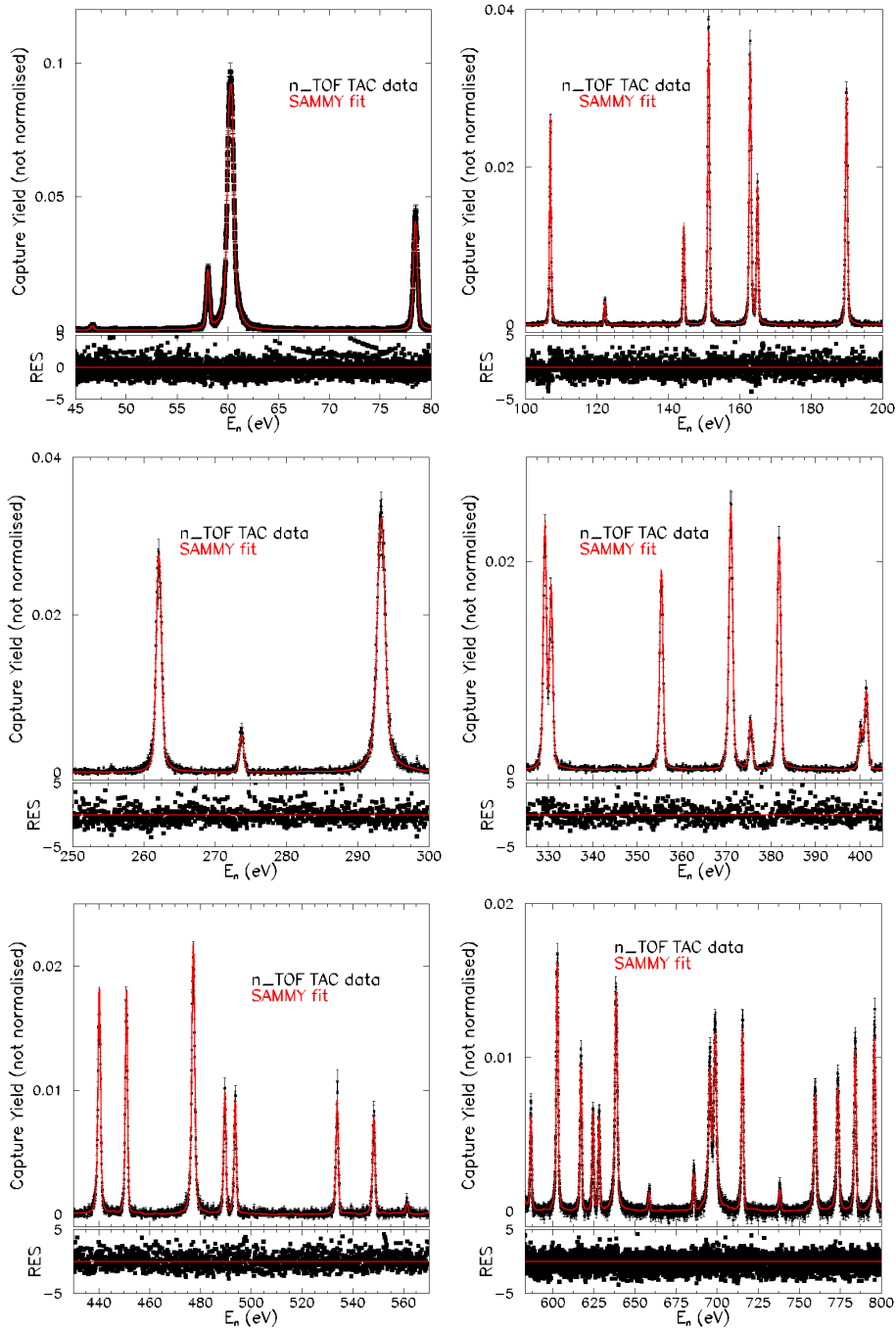


Figure 5.18: Experimental capture yield obtained with TAC and relative SAMMY fit. The capture yield has been divided into several regions for a better visualization. The normalization factor is 0.124.

of the present data with a transmission measurement, which was beyond the goal of the present measurement.

Table 5.4: Radiative kernels (K) for $^{197}\text{Au}+n$ obtained at n_TOF and that ones listed in ENDF/B libraries.

E_R (eV)	TAC		C_6D_6		ENDFVII	ENDFVI
	K (meV)	$\Delta\text{K}/\text{K}$ %	K (meV)	$\Delta\text{K}/\text{K}$ %	K (meV)	K (meV)
46.63	.08	4	.08	3	.06	.05
58.02	1.59	1	1.52	1	1.57	1.59
60.23	26.37	1	28.42	1	25.88	27.90
78.44	5.42	1	5.60	1	5.49	5.55
106.95	4.65	1	4.66	1	4.44	4.58
122.23	.55	3	.53	3	.50	.50
144.30	3.11	2	3.19	2	3.07	3.11
151.28	12.17	1	11.48	4	11.30	11.62
162.94	13.52	2	12.80	5	13.54	13.54
164.95	5.20	2	4.93	2	5.34	5.34
189.91	12.87	1	13.06	2	13.15	12.33
240.44	27.42	4	29.38	3	25.95	26.16
262.05	23.70	3	25.82	3	24.23	23.66
273.67	2.81	3	2.61	3	2.51	2.52
293.20	53.57	1	56.63	2	56.40	65.18
329.16	21.36	1	19.26	2	21.44	21.26
330.57	15.58	1	14.44	3	15.81	16.04
355.31	18.16	1	17.63	2	18.94	18.65
370.91	32.78	1	32.31	4	28.55	29.29
375.36	4.58	2	4.21	3	4.64	4.71
381.77	25.80	1	25.43	3	23.95	24.14
400.08	3.72	2	3.63	3	3.81	3.81
401.31	8.59	1	8.09	3	8.61	8.62
440.07	34.30	1	36.30	2	34.89	33.94
450.80	26.09	1	24.49	3	23.84	24.78
477.12	53.91	1	54.54	2	55.54	57.78
489.50	15.91	1	15.81	3	15.68	14.86
493.58	14.67	1	13.84	3	12.33	14.03
533.65	16.12	1	15.72	3	15.73	17.15
548.15	15.32	1	14.77	3	14.08	14.02
561.22	1.57	4	1.59	6	1.76	1.76
578.52	56.21	1	54.16	2	34.46	66.71
580.40	28.57	1	32.36	3	31.36	24.20
586.34	11.86	2	11.86	3	11.25	10.41

Table 5.4: Radiative kernels (K) for $^{197}\text{Au}+n$ obtained at n_TOF and that ones listed in ENDF/B libraries.

E_R (eV)	TAC		C_6D_6		ENDFVII	ENDFVI
	K (meV)	$\Delta\text{K}/\text{K}$ %	K (meV)	$\Delta\text{K}/\text{K}$ %	K (meV)	K (meV)
602.41	46.75	1	47.04	2	55.01	55.01
616.85	23.20	1	22.66	4	24.24	31.62
624.14	13.98	2	13.69	4	13.14	13.08
627.89	13.19	2	12.87	3	12.04	11.86
638.28	58.62	1	59.06	2	65.73	71.43
658.40	2.80	4	2.47	6	2.31	2.28
685.55	6.03	3	5.31	5	4.53	4.50
695.33	39.68	1	42.75	3	44.15	49.12
698.54	60.46	1	59.16	3	62.16	75.27
715.22	36.57	5	34.80	11	37.47	42.87
737.98	3.96	4	3.86	5	4.50	4.70
759.53	34.04	1	32.99	3	38.46	42.44
773.28	37.37	1	36.78	3	36.40	37.11
783.84	36.79	1	37.25	4	37.30	42.86
795.51	45.17	1	45.49	3	49.32	50.32
812.79	7.41	3	7.11	5	7.08	7.01
819.02	48.54	4	50.27	9	49.69	56.74
824.44	58.01	1	57.11	3	65.87	79.47
863.70	10.55	1	10.69	11	10.24	7.46
878.94	14.42	2	15.81	9	17.01	17.37
931.78	56.89	2	56.88	8	59.91	68.35
955.45	3.46	5	3.43	7	6.44	6.44
960.58	25.73	2	22.68	4	6.38	23.74
983.79	47.04	3	45.26	10	56.39	64.22
987.90	37.51	2	35.12	5	43.02	44.07
994.84	57.87	1	63.94	8	64.38	73.45
1039.06	12.25	3	12.10	6	11.14	12.18
1042.61	37.69	2	33.38	4	37.98	37.27
1063.23	3.93	5	3.54	7	3.69	3.80
1077.31	35.58	2	33.62	4	35.41	34.59
1091.98	50.73	1	48.95	3	55.41	65.08
1119.50	6.89	4	7.46	8	7.52	7.01
1127.86	15.46	3	15.31	5	17.25	17.81
1134.77	59.56	3	58.03	9	60.35	65.29

Table 5.4: Radiative kernels (K) for $^{197}\text{Au}+n$ obtained at n_TOF and that ones listed in ENDF/B libraries.

E_R (eV)	TAC		C_6D_6		ENDFVII	ENDFVI
	K (meV)	$\Delta\text{K}/\text{K}$ %	K (meV)	$\Delta\text{K}/\text{K}$ %	K (meV)	K (meV)
1177.09	4.44	6	4.32	7	4.71	4.70
1182.68	55.79	1	49.51	4	58.99	59.01
1206.63	54.12	2	52.12	4	54.83	63.00
1217.80	12.90	3	13.28	5	14.69	15.90
1222.72	37.90	1	38.69	9	37.06	42.00
1244.58	32.31	5	26.37	12	24.49	24.06
1252.57	19.56	3	19.58	5	25.06	25.06
1281.06	35.12	2	34.97	4	37.53	40.45
1285.51	8.98	4	8.94	9	8.41	8.36
1309.89	46.15	2	45.75	4	53.93	52.01
1327.91	39.21	2	39.18	4	37.07	42.74
1335.20	33.87	2	33.08	6	39.95	38.91
1353.54	54.06	2	52.31	4	39.47	39.47
1358.92	11.87	4	11.42	6	13.68	13.43
1366.91	35.79	2	34.21	10	32.43	31.75
1394.94	16.87	3	16.50	5	17.25	15.90
1425.77	31.36	4	31.71	7	32.22	31.52
1428.10	54.94	3	52.57	5	61.48	60.03
1449.53	46.57	2	47.41	10	44.89	56.16
1468.79	16.34	4	15.03	6	17.25	17.81
1473.76	26.83	3	26.92	8	26.67	26.20
1489.50	70.84	1	76.88	7	74.13	69.71
1500.81	9.31	5	9.09	8	9.21	9.16
1529.46	12.66	4	13.35	7	13.09	13.36
1551.41	40.64	2	39.04	7	44.46	46.88
1568.41	3.87	8	3.92	8	4.17	4.10
1577.84	40.88	2	34.74	5	37.89	45.00
1592.37	19.76	3	20.13	6	24.35	24.99
1614.09	42.78	2	41.55	8	43.58	42.24
1640.76	24.40	3	23.06	8	23.23	22.87
1645.40	35.79	2	33.61	7	34.29	33.82
1659.40	1.61	9	1.59	10	2.19	2.18
1692.44	39.17	3	39.85	7	44.02	40.25
1705.29	53.87	2	49.04	5	56.56	53.11

Table 5.4: Radiative kernels (K) for $^{197}\text{Au}+n$ obtained at n_TOF and that ones listed in ENDF/B libraries.

E_R (eV)	TAC		C_6D_6		ENDFVII	ENDFVI
	K (meV)	$\Delta\text{K}/\text{K}$ %	K (meV)	$\Delta\text{K}/\text{K}$ %	K (meV)	K (meV)
1720.46	14.91	4	14.83	7	17.25	17.81
1733.53	49.73	2	47.11	5	56.90	55.61
1753.49	54.75	4	54.67	6	57.14	55.86
1755.55	39.53	5	36.07	7	39.17	38.17
1810.80	20.39	3	19.24	8	20.57	20.29
1820.70	8.19	6	8.15	8	8.09	7.86
1830.92	19.19	4	18.21	8	19.56	19.30
1855.56	44.69	3	44.40	5	47.00	55.88
1859.63	33.58	3	29.66	7	29.71	31.74
1882.61	30.67	3	28.72	9	34.65	30.07
1887.60	1.27	10	1.39	10	1.52	2.25
1912.72	43.45	3	42.54	5	44.26	52.01
1939.03	39.06	2	40.24	11	38.52	39.00
1959.46	72.19	1	72.57	9	68.07	84.61
2021.06	5.60	8	6.34	8	6.11	36.78
2028.01	35.67	2	35.00	11	32.41	31.75
2032.35	33.61	5	32.54	7	36.91	36.04
2035.31	49.23	3	50.08	10	52.17	51.10
2058.58	10.40	6	9.09	8	8.09	31.21
2074.86	57.12	3	58.67	5	71.52	69.53
2081.65	64.80	2	66.38	11	62.99	61.43
2088.37	38.07	2	38.59	12	37.74	36.83
2111.74	29.27	3	26.70	7	28.80	28.47
2130.65	44.37	1	46.12	9	43.87	43.11
2147.45	58.40	3	55.76	5	63.46	61.87
2153.85	33.31	3	33.43	11	34.68	47.84
2192.90	36.41	2	35.67	11	34.29	33.51
2223.25	15.09	5	14.57	9	14.12	15.90
2240.35	32.20	4	35.85	8	38.71	38.11
2278.11	8.63	6	9.15	8	8.89	8.31
2286.42	46.10	3	43.76	8	40.00	39.37
2331.94	50.32	2	46.02	9	42.35	30.66
2366.06	48.23	2	42.33	8	34.29	33.82
2379.59	3.08	9	2.98	10	2.89	3.00

Table 5.4: Radiative kernels (K) for $^{197}\text{Au}+n$ obtained at n_TOF and that ones listed in ENDF/B libraries.

E_R (eV)	TAC		C_6D_6		ENDFVII	ENDFVI
	K (meV)	$\Delta\text{K}/\text{K}$ %	K (meV)	$\Delta\text{K}/\text{K}$ %	K (meV)	K (meV)
2405.84	35.17	4	37.82	8	38.71	28.70
2414.50	55.69	4	49.48	6	42.86	41.66
2419.06	35.61	5	37.36	7	71.79	69.77
2439.97	27.08	3	26.43	10	26.67	33.82
2469.09	53.06	4	53.13	6	64.39	62.76
2498.05	17.48	6	21.25	8	23.86	19.68
2507.65	25.21	5	26.23	8	29.21	28.96
2535.05	33.81	4	38.82	9	45.03	44.25
2560.14	9.98	8	11.56	9	12.63	11.34
2576.78	31.14	3	29.75	10	28.47	36.78
2581.33	5.64	8	5.11	9	4.71	4.70
2597.64	49.43	3	48.74	7	55.24	47.47
2611.56	47.95	4	48.15	7	55.83	47.99
2627.98	13.47	7	14.06	9	18.46	18.18
2632.28	2.75	9	2.63	10	1.12	1.80
2652.56	1.16	10	1.21	10	.81	.81
2683.82	30.04	4	30.16	8	30.62	30.62
2708.19	38.89	6	33.23	13	22.97	22.97
2722.41	48.32	3	48.48	10	49.07	49.07
2747.17	34.22	4	35.54	9	37.12	37.12
2761.45	35.96	4	37.28	9	39.37	39.37
2774.77	4.49	9	4.82	10	4.72	4.72
2790.47	7.69	7	7.46	9	7.28	7.28
2805.45	47.78	3	47.33	10	47.47	47.47
2831.67	34.45	5	41.54	7	54.99	54.99
2849.45	28.63	5	29.08	9	33.21	33.21
2864.33	44.95	3	45.83	10	48.73	48.73
2875.97	40.18	4	43.90	10	44.81	44.81
2896.10	1.26	10	1.23	10	1.21	1.21
2910.81	7.04	8	6.56	10	7.54	7.54
2926.78	2.43	10	2.49	10	2.42	2.42
2957.06	15.55	6	15.77	9	16.15	16.15
2985.10	40.65	4	43.27	8	49.07	49.07
3023.94	63.07	2	64.43	11	61.32	61.32

Table 5.4: Radiative kernels (K) for $^{197}\text{Au}+n$ obtained at n_TOF and that ones listed in ENDF/B libraries.

E_R (eV)	TAC		C_6D_6		ENDFVII	ENDFVI
	K (meV)	$\Delta\text{K}/\text{K}$ %	K (meV)	$\Delta\text{K}/\text{K}$ %	K (meV)	K (meV)
3036.59	68.97	1	70.16	11	66.25	66.25
3048.40	33.53	3	33.72	12	33.00	33.00
3063.02	3.82	9	4.00	10	4.14	4.14
3078.98	37.20	2	37.76	12	37.29	37.29
3098.32	15.22	6	15.87	10	16.47	16.47
3133.50	51.51	3	51.14	10	49.24	49.24
3160.89	8.50	8	9.37	10	10.24	10.24
3174.22	19.57	5	19.87	10	20.76	20.76
3200.23	5.98	8	6.31	10	6.46	6.46
3214.80	83.07	1	83.75	10	78.47	78.47
3254.00	34.50	5	40.75	10	43.06	43.06
3258.26	22.16	5	22.91	10	21.96	21.96
3268.69	23.14	6	23.70	9	24.11	24.11
3278.15	35.51	4	35.60	10	37.46	37.46
3302.30	3.41	10	3.68	10	4.10	4.10
3309.97	2.98	10	3.08	10	3.00	3.00
3333.45	65.17	2	65.62	12	65.08	65.08
3347.41	78.95	1	79.18	12	76.56	76.56
3362.79	46.86	3	46.51	11	47.84	47.84
3385.05	53.42	3	54.99	11	53.11	53.11
3399.83	72.50	1	71.88	11	69.00	69.00
3416.59	2.47	10	2.59	10	2.48	2.48
3439.08	11.14	7	12.05	10	13.55	13.55
3469.62	52.55	5	49.22	7	61.04	61.04
3489.28	19.26	6	19.43	10	18.91	18.91
3511.93	45.77	4	47.25	10	46.89	46.89
3518.94	14.14	7	14.12	9	12.78	12.78
3540.32	31.42	6	35.67	10	35.35	35.35
3548.67	81.07	5	79.06	6	85.04	85.04
3565.61	41.13	5	40.13	8	50.81	50.81
3593.94	120.20	1	119.75	11	116.43	116.43
3637.72	60.64	2	61.68	12	60.76	60.76
3652.12	2.53	10	2.50	10	2.42	2.42
3671.15	20.80	5	20.35	10	20.76	20.76

Table 5.4: Radiative kernels (K) for $^{197}\text{Au}+n$ obtained at n_TOF and that ones listed in ENDF/B libraries.

E_R (eV)	TAC		C_6D_6		ENDFVII	ENDFVI
	K (meV)	$\Delta\text{K}/\text{K}$ %	K (meV)	$\Delta\text{K}/\text{K}$ %	K (meV)	K (meV)
3690.41	33.28	5	35.44	10	41.24	41.24
3695.71	3.08	9	3.07	10	2.82	2.82
3708.46	14.62	6	14.55	10	13.92	13.92
3727.64	61.85	2	61.92	12	59.60	59.60
3743.86	15.31	6	15.46	10	17.08	17.08
3759.75	13.96	7	13.95	10	14.82	14.82
3762.41	11.51	8	11.69	10	12.13	12.13
3789.43	1.86	10	1.87	10	1.80	1.80
3807.00	47.75	4	48.93	11	49.32	49.32
3841.25	64.94	2	64.72	12	62.69	62.69
3863.15	11.62	8	13.19	10	14.82	14.82
3871.64	58.80	2	59.40	12	58.58	58.58
3887.73	67.35	1	66.86	12	64.23	64.23
3913.88	81.63	1	81.89	11	77.88	77.88
3939.83	88.80	1	88.43	11	83.87	83.87
3964.44	50.43	4	53.37	11	52.98	52.98
3981.90	89.35	1	89.06	9	82.85	82.85
3986.90	9.81	8	10.44	10	9.77	9.77
3999.35	36.45	5	36.80	10	40.25	40.25
4036.59	71.14	1	71.18	11	67.79	67.79
4046.74	3.46	9	3.47	10	3.47	3.47
4072.94	11.62	8	12.30	10	11.77	11.77
4085.85	81.09	1	81.20	11	77.21	77.21
4126.83	92.51	1	91.66	11	86.29	86.29
4137.26	31.00	3	31.62	12	32.61	32.61
4164.12	36.21	5	37.56	10	37.62	37.62
4170.94	42.96	6	43.29	15	46.50	46.50
4232.92	18.47	8	20.60	10	21.30	21.30
4248.13	63.74	2	64.10	12	61.18	61.18
4273.36	14.95	7	15.43	10	15.33	15.33
4288.88	38.88	5	46.22	11	47.84	47.84
4300.56	64.29	2	64.44	12	61.32	61.32
4315.44	60.86	2	60.39	11	57.23	57.23
4332.35	39.40	5	40.75	10	39.06	39.06

Table 5.4: Radiative kernels (K) for $^{197}\text{Au}+n$ obtained at n_TOF and that ones listed in ENDF/B libraries.

E_R (eV)	TAC		C_6D_6		ENDFVII	ENDFVI
	K (meV)	$\Delta\text{K}/\text{K}$ %	K (meV)	$\Delta\text{K}/\text{K}$ %	K (meV)	K (meV)
4355.62	20.23	8	22.96	17	29.39	29.39
4363.91	48.85	4	50.10	12	47.84	47.84
4388.56	35.29	2	35.56	12	33.91	33.91
4422.21	53.25	6	53.58	8	60.90	60.90
4435.83	28.48	6	29.30	10	33.62	33.62
4455.19	20.58	5	21.07	11	21.10	21.10
4521.16	62.32	2	62.58	12	60.46	60.46
4535.70	37.67	2	37.59	12	35.80	35.80
4541.71	33.10	6	35.55	10	34.98	34.98
4551.79	18.43	6	18.89	10	18.64	18.64
4572.62	64.52	2	65.00	12	61.69	61.69
4589.75	31.46	6	33.24	10	34.60	34.60
4610.86	14.26	7	15.87	10	16.78	16.78
4626.64	5.53	9	5.75	10	6.31	6.31
4665.55	80.35	1	79.73	11	75.51	75.51
4684.01	39.03	5	42.61	10	40.25	40.25
4695.88	19.35	6	19.27	10	18.24	18.24
4712.27	26.78	4	25.90	11	24.66	24.66
4732.44	26.84	6	27.01	10	25.27	25.27
4766.18	29.51	6	30.60	10	32.59	32.59
4780.39	51.18	4	55.67	12	53.89	53.89
4789.28	45.53	4	47.63	11	45.89	45.89
4800.10	12.08	7	12.13	10	11.34	11.34
4828.75	37.01	8	48.77	15	48.77	54.17

5.4.3 Comparison between n_TOF data

The capture kernels, as a function of resonance energy, extracted from the TAC and C_6D_6 data are shown in Figure 5.19. As it can be seen from Figures 5.20, which shows the capture kernel ratios, there is an overall agreement between TAC and C_6D_6 data (both obtained at n_TOF). Event though for some small resonances sizeable discrepancies are present, the mean of the kernel ratio distribution is 1.00 ± 0.05 .

To check for residual systematic effects the kernel ratio between TAC and C_6D_6 was plotted as a function of different variables and shown in Figure 5.21. The kernel

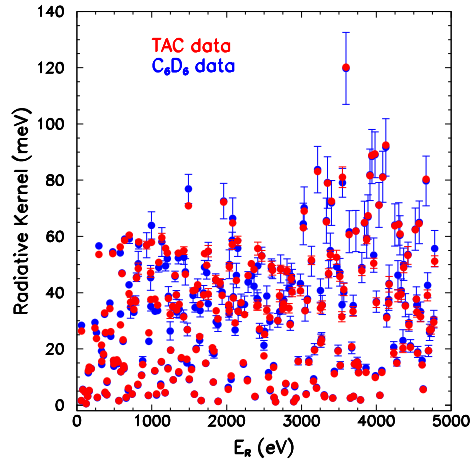


Figure 5.19: Comparison of the capture kernels obtained with TAC data and with C_6D_6 data as a function of resonance energy. Uncertainties from the fit.

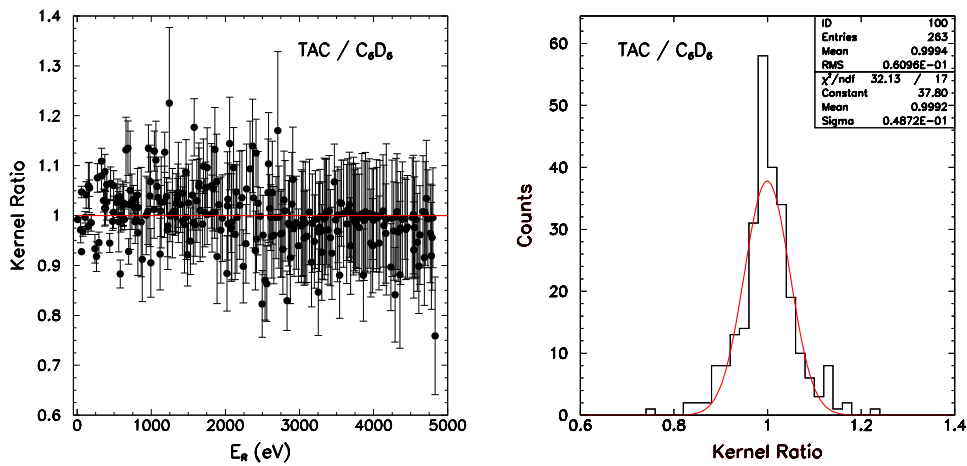


Figure 5.20: Capture kernel ratios, and relative histogram, obtained with TAC and C_6D_6 as a function of resonance energy. Uncertainties from the fit.

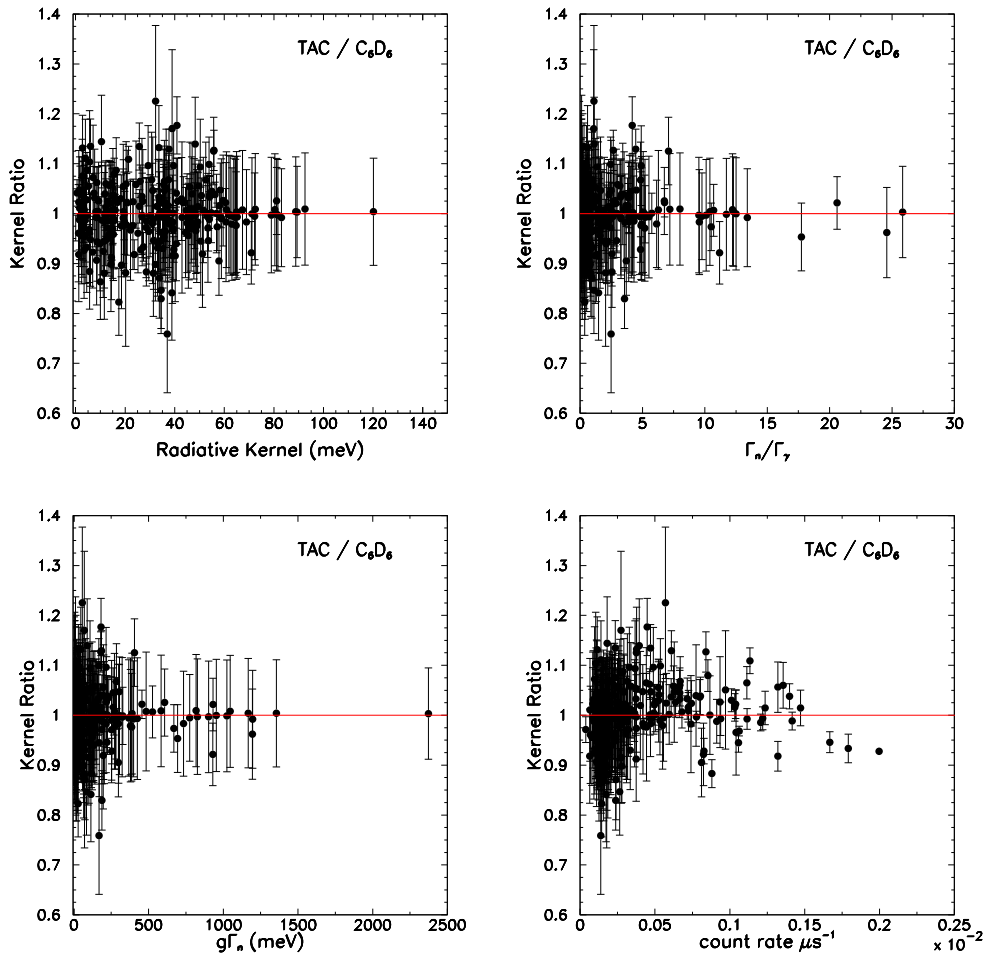


Figure 5.21: Comparison of the capture kernels obtained with TAC and C_6D_6 as a function of: resonance area, Γ_n/Γ_γ ratio, $g\Gamma_n$ and peak resonance counting rate.

ratio confirms the correctness of the following corrections:

- the attenuation of the γ -rays originating in the sample, when the ratio is plotted as a function of the radiative kernel;
- the neutron sensitivity, when the ratio is plotted as a function of Γ_n/Γ_γ ;
- the self absorption term, when the ratio is plotted as a function of $g\Gamma_n$;
- the pile up and dead time, when the ratio is plotted as a function of peak counting rate.

5.4.4 Comparison with libraries

After verifying that both capture detection techniques give consistent results, the capture kernels from the TAC data were compared with previous data. As already mentioned in Section 1.5, evaluations are available in the ENDF/B-VI and ENDF/B-VII libraries, with a 5% discrepancy in average between the two libraries.

As evident from Figure 5.22, the capture kernels measured at n_TOF show a good agreement with the ones calculated from the ENDF/B-VII resonance parameters, with an average difference of 3%. Large discrepancies can however be observed for some resonances, (see for example the resonance at 952 eV in the right panel of Figure 5.23) A careful look revealed that the largest differences are observed for weak resonances, which were probably not accurately measured in the past. In addition,

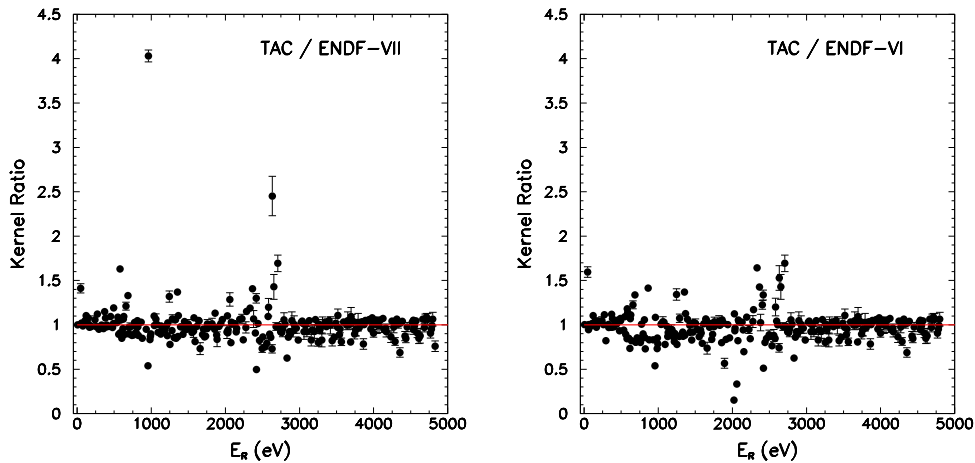


Figure 5.22: Ratio of the area of the resonances measured at n_TOF with the TAC and that listed in ENDF/B-VII (left panel) and that listed in ENDF/B-VI (right panel).

7 resonances have now been clearly resolved, while they were previously considered to be "doubtful" (listed in Table 1.4) and, therefore, only partly included in the ENDF/B-VI and ENDF/B-VII evaluations (see for example Figure 5.23).

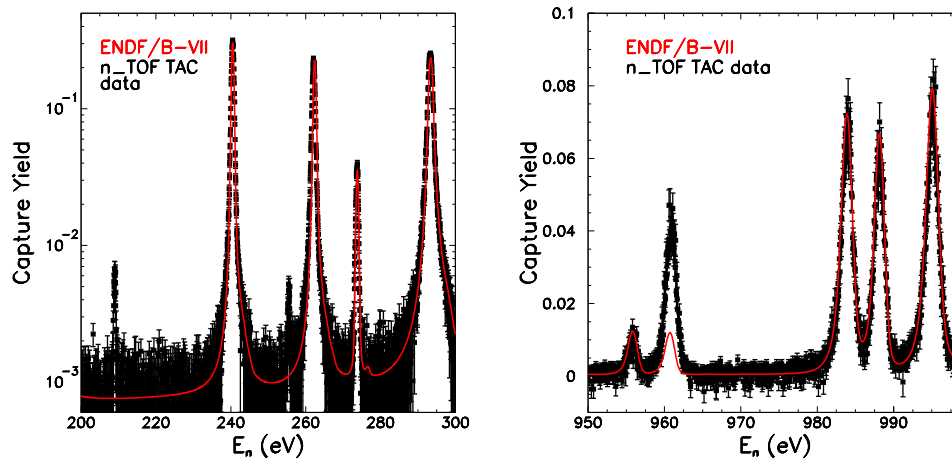


Figure 5.23: Left panel: clearly resolved resonances (at 209.3 and 255.7 eV) from this work, which were only partly considered in previous evaluations. Right panel: huge discrepancies between n_TOF data and ENDF evaluation of resonance at energy 952 eV.

Chapter 6

Measurements at IRMM-GELINA

Transmission, capture and self-indication experiments have been carried out at the neutron time-of-flight facility GELINA of the Institute for Reference Materials and Measurements (IRMM), Geel, Belgium. From a resonance shape analysis of the data, using the R-matrix code REFIT, the parameters for resonances below 200 eV have been determined together with the capture cross section from 10 meV up to the first s-wave resonance at 4.9 eV.

6.1 Introduction

Several Gold samples of different thickness ranging from 5 μm up to 1 mm were employed. The large number of samples guarantees the two conditions pointed out in Chapter 2 of:

- “thin” sample, for capture measurement, for strong resonances;
- “thick” sample, for transmission measurement, for weak resonances;

indeed, in principle, each resonance requires its ideal thickness. Furthermore the use of several samples reduces the uncertainty related to the sample preparation (thickness, homogeneity, contaminations, ...). Moreover we were able to find a good compromise between energy resolution and statistics even for weak resonances. The samples used with their characteristic are listed in Table 6.1. Capture measurements have been carried out at a 12.8, 28, and 60 m (nominal) flight path, while transmission measurements have been performed at the 30 and 50 m (nominal) flight path, both types of measurement with repetition rate of 50 and 800 Hz. Self-indication measurement was carry out at a 28 m flight path, and at 50 Hz operation mode.

Table 6.1: General description of Gold samples measured at GELINA. Uncertainty on areal density is of the order of 0.1%, or less.

Sample name	Thickness		Diameter (mm)	Weight (g)
	nominal (mm)	calculated atoms/barn		
T2	1.10	6.007×10^{-3}	80.00 ± 0.05	98.75 ± 0.05
C2	0.53	3.097×10^{-3}	80.00 ± 0.05	50.920 ± 0.002
TPNP08/16	0.52	3.026×10^{-3}	80.04 ± 0.05	50.9234 ± 0.0005
C1	0.12	6.642×10^{-4}	80.00 ± 0.05	10.9200 ± 0.0005
TPNP08/17	0.11	5.945×10^{-4}	80.06 ± 0.06	9.7685 ± 0.0002
T1	0.11	5.940×10^{-4}	80.00 ± 0.05	9.766 ± 0.002
S1	0.05	2.906×10^{-4}	80.00 ± 0.05	4.777 ± 0.001
TP0736/1	0.01	5.765×10^{-5}	80.02 ± 0.02	0.9483 ± 0.0001
TP0736/2	0.01	5.861×10^{-5}	80.02 ± 0.02	0.9640 ± 0.0001
TP0736/3	0.005	2.772×10^{-5}	80.02 ± 0.04	0.4559 ± 0.0001
squared samples				
TPNP08/14	1.00	5.825×10^{-3}	50.45×50.39	48.4330 ± 0.0005
TPNP08/15	1.00	5.841×10^{-3}	50.42×50.45	48.5957 ± 0.0005
TPNP08/20	1.00	5.905×10^{-3}	50.42×50.45	48.5957 ± 0.0005
FILTER	0.11	5.886×10^{-4}	217×220	91.9 ± 0.1

6.2 Transmission measurements

6.2.1 Experimental conditions

Table 6.2 summarizes the details of the transmission experiments. Transmission measurements have been performed at two different stations with the neutron detectors placed a 26.45 m and 49.34 m distance from the neutron producing target. For these stations the angle between the flight path and the normal to the moderator is 9° . The samples were placed almost halfway between the detector and the neutron producing target in an automatic sample changer which is operated by the data acquisition system. Air-conditioning system was installed at the measurement stations to reduce electronics drifts due to temperature changes and to keep the samples at a constant temperature. The temperature at the sample position was continuously monitored and the average temperature was used in the resonance shape analysis to account for the Doppler broadening of the resonances. Two BF_3 proportional counters were used to monitor the output and stability of the accelerator and to normalise the sample-in and sample-out measurements to the same total neutron fluence. **FP 26.45 m setup.** One setup uses a flight path length of 26.45 m, with the sample position at approximately 10 m. The detector system is a $\frac{1}{2}$ " thick lithium-glass scintillator, with a di-

ameter of 4 inch that is viewed by two photomultiplier tubes (EMI9823QKB), placed perpendicularly to the neutron beam axis. The Al canning was covered with a thin Teflon foil to reflect the light to the entrance window of the photomultiplier. The setup at this flight path is shown in Figure 6.1. To separate a valid neutron event from the photomultiplier noise, a coincidence between the signals of both tubes is required [145].

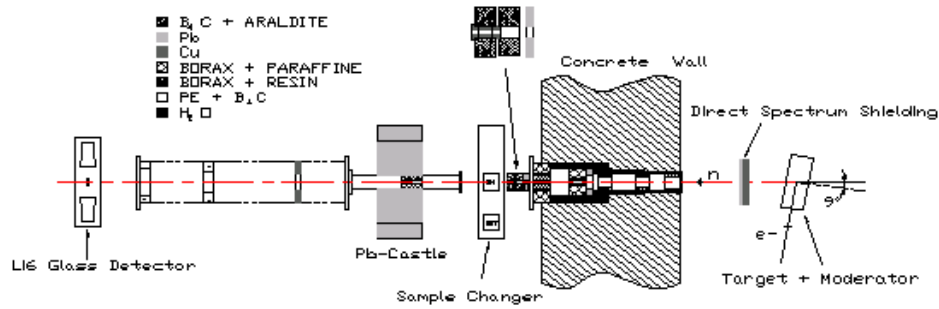


Figure 6.1: A description of a experimental setup for transmission measurements at GELINA (FP 26.45 m). Figure from [145].

FP 49.34 m setup. For the second setup the detector system is stationed at a distance of 49.34 m from the neutron target, the sample position is at 25 m. The detector is a lithium-glass scintillator of $\frac{1}{4}$ " thickness and 4" diameter mounted inside an aluminum sphere, to improve the light collection. Such a design should make the light collection independent of the interaction spot. A pulse-height window selects the alpha-peak of the ${}^6\text{Li}(n,\alpha)$ reaction to distinguish a neutron event from background events. Moreover it has to be noticed that the sample is far from the detector station, to reduce the background [146].

6.2.2 Data reduction

The transmission T_{exp} is obtained from the ratio of the counts of a sample-in measurement C_{in} and a sample-out measurement C_{out} , both corrected for their background contribution B_{in} and B_{out} , respectively:

$$T = N_T \frac{C_{in} - B_{in}}{C_{out} - B_{out}} \quad (6.1)$$

The experimental spectra in Eq. 6.1 are corrected for losses due to the dead time in the detector and the electronics chain. The normalization factor N_T accounts for the

Table 6.2: Transmission measuring sequence at the 26.45 m and at 49.45 m flight paths.

Flight path	Frequency	Sample	filters	
			Overlap	Background
49.34	50Hz	10.0 μm	Cd	Na,Co
49.34	50Hz	20.0 μm	Cd	Na,Co
49.34	50Hz	50.0 μm	Cd	Na,Co
49.34	800Hz	3.0 mm	^{10}B	Na,Co
26.45	50Hz	3.0 mm		Pb, Na, Co, Rh
26.45	400Hz	3.0 mm	^{10}B	Pb, Na, Co, Rh
26.45	800Hz	3.0 mm	^{10}B	Pb, Na, Co, Rh

ratio of the integrated intensities of the incident neutron beam during the out and the in cycles. To avoid systematic uncertainties due to slow variations of the beam profile or detector efficiency as a function of time, the alternating sequences of “in-out” measurements are repeated several times to approach an identical incoming average neutron flux for the “in” and “out” cycles. Such a procedure reduces the uncertainty on the normalization factor N_T to less than 0.5%.

To derive the transmission T_{exp} from the raw TOF spectra the data reduction package AGS (Analysis of Generic TOF Spectra) developed at the IRMM [190] is used. This package includes the most important spectra manipulations, such as: dead time correction, background fitting and subtraction, and normalization. The package includes a full propagation of uncertainties, starting from the uncorrelated uncertainties due to counting statistics [191]. The final transmission, deduced from the raw TOF spectra, includes a complete covariance matrix accounting for both uncorrelated and correlated uncertainty components.

The dead time of the detection chain was monitored continuously by a registration of the time-interval distribution between successive events. From the time interval spectrum a dead time of $\tau_d = 2850 \pm 20$ ns and $\tau_d = 2850 \pm 20$ ns was deduced for the detection set-up at 26 and 50 m, respectively. The dead time corrections for neutron energies below 500 eV was in all cases less than 2%.

The background as a function of TOF was derived by the black resonance technique [192]. To monitor the background level all measurements have been performed with at least one fixed black resonance filter in the beam. The resonance dip due to this filter was used to determine the impact of the sample on the background level for a sample-in measurement. The background over the time range of interest was determined by an analytical expression:

$$B(t) = A_0 + A_1 e^{-\frac{t}{\tau}} + A_2 t^{-\alpha} \quad (6.2)$$

or as a series of 2-3 exponentials, depending on the energy region and thus the filters used.

The parameters were adjusted to the dips observed in the TOF spectrum resulting from measurements with black resonance filters. The black resonance filters used for the different measurement campaigns are listed in Table 6.2. The second term in the analytical expression represents the background due to the 2.2 MeV γ -rays resulting from the $H(n, \gamma)$ reaction in the moderator. Since the energy deposited in a lithium-glass detector is comparable to the energy released by a neutron event, this background component can not be suppressed by pulse-height discrimination. The background contribution due to the 2.2 MeV γ -rays can be represented by an exponential decay with a decay time of about 25 μ s. The decay time is related to the moderation process and was verified by Monte Carlo simulations [193]. The last term in Eq. 6.2 accounts for the contribution of scattered neutrons.

An example of such an evaluation of the background for TOF transmission measurements is shown in Figure 6.2. The results in Figure 6.2 have been obtained from measurements at the 50 m flight path with a 10 μ m thick Au disc as a transmission sample. The dips at about 70 μ s and 300 μ s are due to the 2.8 keV and 132 eV black resonance of Na and Co, respectively. The reduction in count rate above 7000 μ s results from the Cd-overlap filter. Other background points, which have been used to adjust the parameters in the analytical expression, resulted from additional measurements with a S, Bi and Au black resonance filter. The background level at the 4.9 eV resonance for ^{197}Au in case of a sample-in is about 10% while for the sample-out measurement the background is less than 1%.

6.2.3 Results

From a resonance shape analysis of the experimental observed transmission T_{exp} the resonance energy E_n and $g\Gamma_n$ values for 12 resonances below 200 eV have been deduced. From the pattern due to the interference between resonance and potential scattering observed in the transmission through the 3.0 mm thick sample the resonances at 4.90, 60.28, 78.51, 107.05, 151.40, 163.08 and 190.06 have been identified as s-wave resonances. The results of the transmission measurements at the 26.5 m flight path with the 3.0 mm thick sample are shown in Figure 6.3. The interference pattern characterizing an s-wave resonance is illustrated in Figure 6.4 by comparing the expected transmission for an s- and a p-wave 60.3 eV resonance through a 3-mm thick gold disc.

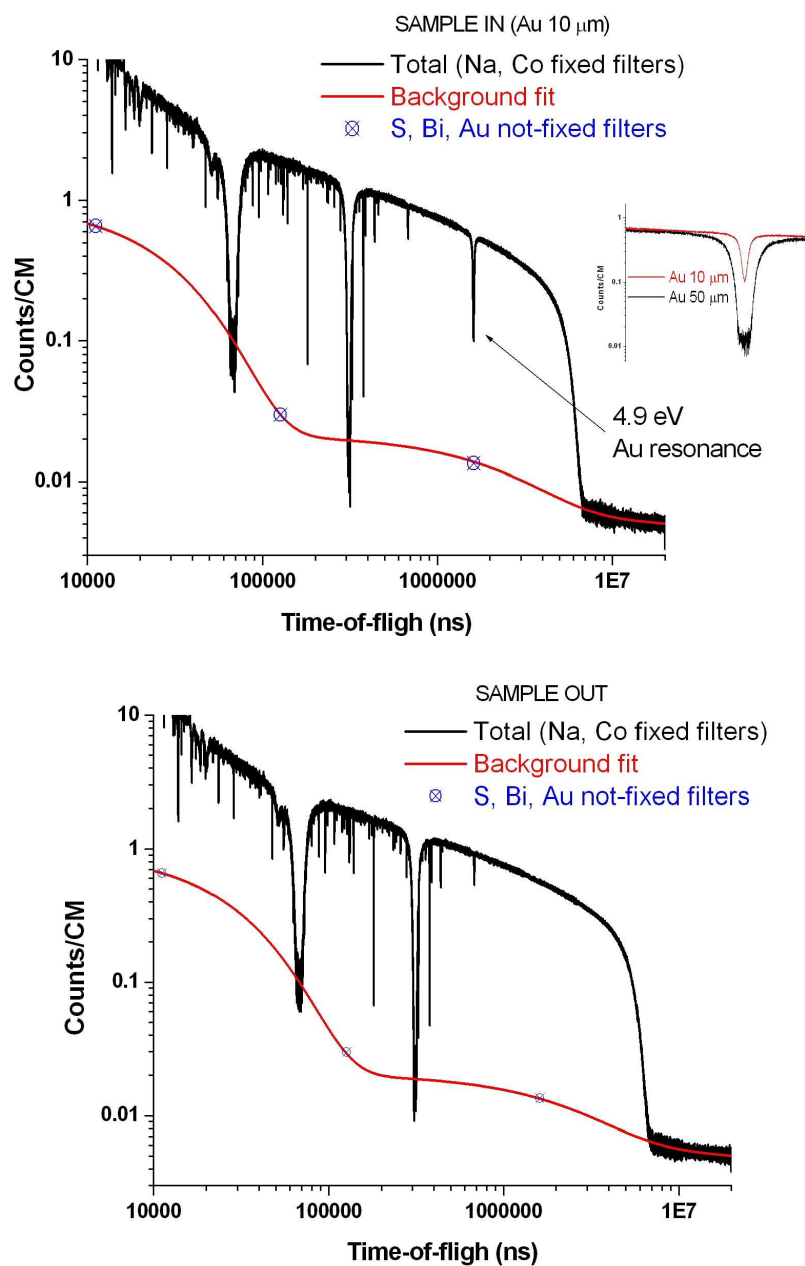


Figure 6.2: The sample in and sample out time-of-flight spectra together with their fitted background.

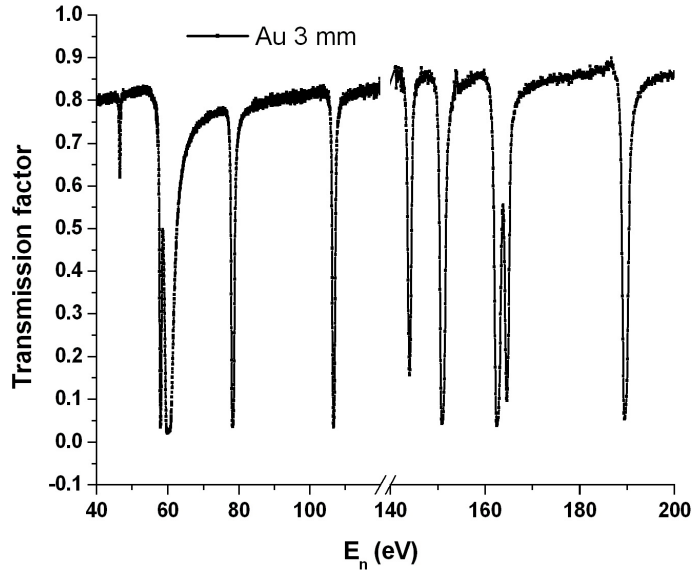


Figure 6.3: The transmission factor of the 1.75×10^{-2} atoms/barn thick sample measured at the 26.45 m flight path. The interference between the potential scattering and the resonance term can be easily identified, for example at the 190 eV resonance. The missing region is due to the presence of the Co black resonance.

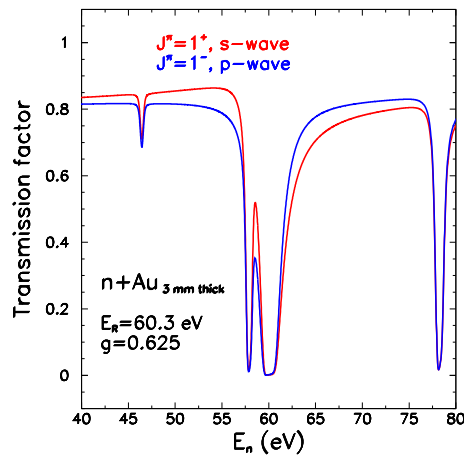


Figure 6.4: A comparison of the calculated transmission factor (broadened for experimental resolution) for a 3 mm Au sample. Red curve: the 60.3 eV resonance is a *s-wave*. Blue curve: the 60.3 eV resonance is a *p-wave*.

6.3 Capture measurements

6.3.1 Experimental conditions

Capture measurements have been performed at three measurement stations with nominal flight path distance 12 m, 30 m and 60 m. Details about the experimental conditions are summarized in Table 6.3. An air-conditioning system was installed in the measurement stations to keep the sample at a constant temperature and to avoid electronic drifts due to temperature changes. The moderated neutron beam was collimated to about 75 mm in diameter at the sample position for each measurement station. The detection set-up, i.e. γ -ray detectors, neutron flux detector, electronics and data acquisition system, at the three measurement stations are very similar (Figure 6.5 shows a description of the 60 m FP setup). A block diagram of the analog electronics used for the capture and flux detection system at the 60 m station is given in Figure 6.6. To reduce dead time effects, separate electronics and data acquisition systems for the flux and capture measurements have been used.

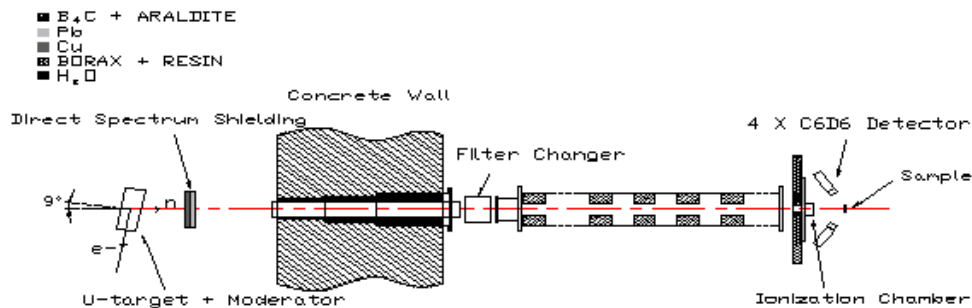


Figure 6.5: A description of the experimental setup for capture measurements at GELINA (FP at 60 m). Figure from [145].

The detection systems consisted of a set of C₆D₆ detectors with each detector positioned at an angle of 125° with respect to the direction of the neutron beam. Each scintillator was coupled to EMI9823-KQB photomultipliers (PMT) through a quartz window, reducing the neutron sensitivity of the detectors as much as possible. For each detector the anode signal of the PMT is used to determine the time arrival of the neutron creating the capture event and the signal of the 9th dynode to provide information about the energy deposited by the detected γ -ray. Both signals have been processed by conventional NIM electronics as shown in Figure 6.6. The discrimination level of the capture detection system at 12m, 30m, and 60m corresponded to 200

Table 6.3: Capture measuring sequence at the 12.8, 28 and 60 m FP. A compromise to cover the energy range of interest with good energy resolution and statistic was found with these combinations.

	Sample	Overlap	filters Background
FP5-12m 50 Hz 4 C ₆ D ₆ "pyramid"	T2 - 1.0 mm		Co, Bi, Na
	C2 - 0.5 mm		Co, Bi, Na
	C2 - 0.5 mm		W, Co, Bi, Na
	C2 - 0.5 mm		Ag, W, Co, Bi, Na
	C2 - 0.5 mm	Cd	Co, Bi, Na
	C1 - 0.1 mm		Co, Bi, Na
	S1 - 0.05 mm		Co, Bi, Na
	N2 - 0.01 mm		Co, Bi, Na
	N3 - 0.005 mm		Co, Bi, Na
FP5-12m 50 Hz 2 C ₆ D ₆ "cylinder"	C2-0.5mm		Co, Bi, Na
	C2-0.5mm	Cd	Co, Bi, Na
FP15-30m 50 Hz 2 C ₆ D ₆ "cylinder"	T2 - 1.0 mm	Cd	Na,Pb
	C2 - 0.5 mm	Cd	Na,Pb
	C2 - 0.5 mm	Cd	W, Co, Na, Pb
	C1 - 0.1 mm	Cd	Na,Pb
	N17 - 0.1 mm	Cd	Na,Pb
	S1 - 0.05 mm	Cd	Na,Pb
	N2 - 0.01 mm	Cd	Na,Pb
	N3 - 0.005 mm	Cd	Na,Pb
FP15-30m 800 Hz 2 C ₆ D ₆ "cylinder"	T2 - 1.0 mm	¹⁰ B	Pb, Al
	C2 - 0.5 mm	¹⁰ B	Pb, Al
	T1 - 0.1 mm	¹⁰ B	Pb, Al
	T1 - 0.1 mm	¹⁰ B	Pb, Al, S
	T1 - 0.1 mm	¹⁰ B	Pb, Al, Na
FP14-60m 800 Hz 4 C ₆ D ₆ "cylinder"	C1 - 0.1 mm	Cd	Co, Na

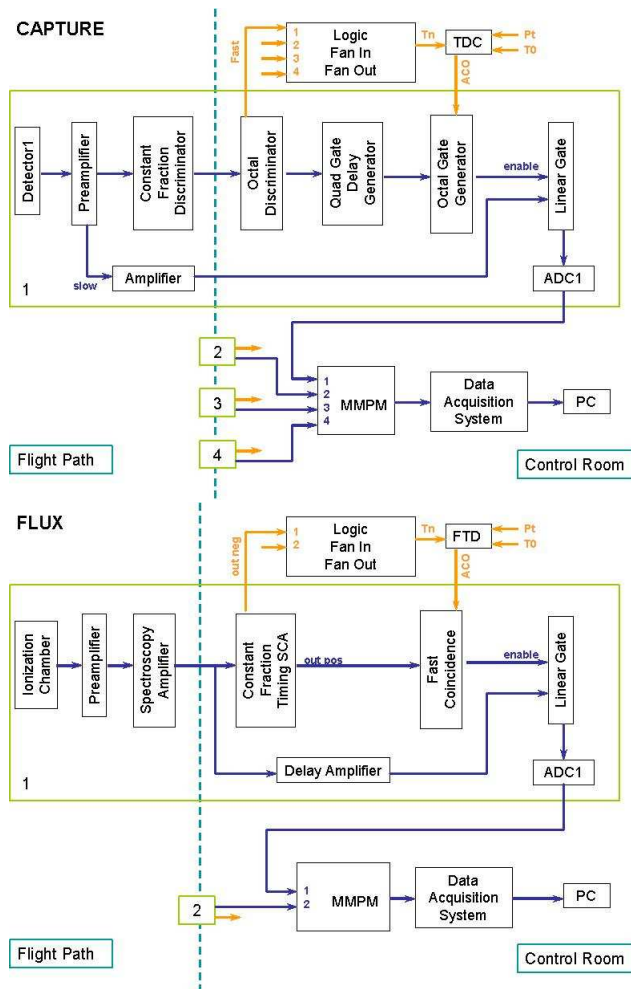


Figure 6.6: Block diagram of the electronic used for Au measurement at both flight paths.

keV, 150 keV and 150 keV deposited energy, respectively.

The shape of the neutron spectrum at each station was continuously measured with ^{10}B Frisch gridded ionization chambers placed about 80 cm before the capture sample. At the 12 m and 30 m station a double chamber was used with a cathode loaded with two back-to-back layers of about $40 \mu\text{g}/\text{cm}^2$ ^{10}B each. The ^{10}B layers were evaporated on a 30- μm -thick Aluminum backing. The chamber at the 60 m station consisted of three back-to-back layers of $40 \mu\text{g}/\text{cm}^2$ ^{10}B evaporated on an Aluminum backing. The chambers were operated with a continuous flow of a mixture of argon (90%) and methane (10%) at atmospheric pressure. The analog electronics used to obtain the time and amplitude signal are shown in Figure 6.6. Both the time and amplitude signal are obtained from the bipolar output pulse of the spectroscopic amplifier.

The TOF of a neutron (or a captured gamma) was determined by the time between the start signal, given at each electron burst, and the stop signal either from the capture detectors or from the ^{10}B -chamber. This time was measured with a Fast Time Coder with a 0.5 ns resolution, designed at the IRMM [195]. The TOF and the pulse height of the detected events were recorded in list mode using a data acquisition system developed at the IRMM [194]. The list mode recording allowed a continuous stability check of the detection systems and an off-line application of the weighting function. The stability of both the detection systems and the accelerator operating conditions (i.e. frequency, current and neutron output) were verified in cycles of 1 hour. The linearity and resolution of the C_6D_6 detectors was monitored weekly by measurements of the 2.6 MeV γ -ray from the ^{232}Th decay chain.

6.3.2 Data reduction

The pulse-height weighting technique was applied to the output pulses from the capture detection systems in order to make the detection efficiency proportional only to the total emitted γ -ray energy. Three different types of C_6D_6 detectors have been used. For each measurement set-up weighting functions have been calculated by Monte Carlo simulations with a geometry input file reflecting as much as possible the measurement conditions. The weighting functions have been calculated for a threshold reflecting the lower discriminator level of the observed pulse height spectrum.

The list mode data are processed off-line. To convert the list mode data into an experimental yield, the weighting function is applied and the flux and weighted capture time-of-flight spectra are corrected for dead time and background. The procedure is divided in two steps. In a first step the list mode data is processed by the AGL (Analysis of Geel List mode data) package [196]. This package is used to reject inconsistent measurement cycles due to instabilities of accelerator conditions, detection chain or measurement conditions in other flight paths. This selection is based

on a statistical analysis of the central monitor counts together with the counts of the individual detectors. The AGL is also used to correct for small drifts in the detections chains. These corrections for drifts are based on an analysis of the amplitude spectra. After converting the amplitude into a deposited energy and rejecting events with a deposited energy deposition lower than the discriminator level, the weighting function is applied. To reduce bias effects due to the detection of coincident events, the amplitude of only one C_6D_6 detector is selected randomly in case more than one γ -ray out of the cascade was detected.

Finally the data are compressed into time-of-flight spectra for further data reduction with the AGS package. This AGS package is used to perform dead time corrections and background subtraction on the weighted capture counts and on the counts resulting from the flux measurement. The final step is the calculation of the experimental yield:

$$Y_{exp} = N(C_{cw} - B_{cw}) \frac{Y_{\varphi}}{C_{\varphi} - B_{\varphi}} \quad (6.3)$$

together with the full covariance matrix. The dead time corrected tof-spectrum of the weighted counts (or counting rates) is denoted by C_{cw} and the background contribution by B_{cw} . The TOF-spectrum resulting from the flux measurements is C_{φ} and the background contribution is B_{φ} . Y_{φ} is the calculated theoretical yield for the flux measurement (see Eq. 4.10-4.14). The AGS package includes a procedure to account for the difference in flight path length between the capture and flux set up and to project the shape of the neutron flux determined at the flux station to the conditions of the capture set-up.

For the flux measurements the dead time was about $3.5 \mu s$ resulting in a maximum dead time correction of 1%. The dead time for the capture systems was about $2.8 \mu s$ (as shown in Figure 6.7). For measurements at 60 m the corrections were less than 1%. At the 30 m station the maximum correction was about 5%. For the measurements at 12 m with the 2 cylindrical C_6D_6 detectors the maximum correction was 20%. When the high efficiency system consisting of 4 pyramid detectors was used at 12 m dead time corrections higher than 50% were observed. To reduce systematic bias effect due to the dead time only the parts of the time-of-flight spectra with a dead time correction less than 20% were considered for the data analysis.

The background for the capture measurements consists of two components, one time (i. e. time-of-flight) independent and the other time dependent. For a stable nuclide, such as ^{197}Au , the time independent component results mainly from the ambient background. The time dependent background is simply the open beam (the measurement with only the sample holder). As a proof the $^{208}Pb+n$ and open beam measurements were carried out. In Figure 6.8 we give an example for the capture measurements at the 12.8 m FP. $^{208}Pb+n$ has been measured to estimate the background of scattered neutrons as well as the background induced by the γ -rays trav-

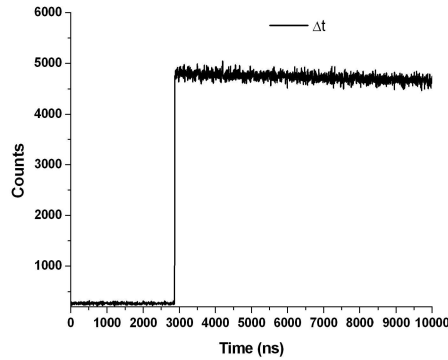


Figure 6.7: Interval time distribution for an Au capture measurements.

elling in the beam with neutrons. As can be seen from the figure the yield of $^{208}\text{Pb}+n$ and open beam measurement are very close. This result make us confident in the minimization of the background. Therefore the background-free Au capture yield ($C_{Au,NET}$), as pointed out in Eq. 5.1, is obtained subtracting bin by bin the net open beam spectra and the ambient background spectra to the Au spectra. this simple subtraction of tof spectra can be done after the normalization to the central monitors.

In Figure 6.9 a TOF spectrum obtained with the ^{10}B ionization chamber is shown together with the calculated background. Like in the transmission runs, the background for the flux measurements was derived from the saturated resonance dips formed by black resonances (of Na, Bi and Co filters in this case). Again, to minimize the influence of the filters on the TOF spectra, the background level was determined with few fixed filters and checked from separate measurements introducing additional non-fixed filter (W and Ag). Moreover when the measurement at 12.8 m is carried out without Cd anti-overlapping filter the neutron background at low energies (below the energy of the black resonance of Ag at 5.2 eV) has to be estimated with a Monte Carlo simulation. In this way the background point at 2×10^7 ns in Figure 6.9 has been determined.

The full propagation of uncertainties, starting from the uncorrelated uncertainties due to counting statistics were performed thanks to AGS code.

6.3.3 Normalization

The saturated resonance technique has been used to normalise the experimental capture yields. Even though the normalization does not change, the correction due to the γ -ray attenuation in the sample modifies the calculated capture yield, in particular for thickness greater than 0.1 mm, as already explained in the Section 4.4 (see Eq. 4.29). Therefore we used REFIT, that allows us to correct the calculated capture

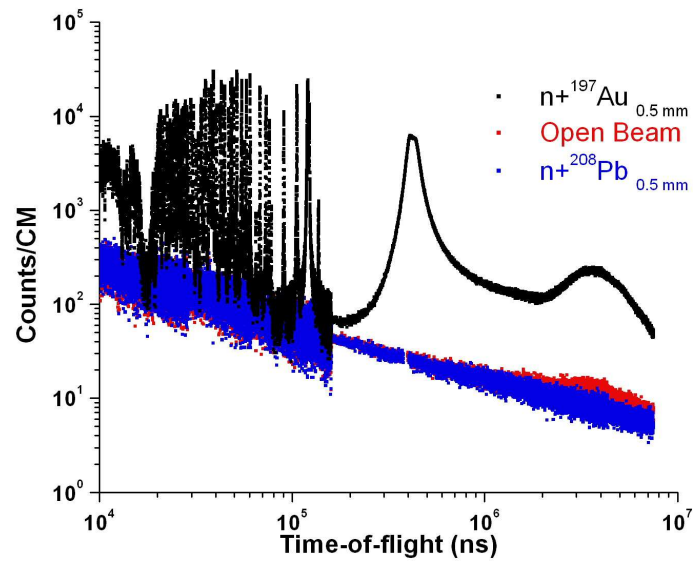


Figure 6.8: Time-of-flight spectra obtained at the GELINA 12.8 m FP, together with the open beam and lead measurement.

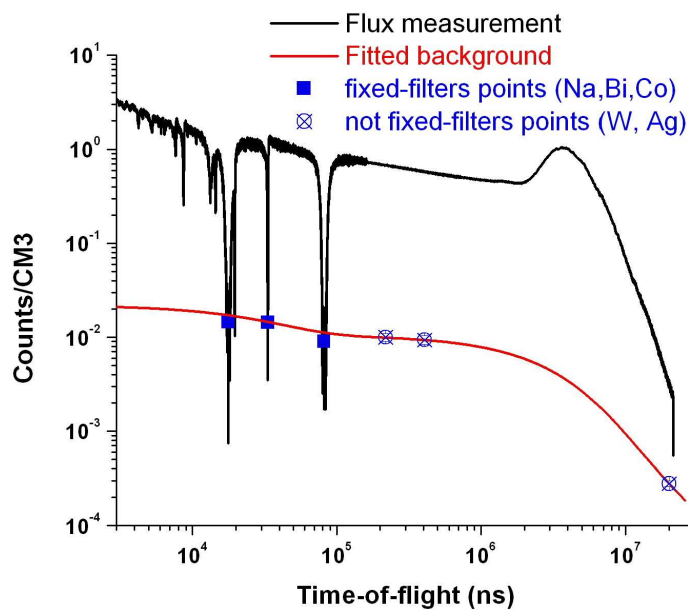


Figure 6.9: Time-of-flight spectra from the ^{10}B for the flux measurements together with the background contribution, resulting from a fit through the black resonance points. The point at 2×10^7 ns has been estimated with Monte Carlo calculations.

yield for this effect, to derive the normalization (and calculate the capture yield, see for example the comparison between GELINA data with ENDF evaluation in Figure 6.11).

The procedure for the correction is the following: the experimental yield is deduced using the weighting function for a homogeneous distribution of the γ -rays in the sample and then, during the resonance shape analysis a correction factor K_c , depending on the resonance strength ($g\Gamma_n$), is applied to the calculated Y_c . Indeed it can not be applied to the experimental yield since the yield due to the neutron sensitivity is not affected by this phenomenon (we recall that $Y = \varepsilon_c Y_c + \varepsilon_n Y_n$), therefore the correction factor K_c needs to be applied on the calculated capture yield.

The correction factor as a function of $n\sigma_{tot}$ is show in Figure 6.10. This correction

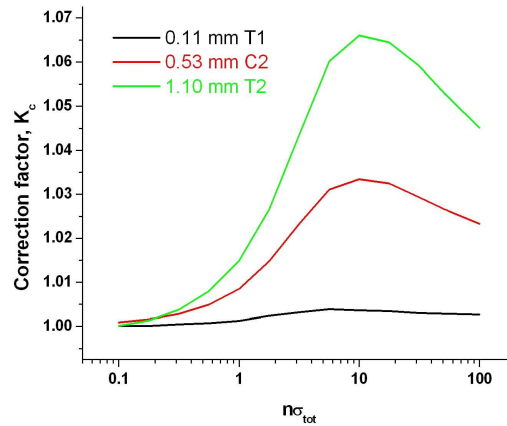


Figure 6.10: The correction factor K_c as a function of the product of the target thickness and the total cross-section, for the capture set-up at the 12.8 m FP with 4 pyramid C_6D_6 .

K_c , calculated by means of MC simulations, depends not only on the target thickness but also on the detector characteristics, geometry, surrounding materials. It has to be noted that it depends on the detector threshold as well, in particular it tends to vanish for detector threshold close to 0.

6.3.4 Results

As already discussed the measurement of the capture yield at thermal energy by means of the time-of-flight technique needs short flight path, because of the gravity. Moreover a high neutron flux is necessary when measuring the capture yield in this region (because of the low cross-section). Therefore we have performed the measurement at the 12.8 m flight path and operating mode of 50 Hz (without anti-overlapping

filter). These conditions allow for the measurement of the capture yield down to the thermal energy. This measurement is very important because it represents an accurate check for the measurement itself. Indeed the cross-section at thermal point is known with 0.1% uncertainty and it is considered as a standard of measure because of its absolute determination. As can be seen from Figure 6.11 we were able to reproduce this point within 1%, when the normalization was obtained from the saturated 4.9 eV resonance. Since several effects, such as the deadtime correction¹, the weighting function, the background, ... have been taken into account in the analysis, this result make us confident on our measurement since it is a further check on the overall procedure.

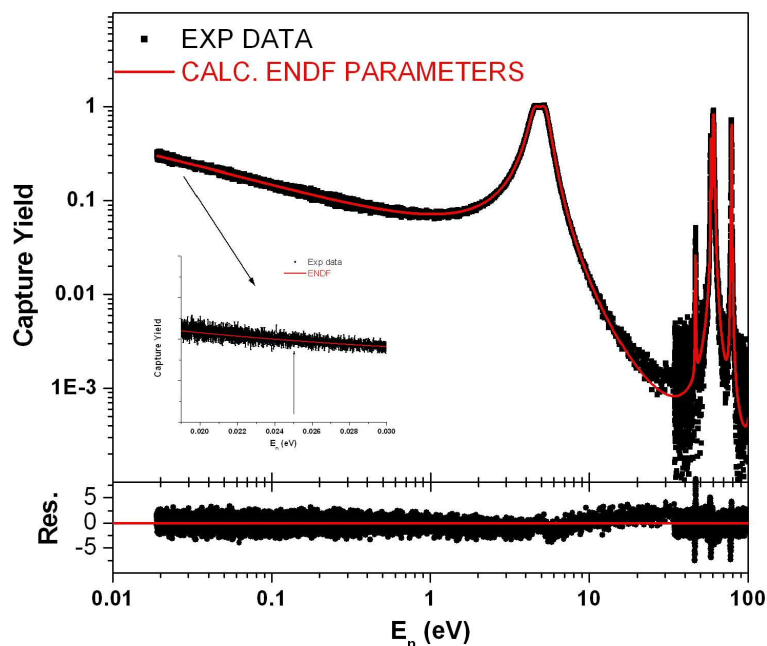


Figure 6.11: The capture yield obtained at the 12.8 m FP with the 2 cylindrical C_6D_6 together with the calculation starting from the ENDF/B-VII parameters. The agreement is within 1%.

Several capture yields have been measured in the resonance region. Indeed to analyze resonances with a proper $n\sigma_{tot}$ value, capture measurements on samples with different thicknesses are required. In the Figure 6.12 the capture yield obtained with a thin (0.05 mm thick) and a thick (1.0 mm thick) Au sample are shown, together with the capture yield normalized to the areal density of the sample. In this last graph it is more evident the effect of the self-shielding term and that of the multiple scattering, it

¹We have studied in detail the different approaches to the dead-time correction, and how accurately they can correct the experimental data. These tests were done with simulated spectra as well as with spectra that were taken with dead-times ranging from 300 ns to 4 μ s. The results is that correction factors (up to a factor of two) have an accuracy better than one percent [119].

results that such corrections are negligible (thus the approximation $Y_c \approx n\sigma_\gamma$ is valid) only for very weak resonances.

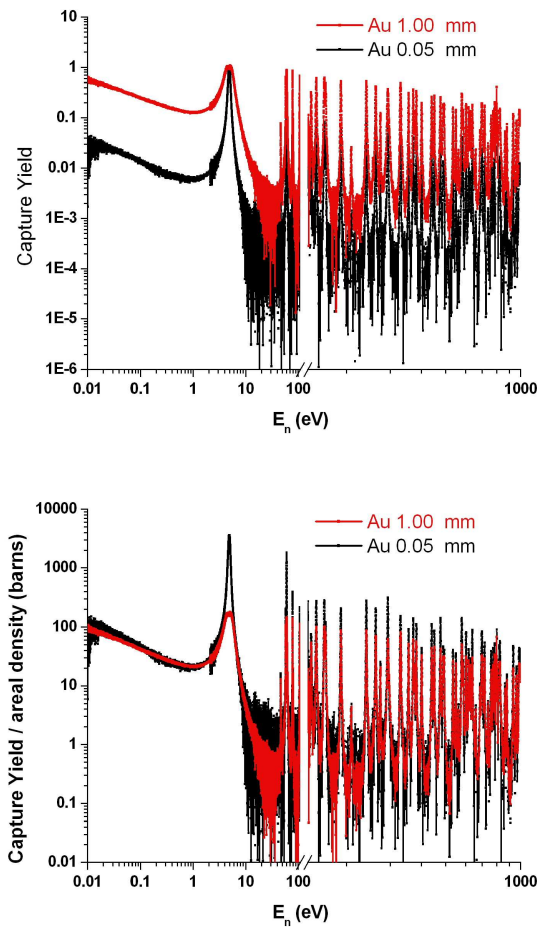


Figure 6.12: The capture yield obtained with a 1 mm thick sample and with a 0.05 mm thick sample, and the same capture yields divided for the areal density of the sample.

As already pointed out in the last section of Chapter 3, the energy resolution plays an important role in the measurement. Therefore depending on the natural width of a resonance different flight path have to be used. As a general rule we have used capture data to extract the resonance parameters in this way: from the 12.8 m FP for energies below 100 eV, and from the 28 m FP for energies up to 200 eV.

6.4 Self-indication measurement

6.4.1 Experimental conditions

This measurement has been carry out at the 28 m FP, usually employed for capture measurements. This section, indeed, could be included in that of capture setup since the electronic and the detectors are the same, and thus the steps of the data reduction. We have just to add the dimension of the the Gold filter placed at the beginning of the neutron beam pipe, far from the measurement station. It was a squared filter 21.7 cm \times 22.0 cm, with a thickness of $n_t = 5.886 \times 10^{-4}$ atoms/barn (nominal thickness 0.11 mm). The thickness of the Gold sample was similar: $n_c = 5.945 \times 10^{-4}$ atoms/barn (nominal thickness 0.11 mm). This combination of sample and filter thicknesses has been chosen for the 4.9 eV resonance.

To determine the self indication ratio, a capture measurement in the same conditions, i. e. the same measurement with the Gold filter removed from the neutron beam line, is needed. Indeed, it is required to extract the self indication yield, moreover it provides the normalization to the measurement. Obviously the anti-overlapping filters as well as the fixed background filters are the same during both measurements. A Cd, Na and Au filters configuration was employed.

6.4.2 Data reduction

The results of the data reduction of the C_6D_6 data are shown in Figure 6.13. It is evident the presence of the Au filter, indeed at the TOF corresponding to 4.9 eV a dip is present. Since the 4.9 Au resonance is saturated, the background identification at the resonance position is clear (as shown in Figure 6.13).

Concerning the flux measurement, there is a small difference to the procedure we have illustrated before (in the Section 6.3.2). Indeed the flux obtained without the Au filter in the beam is used for the self-indication yield. However the flux measurement during the self-indication measurement provides an additional background point, that one of the 4.9 eV resonance. Indeed as can be seen from Figure 6.14 a dip, due to presence of the Au filter in the beam, is observed. This point is of great importance in the determination of the shape of the background (it is the only reference between Na and Cd). It follows that at the position of a saturated resonance the identification of the background is straightforward for the flux as well.

6.4.3 Results

From a resonance shape analysis of the experimental observed self-indication, the (statistical factors, or equivalently) spins of the strong resonances have been assigned,

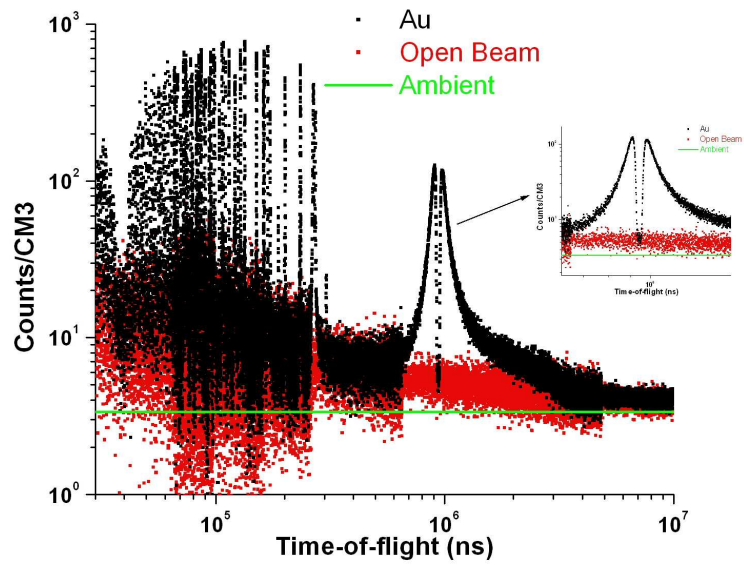


Figure 6.13: Time-of-flight spectra obtained at the GELINA 28 m FP, together with the open beam measurement and the ambient background fit.

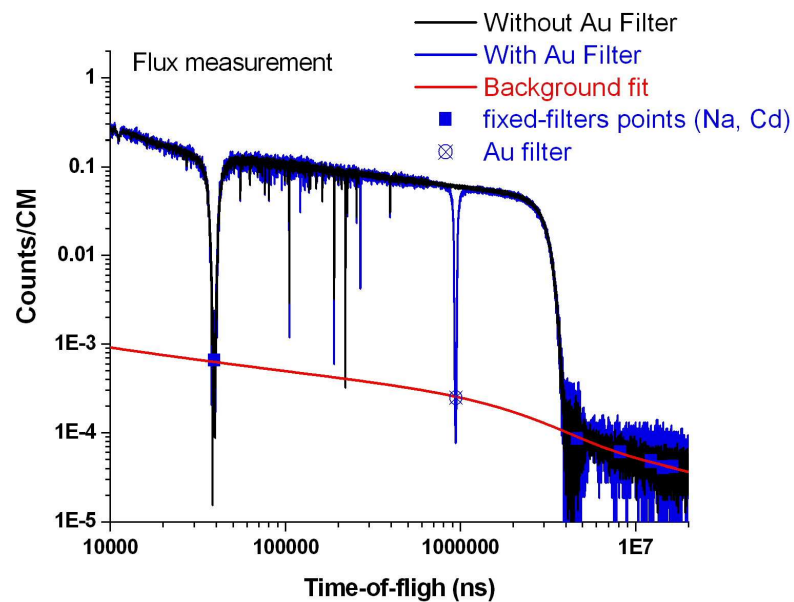


Figure 6.14: Flux measurements at the GELINA 28 m FP with and without the Au filter in the beam. The background contribution, resulting from a fit through the black resonance points is also reported.

and in particular, the spin of the 4.9 eV. As can be seen from Figure 6.15 the normalization is given by the capture measurement, by means of the saturated resonance technique, as usual.

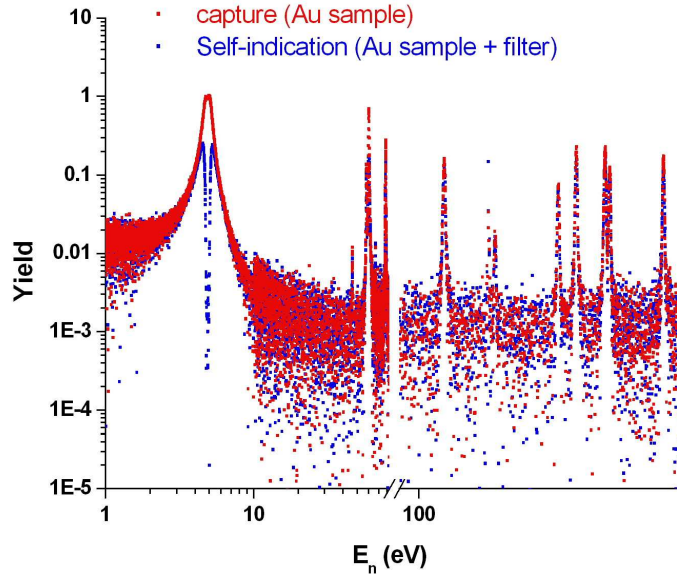


Figure 6.15: The capture yield (i. e. the yield obtained without the Au filter in the beam) and the self-indication ratio (i. e. the yield obtained with the Au filter in the beam) obtained at the 28 m FP with operation mode of 50 Hz.

6.5 Resonance shape analysis of the experimental data

This analysis has been performed from the thermal region up to 200 eV. The REFIT code was used to calculate resonance parameters performing a simultaneous fit of several data sets. Since each resonance requires a different combination of measurements, we choose to employ 4 or 5 data sets: the transmission factor obtained with a thin and a thick sample, the capture yield of a thin sample (extracted at the 28 m and/or at 12.8 m FP, depending on the best compromise between statistics and resolution) and the self-indication measurement. As a further general rule we avoided data sets when the dead time correction was greater than 20% and data sets with several filters (cycles with fixed and not fixed filters).

The time-energy calibration was derived from the measurement of the transmission factor of ^{238}U , since the energy of its resonance at 6.673 ± 0.001 eV is a standard of measurement [1]. This measurement fixed the flight path to 49.3445 ± 0.0006 m. The flight path of the other measurement stations were then adjusted to reproduce the

Au resonance energy obtained with the transmission measurement, thus having self consistence between the data sets.

6.5.1 The new resonance parameters up to 200 eV

The fitted parameters are the energy of the resonance and the partial reaction widths: Γ_γ and Γ_n . The statistical spin factor and, when possible, the parity of the resonance have been determined with the "evaluation of the χ^2 " method. When this last method was sensitive, the total angular momentum J and the angular momentum ℓ have been deduced.

The "evaluation of the χ^2 " technique consists in repeating the fit to the same resonance as many times as the number of the statistical spin factor values allowed (in this case 4, see Table 2.1), determining which g produces the lower χ^2 . The goodness of this method was particularly enhanced by the self-indication measurement, indeed the larger variation on χ^2 values have been observed in this data set. Moreover, when possible, the transmission factor of the 3 mm Au sample (the thickest one measured) helped to assign the parity of the levels. To this end, two additional fit were required to remove the degeneration of the levels with total angular momentum $J=1$ or $J=2$. Indeed both s- and p-wave can form a level of the $^{198}\text{Au}^*$ nucleus with $g=3/8$ and $g=5/8$.

The results are given in Table 6.4, quoted uncertainties on Γ_γ and Γ_n result from the fitting procedure. When it was not possible to assign the statistical spin factor g , we used the one listed in ENDF/B-VII library.

Figure 6.16 shows the values of the radiative widths as a function of the energy. We calculated the average Γ_γ and the weighted average of Γ_γ , obtaining: $\langle \Gamma_\gamma \rangle = 126 \pm 10$ and $\langle \Gamma_\gamma \rangle_W = 121.47 \pm 0.04$ respectively.

In the next section we describe in detail the result obtained for the first Au resonance. The procedure adopted is that we have just explained, and constitute the main example for χ^2 evaluation technique. However it has been carried out only for s-wave ($J=1$ and $J=2$), since it was clearly an s-wave resonance.

6.5.2 The adjusted parameters of the first 4.9 eV resonance

A section dedicated to the first 4.9 eV resonance is justified by the widely use of this Au resonance in the nuclear field. It is often quoted as a well known resonance and it is employed for normalization purpose in neutron facilities. Since its capture cross-section is very high, it is often saturated (a 30 μm thick sample starts to show the saturated behaviour at ambient temperature). As a consequence of this high cross-section, the reaction widths are not simple to measure, because very thin samples are needed. In the literature its resonance parameters are quoted (by Mughabghab [51])

Table 6.4: The new Au resonance parameters up to 200 eV. The uncertainties come from the fit. When the spin assignment was uncertain the value was taken from ENDF/B-VII.

Energy (eV)	fitted quantities		evaluation of the χ^2		remarks
	Γ_γ (meV)	$g\Gamma_n$ (meV)	ℓ	g	
4.8991 ± 0.0002	122.6 ± 0.2	$5/8 \times (14.99 \pm 0.02)$	0	5/8	$J = 2^+$
46.478 ± 0.003	115.0 ± 10	0.0776 ± 0.0004			^a
58.072 ± 0.003	124 ± 4	$3/8 \times (4.24 \pm 0.04)$	0	3/8	$J = 1^+$
60.284 ± 0.002	110.1 ± 0.6	$5/8 \times (71.34 \pm 0.3)$	0	5/8	$J = 2^+$
78.508 ± 0.002	122 ± 3	$3/8 \times (16.36 \pm 0.2)$	0	3/8	$J = 1^+$
107.051 ± 0.003	127 ± 3	$5/8 \times (7.63 \pm 0.09)$	0	5/8	$J = 2^+$
122.334 ± 0.003		0.488 ± 0.013			^b
144.425 ± 0.003	150 ± 4	3.31 ± 0.04			^c
151.402 ± 0.003	125 ± 3	$5/8 \times (22.3 \pm 0.4)$	0	5/8	$J = 2^+$
163.080 ± 0.003	110 ± 3	$3/8 \times (55 \pm 1)$	0	3/8	$J = 1^+$
165.084 ± 0.004	136 ± 6	$5/8 \times (8.8 \pm 0.9)$	0	5/8	$J = 2^+$
190.062 ± 0.002	141 ± 4	$3/8 \times (43.74 \pm 0.8)$	0	3/8	$J = 1^+$

^aSame χ^2 for each J^p combination.

^b Γ_γ and J^p values from ENDF/B-VII.

^cSame χ^2 for $J = 1^+$ and $J = 1^-$.

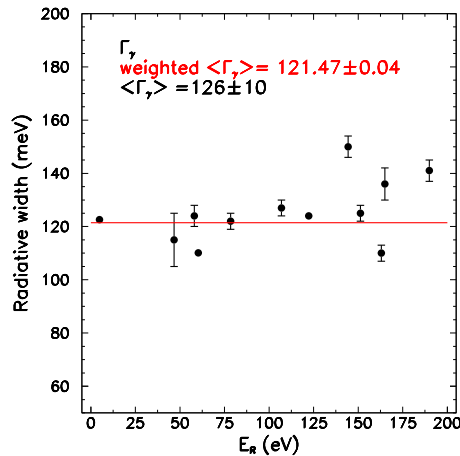


Figure 6.16: The values of the radiative width, from the present analysis, as a function of the resonance energy. The average Γ_γ and the weighted average of Γ_γ are also reported.

with less than 3% uncertainties².

The tail at low energy of this resonance is responsible of the 95% of the capture cross-section at thermal energy, and its resonance parameters are linked to the negative resonances (i. e. with excitation energy below the neutron separation energy) added to reproduce the measured thermal cross-section and to the potential scattering length³ (or radius) R' . Table 6.5 explains how this region is described in the two neutron data libraries.

Table 6.5: The resonance parameters of the 4.9 eV resonance, data from neutron libraries.

	Energy (eV)	Γ_n (meV)	Γ_γ (meV)	Γ (meV)	Radius (fm)	negative resonances
ENDF/B-VI	4.906	15.2	122.5	137.7	7.868	1
ENDF/B-VII	4.89	15.2	124.0	139.2	9.658	2

A series of capture and transmission measurements with very thin samples have been carried out at GELINA to extract the parameters with a higher accuracy. In particular the data sets obtained with thinner samples (5, 10 and 20 μm thick) have been used. It has to be noted that the normalization of capture measurement is not straightforward, since the saturated resonance technique can not be applied. To overcome this problem we deduced the normalization from the nearest resonances, fitting the normalization with resonance parameters fixed to our new values (listed in Table 6.4).

In Figure 6.17 the experimental data together with the fit in the energy region 3 - 7 eV are shown for total angular momentum $J=1$ and in Figure 6.18 the same graphs are presented for $J=2$. The resulting global χ^2 are not so different but looking at the χ^2 per single measurement, it is possible to determine the statistical spin factor and thus the total angular momentum of the first resonance thanks to the self-indication measurement. The list is given in Table 6.6.

As a final remark, for the accuracy of the results we have varied:

- the resolution function (both analytical and MC resolution function have been used);
- the Debye and the ambient temperature (two different Debye temperatures are present in literature);

² $\Gamma_n = 15.2 \pm 0.4$ meV, $\Gamma_\gamma = 124 \pm 3$ meV.

³We recall that R' is related to the coherent scattering length a , by the relation 2.48, or by the following approximation [51]:

$$a \approx R' - 2.277 \times 10^3 \frac{A+1}{A} \sum_j \frac{\Gamma_{nj}^o}{E_{oJ}}$$

where a and R' are expressed in fm. The recommended value [197] for a is 7.9 ± 0.07 fm.

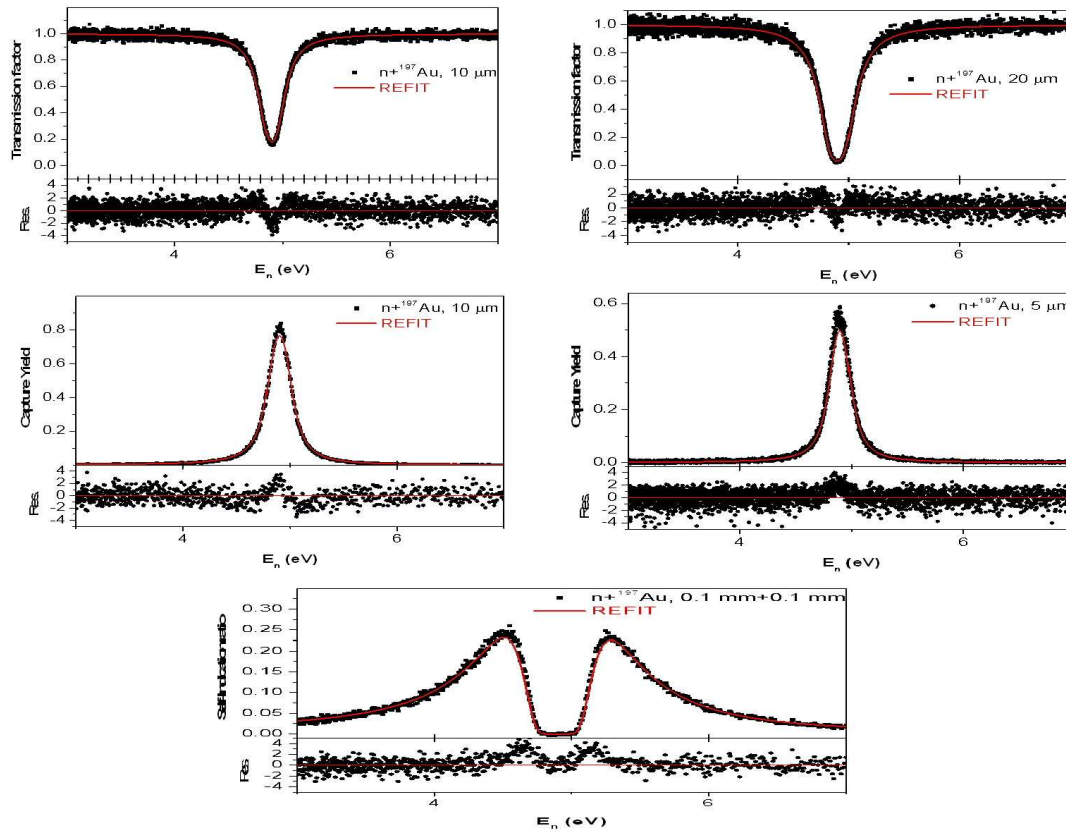


Figure 6.17: The transmission factor, the capture yield and the self indication ratio for a 5, 10, 20, and 100 μm thick samples together with the result of a resonance shape analysis on the 4.9 eV s-wave resonance with total angular momentum $J=1$.

Table 6.6: The χ^2 evaluation, of the 4.9 eV resonance, for total angular momentum $J=1$ and $J=2$. The self-indication measurement presents the larger variation on χ^2 .

Measurement	sample thickness	χ^2	
		J=1	J=2
Transmission	10 μm	1.11	0.97
Transmission	20 μm	1.09	0.98
Self-indication	0.1 mm	1.66	1.04
Capture	5 μm	1.28	1.16
Capture	10 μm	1.27	1.20
Global	-	1.28	1.07

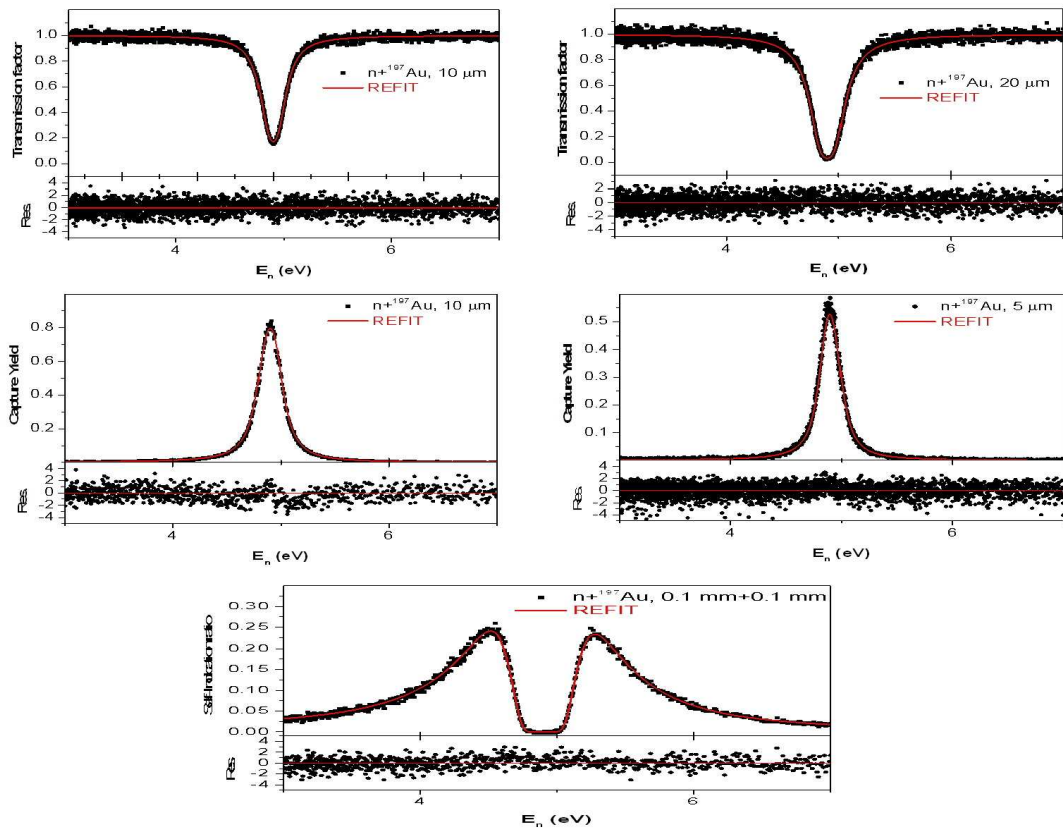


Figure 6.18: The transmission factor, the capture yield and the self indication ratio for a 5, 10, 20, and 100 μm thick samples together with the result of a resonance shape analysis on the 4.9 eV s-wave resonance with total angular momentum $J=2$.

and checked:

- the influence of negative resonances (Radius and negative resonances from ENDF/B-VI and from ENDF/B-VII);
- the influence of a single measurement (only transmission data and transmission plus capture data).

All the results agreed within less than 0.5%. When the new parameters were used to fit the capture data of the thick sample shown in Figure 6.11 an overall better agreement was found using the ENDF/B-VII values for the Radius, and the two negative resonances.

6.6 Comparison with n_TOF TAC data

The last comparison concerns the kernels obtained at n_TOF with the BaF₂ array and the kernels extracted from the new parameters determined at GELINA (listed in Table 6.4). In the Figure 6.19 the kernel ratio is shown. We did not consider the discrepancy for the very weak resonance at about 122 eV (which suffers for the background), the kernel ratio is below 1.05. In average the kernel ratio is 1.01 ± 0.02 , and 1.01 ± 0.03 considering the gaussian fit of the distribution of the kernel ratios.

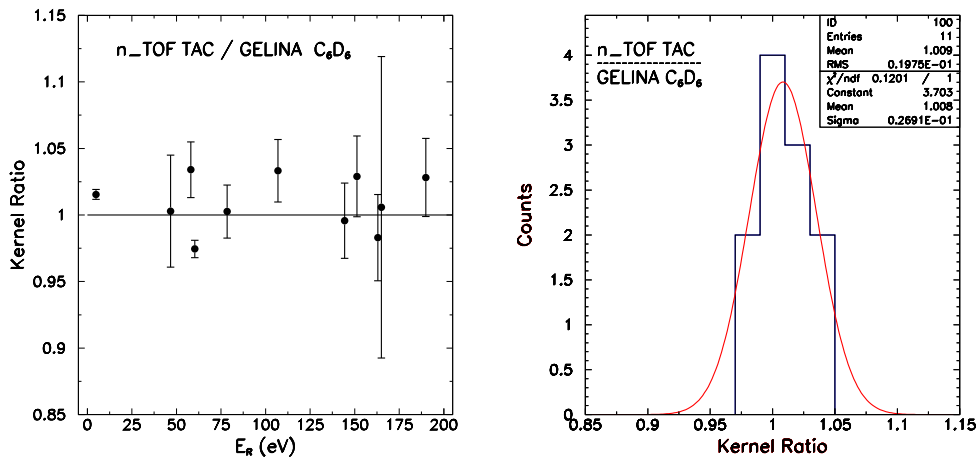


Figure 6.19: The kernel ratio as a function of the resonance energy, between GELINA data and at n_TOF-TAC data, and the relative histogram. The point at 122.334 eV has been excluded, since the resonance parameters have not been determined at GELINA.

Conclusions

The $\text{Au}(n, \gamma)$ is a very important reaction, widely used in nuclear reactors and other applications for neutron flux determination, and commonly employed in neutron facilities as reference for capture reaction measurements. While its cross-section is a standard of measurement at thermal energy and between 0.2 and 2.5 MeV, it is not equally well known in the resonance region, i.e. between 1 eV and a 0.2 MeV. In particular, the R-matrix description of the $\text{Au}(n, \gamma)$ cross section suffers from the lack of transmission data, deterministic spin assignment and accurate neutron capture data.

With the aim of improving the accuracy of the neutron capture cross section of Au in the resolved resonance region, a series of transmission and capture cross-section measurements have been performed at two different neutrons time-of-flight facilities: n_TOF at CERN and GELINA at EC-JRC-IRMM. The measurements reported in this thesis have been performed at the two neutron facilities in completely different conditions of neutron beam, background, flight path length, experimental set-ups, data acquisition, etc... In particular, two conceptually different capture detection systems have been employed: a total absorption calorimeter (TAC), and a total energy system. The motivation for this choice is that a comparison of data obtained with different set-ups would allow to identify and minimize systematic uncertainties related to important experimental effects, such as detection efficiency and neutron sensitivity.

The work here presented was intended to provide an important contribution to an ongoing effort towards the extension of the energy region in which the $\text{Au}(n, \gamma)$ reaction is as considered standard. In this thesis, we have concentrated on the resolved resonance region where, for each resonance, an accurate analysis requires proper experimental conditions, e.g. suitable sample thickness, suitable combination of neutron flux and background level, suitable combination of energy resolution and statistics. Therefore transmission, capture and self-indication measurements have been performed on a large variety of Au samples and experimental conditions.

At the CERN n_TOF facility, the $\text{Au}(n, \gamma)$ cross section has been measured with two C_6D_6 as well as with a new TAC detector, a 4π calorimeter made of BaF_2 scintillators. Although both set-ups are based on the detection of prompt γ -rays following neutron capture reactions, their characteristics, in terms of γ -ray and neutron

response, are completely different, and in some respect complementary. In particular, while the C_6D_6 apparatus is characterised by a low efficiency and low neutron sensitivity, the TAC detector has a very high γ -ray efficiency and good background rejection capability, but suffers from a relatively high neutron sensitivity. Furthermore, while C_6D_6 detector have been extensively used, the n_TOF TAC had never been used prior to the measurement presented in this thesis. For this reason, the comparison with C_6D_6 data has been of great importance for studying the performances of the calorimeter and gaining confidence on the reliability of the results, in view also of the use of the TAC in neutron reaction measurements on radioactive and rare samples (such as minor actinides of interest for advanced nuclear reactors).

The first part of this thesis has been devoted to the analysis of the BaF_2 total absorption calorimeter. A preliminary step consisted in determining the optimal analysis conditions in terms of energy deposited and multiplicity of the γ -ray de-excitation cascade following the neutron capture event. A method was then developed for correcting the capture yield for systematic effects such as pile up and neutron background, relying purely on experimental data. In particular, the pile up has been minimized by imposing a proper threshold on each crystal. A correction for a non-paralyzable dead-time was also included in the analysis, with an additional second order correction related to the particular conditions used in the analysis.

In order to correct for the neutron background in the TAC, two methods have been tested. The first one calculates the contribution of the neutron background starting from neutron scattering data available in literature, while the second method is based on the experimental determination of the background through a dedicated neutron scattering measurement on Carbon. It was found that this second method, although preferable in principle, presents a problem for high counting rates, so that additional information extracted from the first method were used.

With a preliminary R-Matrix analysis, the capture kernels of 263 resonances, from 1 eV to 4830 eV, have been extracted from the TAC data. These kernels (related to the area of the resonances in the $Au(n, \gamma)$ cross section) were compared with the results obtained with the C_6D_6 apparatus at n_TOF, showing in average a very good agreement, with differences of only a few percent. The n_TOF results were also compared with evaluated data available in literature, showing an overall agreement within 4%. However, for some resonances, large discrepancies were found, up to a factor 4, due to the poor accuracy of previous measurements, in particular for small resonances.

In addition, seven resonances, observed before but not included in the ENDF/B-VI or in the ENDF/B-VII evaluations, have been clearly resolved in the present capture measurements.

The results of this first part, i.e. the accurate capture measurements performed at n_TOF, covering in a single measurement the whole resolved resonance region, constitute an important contribution towards a new evaluation of $Au(n, \gamma)$ cross section

in terms of R-matrix.

To further improve the accuracy of the Au(n,g) cross section, the n_TOF data were complemented with capture measurements performed at the GELINA neutron facility with C₆D₆, as well as with transmission and self-indication measurements carried out on a large number of Au samples. The objective of these high resolution measurements was to extract accurate resonance parameters for the parameterization of the Au(n, γ) cross-section in terms of R-matrix. In fact, the combination of complementary measurements allows to derive resonance parameters in a deterministic way, overcoming all possible distortions of the partial widths caused by the experimental conditions.

In the present work, the total angular momentum of 9 resonances, and energy and partial widths of 12 resonances up to 200 eV have been extracted with high accuracy. A particularly important result of this work is the determination of the total angular momentum and partial widths of the 4.9 eV resonance, which is often employed for normalization purposes.

Thanks to a self-indication measurement, and to the use of very thin samples in transmission and capture measurements, it was possible to determine the total angular momentum of this resonance, confirming the value present in evaluated data files. Furthermore, the analysis allowed us to extract the following values for the radiation and neutron widths, respectively: $\Gamma_\gamma = 122.6 \pm 0.2$ meV and $\Gamma_n = 14.99 \pm 0.02$ meV. Including all systematic effects, the uncertainty on the resonances parameters is slightly above 0.5%. Such a very high accuracy, reported for the first time on this resonance, represents an important step forward towards the adoption of a new standard.

An important validation of the results presented in this thesis was provided by the measurement of the Au(n, γ) cross section at thermal energy, which is quoted with 0.1% uncertainty. When using the normalization obtained from the saturated resonance at 4.9 eV resonance, the thermal cross-section was reproduced within 1%, thus confirming the reliability of the measurement data reduction and analysis procedure.

As a final remark, we would like to say that during this thesis, besides all, we had the opportunity of working on different neutron time-of-flight facilities, on different neutron capture detectors, and on different R-matrix codes. The good agreement, within 3%, for the 12 resonances up to 200 eV between n_TOF TAC data and GELINA C₆D₆ data is the starting point for a new evaluation of ¹⁹⁷Au(n, γ) reaction cross-section. We believe that, thanks to these results, the extension of the standard in the resolved resonance region is now within reach.

Appendix A

Boundary conditions to the R-matrix

Different choices on the boundary parameters B_c are possible. For neutron induced reactions ($c = n$), a good choice is $B_c = -\ell$ [89]. The hard sphere phase φ_n , the shift factor S_n and the penetration factor P_n for s-, p- and d-waves can be expressed as indicated in Table A.1. The term $\rho = ka_c$ stands for a function of the channel radius a_c and of the neutron wave number in the centre-of-mass system, which is defined as:

$$k = \frac{1}{\lambda} = \frac{A}{1+A} \frac{\sqrt{2m_n E}}{\hbar}, \quad (\text{A.1})$$

where A is the target to neutron mass.

Table A.1: The hard-sphere phase φ_n , the shift factor S_n and the penetration factor P_n as a function of ρ for s-, p- and d-wave neutrons.

ℓ	0	1	2
φ_n	ρ	$\rho - \arctan(\rho)$	$\rho - \arctan \frac{3\rho}{3 - \rho^2}$
S_n	0	$-\frac{1}{1 + \rho^2}$	$-\frac{3(\rho^2 + 6)}{9 + 3\rho^2 + \rho^4}$
P_n	ρ	$\frac{\rho^3}{1 + \rho^2}$	$\frac{\rho^5}{9 + 3\rho^2 + \rho^4}$

Appendix B

Practical approximations to the R-matrix

B.1 Reich-Moore approximation

The Reich-Moore approximation neglects the off diagonal contribution of photon channel in the so called level matrix. This approximation is valid when there are many channels, which have a decay amplitude with comparable magnitude and random sign. Therefore, their contribution to the sum over the channels ($c \in \gamma$) tends to cancel for $c \neq c'$ [99]:

$$\sum_{c \in \gamma} \sum_{r \neq r'} \gamma_{rc} \gamma_{r'c} \simeq 0 \quad (\text{B.1})$$

It can be shown [100] that the collision matrix becomes a function of a reduced R-matrix:

$$R_{cc'} = \sum_r \frac{\gamma_{rc} \gamma_{r'c}}{E_r - E - i\Gamma_{r\gamma}/2} \quad (\text{B.2})$$

It is a reduced matrix in the sense that $R_{cc'}$ is only defined over the non-photonic channels. The photon channel is explicitly taken into account through the total radiation width $\Gamma_{r\gamma}$:

$$\Gamma_{r\gamma} = \sum_{c \in \gamma} \Gamma_{rc} \quad (\text{B.3})$$

The reduced R-matrix dimension for fissile target nuclei is usually a 3×3 (1 elastic and 2 fission channels). For non-fissile nuclei, the only energetically allowed processes are elastic scattering ($c = n$) and radiative capture ($c = \gamma$) for which the neutron-channel Reich-Moore expression suffices. In the most case the reduced R-matrix is merely a R-function expressed as follow:

$$R_{nn} = \sum_r \frac{\gamma^2}{E_r - E - i\Gamma_{r\gamma}/2} \quad (\text{B.4})$$

From this reduced R-matrix, we get a reduced collision matrix. For the s-wave it is given by:

$$U_{nn} = e^{-2i\varphi} \frac{1 + ik a_n R_{nn}}{1 - ik a_n R_{nn}} \quad (\text{B.5})$$

The elastic (σ_n) and total (σ_{tot}) cross-section are obtained from Eq. 2.11 and 2.13. The capture cross-section (σ_γ) is obtained by the difference:

$$\sigma_\gamma = \sigma_{tot} - \sigma_n \quad (\text{B.6})$$

In the present analysis, n+ ^{197}Au in the resonance region, as well as in the often occurring case, at low energy that only the elastic scattering and neutron capture channel are open, the number of channel in the R-matrix is one, namely that of the neutron channel, the photon channel being excluded explicitly.

B.2 Multi Level Breit Wigner approximation

Several resonances can be taken into account as a sum of Breit and Wigner single level cross-section, also called many-level SLBW. This is the most simple treatment of cross-section of many resonances. It neglects any possible interference between channels and levels (resonances).

The MLBW approximation involves a simple sum over resonances in the collision matrix:

$$U_{cc'} = e^{-ikR'} \left(\delta_{cc'} + i \sum_r \frac{\sqrt{\Gamma_{rc}\Gamma_{rc'}}}{E_r - E - i\Gamma_r/2} \right) e^{-i\varphi_{c'}}. \quad (\text{B.7})$$

In the inverse of the level matrix all off-diagonal element are neglected, which means neglecting all interference terms between channels, but not between levels.

Appendix C

Statistical properties of the resonance parameters

The essential idea of the compound nucleus is that the energy of the incident particle is shared amongst the other nucleons in a time that is short compared to the lifetime of the compound state. According to the Bohr's assumption the decay of the compound nucleus is independent of the way it has been formed. In this way the decay depends only on the energy, spin and parity of the compound state and no correlations exists between the partial widths, e.g. neutron and radiation width in case of neutron radiative capture. The compound nucleus is extremely complex and the density of levels is much higher at the neutron separation energy compared to the density in the region just above the ground state. Due to extreme configuration mixing, the nuclear system at the neutron threshold has a statistical behaviour. The basic assumption is that the compound nucleus states are so complex that the values of the nuclear matrix elements have a Gaussian distribution with zero mean. The distribution of the spacing D of compound nucleus levels of the same spin and parity has been explained by Wigner, who derived the so-called Wigner distribution of level spacings assuming a random matrix ensemble [102]:

$$P\left(\frac{D}{\langle D \rangle}\right) dD = \frac{\pi}{2 \langle D \rangle^2} e^{-\frac{\pi}{2 \langle D \rangle^2} \frac{D^2}{2}} D dD \quad (\text{C.1})$$

where D is the level spacing and $\langle D \rangle$ is the mean level spacing. Eq. C.1 expresses the "level repulsion" effects, which predicts a zero probability of finding levels with zero spacing. An example of level spacing distribution for ^{197}Au is given in Figure C.1. A graphical method of evaluating the average level spacing for the case of s- (and p-) wave resonances of ^{197}Au is illustrated in Figure C.2. The total number of resonances is plotted as a function of energy, then a least squares fit in the linear region is performed, and finally the inverse slope, which is equal to the average spacing, is found. A departure from linearity may indicate that resonances are missed or p-levels are

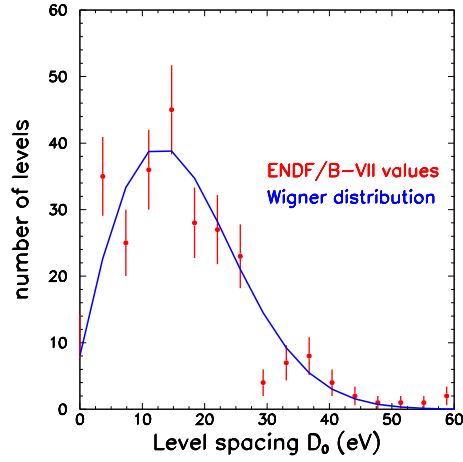


Figure C.1: The Au(n, γ) level spacing distribution of spin $J=1$ and $J=2$ resonances from ENDF/B-VII [55]. The smooth curve is the corresponding Wigner distribution.

included.

In the case of neutron induced reactions, the neutron widths fluctuate strongly among resonances with the same total angular momentum and parity. The theoretical framework for the study of the distribution of reaction widths of compound nucleus states has been provided by Porter and Thomas [99]. The distribution of the reduced neutron widths Γ_n^ℓ normalized to their average values $\langle \Gamma_n^\ell \rangle$ for one single channel is given by the so-called Porter-Thomas distribution:

$$P(x)dx = \frac{e^{-x/2}}{\sqrt{(2\pi x)}} dx, \quad x = \frac{\Gamma_n^\ell}{\langle \Gamma_n^\ell \rangle} \quad (\text{C.2})$$

which is a chi-squared distribution with one degree of freedom (defined as the number of exit channels). This distribution is valid for the widths of any compound reaction related to single exit channels, i.e. for the reduced neutron width Γ_n^ℓ as well as for the partial radiative widths $\Gamma_{\gamma if}$ from an initial state i to a final state f in which case we have $x = \Gamma_{\gamma if} / \langle \Gamma_{\gamma if} \rangle$. Instead of matching the Porter Thomas distribution for neutron channel (Eq. C.2) with observed data, it is more convenient to use a kind of reverse cumulative distribution and compare the number of resonances with a value of x larger than a threshold value x_t :

$$N(x_t) = N_0 \int_{x_t}^{\infty} P(x)dx = N_0(1 - \text{erf}\sqrt{x_t/2}) \quad (\text{C.3})$$

The value N_0 gives the real number of resonances in the energy region considered. At

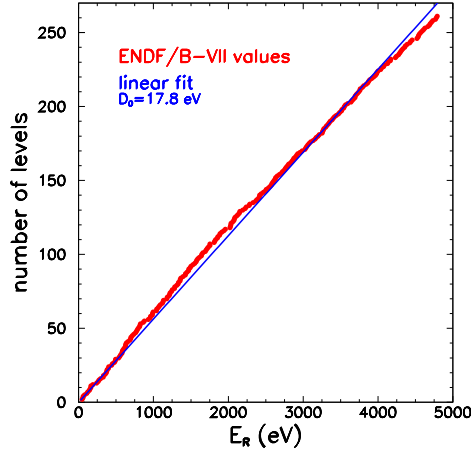


Figure C.2: Cumulative number of s-wave resonances of ^{197}Au as a function of neutron energy. Au data is from ENDF/B-VII nuclear data file.

low thresholds the resonances are generally missing and the data set deviates from the expectation. At higher threshold values, the observed data should be in agreement with the integrate distribution. An example for $n+^{197}\text{Au}$ data present in literature is given in Figure C.3, the expected behaviour is not well reproduced at low $g\Gamma_n$. This could be related to a wrong assignment of resonance parity (p-waves resonances classified as s-wave resonances). Because of the Porter Thomas fluctuations to which all statistical gamma rays are subject, the high-energy primary gamma-ray spectrum in radiative neutron capture varies from resonance to resonance. When several exit channels contribute to the process, the total width is the sum of the relevant partial widths, and the distribution for the corresponding reduced total width can be derived from the Porter-Thomas distribution if the partial width are uncorrelated and have equal mean averaged over many states. Under these conditions the distribution of the total radiation width Γ_γ , which is the sum of all the partial radiation widths, will follow a chi-squared distribution:

$$P(x)dx = \frac{\nu/2}{\Gamma(\nu/2)} \left(\frac{\nu}{2}x\right)^{\frac{\nu}{2}-1} e^{-\frac{\nu}{2}x} dx, \quad \text{with } x = \frac{\Gamma_\gamma}{\langle \Gamma_\gamma \rangle} \quad (\text{C.4})$$

with ν the number of degrees of freedom, representing the number of exit channels or different radiative cascades. In this expression $\Gamma(\nu/2)$ represents the gamma function. The mean value of this distribution is 1 and the variance is:

$$\langle (x - \langle x \rangle)^2 \rangle = 2/\nu \quad (\text{C.5})$$

For most of the compound nuclear reactions, the experimentally determined neu-

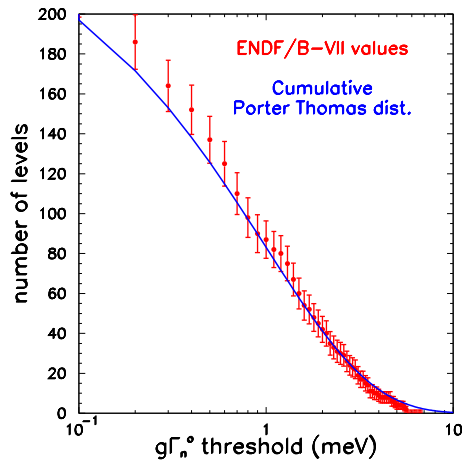


Figure C.3: An example of the integrate number of levels (for $\ell = 0$) above a threshold value of the neutron width together with the prediction of equation C.3 for $n+^{197}\text{Au}$ (data listed in ENDF/B-VII).

neutron reduced widths are in very good agreement with the Porter-Thomas distribution ($\nu=1$). From an analysis of an extensive set of experimental data, Bollinger et al. [103] confirmed the Porter-Thomas distribution for the partial radiation widths of compound nucleus reactions. Some of the experimental data have led to ν values different from one. This can mostly be ascribed to a lack of sufficient resonance data, since the primary problem in such an analysis is that the data are usually too fragmentary for large-sample statistical theory. For many nuclei the total radiation width of resonances with given spin and parity corresponds with a large number of degrees of freedom ν . Therefore, the distribution of the total radiation width approaches a Gaussian.

It was already mentioned that one of the reasons for parameterization of resolved resonance cross-section data is the need to determine level-statistical parameters such as mean level spacing, average widths and strength functions. These average parameters permit the extrapolation to the URR and to the high-energy region¹. An important parameter is the neutron strength function, which is a dimensionless quantity related to the average reduced neutron width. The neutron strength function for a

¹For example, in the unresolved energy region, by averaging the Breit-Wigner total cross-section over an energy region containing many s-wave resonances, one obtains [51]:

$$\langle \sigma_{tot} \rangle = 4\pi(R')^2 + 2\pi\lambda^2\sqrt{E}S_0 + O(S_0)^2,$$

where S_0 is the s-wave strength function.

given orbital angular momentum ℓ are defined by the relation:

$$S_\ell = \frac{1}{\ell + 1} \frac{\langle g\Gamma_n^\ell \rangle}{D_\ell} \quad (\text{C.6})$$

where D_ℓ is the average level spacing of resonances with orbital angular momentum ℓ and g is the statistical weight factor. This expression reduces to:

$$S_\ell = \frac{1}{\Delta E(\ell + 1)} \sum_{i=1}^N g_i \Gamma_{ni}^\ell \quad (\text{C.7})$$

when resonances in the energy interval ΔE are considered. The neutron strength functions is directly related to the average compound nucleus cross-section. In the extreme application of the statistical model, the neutron strength function is energy independent and constant for all nuclei[51]. However, nuclear shell structure effects become apparent when the observed strength functions are plotted as a function of the mass number. These structures (minima in the observed strength functions as a function of the mass number) can be well reproduced by optical model calculation when the s-strength function is related to the imaginary part of the optical model phase shift [51].

Various expressions have been derived for the gamma strength function. The different expression were mostly used to test a particular theoretical model. This has led to a certain degree of confusion and difficulty in using values from one formalism to test predictions of another model. An overview of the different formalisms is given by Lone [104] and Allen [105]. The gamma-ray strength function (downwards) for multipole type XL (E1, M1, ...,), which is universally accepted in nuclear theory and cross-section calculations, is defined as [106]:

$$f_{XL}(E_\gamma) = \frac{1}{D} \frac{\langle \Gamma_{XL}(E_\gamma) \rangle}{E_\gamma^{2\ell+1}} \quad (\text{C.8})$$

where $\langle \Gamma_{XL} \rangle$ is the partial radiation width in eV for a primary transition from an excited state to a lower level state, D is the average level spacing in eV and E_γ is the transition energy in MeV. This function is an important ingredient for theoretical nuclear reaction calculations of capture cross-sections and gamma-ray production spectra. High energy primary transitions with energies ranging from 5 to 7 MeV are mainly of dipole character: E1 and M1 transitions are observed in most cases, while higher multipole transitions are much weaker. Another interesting property of high-energy transitions is that, at least for nuclei with $A > 100$, the E1 transitions are stronger than the M1 by almost one order of magnitude. For the neutron capture in

^{107}Ag For the neutron capture in ^{107}Ag , Zanini et al. [107] reported the value:

$$\frac{f_{E1}}{f_{M1}}(E_\gamma \approx 7\text{MeV}) = 7 \pm 1 \quad (\text{C.9})$$

Several theoretical ideas have been proposed to explain the experimentally observed radiation widths [104, 105]. The simplest model for the strength function, the single particle model, results in energy independent strength functions. However, a large amount of information shows that in case of the predominant E1 radiation the single-particle model overestimates the experimental data by far. Accurate measurements of the primary E1 radiation from neutron resonances indicate that the giant dipole resonance (GDR) model describes the experimental data much better than the single particle model [108]. Another hypothesis, which was first proposed by Brink and later applied by Axel [109], is that giant resonance built on the ground state are similar in shape and size to those built on any excited state. Therefore, the form for the photoabsorption cross-section is equally valid whether applied to the ground state or any excited state. A consequence of Brink's hypothesis is that the photon strength function depends only on the energy of the transition, while it is not dependent on the excitation energy, and one can assume that the radiative width for gamma decay is related to the photon absorption cross-section σ_a as:

$$f_{XL}(E_\gamma) = \frac{1}{E_\gamma^{2L+1}} \frac{1}{s\pi^2\lambda^2g} \langle \sigma_a(E_\gamma) \rangle \quad (\text{C.10})$$

where g is the statistical weight factor for the (γ, x) reaction and λ is the photon wavelength. Simple semiclassical models predict a Lorentzian shape for the photoabsorption cross-section that is dominated by a giant resonance. Applying these ideas, the general expression for the gamma strength function becomes:

$$f_{XL}(E_\gamma) = CE_\gamma \frac{\sigma_R \Gamma_R^2}{(E_\gamma^2 - E_R^2)^2 + E_\gamma^2 \Gamma_R^2} \quad (\text{C.11})$$

where E_γ is the gamma-ray energy and E_R , σ_R and Γ_R are the giant resonance parameters which are mostly derived from photonabsorption experiments. C is a proportionality constant, which for E1 transitions is $8.68 \times 10^{-8} \text{ mb}^{-1}\text{MeV}^{-2}$. In Eq. C.11 the gamma energy E_γ , the resonance energy, and spreading width are expressed in MeV and the peak cross-section σ_R in mb. The simple Lorentzian shape of the absorption cross-section proves to be inadequate at energies close to the binding energies. Various empirical prescriptions have been proposed to correct for insufficiencies of the shape of E1 absorption cross-section. A comprehensive compilation of functional form for the GDR can be found in the review of Allen et al. [105] and Kopecky and Uhl [106]. The uncertainties in the parameterization of the E1 absorp-

tion cross-section affect the ability to calculate capture cross-sections and gamma-ray spectra. As a consequence, such calculations often use relative strength functions of a given shape and apply some normalization based on experimental data. A popular approach is to normalize the M1, E2, ..., strength relative to the predominant E1 contribution and to find the absolute value of the latter by reproducing the experimental f_{E1} strength function observed for s-wave resonances. Recommended average resonance parameters can be found in database "Reference Input Parameter Library" or RIPL, which is produced by and made available from the IAEA. This data has been especially developed to test and improve nuclear model parameters for theoretical calculations of nuclear reaction cross-sections at incident energies below 100 MeV and is of special interest for ADS and Astrophysical applications. The data base reports also systematics neutron and gamma strength functions for most of the nuclei.

Appendix D

Principles of neutron flux measurement

Neutrons coming from the producing target plus moderator assembly are characterized by a broad neutron energy spectrum. To determine the energy dependent neutron flux, the well known $^{10}\text{B}(n,\alpha)^7\text{Li}$ or $^6\text{Li}(n,\alpha)^3\text{H}$ reaction cross-section can be used. Several factors have to be considered in searching for the most appropriate reaction to be used for flux monitoring. First, the cross-section for the reaction must be as large as possible, so that efficient detectors can be built with small dimensions. Second, since gamma-rays are often present with neutron beams, the Q-value of the reaction is important as well as the products of the reactions. The higher the Q-value, the greater is the energy carried by the reaction products, and the easier is the task of discriminating against γ -rays.

Figure D.1 shows a plot of the cross-section versus neutron energy for a number of nuclear reactions of interest in neutron detection: $^{10}\text{B}(n,\alpha)^7\text{Li}$, $^6\text{Li}(n,\alpha)^3\text{H}$ together with $^3\text{He}(n,p)^3\text{H}$. These large and structureless cross-section are proportional to $1/v$ over a large energy range. Although the best solution would be to use ^3He , it can not be used in a efficient way in detectors. Since these reactions are considered as a standard up to 250 keV and 1 MeV respectively, they are widely used in neutron flux detectors (most of them ionization chamber) up to several keV neutron kinetic energy. For higher energies, the reaction used to measure the neutron flux is the standard $^{235}\text{U}(n,f)$ with ionization chamber as fission fragment detector.

D.0.1 The $^{10}\text{B}(n, \alpha)$ reaction

Probably the most popular reaction for the conversion of slow neutrons in directly detectable particle is the $^{10}\text{B}(n, \alpha)$ reaction. It is used at the GELINA facility (see section 3.4 for more details) to measure the neutron flux. The reaction may be written

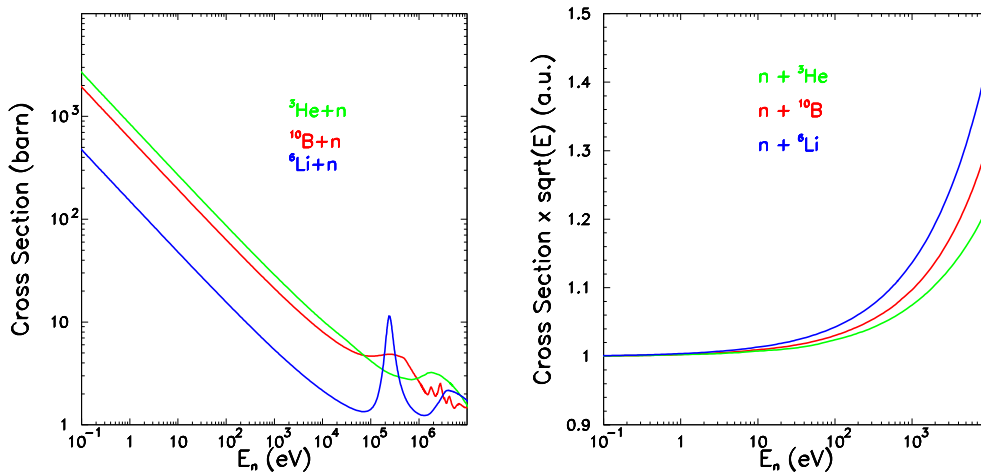
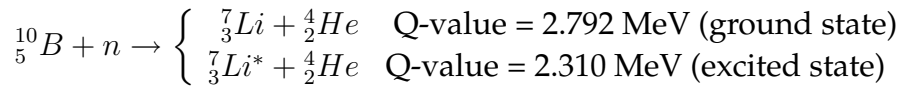


Figure D.1: The $^{10}\text{B}+n$, $^6\text{Li}+n$ and $^3\text{H}+n$ cross-sections as a function of the energy, and the same cross-sections multiplied $1/v$ and normalized to 1, in which the deviation from $1/v$, due to high energy resonances, becomes more clear. Data from ENDF/B-VII.

as:



where the branching indicates that the reaction product ^7Li may be left either in its ground state or in its first excited state. The excited Lithium nucleus quickly returns (half-life of $\approx 10^{-13}$ s) to its ground state with the emission of a 0.48 MeV gamma-ray. When thermal neutrons are used to induce the reaction, about 94% of all reactions lead to the excited state and only 6% directly to the ground state.

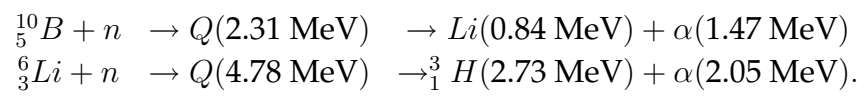
D.0.2 The $^6\text{Li}(n, \alpha)$ reaction

Another popular reaction for the detection of slow neutrons is the (n, α) reaction in ^6Li . This reaction is used at the n_TOF facility as a flux monitor and has been employed in the commissioning phase to measure the flux. In this case the reaction proceeds only to the ground state of the product and is written simply as:



While the $^{10}\text{B}(n, \alpha)$ reaction has the advantage of the $1/v$ shape over a longer energy range and its cross-section is higher, the product of the $^6\text{Li}(n, \alpha)$ are more

energetic¹:



This last feature is the main reason for using this reaction at n_TOF for flux monitor.

¹The calculation of the energy of the reaction products are valid only for negligible neutron incoming energy.

Bibliography

- [1] NEA nuclear data committee, *Nuclear data standards for nuclear measurements*, 1991 NEANDC / INDC nuclear standards file, (1992) NEA/OECD
- [2] V.G. Pronyaev, S.A. Badikov, Chen Zhenpeng et al., in: Proc. Int. Conf. Nuclear Data for Science and Technology, Santa Fe, NM, 2004, AIP Conf. Proc. No. 769, 808 (2005)
- [3] <http://www.nndc.bnl.gov/exfor7/4web/zips/std-ENDF-VII0.endf.zip> (2007)
- [4] <http://www-nds.iaea.org/standards/data.html> (2007)
- [5] R.A. Alpher, H.A. Behte, G. Gamow, Phys. Rev. **73** (1943) 803
- [6] http://www.le.ac.uk/ph/faulkes/web/stars/o_st_overview.html, University of Leicester
- [7] E.M. Burbidge, G.R. Burbidge, W.A. Fowler, F. Hoyle, *Synthesis of the elements in stars*, Rev. Mod. Phys. **29** (1957) 547-650
- [8] C.E. Rolfs and W.S. Rodney, *Cauldrons in the Cosmos*. University of Chicago Press, Chicago, 1988
- [9] G. Wallerstein et al., *Synthesis of the elements in stars: forty years of progress*, Rev. Mod. Phys. **69** (1997) 995
- [10] M. Arnould, K. Takahashi, *Nuclear Astrophysics*, Rep. Prog. Phys. **62** (1999) 395-464
- [11] A.G. Cameron, Pub. Astr. Soc. Pacific **69** (1957) 201
- [12] P.W. Merrill, Science **115** (1952) 484
- [13] F. Gunsing, *Neutron resonance spectroscopy*, CEA/Saclay, DSM/DAPNIA/SPhN
- [14] D.D. Clayton, Ap. J. **139**, 637 (1964).

- [15] D.D. Clayton, Mon. Not. R. Astro. Soc. **234**, 1 (1988).
- [16] K. Fujii, *Resonance analysis of the neutron capture cross sections of $^{186,187,188}\text{Os}$ for the application to Re/Os cosmochronometer*, PhD thesis, University of Padova, Italy, 2009
- [17] M. Mosconi et al. (n_TOF collaboration), *Nuclear physics for the Re/Os clock*, Journal of Physics 014015 (2008)
- [18] International Atomic Energy Agency, www.iaea.org
- [19] Bp statistical review of world energy (2004)
- [20] M. Salvatores, I. Slessarev, A. Tchistiakov, *The transmutation of long-lived fission products by neutron irradiation*, Nucl. Sci. & Eng. **130** (1998) 309-319
- [21] W. Gudowsky, Nucl. Phys. A **654** (1999) 436c
- [22] S. David, A. Billebaud, M.E. Brandan, R. Brissot, A. Giorni, D. Heuer, J.M. Loiseaux, O. Meplan, H. Nifenecker, J.B. Viano, J.P. Schapira, *Fast subcritical hybrid reactors for energy production: evolution of physical parameters and induced radiotoxicities*, NIM A **443** (2-3) (2000) 510-530
- [23] G. Aliberti, G. Palmiotti, M. Salvatores, C.G. Stenberg, *Impact of nuclear data uncertainties on transmutations of actinides in accelerator-driven assemblies* Nucl. Sci. & Eng. **146** (1) (2004) 13-50
- [24] A. Bideau et al., *Sensitivity analysis of nuclear data on k_{eff} for graphite moderated innovative reactors*, OECD/NEA, 2005
- [25] US DOE Nuclear Energy Research Advisory Committee (2002), *A Technology Roadmap for Generation IV Nuclear Energy Systems*
- [26] T.R. England, B.F. Rider, Evaluation and compilation of fission products yields, Tech. Rep. LA-UR-94-3106, ENDF-349, LANL(1994)
- [27] F. Gunsing, A. Brusegan, A. leprête, E. Macavero, C. Mounier, C. Raepsaet, *Neutron resonance spectroscopy of ^{99}Tc from 3 eV to 150 keV*, Phys. Rev. C **61** (054508) (2000) 1-13
- [28] G. Tagliente, K. Fujii, P.M. Milazzo, C. Moreau et al. (the n_TOF collaboration), *Neutron capture cross section of ^{90}Zr : bottleneck in the s-process reaction flow*, Phys. Rev. C **77**, 035802 (2008)
- [29] G. Tagliente, K. Fujii, P.M. Milazzo et al. (the n_TOF collaboration), *Experimental Study of the $^{91}\text{Zr}(n,\gamma)$ reaction up to 26 keV*, Phys. Rev. C **78**, 045804 (2008)

- [30] G. Tagliente, K. Fujii, P.M. Milazzo et al. (the n_TOF collaboration), paper in preparation
- [31] M. Salvatores, A. Zaetta, *Les déchets nucléaires*, Les Editions de Physique, Paris, 1997
- [32] C. Rubbia et al, *Conceptual design of a fast neutron operated high power energy amplifier*, Tech. Rep. CERN/AT/95-44(ET), CERN(1995)
- [33] C.D. Bowman, *Annu. Rev. Nucl. Part. Sci.* **48** (1998) 505
- [34] J. García-Sanz et al., in: *Prot. Int. Conf. Accelerator Driven Transmutation Techn. Appl. ADTTA*, 1999
- [35] C. Rubbia et al., *A realistic plutonium elimination scheme with fast energy amplifiers and thorium-plutonium fuel*, Tech. Rep. CERN/AT/95-53(ET) CERN (1995)
- [36] The NEA high priority nuclear data request list, in:
<http://www.nea.fr/html/dbdata/hpr1>
- [37] B.D. Kuzminov, V.N. Manokhin, in: *Proc. Int. Conf. Nuclear Data for science and technology*, edited by G. Reffo, A. Ventura, C. Grandi, 1997, 1167
- [38] V.G. Pronyaev, Tech. Rep. INDC(NDS)-408, IAEA (1999)
- [39] W.Y. Baek et al., *NIM B* **168** (2000) 453
- [40] Y.V. Grigoriev et al., in: *Proc. Int. Sem. Interact. Neutrons with Nuclei*, ISINN-8, 2000, 68
- [41] G. Lobo et al., *Nucl. Data Sci. Techn.*
- [42] D. Karamanis et al., *Nucl. Sci. & Eng.* **137** (2001) 183
- [43] K. Wisshak, F. Voss, F. Käppeler, *Nucl. Sci. & Eng.* **137** (2001) 183
- [44] P. Schillebeeckx et al., submitted to *Nucl. Sci. & Eng.*
- [45] G. Aerts et al. (the n_TOF collaboration), *Measurement of ^{232}Th neutron capture cross section at the CERN n_TOF facility*, in: *Proc. Int. Conf. Nuclear Data for Science and Technology*, Santa Fe, NM, 2004
- [46] G. Aerts et al. (the n_TOF collaboration), *Neutron capture cross section of ^{232}Th measured at the n_TOF facility at CERN in the unresolved resonance region up to 1 MeV*, *Physical Review C* **73** 054610 (2006)
- [47] M. Calviani et al. (n_TOF Collaboration), *Proc. Int. Conf. Nuclear Data for Science and Technology*, edited by O. Bersillon et al. (CEA, Paris, 2008)

- [48] M. Calviani, *Neutron induced fission cross section on actinides at n_TOF* PhD thesis, University of Padova, Italy, 2009
- [49] *Neutron Fluence Measurements*, Technical Report Series (International Atomic Energy Agency) 107, VIENNA: IAEA, 1970
- [50] *Standard method for determining thermal neutron reaction and fluence rates by radioactivation techniques*, E262-97, ASTM International
- [51] S.F. Mughabghab, *Atlas of Neutron Resonances, Resonance Parameters and Thermal Cross Sections, Z=1-100* Elsevier, 2006
- [52] S.I. Sukhoruchkin, Z.N. Soroko, V.V. Deriglazov, *Low energy neutron physics Volume I/16B, Tables of Neutron Resonance Parameters*, Springer, Landolt-Börnstein, 1998
- [53] JEFF, Joint European fission and fusion file.
- [54] JENDL, Japanese evaluated nuclear data library
- [55] ENDF, ENDF/B-VI, ENDF/B-VII, evaluated nuclear data file
- [56] BROND, Russian nuclear data library
- [57] CENDL, Chinese evaluated nuclear data library
- [58] V. McLane, *ENDF-102, data formats and procedures for the evaluated nuclear data file ENDF-6* Tech. Rep. BNL-NSC-44945-01, Brookhaven National Laboratory (2001)
- [59] Njoy 99, nuclear data processing system (1999)
- [60] PREPO2002: Pre-processing code system for data in ENDF/B format (2002)
- [61] F. Corvi, *Nuclear Data Standards for Nuclear Measurements*, Technical Report Series Na 227, IAEA, Vienna (1983) 83
- [62] International Atomic Energy Agency, *International evaluation of neutron cross section standards*, Tech. Rep. ISBN 92-0-100807-4, Vienna 2007
- [63] R.L. Macklin, *Phys. Rev. C* **9** (1974) 1270
- [64] R.N. Alves, J. Julien, J. Morgenstern and C. Samour, *Détermination du spin et des paramètres des résonances pour $^{197}\text{Au}+n$ DE 1000 eV à 2100 eV*, *Nucl. Phys. A* **131** 2 (1969) 450-480
- [65] M. Alix *Device for the measurement of the neutron radiative capture cross section*, (Thesis) Report CEA-N-1806,7505

- [66] M. Asghar, M.C. Moxon, C.M. Chaffey, *The low energy neutron resonance parameters of $^{107,109}\text{Ag}$, ^{169}Tm , ^{197}Au , ^{159}Tb and ^{165}Ho* , in: Proc. Int. Conf. Nuclear Structure, Antwerp Belgium (1965) 522
- [67] J.S. Desjardins, J.L. Rosen, W.W. Havens, Jr., and J. Rainwater, Phys. Rev. **120** (1960) 2214
- [68] R.C. Block, Y. Danon, R.E. Slovacek, C.J. Werner, G. Youg, *Neutron time-of-flight measurements at the Rensselaer Linac* in: Proc. Int. Conf. Nuclear Data for Science and Technology, Gatlinburg, (1994) 81
- [69] http://irfu.cea.fr/Sphn/NRA_school_2008/, *Resonances in neutron induced reactions*, presented by F. Gunsing at the Summer School on Neutron Resonance Analysis, EC-JRC-IRMM, Geel, June 2008
- [70] J.M. Salomé, Physica, **8** (4) (1986) 261
- [71] K.H. Böckhoff, A.D. Carlson, O.A. Wasson, J.A. Harvey, and D.C. Larson, Nucl. Sci. & Eng. **106** (1990) 192
- [72] K.H. Böckhoff, *Electron linear based pulsed white neutron sources of high resolution neutron time-of-flight spectroscopy, status and perspectives*, Proceedings of Neutron Sources, Group Meeting on Properties of Neutron Sources, Leningrad, USSR, 9-15 June 1986, Published as IAEA Tecdoc 410, 1987
- [73] W. Mondelaers and P. Schillebeeckx, *GELINA a neutron time-of-flight facility for high-resolution neutron data measurements*, Notiziario Neutroni e Luce di Sin-crotrone **11** (2006) 19
- [74] J.M. Salomé, R. Cools, Nuclear Instruments and Methods in Physics Research **179** (1) (1981) 13
- [75] D. Tronc, J. Salomé K.H. Böckhoff, NIM A **228** (1985) 217
- [76] <http://www.phy.orln.gov/nuclear/orela/>
- [77] D.P. Barry, M.J. Trbovich, Y. Danon, R.C. Block, R.E. Slovacek, G. Leinweber, J.A. Burke, N.J. Drindak, Nucl. Sci. & Eng. **153** (2006) 8
- [78] K. Kobayashi, S. Lee, S. Yamamoto, T. Kawano, Nucl. Sci. & Eng. **146** (2004) 209
- [79] P.W. Lisowsky, C.D. Bowman, G.J. Russell, S.A. Wender, Nucl. Sci. & Eng. **106** (1990) 209
- [80] U. Abbondanno et al. (the n_TOF collaboration), *Neutron capture cross section measurement of ^{151}Sm at the CERN neutron time of flight facility (n_TOF)*, Phys. Rev. Lett. **93** (2004) 161103

- [81] U. Abbondanno et al. (the n_TOF collaboration), *New experimental validation of the pulse height weighting technique for capture cross-section measurements*, NIM A **521** (2-3) (2004) 454-467
- [82] G. Lorusso et al. (the n_TOF collaboration), *Time-energy relation of the n_TOF neutron beam: energy standard revisited*, NIM A **532** (3) (2004) 622-630
- [83] S. Marrone P.F. Mastinu, U. Abbondanno, R. Baccomi, E.B. Marchi, N. Bustreo, N. Colonna, F. Gramegna, M. Loriggiola, S. Marigo, *A low background neutron flux monitor for the n_TOF facility at CERN*, NIM A **517** (1-3) (2004) 389-398
- [84] C. Borcea et al., *Results from the commissioning of the n_TOF spallation neutron source at CERN*, NIM A **513** (2003) 524-537
- [85] C. Borcea et al., *First results from the neutron facility (n_TOF) at CERN*, Appl. Phys. A **74** (2002) S55-7
- [86] P.M. Milazzo et al., *Measurements of neutron capture cross-sections for ADS-related studies*, NIM B **213** (2004) 36-41
- [87] J.L. Tain, F. Gunsing, D. Cano-Ott, N. Colonna, C. Domingo Pardo, E. González, M. Heil, F. Käppeler, S. Marrone, P.F. Mastinu, P.M. Milazzo, T. Papaevangelou, R. Plag, R. Reifarth, G. Tagliente, K. Wisshak, *Accuracy of the pulse height weighting technique for capture cross section measurements*, J. Nucl. Sci. Techn., Sup. 2 (2002) 689-692
- [88] S. Marrone, D. Cano-Ott, N. Colonna, C. Domingo, E. González, F. Gunsing, M. Heil, F. Käppeler, P.F. Mastinu, P.M. Milazzo, T. Papaevangelou, P. Pavlopoulos, R. Plag, R. Reifarth, G. Tagliente, J.L. Tain, K. Wisshak, *Pulse shape analysis of liquid scintillators for neutron studies*, NIM A **490** (2002) 299-307
- [89] F.H. Fröhner, *Evaluations and Analysis of Nuclear Resonance Data*, AEN-NEA JEFF Report 18, 2000
- [90] F.H. Fröhner, *Nuclear theory for Applications*, Report IAEA-SMR-43, ICPT Trieste (1980) 59
- [91] H. Feshbach, A.K. Kerman and R.H. Lemmer, *Intermediate structure and doorway states in nuclear reactions*, Annals of Physics **41** (1967) 230
- [92] M.C. Moxon and J.B. Brisland, *REFIT, A least squares fitting program for resonance analysis of neutron transmission and capture data computer code*, AEA-InTec-0630, AEA Technology, October 1991
- [93] A.M. Larson, *Updated Users' guide for SAMMY: Multilevel R-Matrix Fits to Neutron Data Using Bayes' Equation*, ORNL/TM - 9179/R6 ENDF-364, July 2003

- [94] A.M. Lane and R.G. Thomas, *R-Matrix Theory of Nuclear Reactions*, Rev. Mod. Phys. **30** (1958) 257
- [95] A.M. Lane and R.G. Thomas, *R-Matrix Theory of Nuclear Reactions*, Rev. Mod. Phys. **17** (1960) 563
- [96] F.H. Fröhner, *Evaluation of the Unresolved Resonance Region of $^{238}\text{U} + n$, Part II: differential data tests* Nucl. Sci. & Eng., **111** (1992) 404
- [97] N. Koyumdjieva, N. Janeva and K. Volev, *Validation of the characteristic function model for the unresolved resonance region*, Nucl. Sci. & Eng., **137** [2] (2001) 194
- [98] J.E. Lynn, *The theory of neutron resonance reactions*, Clarendon Press, Oxford(1968)
- [99] C.E. Porter and R.G. Thomas, *Fluctuations of nuclear reactions widths*, Phys. Rev. **104** (1956) 483
- [100] C.W. Reich, M.S. Moore, *Multilevel Formula for the fission process*, Phys. Rev. **111** (1958) 929
- [101] G. Breit, E. Wigner, *Capture of slow neutrons*, Phys. Rev. **49** (1936) 519
- [102] E.P. Wigner, Can. Math. Congr. Proc., Toronto (1957) 174
- [103] L.M. Bollinger, R.E. Coté, R.T. Carpenter and J.P. Marion, *Distribution of partial radiation widths*, Phys. Rev. **132** (1963) 1640
- [104] M.A. Lone, *photon strength functions*, Proceedings of the third international symposium on neutron capture gamma-ray spectroscopy and related topics, Brookhaven National Laboratory and State University of New York, 18-22 September, 1978, 161-180
- [105] B.J. Allen, *Theory of slow neutron radiative capture*, in Neutron Radiative Capture, edited by R.E. Chrien, Pergamon Press 1984, 1-32
- [106] J. Kopecky and M. Uhl, *Test of gamma-ray strength functions in nuclear reaction model calculations*, Phys. Rev. C **41** (1990) 1941
- [107] L. Zanini, F. Corvi, H. Postma, F. Becvar, M. Krticka, J. Honzatko, I. Tomandl, *Cascade gamma decay of ^{108}Ag following thermal and resonance neutron capture in ^{107}Ag* , Phys. Rev. C **68** (2003) 014320
- [108] J. Kopecky and R.E Chrien, *Observation of the M1 giant resonance by resonance averaging in ^{106}Pd* , Nucl. Phys. A **468** (1987) 285
- [109] P. Axel, *Electric dipole ground-state transition width strength function and 7-MeV photon interactions*, Phys. Rev. **126** (1962) 285

- [110] A.J. Ferguson, *Angular correlation methods in gamma-ray spectroscopy*, North-Holland publishing company, Amsterdam 1965
- [111] F.H. Fröhner, E. Haddad, W.M. Lopez and S.J. Friesenhahn, *Accuracy of resonance parameters from combined area and self-indications measurements*, Proceedings of the International Conference on Neutron Cross Section Technology, Washington, D.C., 22-24 March, 1996, 55-66
- [112] D.J. Hughes, *A method for rapid analysis of neutron resonances*, J. Nuclear Energy **1** (1955) 237
- [113] J.E. Lynn and E.R. Rae, *The analysis of neutron spectrometer resonance data*, J. Nuclear Energy **4** (1957) 418-444
- [114] E.R. Rae, E.R. Collins, B.B. Kinsey, J.E. Lynn and E.R. Wiblin, *An analysis of slow neutron resonances in silver*, Nucl. Phys. **5** (1958) 89
- [115] J.E. Lynn, *A new development in the area method of neutron resonance analysis*, Nucl. Phys. **7** (1958) 559-612
- [116] F.H. Fröhner, O. Bouland, *Treatment of external levels in neutron resonance fitting: application to the non-fissile nuclide ^{52}Cr* , Nucl. Sci. & Eng. **137** (2001) 70
- [117] A. Foderaro, *The elements of neutron interaction theory*, Cambridge, MIT Press (1971)
- [118] A. Brusegan, G. Noguere, F. Gunsing, *The Resolution Function in Neutron Time-of-Flight Experiments*, J. Nucl. Sci., Supp.2 (2002) 685-688
- [119] L.C. Mihailescu, A. Borella, C. Massimi, P. Schillebeeckx, *Investigations for the use of the fast digitizers with C_6D_6 detectors for radiative capture measurements at GELINA*, NIM A **600** 2 (2009) 453-359
- [120] S. Marrone, E. Barthomieux, F. Becvar, D. Cano-Ott, N. Colonna, C. Domingo Pardo, E. González, F. Gunsing, R.C. Haight, M. Heil, F. Käppler, M. Krticka, P.F. Mastinu, A. Mengoni, P.M. Milazzo, J. O'Donnell, R. Plag, P. Schillebeeckx, G. Tagliente, J.L. Tain, R. Terlizzi, J. L. Ullmann, *Pulse shape analysis of signals from BaF_2 and CeF_3 scintillators for neutron capture experiments*, NIM A **568** (2006) 904-911
- [121] G.F. Knoll *Radiation Detection and Measurement*, 3rd edn. (John Wiley & Sons, 2000)
- [122] M.S. Moore, *Nuclear Instruments and Methods* **169** (1980) 245

- [123] C. Coceva, M. Frisoni, M. Magnani, A. Mengoni, *On the figure of merit in neutron time-of-flight measurements*, NIM A **489** (2002) 346-356
- [124] H.J. Groenewold and H. Groendijk, *Non-thermal neutron cascade* Physica **13** (1947) 141
- [125] F. Gunsing, A. Brusegan, *The resolution function of GELINA modelled in REFIT*, Internal Report DAPNIA/SPhN-00-33.
- [126] F. Gunsing et al. (n_TOF collaboration), *Status and outlook of the neutron time-of-flight facility n_TOF at CERN*, NIM B **261** (2007) 925-929
- [127] C. Rubbia et al., Tech. Rep. CERN/LHC/98-02, CERN (1998)
- [128] A. Ferrari and P.R. Sala, *Intermediate and High Energy Physics Models in FLUKA: Improvements, Benchmarks and Applications*, Proc. Int. Conf. on Nuclear Data for and Technology, NDST-97, ICTP, Miramare, Trieste, Italy, (19-24 May 1997)
- [129] Y. Kadi et al., *The EA-MC Monte Carlo Code Package*, Proceeding of the 5th Meeting on Shielding Aspects of Accelerators, Targets and Irradiation Facilities (SATIF5), Paris (18-21 July 2000)
- [130] S. Andriamonje et al., *Neutron TOF facility (PS213) Technical Design Report*, CERN/INTC/2000-004, Editor: E. Radermacher
- [131] A. Abánades et al., *Results from the TARC experiment: spallation neutron phenomenology in lead and neutron-driven nuclear transmutation by adiabatic resonance crossing*, NIM A **478** (2002) 577-730
- [132] http://www.cern.ch/n_TOF
- [133] U. Abbondanno et al., Tech. Rep. CERN-SL-2002-053 ECT, 2003
- [134] V. Vlachoudis et al., *Particle distribution entering the vacuum tube from a $80 \times 80 \times 60$ cm³ lead target*, SL-Note-2000-029 (EET), (30 March 2000). See also the MC-2000 Conference Proceedings, Lisbon (23-26 October 2000)
- [135] Y. Giomataris, et al., *Micromegas: a high granularity position sensitive gaseous detector for high particle-flux environments*, NIM A **376** (1996) 29-35
- [136] G. Charpak et al., *First beam test results with Micromegas, a high-rate, high-resolution detector*, CERN-LHC/97-08 (EET), DAPHNIA-97-05
- [137] S. Andriamonje et al., *Experimental studies of a MICROMEAS neutron detector*, NIM A **481** (2002) 36-45

- [138] The n_TOF Collaboration, *n_TOF Technical Report*, CERN/INTC 2000-018, (3 November 2000)
- [139] R. Plag, M. Heil, F. Käppeler, P. Pavlopoulos, R. Reifarh, and K. Wisshak. *An optimized C_6D_6 detector for studies of resonance-dominated (n, γ) cross sections*, NIM A **496** (2003), 425
- [140] M. Calviani, P. Cennini, D. Karadimos, V. Ketlerov, V. Konovalov, W. Furman, A. Goverdowski, V. Vlachoudis, L. Zanini and the n_TOF Collaboration, *A fast ionization chamber for fission cross-section measurements at n_TOF*, Nuclear Instruments and Methods in Physics Research Section A **594** 2 (2008) 220-227
- [141] U. Abbondanno et al., NIM A **538**, (2005) 692
- [142] http://irfu.cea.fr/Sphn/NRA_school_2008/, *Time Of Flight Cross Section Measurements*, presented by P. Schillebeeckx at the Summer School on Neutron Resonance Analysis, EC-JRC-IRMM, Geel, June 2008
- [143] Flaska et al., NIM A, **531**, 394 (2004)
- [144] F. Gunsing, CEA/Saclay, presented at WONDER 2006, Cadarache.
- [145] A. Borella, F. Gunsing, M.C. Moxon, P. Schillebeeckx and P. Siegler, Phys. Rev. C **76** (2007) 014605 1-10
- [146] S. Kopecky and A. Brusegan, Nucl. Phys. A **773** (2006) 173
- [147] K. Berthold, C. Nazareth, G. Rohr and H. Weigmann, *Very high resolution measurements of the total cross section of natural Iron*, in Proc. Intern. Conf. on Nuclear Data for Science and Technology, Gatlinburg, Tennessee, May 9-13, 1994 218-220
- [148] S. Kopecky, P. Siegler and A. Moens, *Low energy transmission measurements of $^{240,242}\text{Pu}$ at GELINA and their impact on the capture width*, Proc. Int. Conf. Nuclear Data for Science and Technology, edited by O. Bersillon et al. (CEA, Paris, 2008) 623-626
- [149] J. Heyse, C. Wagemans, L. De Smet, O. Serot, J. Wagemans and J. Van Gils, Nucl. Sci. & Eng. **156** (2007) 211-218
- [150] L. De Smet, C. Wagemans, G. Goeminne, J. Wagemans, J. Heyse and J. Van Gils, Nucl. Phys A **758** (2005) 80-83
- [151] L. C. Mihailescu, C. Borcea, A. J. Koning, A. Pavlik, and A. J. M. Plompen, Nucl. Phys A **799** (2008) 1-29

- [152] A. Borella, *Determination of the neutron resonance parameters for ^{206}Pb and of the thermal neutron capture cross section for ^{206}Pb and ^{209}Bi* , PhD thesis, University of Gent, Belgium, 2005
- [153] P.E. Koehler, R.R. Winters, K.H. Guber, T. Rauscher, J.A. Harvey, S. Raman, R.R. Spencer, J.C. Blackmon, D.C. Larson, D.W. Bardayan, T.A. Lewis, *Phys. Rev. C* **62** (2000) 055803-1
- [154] F. Corvi, *The measurement of neutron capture cross section via prompt gamma-ray detection*, in C. Coceva et al. (Eds.), *Proceedings Specialists Meeting on Measurement, Calculation and Evaluation of Photon Production Data*, Bologna November 9-11, 1994, Report NEA/NSC/DOC (95)1 229-246
- [155] F.H. Beer, F. Corvi, P. Mutti, *Astrophys. J.* **474** (1997) 843
- [156] F.-J. Hamsch, A.D. Carlson, H. Vonach, in: *Proc. Int. Conf. Nuclear Data for Science and Technology*, Santa Fe, 2004
- [157] F.G. Perey, in: *Proc. Int. Conf. Nuclear Data for Basic and Applied Science*, Santa Fe, NM, 1985, 1523-1525
- [158] F. Corvi, G. Fioni, F. Gunsing, P. Mutti, L. Zanini, *Nucl. Phys. A* **697** (2002) 581
- [159] R.L. Macklin, J. Halperin, R.R. Winters, *Nuclear Instruments and Methods in Physics Research* **164** (1979) 213
- [160] A. Borella, G. Aerts, F. Gunsing, M.C. Moxon, P. Schillebeeckx, R. Wynants, *NIM A* **577** (3) (2007) 626
- [161] P. Schillebeeckx, A. Borella, S. Kopecky, C. Massimi, L. C. Mihailescu, M.C. Moxon, P. Siegler, I. Sirakov and T. Ware, *Proc. of the XIII International Symposium on Capture Gamma-Ray Spectroscopy and Related Topics*, 2008 Cologne, Germany, in press
- [162] D.B. Gayter, R.B. Thom, *Prompt gamma-ray detectors for the measurement of the neutron capture cross-section*, *Proceeding Meeting on Fast Neutron Capture*, Argonne, April 1982, Report ANL-83-4, 1983, 205-238
- [163] G.V. Muradyan, Y.V. Adamchuk, Y.V. Shchepkin, M.A. Voskanyan, *Nucl. Sci. & Eng.* **90** (1985) 60
- [164] K. Wisshak, K. Guber, F. Käppeler, J. Krisch, H. Müller, G. Rupp, F. Voss, *NIM A* **292** (1990) 595
- [165] K. Wisshak, F. Voss, F. Käppeler, G. Reffo, *Phys. Rev. C* **42** (1990) 1731

- [166] J.L. Ullmann, U. Agvaanluvsan, A. Alpizar, E.M. Bond, T.A. Bredeweg, E.-I. Esch, C.M. Folden, U. Greife, R. Hatarik, R.C. Haight, D.C. Hoffman, L. Hunt, A. Kronenberg, J.M. O'Donnell, R. Reifarh, R.S. Rundberg, J.M. Schwantes, D.D. Strottman, D.J. Viera, J.B. Wilhelmy, J.M. Wouters, *The detector for advanced neutron capture experiments: a 4π BaF₂ detector for neutron capture measurements at LANSCE*, in: Proc. Int. Conf. Nuclear Data for Science and Technology, Santa Fe, NM, 2004 918-923
- [167] M. Heil, R. Reifarh, M.M. Fowler, R.C. Haight, F. Käppeler, R.S. Rundberg, E.H. Seabury, J.L. Ullmann, J.B. Wilhelmy, K. Wisshak, *A 4π BaF₂ detector for (n, γ) cross-section measurements at a spallation neutron source*, NIM A **459** (2001) 229-246
- [168] R. Reifarh, T.A. Bredeweg, A. Alpizar-Vicente, J.C. Browne, E.-I. Esch, U. Greife, R.C. Haight, A. Kronenberg, J.M. O'Donnell, R.S. Rundberg, J.L. Ullmann, D.J. Viera, J.B. Wilhelmy, J.M. Wouters, *Background identification and suppression for the measurement of (n, γ) reactions with the DANCE array at LANSCE*, NIM A **531** (2004) 530-543
- [169] R. Macklin and J.H. Gibbons, Phys. Rev. **159** (1967) 1007
- [170] K. Kobayashi, Y. Fujita, N. Yamamuro, J. Nucl. Sci. Technol. **18** (1981) 823
- [171] M. C. Moxon and E. R. Rae, Nuclear Instruments and Methods in Physics Research **24** (1963) 445
- [172] F. Corvi, G. Fioni, F. Gasperini, P. B. Smith, *The weighting function of a neutron capture detection system* Nuclear Science & Engineering **107** (1991) 272
- [173] GEANT, *Detector description and simulation tool*, CERN Program Library W5013 (1994)
- [174] J. Briesmeister, *MCNP-A General Monte Carlo N-Particle Transport Code-Version 4c2*, LA-13709-M, 2000
- [175] D. Habs, F.S. Stephens, R.M. Diamond, Report LBL-8945, Lawrence Berkeley Laboratory, USA, 1979
- [176] D. Cano-Ott et al. (n_TOF Collaboration), Proc. Int. Conf. Nuclear Data for Science and Technology, edited by O. Bersillon et al. (CEA, Paris, 2008) 627
- [177] E. Berthoumieux et al. (n_TOF Collaboration), Proc. Int. Conf. Nuclear Data for Science and Technology, edited by O. Bersillon et al. (CEA, Paris, 2008) 571
- [178] C. Massimi et al. (n_TOF Collaboration), Proc. Int. Conf. Nuclear Data for Science and Technology, edited by O. Bersillon et al. (CEA, Paris, 2008) 1265

- [179] D. Cano-Ott et al., *Monte Carlo simulation of the 4π Total Absorption Calorimeter at n_TOF*, n_TOF Internal Report (2003)
- [180] I. Dillmann et al., *The neutron absorber of the n_TOF TAC*, n_TOF Internal Note (2004)
- [181] R. Reifarth et al., *(n, γ) measurement on radioactive isotopes with DANCE*, NIM B **241** (2005) 176179
- [182] F.H. Fröhner, Nucl. Sci. & Eng. **111** (1992) 404-414
- [183] C. Domingo-Pardo et al. (n_TOF collaboration), *Measurement of the radiative neutron capture cross section of ^{206}Pb and its astrophysical implications*, Phys. Rev. C **76** 045805 (2007)
- [184] <http://www.acqiris.com>
- [185] S.D. Jastaniah and P.J. Sellin, *Digital Pulse Shape Algorithms for Scintillation Based Neutron Detectors*, IEEE Trans. Nucl. Sci. **49** (2002) 1824
- [186] S.D. Jastaniah and P.J. Sellin, *Digital techniques for n/ γ pulse shape discrimination and capture-gated neutron spectroscopy using liquid scintillators* NIM A **517** (2004) 202-210
- [187] N.V. Kornilov et al., *Neutron spectroscopy with fast waveform digitizer*, NIM A **497** (2003) 467-478
- [188] Q. Yue et al., *Effective dynamic range in measurements with flash analog-to-digital converter*, NIM A **511** (2003) 408-416
- [189] E. Berthoumieux, *Preliminary report on BaF₂ Total Absorption Calorimeter test measurement*, Tech. Rep., CEA Saclay, DAPNIA/SphN (2004)
- [190] C. Bastian, *AGS, a set of UNIX commands for neutron data reduction*, Proc. Int. Conf. On Neutron Research and Industry, Crete, Greece, 1996, Ed. G. Vourvopoulos, SPIE - The International Society for Optical Engineering, Vol. 2867, 611, 1997
- [191] F. Gunsing *Uncertainty propagation in AGS*, Int. Report DAPNIA/SPh-98-37
- [192] D.B. Syme, *The black and white filter method for background determination in neutron time-of-flight spectrometry*, NIM **198** (1982) 357-364
- [193] D. Ene et al., Proc. Int. Conf. Nuclear Data for Science and Technology, edited by O. Bersillon et al. (CEA, Paris, 2008) 106

- [194] J. Gonzalez, C. Bastian, S. de Jonge and K. Hofmans, *Modular MultiParameter Multiplexer MMPM. Hardware description and user guide*, Internal Report GE/R/INF/06/97, IRMM, Geel
- [195] S. de Jonge, *Fast Time Digitizer Type 8514 A*, Internal Report GE/DE/R/24/87, IRMM, Geel
- [196] A. Borella, *Analysis of GELINA List mode data file*, private communication
- [197] <http://www.ati.ac.at/neutropt/scattering/table.html>